Università degli Studi di Padova

Corso di Dottorato in UNIVERSIT DEGLI STUDI DI PADOVA
Dipartimento di Fisica e Astronomia Galileo Galilei

———————

SEARCHING ELECTROMAGNETIC COUNTERPARTS OF GRAVITATIONAL WAVE SIGNALS

Candidate
Sheng Yang

Supervisors
Prof. Enrico Cappellaro

Prof. Stefano Valenti

PhD Coordinator
Ch.mo Prof. Giampaolo Piotto

———————

ciclo XXXI, 2015-2018

Università degli Studi di Padova, Dipartimento di Fisica e Astronomia Galileo Galilei.

Acknowledgments

I am especially indebted to the great efforts and input of my supervisor, Enrico Cappellaro. Thank you for being my endless source of knowledge. Your patience and inspiration make me into the researcher I am today. I enjoy to work with you and hope that would lasts forever.

I am grateful to my co-advisor, Stefano Valenti. I appreciate your kindly help and selfless support. Thank you for making my Californian year so impressive.

I would especially like to thank all my colleagues from the Padova supernova group: Massimo Turatto, Stefano Benetti, Andrea Pastorello, Lina Tomasella, Nancy Elisa-Rosa, Leonardo Tartaglia, Giacomo Terreran... for helping me rapidly adapt to the Italian lifestyle. I regard Italy as my second hometown not only because of food and coffee.

I'm thankful to all my colleagues from GRAWITA team: Enzo Brocato, Alino Grado, Stefano Covino, Marica Branchesi, Elena Pian, Luciano Nicastro... I enjoy working with you, and indeed, I have learned so much from you. Thanks for your every minute for me.

My gratitude goes to David Sand, for building DLT40, which gave me a chance to discover the kilonova. That's so awesome an experience I will never forget in my life.

Many thanks to my PhD coordinate, Giampaolo Piotto, and our secretaries, Alessandra Zorzi, Anna Bologna, for helping me understand every Italian circular and news, and all staffs from UNIPD, OAPD, and UC Davis, for providing me high quality environments.

Words cannot express how thankful I am to my master supervisor, Zong-Hong Zhu, for giving me the first opportunity to work as an astronomer. Thank you, Jun-Qin Xia, my master co-advisor, for introducing me a coding life. Thank you, Yun-Wei Yu, my bachelor tutor, for your inspiring me to engage in astronomical researches.

I want to thank all the lecturers, teachers and instructors, that have taught and helped me in my life, for helping me better understand what the life is, what the world is, and what the universe is. Thanks, Cesare Chiosi, Laura Greggio, Bianca Poggianti, Chris Sneden, Alessandro De Angelis,..., in my doctoral phase; Bi-Wei Jiang, Jian-Nin Fu, Shao-Lan Bi, Li Chen,..., during my master stage; and when I was an

Abstract

Gravitational-wave (GW) were detected on 14 September 2015 by the Laser Interferometer Gravitational-wave Observatory (LIGO). The following challenge was the joint observation of a Compact binary coalescence (CBC) in both GW and Electromagnetic (EM) channels. This is difficult because GW sky location uncertainties are typically tens or hundreds of square degrees. Multimessenger observations of binary system containing a neutron star were expected to answer many open questions of modern astrophysics, from the nature of short GRB to the origin of heavy elements. For this reason the astronomical community worldwide was preparing for this event. The work of this thesis was developed in this context. My work focused on the search of the possible optical counterparts of GW events. For the search of the expected optical transient I tested, implemented and exploited two complementary approaches using the data of the observing facilties available to the calloborations of which I am member:

a) The GRAvitational Wave Inaf TeAm (GRAWITA), which performs an optical transient search with the 2.6 meter VLT survey telescope (VST). As part of GRAWITA, I developed the transient detection pipeline based on image difference of the wide field survey. I applied this tool to the follow up of three GW triggers, GW150914, GW151226 and GW170814.

b) The Distance Less Than 40 Mpc survey (DLT40), which makes use of 40 cm robotic telescopes for targeting individual galaxies. In this project, I developed a prioritization algorithm to select galaxies inside the GW error-box, with the aim to maximise the detection probability in case of nearby triggers. My algorithm was used to define the strategy and follow-up ten GW triggers.

After a few inconclusive attempts, on August 17, 2017 with DLT40, I contributed to the discovery of the first optical counterpart of a GW source, DLT17ck (labelled also AT2017gfo and SSS17a). With GRAWITA we observed this source with an almost daily cadence for two weeks both in imaging and spectroscopy, proving that the binary neutron star (BNS) merging produces r-process elements. I used the previous record of the DLT40 SN search to derive one of the first direct estimate of the BNS rates. I also contributed to a first attempt to measure the Hubble constant from combined GW-EM observations.

Finally, I developed a machine learning algorithm with the aim of a more rapid and efficient transient candidate selection. This tool is already implemented in the ongoing DLT40 SN survey and it will be used by GRAWITA in the incoming LIGO-VIRGO collaboration (LVC) O3 run.

Sommario

Il 14 settembre 2015, le onde gravitazionali (GW) sono state finalmente rivelate dai due interferometri della collaborazione LIGO e Virgo. Un'ulteriore sfida che si presentava era l'osservazione congiunta della fusione di due stelle a neutroni sia attraverso le onde gravitazionali che come segnale elettromagnetico (EM). Il problema di tale ricerca la localizzazione incerta dei rivelatori di onde gravitazionali, con zone di cielo da osservare, decine o anche centinaia di gradi quadrati. D'altro canto, osservazioni multi-messengero di questo tipo di eventi consentono di rispondere a molte questioni aperte della moderna moderna, fornendo informazioni sull'equazione di stato della materia nelle stelle a neutroni, alla natura dei lampi di luce gamma corti fino all'origine degli elementi pesanti. Per questa ragione gli astronomi di tutto il mondo si sono preparati per questo evento. In questo contesto, il mio lavoro si focalizzato principalmente alla rivelazione delle possibili controparti ottiche di eventi GW. Nel mio lavoro di tesi, ho sviluppato, testato ed infine utilizzato due approcci complementari utilizzando i dati ottenuti dagli strumenti di osservazione accessibile alla nostre collaborazioni:

a) la collaborazione INAF GRAWITA che utilizza per la ricerca di transienti ottici il telescopio VST di 2.6m. Come membro di GRAWITA, ho sviluppato le procedure per la rivelazione dei transienti sulle immagini a grande campo. Ho applicato queste procedure nella ricerca di controparti per the eventi GW: GW150914, GW151226, GW170814.

b) il progetto "Distance Less Than 40 Mpc survey" (DLT40) che utilizza telescopi robotici di 40cm per puntare singole galassie. In questo progetto, ho sviluppato l'algoritmo per assegnare le priorita' alle galassie selezionate all'interno della regione di incertezza delle GW, con l'obbiettivo di massimizzare la probabilitá di rivelazione nel caso di segnali a distanza relativamente piccola. Ho utilizzato queste strategia di ricerca per 10 eventi GW.

Dopo alcuni tentativi infruttuosi, il 17 agosto 2017, nel contesto delle programma DLT40 ho dato il mio contributo alla scoperta della prima controparte ottica di una sorgente GW, DLT17ck (anche chiamata AT2017gfo e SSS17a). Con la collaborazione GRAWITA abbiamo osservato questa sorgente sia con immagini che con spettroscopia con cadenza quasi giornaliera per due settimane dimostrando che nel processo di fusione di due stelle di neutroni vengono prodotti elementi pesanti con il processo. Allo stesso tempo, ho usato l'archivio delle osservazioni della ricerca di supernovae di DLT40 per derivare una prima stima della frequenza di BNS. Ho anche contribuito ad un primo tentativo di misurare la costante di Hubble attraverso la combinazione di osservazioni GW/EM.

Infine, ho sviluppato un algoritmo di "machine learning" con lo scopo di semplificare e velocizzare la selezione dei candidati dalle immagini. Questo algoritmo e' gia in funzione per la ricerca di supernovae in DLT40 e sara' utilizzato in GRAWITA per il prossimo run della collaborazione LIGO-VIRGO (O3).

摘要

2015年9月14日，激光干涉引力波天文台（LIGO）终于探测到了引力波信号。 对于天文学家而言，下一个具有难度的挑战则是同时观测双致密天体合并事件产生的引力波信号与电磁波信号。 因为在现阶段引力波信号通常可以达到几百个平方度，其定位还并不精确。然而这很有意义，对这种天体的多信使观测，可以回答现代天文物理的很多开放问题，诸如短伽马射线暴的本质、重元素的起源等。 本论文的工作也正是在这种背景下开展的，且更侧重于搜寻引力波源的光学波段。 本研究所涉及的合作项目主要通过两种互辅的方法，来搜寻引力波光学对应体：

a）GRAWITA项目组通过一台主镜为2.6米口径的VST望远镜进行光学波段搜寻。 作为GRAWITA的一员，我主要贡献设计了它的变源搜索软件。此软件主要使用图像差的方法，处理大视场巡天观测图像进行差值，进而搜寻其中的瞬变源 我们利用这个工具，分析了GRAWITA跟随的三颗引力波信号源图像：GW150914，GW151226和GW170814。

b）DLT40项目组则采用40厘米自动化望远镜来进行星系搜寻。作为项目一员，我主要设计了一个星系选择程序。此程序可以筛选评估引力波源范围内的临近星系，从而最大化跟随观测概率。 我们采用此策略，追踪了十颗引力波源。

在2017年8月17日，DLT40独立发现了引力波源GW170817的光学对应体DLT17ck（也被称为AT17fgo或者SSS17a）。 GRAWITA项目组在随后两周内，对DLT17ck进行了测光和光谱上的跟踪观测，结果显示这颗源与快中子俘获所产生的千新星模型所相符，是引力波源GW170817的光学对引体。 同时，我也利用DLT40对DLT17ck的观测记录，预测了此类双中子星并合事件的概率。

最后，我开发了一套机器学习算法，用以提高变源候选体筛选的效率，此算法已经在进行中的DLT40超新星巡天项目运用，并且也将在即将到来的第三次LIGO和VIRGO联合引力波巡天中，应用到GRAWITA的电磁对应体搜寻中。

Contents

List of Figures

List of Tables

Chapter 1

Multi-messenger astronomy

In this chapter, I give a brief review of the multi-messenger astronomy (MMA), its motivations, targets, approach and difficulties. In particular, I will give more emphasis to electromagnetic and gravitational waves to which I devoted most of my efforts. Unlike the electromagnetic messenger, which is known since the dawn of human history, gravitational wave is predicted by Albert Einstein in his General Relativity theory. On Sep 14 2015, the detection of the first gravitational wave signal by the two advanced LIGO interferometers provided the definitive confirmation of Einstein theory. On Aug 17 2017, one binary neutron star system was detected in both gravitational wave and electromagnetic radiation. A new multi-messenger astronomy era has begun.

1.1   Introduction

Physics is the natural science that studies matter and describes forces and motion. The matters and forces in the universe are described well by the standard model of elementary particles, see Fig. 1.1. The standard paradigm is that matter is made of quarks and leptons. There're two kinds of leptons, electrons and neutrinos. Quarks and electrons form protons and neutrons, which can then build up different nuclei of elements. Neutrinos are particles created by various radioactive decays and are only affected by the weak force and gravity. Besides matter particles, there're some specific bosons [1], creating different fundamental forces that affect the particle motion: strong interaction

---

[1]In quantum mechanics, a boson is a particle that follows Bose-Einstein statistics. Unlike Fermions, two bosons can occupy the same quantum state.
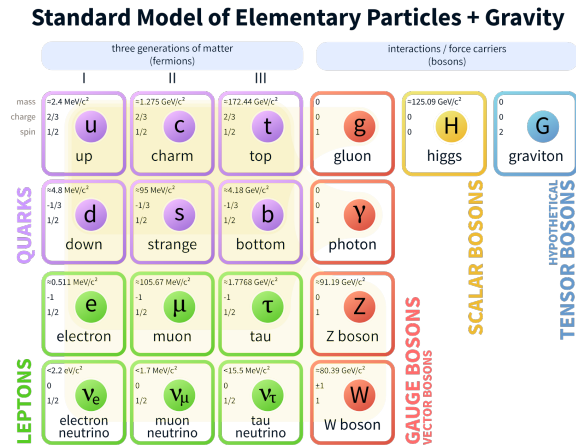
Figure 1.1: The Standard Model of elementary particles with the three generations of matter, gauge bosons in the fourth column, and the Higgs boson in the fifth. Wiki

with gluons, electromagnetic interaction with photons, weak interaction with W and Z bosons, and gravitational interaction with gravitons which is still hypothetical. Higgs field in standard model is a hypothetical field that is supposed to be responsible for giving particles their masses. The quantum theory proclaim that matter particles may also have the wave-like nature in macro world, which is called the wave-particle duality. As a consequence of wave-particle duality, all quantum fields have a fundamental particle associated with them and vice versa. The particle associated with the Higgs field is called the Higgs boson. Likewise, matter particles can be explained as matter waves. Light can be explained as a set of photons, inferred from the photoelectric effect, meanwhile in macro world, Maxwell's equations describe light as an electromagnetic wave. Although the graviton has not beed detected yet, Albert Einstein introduce the spacetime in his General Relativity [GR; Einstein , 1914, 1915a,b,c] to explain the gravity at the macro world and on that basis predicted the existence of gravitational waves, which has achieved a great success.

In astronomical researches, astronomers study the physics of universe by collecting and extracting informations from particles or waves outside the atmosphere. Considering the standard model of elementary particles, the matter and antimatter [2] particles in the universe can be the messenger, which are collected as cosmic rays and neutrinos.

---

[2] In particle physics, every type of particle has an associated antiparticle with the same mass but with opposite physical charges, such as electric charge.
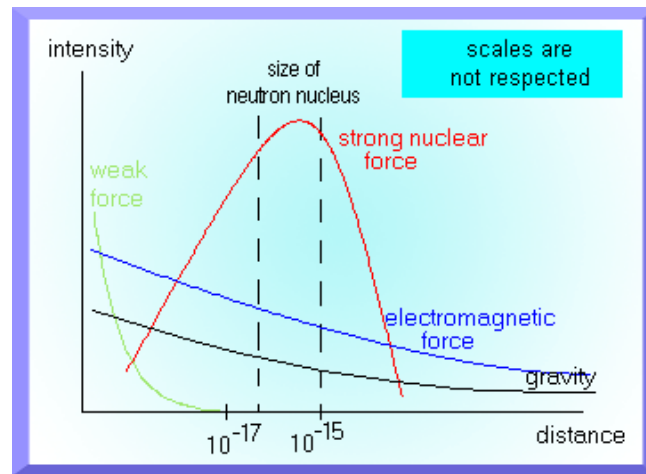
Figure 1.2: On a great scale, only gravitation and electromagnetism can play a part. http://nrumiano.free.fr/PagesU/Eindex.html

For the four kinds of bosons [3], After considering the functional scale, see Fig. 1.2, EM and GW deemed to be important on cosmological scales. Therefore, there are four messengers in astronomy so far, namely EM, GWs, neutrinos, and cosmic rays, which are created in different astrophysical and cosmological processes, and can probe different physics properties of their sources. Fig. 1.3 presents different sky maps from different messengers, showing their distance horizons and energy scales.

MMA is the investigation of the cosmos based on the coordinated observation and interpretation of multiple messengers. MMA is expected to tell us more about the sources than single messenger since each messenger gives complementary insight about the inner physical process. In this following, I will briefly review the four known astronomical messengers, the mechanics, astrophysical sources and dedicated detectors. Afterwards, I describe the potential MMA astrophysical sources and implements.

1.2   Electromagnetic radiation

EM radiation is the most used messenger in astronomy, including light, which is visible to the human eye. Morden optics started in 17th century, Sir Isaac Newton believes that light is composed of particles, which explained well the reflection of light, but not refraction. Also, with the use of a prism, he demonstrated that light is a mixture of

---

[3]gluon, photon, W/Z boson and graviton.
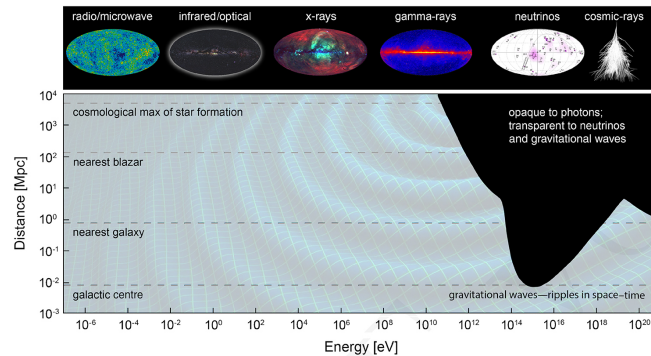
Figure 1.3: Distance horizon at which the Universe becomes optically thick to electromagnetic radiation. While lower-energy photons can travel to us from the farthest corners of the Universe, the highest energy photons and cosmic rays are attenuated after short distances, obscuring our view of the most energetic cosmic events. In contrast, the Universe is transparent to gravitational waves and neutrinos, making them suitable probes of the high-energy sky [Bartos et al., 2017].

various colours having different refractivity. At the same time, Christiaan Huygens advocated his theory that light is a wave, which is then proved by Thomas Young's diffraction experiment. In this context, Young proposed that different colours are caused by different wavelengths of light. The light wave was subsequently proved to be an EM wave whose behaviour and propagation are described by the Maxwell's equations. The wave theory of light has achieved a great success until the end of 19th century. With the coming of 20st century, the wave-like nature of light can be hard to explain the black body radiation. Albert Einstein revived the particle theory of light to explain the photoelectric effect, opening the debate of wave-particle duality and quantum theory. EM radiation in astronomy shows more wave-like nature in the process of its passing through the inter-galactic and inter-stellar medium while behaviours as photons when they're collecting by detectors.

Apart from visible light, X ray, gamma ray and radio were successive discovered. Now, we know EM radiation is a distribution of several EM messengers, from high energy gamma rays to long radio waves, see Figure 1.4. In general, astrophysical sources can emit EM radiation of different wavelength. Astronomical researches with joint multi bands observations is known as Multi-wavelength astronomy (MWA). MWA observations of astrophysical systems can yield insights in to the system that are not available from a single wavelength. For instance, one of the most mysterious astrophysical event, Gamma-Ray Burst (GRB), the gamma detection is limited in use to
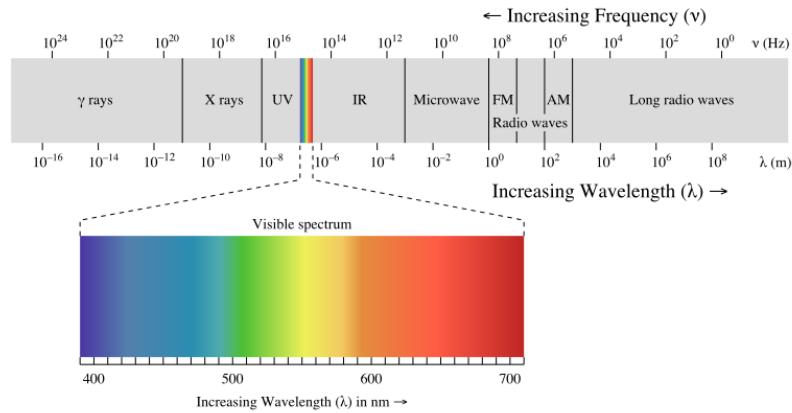
Figure 1.4: Electromagnetic spectrum with light. Wiki

know its inner nature, however, the X ray, optical and radio follow-up would allow us to learn more, at least for long GRBs by allowing to

- measure the source position (X ray);

- find the redshift and the associated SN (optical);

- measure the long term afterglow (radio) indicative of a beamed jet.

MWA is also applied in cosmology that both optical data, type Ia SNe, and radio data, cosmic microwave background (CMB), are combined to constrain the dark energy.

Comparable benefits may be also expected from the MMA sources. The EM radiation provide us rich knowledges and play an important role in MMA research since light is the most frequent and fastest [4] messenger.

In order to accumulate the astrophysical knowledges, the astronomers design kinds of detectors to collect and refine informations from the messengers. Depending on their internal properties, several facilities are built to collect lights with different wavelength, e.g. traditional telescope are used to trace visible light, parabolic antennas for the radio light and photo counters used to reveal high energy light. After photons acquirement, several equipments are used to extract light's informations, e.g. the novel CCD technology output the photometry indicating the brightness of source, the spectroscope can be used when the source is relatively bright and reveal details of lights in various wavelengths.

---

[4]In the speed of light. Considering the other messengers: gravitational wave and neutrino travel with the same speed, and cosmic rays is slower than light.

Table 1.1: Most common reactions involving electronic neutrinos and antineutrinos with neutrons and protons (n and p) and their traditional names: $\beta^{\pm}$ decay, electron (positron) capture, Inverse Beta Decay (IBD). Table taken from Gallo Rosso et al. [2018]

name	reaction
β^- decay	$n \to p + e^- + \bar{\nu}_e$
β^+ decay	$p \to n + e^+ + \nu_e$
β^- capture	$p + e^- \to n + \nu_e$
β^+ capture	$n + e^+ \to p + \bar{\nu}_e$
IBD	$p + \bar{\nu}_e \to n + e^+$
IBD on n	$n + \nu_e \to p + e^-$

1.3   Neutrinos

Neutrino is a kind of lepton that interacts only via the weak force and possibly gravity. The weak force has a very short range, and gravity is extremely weak on the subatomic scale, see Fig. 1.2, so that neutrinos typically pass through normal matter unimpeded and undetected. This explains why it is very difficult to be detected. There are 3 types of neutrinos, i.e. v_e, v_μ, v_τ, traditionally called 'flavors', corresponding to the charged particles, electron (e), the muon (μ), the tau (τ), however, with no charge. In Tab. 1.1 is showing reactions that involving neutrinos and its corresponding particles, when interacting with matter. Neutrino detection relies on inverse beta decay, electron or muon classification via Cherenkov radiation, etc.

Because of the neutrinos' elusive behavior, their existence was not even known until 1959 even though they had been predicted back in 1931. Wofgang Pauli first predicted the neutrino in order to account for the apparent loss of energy and momentum that he observed when studying radioactive beta decays. He predicted that the energy was being carried off by some unknown particle. Then in 1959, Clyde Cowan and Fred Reines finally found a particle that fit the description of the proposed neutrino by studying the particles created by a nuclear power plant. By doing this they actually discovered the electron neutrino. The next big discovery was that of the muon neutron found by Leon Lederman, Mel Schwartz, and Jack Steinberger, scientists at CERN. They did this by firing a GeV proton beam through a target thus producing pions, muons, and muon neutrinos.

Astrophysical neutrinos are created by radioactive decays, including beta decay of atomic nuclei or hadrons, nuclear reactions such as those that take place in the core

of a star during core collapse, in the spin-down of a neutron star, or when accelerated particles strike atoms. In general, there are three types of astrophysical neutrinos, namely, solar neutrinos, supernova neutrinos, and high energy cosmic neutrinos.

The first experiment to attempt to detect electron neutrinos from the sun was conducted by a detector in the bottom of the Homestake mine in South Dakoda in 1968. However they detected only neutrinos about twice a week. It was predicted however that the detector should find about one of the 10^{16} solar neutrinos a day. This unexplainable lack of solar neutrinos detected became known as the Solar Neutrino Problem. The discrepancy was finally resolved around 2002 that the neutrinos actually oscillate between the different 'flavors' after being emitted from the sun as electron-neutrinos. Therefore they were not detecting all of the neutrinos because some had changed into muon and tau neutrinos. The MMA search with light and neutrinos achieved a great success in 1987, when SN 1987A was detected with optical telescopes and neutrinos were then detected with the Kamiokande-II, IMB and Baksan neutrino observatories [Hirata , 1987]. The only astronomical sources previously observed by neutrino detectors were the Sun and supernova 1987A, which were detected at low neutrino energies. On 2018 July 12, an international team of scientists led by the IceCube Neutrino Observatory provided evidences for detecting high energy astrophysical neutrinos from a known blazar, TXS 0506+056 [IceCube , 2018], which was detected on 22 September 2017. The neutrino follow-up of GW sources is active, however, no neutrino/GW connection has been found, yet [Adrián-Martínez et al., 2016; Agostini et al., 2017; Albert et al., 2017d; Moharana et al., 2016].

1.4   Cosmic rays

Cosmic rays (CR) are high-energy particles mainly originating outside the atmosphere and even from distant galaxies. Such solar, galactic or even extra-galactic particles are electrons or atomic nuclei, including simple protons, alpha particles or nuclei of heavier elements, or even antimatter particles, such as positrons or antiprotons. In Fig. 1.5 is showing the CR spectrum with different origins and different types. The detectable CR flux decreases when its energy increases, with protons dominating. Upon impact with the Earth's atmosphere, CRs produce showers of secondary particles, including neutrons, pions, positrons and muons. In order to collect messages from CRs, detectors are designed to search either Cherenkov radiation for primary CRs, or secondary particles created in nuclear reactions, e.g. muons or neutrinos.

In 1940s, some CRs are identified as forming in solar flares [Spurio, 2015], which is
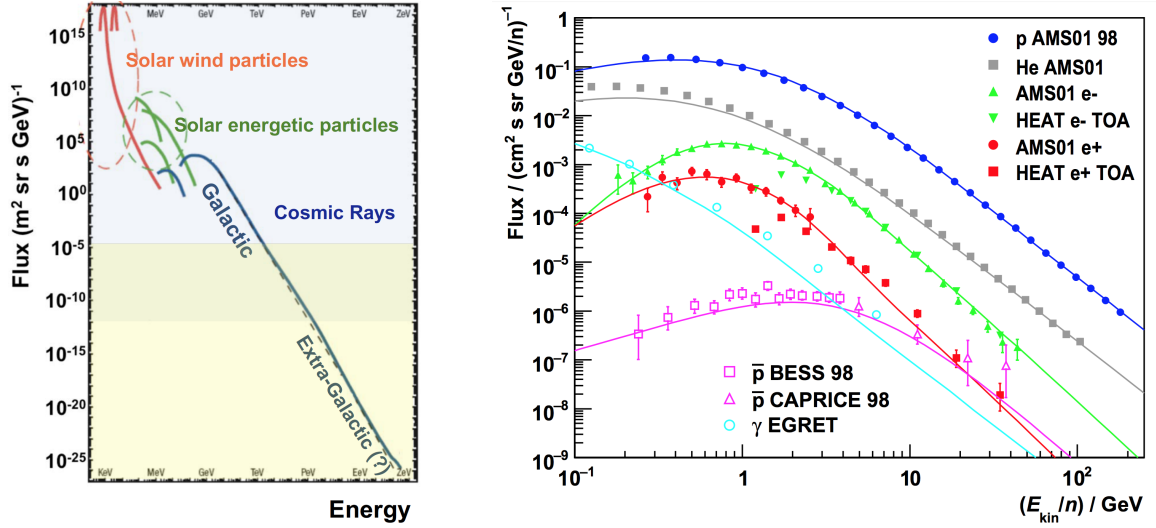
(a) The CR spectrum. Credit by Roberto Battiston

(b) Spectrum of different CR particles [Beischer et al., 2016].

Figure 1.5: The spectrum of cosmic rays.

the first MMA source combining light with CRs. However for CRs originating in further place, it's challenging to identify their sources, since they are electrically charged and as a consequence, they would be bent in the magnetic fields that fill space. Neutrinos are used as a probe to trace further CRs since they are electrically neutral and are unaffected by magnetic fields. Beside the charge problem of CRs, another innegligible matter is that the velocity of CRs is not equal to the speed of light. The discrepancy would result in the time delay of CRs compared with the other messengers, especially when sources placing distantly. Such time delay would pose a challenging for the MMA observations between CRs, with interval signals travelling in the speed of light, e.g. GW from burst events.

Supernovae explosion, pulsars, relativistic jets, active galactic nuclei (AGN) have been proposed as sources of CRs although unambiguous evidences have still to be found. These sources can emit photons, neutrinos or GW at the same time, which let them turn to potential MMA sources. As shown in section 1.3, neutrinos originating from blazar, TXS 056+056 has beed detected, which thus indicate a cosmic engine powerful enough to accelerate high-energy cosmic rays and produce the associated neutrinos.

1.5 Gravitational Waves

While in the standard particle model, graviton is still hypothetical, the wave nature, GW were predicted by Albert Einstein in his General Relativities in 1916 and detected by LIGO in 2015. GW is a unique messenger which is hard to interact with intermedium.

1.5.1 Gravity and Gravitational Wave

The investigation on the nature of gravity has a long history going back at least to Aristotle who believed that objects fall with a speed that is proportional to their weight. About 2,000 years later in the 17th century, Galileo's Pisa tower experiment [5] showed that all objects accelerated equally when falling. In the late 17th century, Robert Hooke proclaimed that there is a gravitational force which depends on the inverse square of the distance. And, Isaac Newton was able to mathematically derive Kepler's three kinematic laws of planetary motion. The classical Newtonian mechanics [Newton , 1687] consider gravity being some force which acts between two bodies:

$$F = G\frac{m_1 m_2}{r^2} \tag{1.1}$$

while F is the gravity, G is the gravitational constant, $m_{1,2}$ are the masses while r is the distance.

Also, the Newtonian mechanics proclaims that the force of object relies on its own motion state. Newtonian mechanics assumes the existence of a special family of reference frames in which the mechanical laws of nature take a comparatively simple form. These special reference frames are called inertial frames, whose relationships are described by the Galilean transformation,

$$
\begin{aligned}
x' &= x - vt \\
y' &= y \\
z' &= z \\
t' &= t
\end{aligned}
\tag{1.2}
$$

while these equations describes an object moving along x axis. We can then derive the first equation with respect to time,

$$u' = u - v \tag{1.3}$$

---

[5]Most historians consider it to have been a thought experiment rather than a physical test.

The Newtonian classical mechanics works well for the macro, low speed objects in inertial frame of reference. However, the results from Michelson-Morley experiment and Fizeau interferometer show that light would travel with constant speed, which is obviously against the Galilean transformation, i.e. equation 1.3. Albert Einstein solved the light speed problem in his Special Relativities [SR; Einstein , 1905a,b] by adopting a relative time and space with Lorenze transformation:

$$
\begin{aligned}
x' &= \frac{x - vt}{\sqrt{1 - \frac{v^2}{c^2}}} \\
y' &= y \\
z' &= z \\
t' &= \frac{t - \frac{v}{c^2}x}{\sqrt{1 - \frac{v^2}{c^2}}}
\end{aligned}
\tag{1.4}
$$

The Einstein's SR concerns only the electromagnetic interaction in inertial coordinate system. In order to make his theory more universal, Einstein's General Relativity [GR; Einstein , 1914, 1915a,b,c] includes gravity, which is described as the curvature of spacetime determined by the distribution of energy-momentum. In standard tensor notation, the gravity and the spacetime are given as,

$$
G_{\mu,\nu} = R_{\mu,\nu} - \frac{1}{2}g_{\mu,\nu}R = \frac{8\pi G}{c^4}T_{\mu,\nu}
\tag{1.5}
$$

where $R_{\mu,\nu}$ is the Ricci tensor, $g_{\mu,\nu}$ is the four dimensional spacetime metric, R is the Ricci scalar and $T_{\mu,\nu}$ is the energy-momentum tensor of matter. $G_{\mu,\nu}$ is the space-time geometry while $T_{\mu,\nu}$ is the mass-energy, which reads that the gravity is a consequence of the curvature of spacetime, while in turn spacetime curvature is a consequence of the presence of matter. John Wheeler sum this up neatly as follows: "Spacetime tells matter how to move, matter tells spacetime how to curve." That is, matter creates gravity, which is not a force attracting other matter, but a curvature of spacetime that create a potential well, forcing other matter falling inside, see Figure 1.6. So far all tests of GR predictions have been confirmed, e.g. the precession of the perihelion of Mercury [6], the gravitational redshift [7], the deflection of light [8] and the existence of gravitational waves [Abbott et al., 2016b].

---

[6]As seen from Earth the precession of Mercury's orbit is measured to be 5600 arcseconds per century with a discrepancy of 43 arcseconds compared with Newton's prediction

[7]the Pound-Rebka experiment which measures the redshift of light moving in a gravitational field

[8]Bending of light by gravity is predicted by GR to be twice than Newton, and was proved during a solar eclipse in 1919
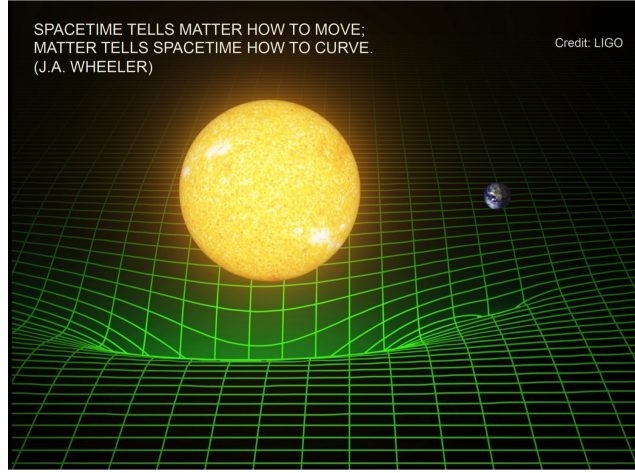
Figure 1.6: A metaphor for gravity as spacetime curvature is to visualise a stretched sheet of rubber, deformed by the presence of a massive body. Spacetime curvature affects the movement of matter, which reciprocally determines the geometric properties and evolution of spacetime.

Due to the symmetry in $R_{\mu,\nu}$, $g_{\mu,\nu}$ and $T_{\mu,\nu}$, the resulting field equation comprises of a set of 10 coupled non-linear differential equations. In order to mathematically solve these equations, it is useful to consider a GR simple approximation. The linearized gravity is only valid when an observer is placed at large distance from a source so that the gravitational field is weak, which is known as the weak-field approximation, with $T_{\mu,\nu} \sim 0$. In this weak field scenario, the spacetime metric may be written as

$$g_{\mu,\nu} = \eta_{\mu,\nu} + h_{\mu,\nu} \qquad (1.6)$$

where $\eta_{\mu,\nu}$ is the Minkowksi flat space metric which described vacuum, that is empty space, and $h_{\mu,\nu}$ represents a small mass perturbation. Once the Lorenz gauge condition applied,

$$\bar{h}_{\mu,\nu} = h_{\mu,\nu} - \frac{\eta_{\mu,\nu}}{2} h \qquad (1.7)$$

the perturbed Einstein equation can be written as:

$$\begin{aligned} \Box \bar{h}_{\mu,\nu} &= -\frac{16\pi G}{c^2} T_{\mu,\nu} \\ &= 0 \ (in \ vacuum) \end{aligned} \qquad (1.8)$$

where $\Box = -\frac{1}{c^2}\frac{\partial^2}{\partial t^2} + \nabla^2$. This is a simple wave equation for the metric perturbation, $h_{\mu,\nu}$, indicating that there exists GW that are transverse plane waves and propagate at the speed of light.

This wave equation has the general solution:

$$\bar{h}_{\mu,\nu}(t,\vec{r}) = \frac{4G}{c^2}\int\frac{T_{\mu,\nu}(\vec{r}_s, t - R/c)}{R}d^3\vec{r}_s + \phi_{\mu,\nu} \tag{1.9}$$

where $R = |\vec{r} - \vec{r}_s|$ and $\phi_{\mu,\nu}$ is any tensor that satisfies $\Box\bar{h}_{\mu,\nu} = 0$. Applying tensor virial theorem derive the solution as a quadrupole moment formalism,

$$\bar{h}^{0,\nu} = 0$$
$$\bar{h}^{i,j}(R,t) = \frac{2G}{c^4 R}\frac{d^2}{dt^2}q^{ij}\left(t - \frac{R}{c}\right) \tag{1.10}$$

where q^{ij} is a quadrupole moment tensor. It shows that GW is created through the quadrupole moment of mass, with the amplitude decline with r, but not r^2 as for electromagnetic signal.

The Lorenz gauge proved useful to demonstrate the reality and properties of GW. There are however further gauge freedoms which can be considered to further simplify the form of $h_{\mu,\nu}$. For instance, there is a particular choice of coordinates called transverse-traceless (TT) gauge conditions for which $h_{\mu,\nu}$ takes the simple form:

$$h_{\mu,\nu}^{TT} = \begin{bmatrix} 0 & 0 & 0 & 0 \\ 0 & h_+ & h_\times & 0 \\ 0 & h_\times & -h_+ & 0 \\ 0 & 0 & 0 & 0 \end{bmatrix} e^{-i\omega(t - z/c)} \tag{1.11}$$

where h_+ and $h_\times$ are the 2 GW's polarisations, see Figure 1.7.

1.5.2 Gravitational Wave Sources and Detectors

As shown in Equation 1.10, any system with quadrupole moment of mass could emit GW, but most of them cannot be detected because the coupling between space-time and matter-energy is very weak,

$$\frac{G}{c^4} \approx 8\times 10^{-45}\frac{s^2}{m\ kg} \tag{1.12}$$

As a consequence, the main detectable GW signals are originated from the astronomical or cosmological catastrophic events which involve very massive compact objects
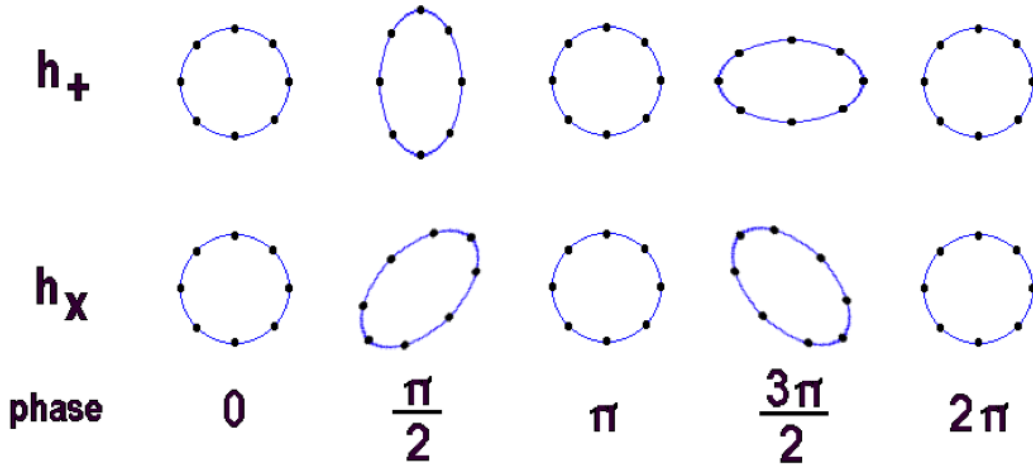
Figure 1.7: The effect on a ring in the xy plane caused by a GW propagating in the z-direction. The top plot illustrates + case polarised GW and the bottom plot × case polarised GW. The five sketches show at phase of 0, $\frac{\pi}{2}$, π, $\frac{3\pi}{2}$, 2π.

with large quadrupole moment. LIGO collaboration define four main GW source categories - continuous, inspiral, burst and stochastic, whose representative GW waveforms are shown in Fig. 1.8 .

Similar to Cosmic Microwave Background (CMB), the stochastic GW spread in GW sky as a background (GWB). It majorly comes from two processes: A relic GWB was created by the Big Bang, which is expected from quantum fluctuations in the initial explosion which have been amplified in the early expansion of the Universe. As one of components contributing to the CMB perturbation, the observed CMB temperature fluctuations limit the maximum strength of the relic GW at cosmological length scales. Another stochastic GW component is arising from thousands of weak, independent, and unresolved binary sources.

Continuous GW are produced by astronomical systems that have a fairly constant frequency, e.g. binary star or black hole systems orbiting each other, or a single star swiftly rotating about its axis. These sources are expected to produce comparatively weak GW since they evolve over longer periods of time and are usually less catastrophic than sources producing inspiral or burst GW.

Burst GW are expected to be produced by gravitational collapse that occurring in

(a) continuous

(b) burst

(c) inspiral

(d) stochastic
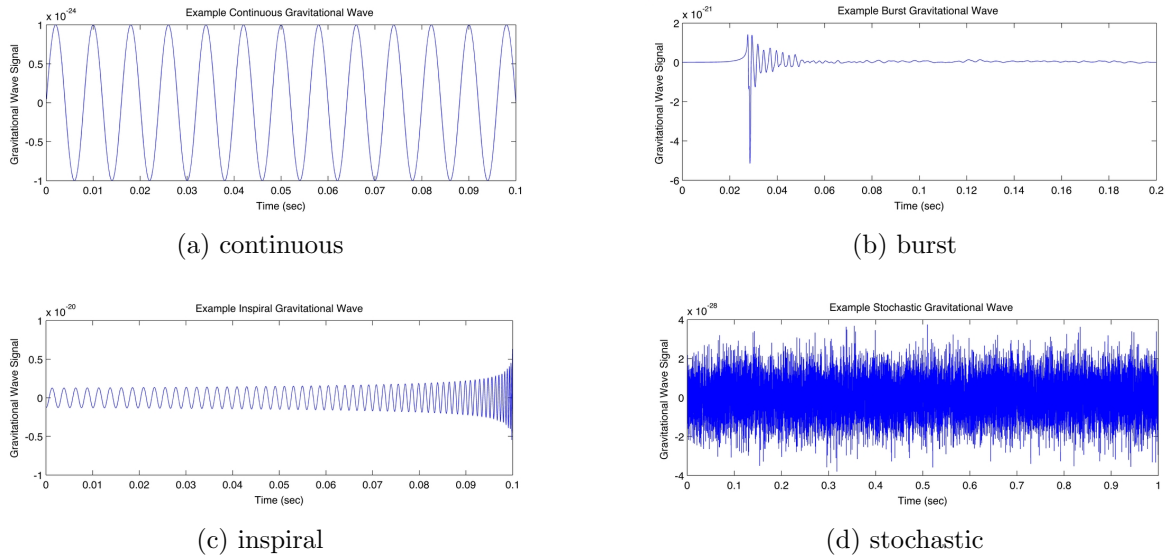
Figure 1.8: Four different kinds of GW signals originated in the astronomical or cosmological process, credit by LIGO, `https://www.ligo.org/science/GW-Sources.php`.

the death of massive star. There are hypotheses that some systems such as supernovae or gamma ray bursts may produce burst GW, which is still a mystery. Meanwhile, it's hard to anticipate their waveforms since too little is known by astronomers about the details of neutron stars or black holes, e.g. the mass trajectory, in order to predict their asymmetry.

Inspiral GW are generated by the merger of compact binaries, e.g. binary neutron stars, binary black holes, or neutron star/black hole. The waveform of such binary systems depends on limited factors, i.e. the companion object's mass, spin, and their separation distance, so that their waveforms can be well predicted. There're three phases for inspiral waveform, namely, inspiral, merger and ringdown. Different methods are designed for the waveform construction at different phase. In general, numerical relativity is precise, however, time consuming, and via analytic approximations is faster but not very robust. The constructed waveforms are stored in 'GW bank', enabling a further modelled search for inspiral GW.

GW are predicted in 1916, but the attempts to detect them began only in 1960s. Initially there was some debates on their actual existence due to two theoretical problems: 1. GW were derived by using coordinate transformation so that was not obvious whether GW came from the source's inherent property rather just abstract mathematical objects. 2. It's also doubtful if GW were transporting detectable energy. These
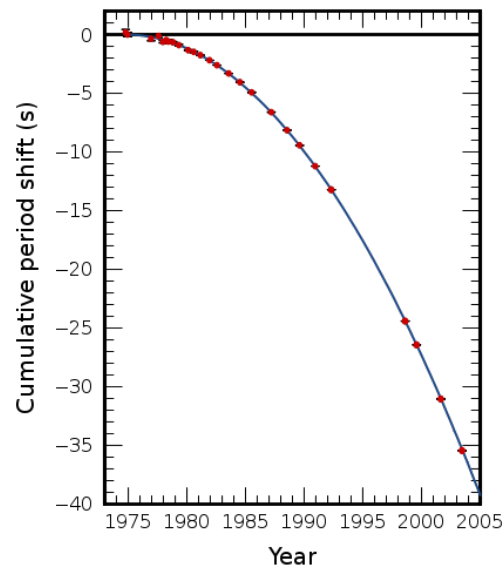
Figure 1.9: Orbital decay of PSR B1913+16. The data points indicate the observed change in the epoch of periastron with date while the parabola illustrates the theoretically expected change in epoch according to general relativity. `https://en.wikipedia.org/wiki/Hulse%E2%80%93Taylor_binary`

issues were positively solved at the end of 50s, and at this point, attempts for GW detection could start.

The first observational evidence of GW was indirect. Binary pulsars were predicted to emit gravitational waves at the expense of loss of angular momentum. This prediction was confirmed by Hulse and Taylor through observation of pulsar, PSR B1913+16, orbiting along with a companion neutron star around a common center of mass. Fig. 1.9 shows the progressive delay of PSR B1913+16 in reaching periastron, which matches well with the GW power.

The attempts of direct GW detection begun in 1962 with Joseph Webber who conceived the first resonant bar detector [weber , 1960]. See Fig. 1.10, the idea of Weber bar is that a GW traveling perpendicular to the cylinder's axis will produce tidal forces that stretch and contract the length of the cylinder. If the frequency of the GW is close to the resonant frequency of the bar, the change in length will be detectable. It is worth mentioning that in 1968, Weber claimed GW detection [weber , 1967, 1968, 1969, 1972]. This result however, was not confirmed, his experiments were duplicated several times, always with a null result. Compared with interferometers,
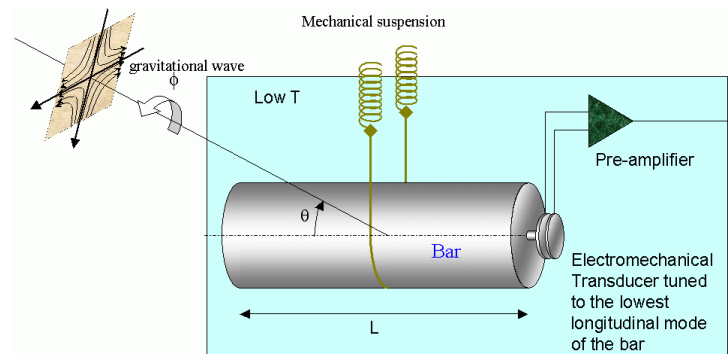
Figure 1.10: Schematics of a gravitational wave bar detector. The impinging gravitational wave excites the fundamental longitudinal resonance of the bar, kept at low temperatures: the induced vibration of the bar end face is amplified mechanically by the resonant transducer, which also converts the signal into an electromagnetic one. The signal is the amplified and acquired. Credit by AURIGA `http://www.auriga.lnl.infn.it/auriga/detector/overview.html`.

which would be discussed later, bar detectors are cheaper, easier to build. The main limiting factor is that they have a very narrow bandwidth which make the GW detection herculean. Resonant bar detectors include ALLEGRO [Mauceli et al., 1996], NIOBE [Aguiar et al., 2010], AURIGA [Cerdonio et al., 1997], EXPLORER [Astone et al., 2008], NAUTILUS [Astone et al., 2008], ALTAIR [Bonifazi et al., 1992], however, most of them are not active anymore.

In Fig. 1.13 is showing four types of feasible detectors, which are currently operating or designed, in order to search GW in various frequency scales. Among them is Michelson interferometer. The Michelson interferometer was first employed in the Michelson-Morley experiment in 1887 providing the constant value of the speed of light. See Fig. 1.11, Michelson interferometer splits an input laser beam into two identical beams. One beam passes straight through the mirror while the other is reflected at 90 degrees. After travelling forth and back in each arm, the two beams are recombined to produce an interference pattern. Even a small change of the two arms length will destroy the interference pattern. Such feature of Michelson interferometer are well suitable to detect the strain of GW. GW propagating perpendicular to the plane of the interferometer will result in one arm of the interferometer being increased in length while the other arm decreased. The change in the length of the interferometer arms results in a small change in the intensity of the light pattern observed at the interferometer output.
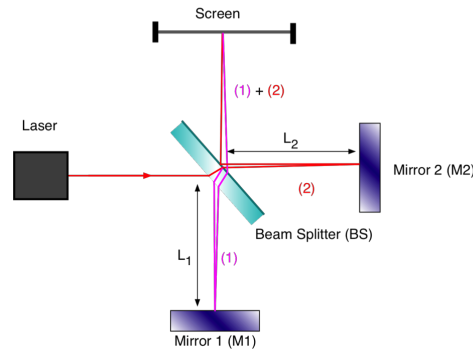
Figure 1.11: Schematic diagram of Machelson interferometers, showing the light paths.

There're two types of laser interferometer for GW detection so far, namely terrestrial interferometer and space interferometers. With arm length around kilometers, terrestrial interferometers are sensitive to astrophysical sources with a range of frequencies from 10 hertz to 10^4 hertz, including compact binaries, namely, neutron stars and stellar size black holes, supernova and rotating neutron stars. The most sensitive terrestrial interferometer currently are the advanced Laser Interferometer Gravitational Wave Observatory [aLIGO; Aasi et al., 2015] and european advanced VIRGO [Acernese et al., 2015].

Another approach of GW interferometry is to fly a laser interferometer in space, which can significantly enlarge the arm lengths in order that that the detector would be sensitive for GW signals lying in the region of $10^{-4} - 10^{-1}$ Hertz. For instance, the Laser Interferometer Space Antenna (LISA) mission, which will launch in 2022, is designed as a constellation of three spacecrafts, arranged in an equilateral triangle with sides 2.5 million kilometers long, flying along an Earth-like heliocentric orbit. See Fig. 1.13, LISA would have the ability to detect GW signals emitted from low frequency astrophysical sources, e.g. binary white dwarfs, binary supermassive black holes, binaries of extremely unequal masses, or even relic of big bang.

Another approach for the detection of ultra low frequency GW is based on pulsar timing arrays, such as the European Pulsar Timing Array (EPTA), the North American Nanohertz Observatory for Gravitational Waves, and the Parkes Pulsar Timing Array (PTA). These projects aim to detect GW by looking at their effects on an array of well-known millisecond pulsars. When GW passes through the pulsar locations, the arrival times of pulsar signals from those directions are shifted correspondingly. By studying a fixed set of pulsars across the sky, these arrays should be able to detect GW in the nanohertz range. Such signals are expected to be emitted by merging of
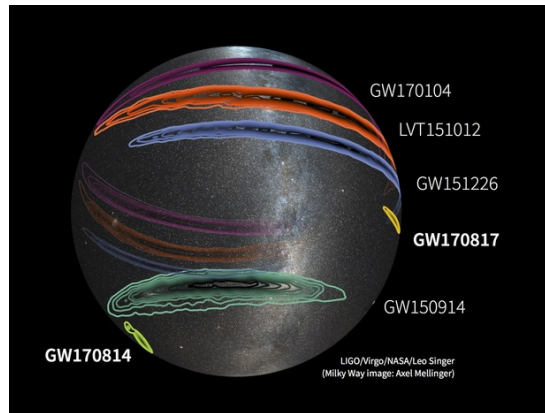
Figure 1.12: Sky localizations of gravitational-wave signals detected by LIGO beginning in 2015 (GW150914, LVT151012, GW151226, GW170104), and, more recently, by the LIGO-Virgo network (GW170814, GW170817). After Virgo came online in August 2017, scientists were better able to localize the gravitational-wave signals. The background is an optical image of the Milky Way. The localizations of GW150914, LVT151012, and GW170104 wrap around the celestial sphere, so the sky map is shown with a translucent dome.

supermassive black holes.

For even lower frequency, we could try to analysis the cosmic microwave background (CMB). The polarization pattern of CMB can be split into two classes called E-modes and B-modes. The E-modes can be created by a variety of processes, however, the B-modes can only be produced by primordial GW, lensing or dust scattering. It is noteworthy that primordial GW were allegedly detected by the BICEP2 instrument, an announcement made on 17 March 2014, which was withdrawn on 30 January 2015. It turned out that the signal could be entirely attributed to dust of Milky Way.

1.5.3   Current situation

The joint GW detection conducted by the LIGO and VIRGO collaboration (LVC) has achieved a great success. See Fig. 1.12, during its first observing run (O1), aLIGO detected 2 events originated from binary black hole (BBH) mergers: GW150914 [Abbott et al., 2016b], GW151226 [Abbott et al., 2016c] and 1 possible BBH GW source, LVT151012 [Abbott et al., 2016d]. The first detection of GW by LIGO/VIRGO interferometers indicate properties and astrophysical consequences, e.g. BBH ere more massive than expected. In LVC second observing run (O2), there're 3 GW events an-
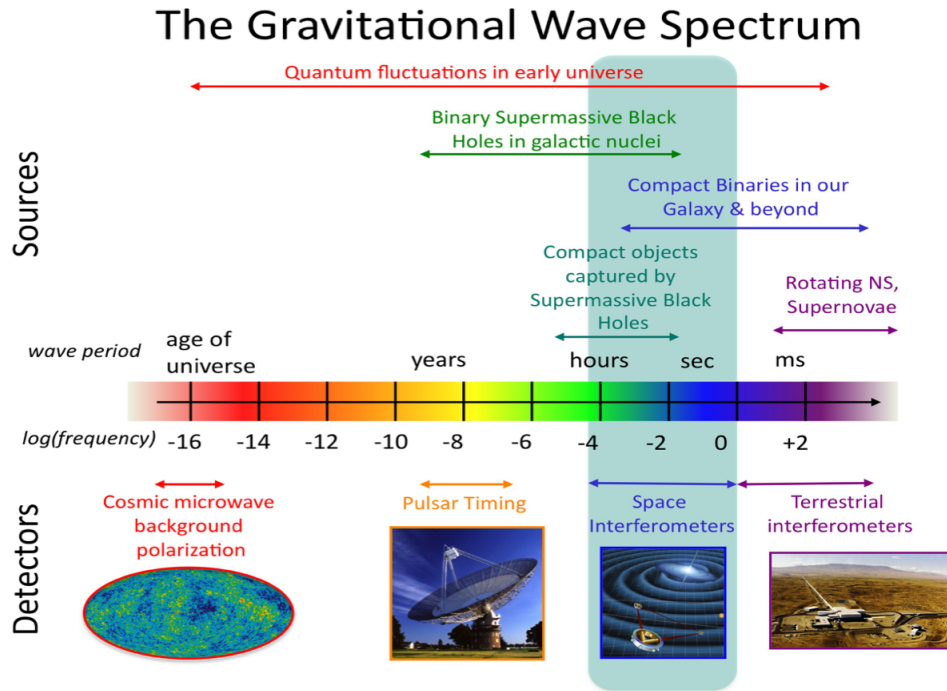
(a) The gravitational wave spectrum with sources and detectors. Credit: NASA Goddard Space Flight Center science.gsc/nasa.gov
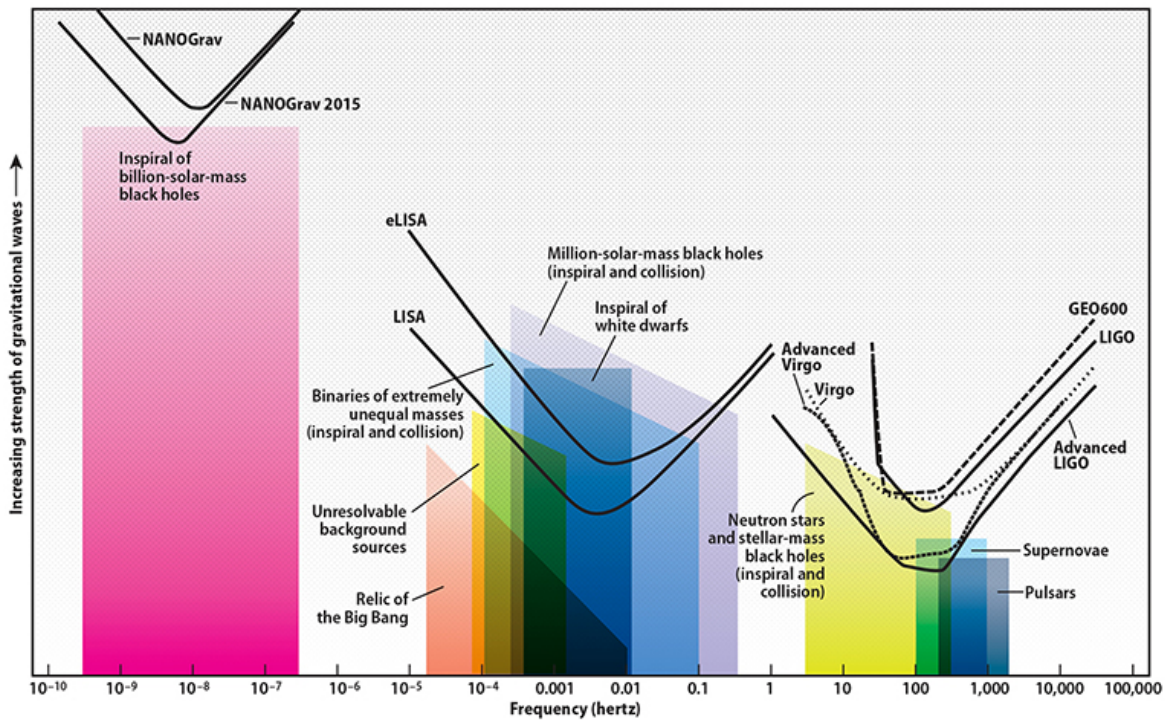
(b) Different events produce gravitational waves of different frequencies. This plot compares those sources against operating and future detectors. Credit by Institute of Astronomy, Univ. of Cambridge `http://discovermagazine.com/bonus/gravity`

Figure 1.13: Four different kinds of GW signals originated in the astronomical or cosmological process, credit by LIGO.

nounced so far by LVC: two BBH source GW170104 [Abbott et al., 2017a], GW170814, and GW170817 [Abbott et al., 2017b], which is possibly created by binary neutron star system (BNS). The next LVC runs are expected to be started from the early of 2019, and at that time, more interferometers, e.g. KAGRA, LIGO-India, are expected to join the searching network. Also, the next generation of terrestrial interferometers, e.g. Einstein telescope, are being prepared and would operate in 2030s.

Besides terrestrial interferometers, Pulsar timing array and CMB measurements are currently operating. And the space interferometers, e.g. LISA, is coming soon, as expected in 2022.

1.6 Electromagnetic counterpart of Gravitational-Wave

Beside the CR, which is not suitable for MMA observations, the coincident search between the rest three messengers, namely light, neutrino and GW, is worth to be tested. In this thesis, I mainly talk about the optical follow up search of GW signals.

In this section, I discuss the potential sources which can emit GW signals and also EM emission, considering GW sources detectable by the ground-based interferometers, namely, LIGO and VIRGO. There're mainly three types of sources: core-collapse supernova, compact object binary merger, and isolated neutron star instability.

1.6.1 Isolated Neutron star instability

Fast spinning isolated neutron stars are considered as possible persistent gravitational wave sources if they possess some degree of asymmetry. This can result from the certain types of oscillation modes possibly excited in the star, or because of the presence of static density inhomogeneities ('mountains') that the neutron star crust can hold. However, Glampedakis & Gualtieri [2017]; Mukhopadhyay et al. [2018] shows that such transient GW signal due to star-quake of single neutron stars [9] are not expected to be as loud as the ones produced by binary systems of black holes or neutron stars. GW

---

[9]It's easy to mix such transient GW signals with the continuos GW signals, since both of them can be generated by isolated spinning objects. However, the continuos GW signals are produced by single star that have a fairly constance frequency. Such systems are more mild and less catastrophic so that their GW intensities are weak while GW periods are longer, up to years. Nevertheless, the fast spinning neutron stars are much violate. The corresponding GW intensities are stronger while the waveforms are shorter.

from single neutron stars are more likely to be detected by future ET-class observatories [10].

1.6.2   Galactic core-collapse Supernova and long GRBs

The supernovae (SN) is a violent event occurring at the end of the evolution of stars. When the nuclear material of star is ran out, the nuclear reaction cannot create sufficient radiation pressure to contrast the self-gravity, and an explosion occurs. This causes the sudden appearance of a new bright star that slowly fades over several weeks to months. The catastrophic gravity compress the star core continuously, till the degeneracy pressure created by atoms, neutrons, or even quarks, of the core, is strong enough to balance the gravity, which leaves the core as white dwarfs (WD), neutron stars (NS), quark stars or black holes (BH), correspondingly.

SN can be divided into different types according to the light curve and spectrum features (Fig. 1.14). From the progenitor point of view we now know that there're two classes of SN, namely thermonuclear and core-collapse SNe (CCSN). Thermonuclear SN, that identifies with the observed Type Ia SN, are the result of the thermonuclear explosion of WD stars in close binary systems. A WD star accretes mass from a companion, raising its core temperature enough to ignite the carbon deflagration, which leads to the complete destruction of the progenitor star. CCSN, that correspond to the observed type Ib, Ic and II, are the explosions of isolated stars with an initial mass greater than 8 solar mass. Such massive stars go through nuclear sequential burning stages and eventually they build up a degenerate iron core. When such iron core larger than Chandrasekhar mass, it will no longer be able to support itself by electron degeneracy pressure and will collapse further to a NS or BH. In the current paradigm, the deposition of a small fraction of neutrinos created during the neutronization of the core can power the ejecta that propagate outward, creating SN explosion.

The death of massive star can not only produce SNe, but also long Gamma-Ray burst (lGRBs) in the special case of strongly asymmetric explosion of stripped envelope progenitors. Till now, several examples of SNIc-lGRBs connection has been detected. In addition to the EM radiation, SN explosions emit neutrinos and GW which, however, are very difficult to detect.

Seitenzahl et al. [2015] run a simulation for Type Ia SN with the thermonuclear incineration of a near-Chandrasekhar mass carbon-oxygen WD star model. The results suggest that neutrino energy losses are indeed small, only two per cent of 2×10^{49} erg

---

[10]Einstein telescope is a proposed third-generation ground-based gravitational wave detector, currently under study by some institutions in the European Union.

of energy. Instead, the future space-based gravitational wave missions, e.g. DECIGO and BBO, would be able to detect their GW source [11] to a distance of ~ 1.3 Mpc in the frequency range between 0.1 Hertz and 10 Hertz, depending on viewing angle and polarization.

Neutrinos from a CCSN were detected for the first time in 1987, with the SN in the Small Magellan Clouds. Current facilities can detect neutrinos originating from CCSN, up to galactic, or a little bit further. In GW channel, the range of CCSN, that produce detectable GW signals, lies from Milky way [Ott et al., 2013] to a few Mpc [12] [Fryer et al., 2011], e.g. in [Gossan et al., 2016] shows that a three-detector GW network (LVC+KAGRA) will be able to detect neutrino-driven CCSN explosions out to ~ 5.5 kpc, while rapidly rotating core collapse will be detectable out to the Magellanic Clouds at 50 kpc.

CCSNe produce short duration signals (1 s or even less) with a large uncertainty in the waveform. GW sources of this sort are collectively known as 'unmodeled sources' to indicate that an exact waveform is not available. Therefore, the CCSN rate that detectable by LVC remains unknown. Hence considering the CCSN rate from local SN search, the CCSN rate is only 2 per century in the Milky Way [Cappellaro et al., 1999].

1.6.3   Coalescence of binary systems of compact objects

Sources expected to emit GW signals detectable by the ground-based interferometers are compact binary coalescences (CBC), that is the inspiral and merger of two compact objects. Abbott et al. [2018] suggested that, for the ongoing LVC run, the average range for NS-NS (BNS) merger would go up to ~ 200 Mpc in the upcoming runs. Tab. 1.2 predicts that there will be 1-50 BNS mergers would be detected in O3 run and up to 180 in the near future. As the mass of NS is smaller than BH, the range for NS-BH, BH-BH (BBH) merger would be even higher, while the expected detections are larger meanwhile. Considering the waveform is well predicted at the same time, therefore, CBC is a very promising source for ground-based interferometer.

1.6.3.1   Binary black hole mergers

In 2015, one BBH GW source, GW150914 [Abbott et al., 2016b], was detected by aLIGO, opening the era of GW astronomy. Till now, there's no doubt that the BBH are very promising sources, from the GW's perspective. However, we know very few

---

[11]Their model radiates 7×10^{39} erg in GW and the spectrum has a pronounced peak around 0.4 Hz

[12]Only strongly asymmetric CC-SN may be detected up to several Mpc, but this are a small fraction of core collapse.
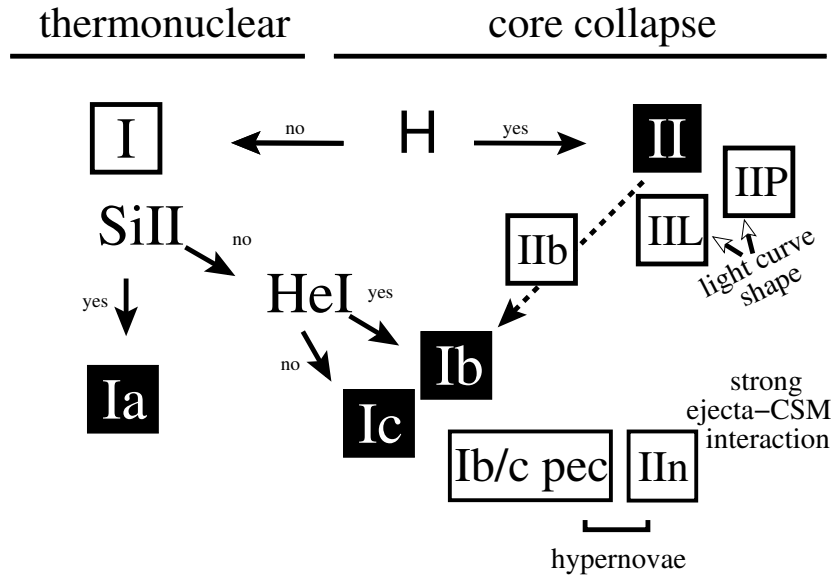
Figure 1.14: Supernovae classes. Figure taken from Turatto [2003]

about BH [13] so that it still remains unclear to us if BBH can create EM signal [14]. Although, the Fermi satellite reported the detection of a transient signal at photon that lasted 1 second and appeared 0.4 second after the GW signal [Connaughton et al., 2016], and Loeb [2016] explain the possible scenario that a BBH merger create EM signal, the fact that Fermi detection is not robust make it still an open question if BBH can emit EM signal.

1.6.3.2 Binary neutron star mergers

The situation would be different if at least one NS involved in such binary systems. The mergers of binary system including a NS are predicted to power a short GRB and an r-process kilonova in optical/near-infrared [Li & Paczyński, 1998]. One BNS source was detected by aLIGO and aVIRGO at a distance of 40 Mpc in 2017 Aug 17 [Abbott et al., 2017b] and the EM follow-up was very successful [Abbott et al., 2017e].

---

[13]The no-hair theorem postulates that all BH can be completely characterized by only three observable parameters: mass, electric charge, and angular momentum.

[14]It's believed that there're no accreting material in BBH merger to produce EM emission, however, some mechanisms that could produce unusual presence of matter around BHs have been recently discussed [Bartos et al., 2017; , De Mink et al. 2017; Loeb, 2016; Perna et al., 2016; Zhang et al., 2016]

In this section, I would like to discuss the EM emission of BNS system, which is still uncertain to us (such process is very complicated by balancing a number of factors, e.g. neutrino emission, magnetic fields, electron synchrotron radiation, etc). In Fig. 1.15 is showing a possible scenario of BNS merger: Two NSs with small radii and comparable masses coalesce, producing a hypermassive NS, which generates a large accretion torus as it sheds its angular momentum and collapses into a BH in a short timescale. The torus-BH powers a collimated GRB jet, which burrows through the polar dynamical ejecta. Gamma-rays from the core of the GRB jet are relativistically beamed away from our sight line, but a weaker GRB is nevertheless observed from the off-axis jet or the hot cocoon created as the jet breaks through the polar ejecta. On a similar timescale, the accretion disk produces a powerful wind which expands quasi-spherically and synthesizes also heavy r-process nuclei. After several hours of expansion, the polar ejecta becomes diffusive, powering visual wavelength ("blue") kilonova emission, lasting for a few days. Over the following week, the deeper disk wind ejecta becomes diffusive, powering red kilonova emission. The initially on-axis GRB jet decelerates by shocking the ISM, after several weeks, its X-ray and radio synchrotron afterglow emission rises.

As shown, there're two major EM counterpart for BNS merger, short Gamma-ray bursts and kilonova.

1.6.3.2.1   Short Gamma-ray bursts and afterglow

Gamma-ray bursts (GRB) are short and intense pulses of gamma-rays from extremely energetic explosions observed from the sky in arbitrary directions. They can last from milliseconds to several minutes and based on that they are divided in two different types, see Fig 1.16, long-duration GRBs (lGRB) and short-duration GRBs (sGRB) whose origin is different. As mentioned in Section 1.6.2, lGRBs have been related to the collapse of highly energetic SNIc. The origin of sGRBs was debated but it has been suggested that they can originate from CBC, i.e. BNS or NS-BH.

The initial GRB is usually followed by a longer-lived 'afterglow' emitted at wavelengths from X-ray, ultraviolet, visible light, infrared to radio waves, see Figure 1.17. The discovery of afterglows in 1997 made it possible to measure GRBs' redshifts and find their host galaxies. The initial GRBs standard model, include the prompt emission arises from the internal dissipation of GRB ejecta, while the afterglow emission is produced by the external shock due to the interaction between the GRB ejecta and circum-burst media.

The radiation of prompt GRB is strongly beamed, and this makes that most of
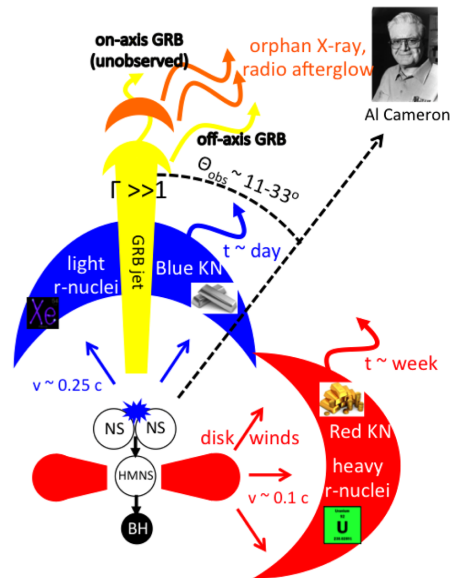
Figure 1.15: Scenario for the EM counterparts of GW170817, as viewed by the observer from the inferred binary inclination angle $\theta_{obs} \sim 0.2 - 0.5$ [Metzger, 2017].
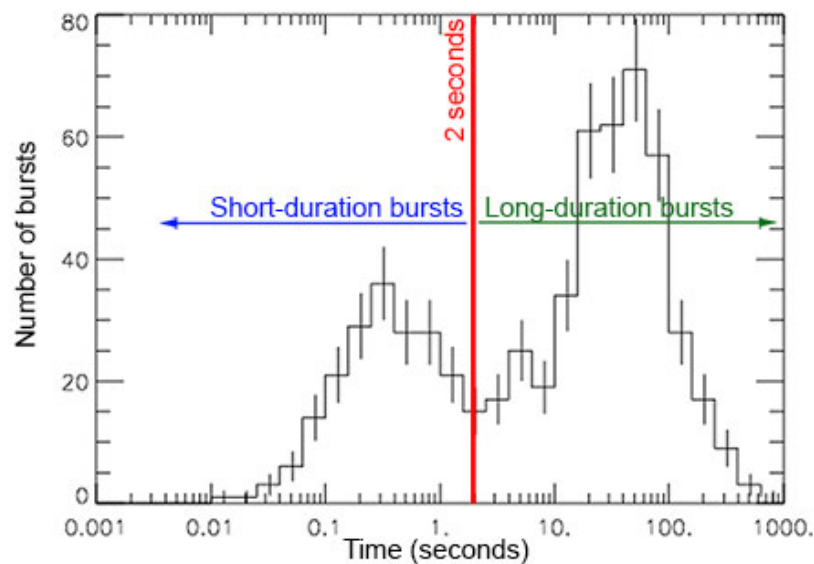
Figure 1.16: Graph of the time versus number of bursts for the gamma-ray bursts observed by the BATSE instrument on the Compton Gamma-ray Telescope. Picture is taken from https://imagine.gsfc.nasa.gov/science/objects/bursts1.html.

Table 1.2: Summary of a plausible observing schedule, expected sensitivities, and source localization with the Advanced LIGO, Advanced Virgo and KAGRA detectors, which will be strongly dependent on the detectors' commissioning progress. Table is taken from Abbott et al. [2018] where one can know more details.

Epoch			$2015-2016$	$2016-2017$	$2018-2019$	$2020+$	$2024+$
Planned run duration			4 months	9 months	12 months	(per year)	(per year)
Expected burst range/Mpc	LIGO		$40-60$	$60-75$	$75-90$	105	105
	Virgo		—	$20-40$	$40-50$	$40-70$	80
	KAGRA		—	—	—	—	100
Expected BNS range/Mpc	LIGO		$40-80$	$80-120$	$120-170$	190	190
	Virgo		—	$20-65$	$65-85$	$65-115$	125
	KAGRA		—	—	—	—	140
Achieved BNS range/Mpc	LIGO		$60-80$	$60-100$	—	—	—
	Virgo		—	$25-30$	—	—	—
	KAGRA		—	—	—	—	—
Estimated BNS detections			$0.05-1$	$0.2-4.5$	$1-50$	$4-80$	$11-180$
Actual BNS detections			0	1	—	—	—
90% CR	% within	5 deg^2	< 1	$1-5$	$1-4$	$3-7$	$23-30$
		20 deg^2	< 1	$7-14$	$12-21$	$14-22$	$65-73$
	Median/deg^2		$460-530$	$230-320$	$120-180$	$110-180$	$9-12$
Searched area	% within	5 deg^2	$4-6$	$15-21$	$20-26$	$23-29$	$62-67$
		20 deg^2	$14-17$	$33-41$	$42-50$	$44-52$	$87-90$

GRBs are not detected. Apart from the anisotropic EM emission, i.e. prompt GRB and its X ray, optical afterglow emission, such system can still produce some isotropic emissions, radio afterglow and kilonova phenomenon in optical and near-infrared (NIR).

1.6.3.2.2 Kilonova

A kilonova, or macronova, peaks at a luminosity that is a factor 1000 higher than a typical nova [Metzger et al., 2010]. Kilonova are thought to emit strong EM radiation due to the radioactive decay of heavy nuclei created in the rapid neutron capture process (r-process). The r process happen when matter has a high neutron density and high temperature. The neutrons are absorbed by nuclei until the neutron separation
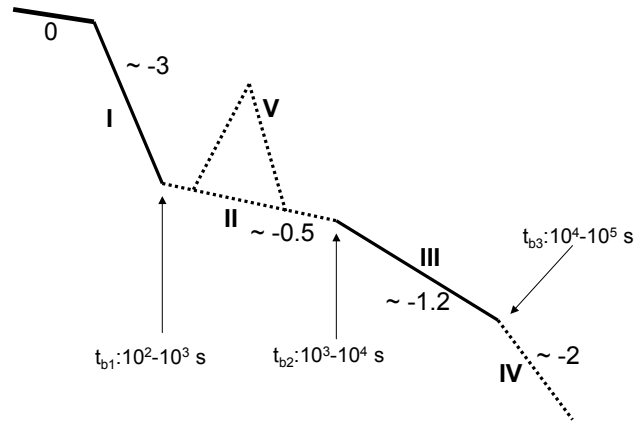
Figure 1.17: Schematic diagram of the GRB X-ray afterglow light curve, summarized in the Swift era [Zhang et al., 2006].

energy is less than zero, which is called the Neutron drip line. Neutron rich isotopes are unstable to beta decay, see Fig. 1.18a. After beta decay, the new nucleus will have a new neutron drip line and in most cases be able to capture more neutrons. Fig. 1.18b shows that heavy elements in the universe are created by the r process.

`https://kilonova.space/` summarize all the kilonova detected so far, including one event and five candidates. All of them are detected thanks to MWA or MMA observations. As shown in Fig. 1.19 that kilonova event has a very short timescale, e.g. roughly stay detectable for the 2.6 meter, very large telescope survey telescope (VST), for only couple of days, when the source placing at a distance of 400 Mpc.

1.7 Multi-messenger implementation

The MMA typical operation begin with the detection of one messenger, which provides the target to be followed up to search for other messengers. By covering the same uncertainty region of the trigger, the follow-up search aims to detect possible related signals. In this thesis, I focus on combined detections of GW and EM. GWs trace the bulk motion of the mass of the source, whereas EM radiation typically arises from

(a) Mechanics of r process.

(b) Periodic table showing the cosmogenic origin of each element. The elements heavier than iron with origins in supernovae are typically those produced by the r-process, which is powered by supernovae neutron bursts.
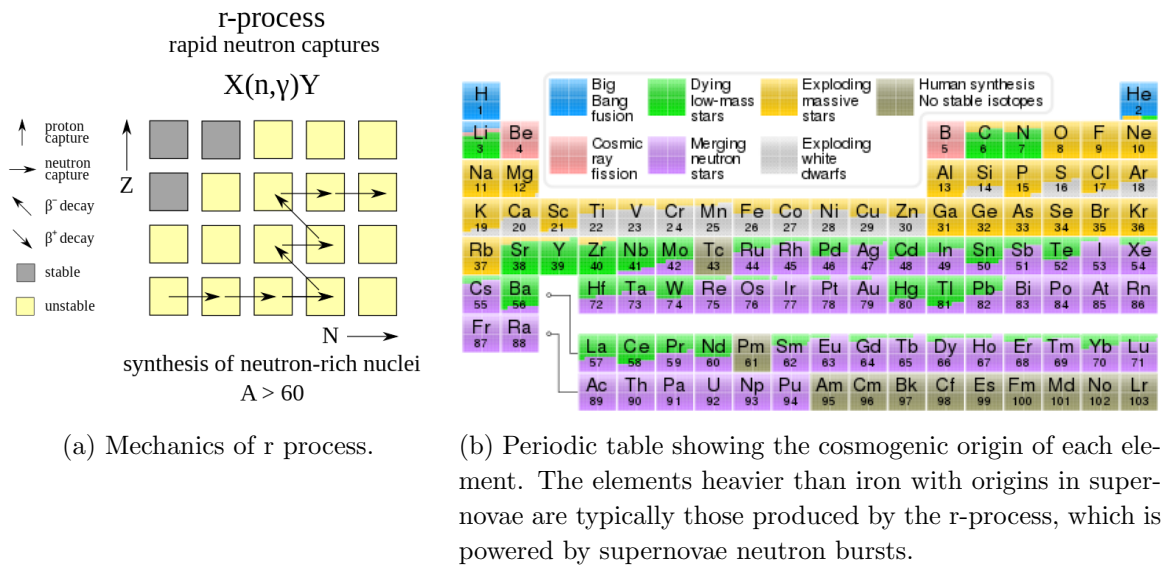
Figure 1.18: The systhensis of heavy elements produced by r-process produced in kilonovae. Figure is taken from `https://en.wikipedia.org/wiki/R-process`.

the interaction of matter with the interstellar medium, thermal processes, and the internal shocks of GRBs, which provide critical insight into the physics of the event, helping to determine the distance scale, energy scale, and the progenitor environment, as well as insight into the behaviour of post-merger matter. The joint observation of astrophysical source in both GW and EM channels can be useful to probe cosmology, e.g. to constrain the Hubble constant [Abbott et al., 2017f]; fundamental physics, e.g. the GW speed [Tattersall et al., 2018], NS equation of state [The LIGO Scientific Collaboration et al., 2018], and so on.

Here, I describe the approaches to realize MMA with GW/EM connections.

1.7.1 Gravitational wave search associated with electromagnetic signal

In principle, GW follow-up of EM source can be achieved if the EM source is detected at very early phase. Previous EM triggering GW searches have been carried out for gamma ray bursts, soft-gamma repeater flares, and pulsar glitches. Abbott et al. [2016a] presented a first attempt of such 'reversed search' looking at the LIGO log for GW bursts coincident with two recent nearby CCSN. Yet, no plausible GW signal was detected.
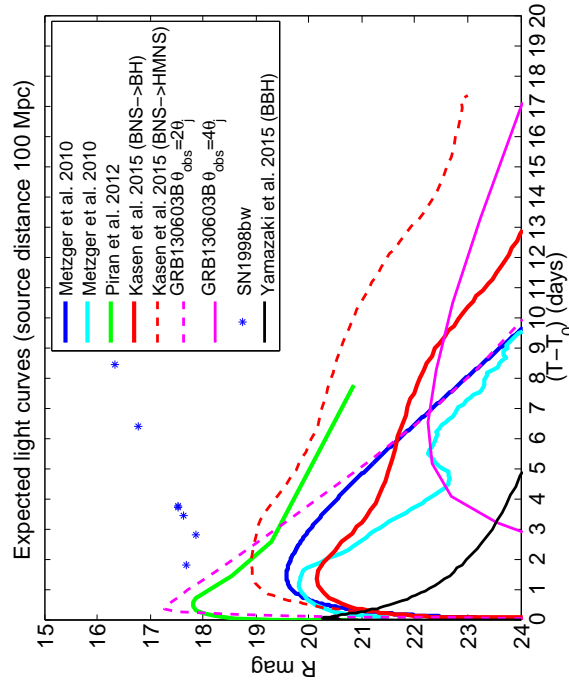
Figure 1.19: The expected fluxes (r band magnitudes) versus observed time from the GW150914 trigger, assuming several possible electromagnetic GW source emission models at the given distance of 100 Mpc, plotted against the 6 epochs VST observation 5σ limiting magnitude (*dark green triangles*) and the detection upper limits computed from artificial stars in frame P31 (*light green triangles*) [Brocato et al., 2018].

The approach is to use EM observations to determine the position and time of a possible GW source, and then, search in the recorded GW data, for potential signal candidates, which are required to be in a well-defined temporal on-source window and must be consistent with GW arriving from the sky location of the source. The searching algorithms evaluate the signal consistency across different interferometers and apply thresholds on these measures to reject background noise events. The event's significance is measured through the false alarm rate (FAR): the rate at which the background noise produces events of equal or higher loudness than events that pass all coherent tests and data quality cuts. The event with lowest FAR is termed the loudest

event. Furthermore, the False Alarm Probability (FAP) is defined, which should be low enough that it is implausible to have been caused by background noise. The threshold on a FAP is decided, in order to consider an event to be a possible GW detection candidate.

Such reverse search is at present always activated only for GRBs, magnetars, but not CCSN. The reason is typically from the optical light curve of CCSN, whose timescale is from days to years, one can predict the on-source window at best with accuracy of few $\sim hours$, still not precise enough for GW signal search, which lasts just few seconds.

1.7.2 Electromagnetic search associated with gravitational wave signal

Another approach is the follow up of GW sources in EM channel. In this thesis, I mainly talk about the optical follow-up. After the sky position of a GW trigger estimated by LVC, its localization map [15] was archived to GraceDB website. In optical channel, telescopes are used to cover the sky localization of the GW signal and then after the optical counterpart selection to follow-up the candidates for a detailed classification.

The main challenge is the large uncertainty of GW source localization. As it can be seen in Fig. 1.20, for the BBH source GW150914, the standard sky uncertainty region from the two LIGO detectors was several hundred square degrees. With aVirgo, the simultaneous operations of 3 interferometers enable a substantial reduction of the error areas thanks to the time delay triangulation. Nevertheless the error areas will still be dozens to hundred of square degrees. For instance, the first BNS GW source detected by aLIGO, GW170817 Abbott et al. [2017b], remains only 33 square degrees with the aVIRGO upper limit constrains. The situation will improve when other interferometers will join the network.

In general the sky localization is poor, thus two complementary approaches are employed: wide-field tilling search on high probability GW region and pointed search of selected galaxies within the high probability GW region. This thesis employ both approaches, and will present the effort of the GRAWITA project for tiled searches with the VST in Chapter 2, and the results of the DLT40 as example of a galaxy pointed search in Chapter 3.

---

[15]In its O1 and O2 run, LVC announce the localization immediately when detecting a possible GW source in order to enable a prompt EM or neutrino follow-up. The GW candidates are searched in low-latency [Abbott et al., 2016h; Adrián-Martínez et al., 2016; Agostini et al., 2017]. The distance would be either public promptly, or sometimes later when the GW waveform estimated again by other pipelines.
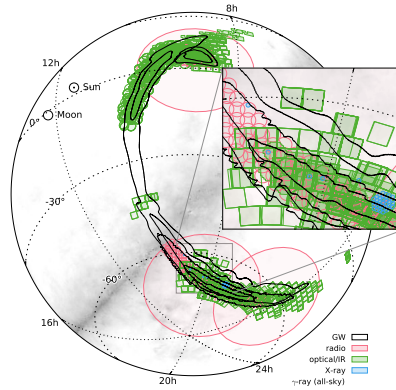
Figure 1.20: Footprints of observations in comparison with the 50% and 90% credible levels of the initially distributed GW localization maps. Radio fields are shaded in red, optical/infrared fields are in green, and the XRT fields are indicated by the blue circles [Abbott et al., 2016h].

Besides the sky area, distance is another key factor. If the GW source is located in close volume, tens of Mpc, the galaxy strategy is more efficient. However, if the source is further than hundred of Mpc, a tile strategy is more efficient, since with a single shot of a wide field camera, one can cover many distant galaxies, saving significant observing time. Also, in Fig. 1.21 shows that our knowledges of galaxies are poor up to hundred of Mpc, thus, the galaxy strategy is unachievable.

A further challenge for the EM counterpart search is the short timescale of the emission. As shown in Fig. 1.19 that the expected EM emission of GW sources, namely the kilonova or GRB optical afterglow, declines fast, making difficult the verification and further follow up classification. In Fig. 1.19 is also showing that the expected EM emission is relatively faint, compared to a standard Ic SN, 1998bw. Depends on these properties, the EM follow-up should be rapid, and reach the appropriate depth. However, the number of candidates is large, especially for the tiling search. In order to classify candidates fast, it is crucial to develop ranking algorithms that make pretreatment for candidate sources, and select only the interesting candidates fo manual visual inspection. The present algorithms for candidates selection use thresholds on several selected parameters of candidates. In this thesis, I would describe my effort of introducing a machine learning approach for the automatic transients evaluation, in Chapter 4.
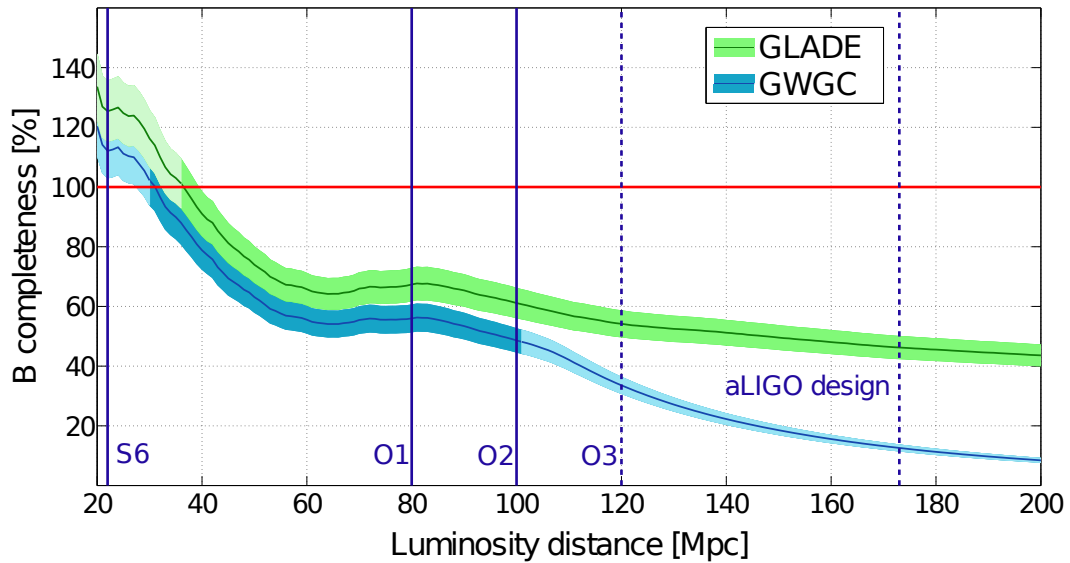
Figure 1.21: The plots show the normalized integrated B-band luminosity of galaxies in GLADE (green) and in GWGC (blue) within luminosity distances indicated on the x-axis [Dálya et al., 2018].

After survey of sky area and candidates identification, further follow-up in photometric and spectroscopic are required. In chapter 5, I show two examples of EM candidates that were proved uncorrelated to GW signals, iPTF15dld and G194575, AT-LAS17aeu and GW 170104/GRB 170105A . In Chapter 6, I present a successful case, kilonova AT17fgo and GW170107. I describe the independent discovery of DLT40, the kilonova identification of GRAWITA. This discovery had astrophysical and cosmological implications. I evaluated the BNS rate and I participate in the constrain of the Hubble constant.

Chapter 7 summarizes work and results of the thesis. More details of pipelines and codings is shown in the appendices.

Chapter 2

Search for optical counterparts of Gravitational Wave Sources: tiling strategy

In this chapter, I present our implementation of the sky tiling strategy for the search of optical counterpart of Gravitational Wave sources, in the framework of the GRAWITA. In particular, I report the results on the deep optical follow-up surveys performed using the VST of three gravitational-wave events discovered by the LVC in the O1 and O2 seasons, namely, GW150914, GW151226 and GW170814. I outline the VST observational strategy and describe two independent procedures developed to search for transient counterpart candidates in multi-epoch VST images. The detection efficiency of VST observations for different types of optical transients that can be associated to GW events are evaluated. What follows in this chapter is an excerpt of the results published in [a] and [b]. As menber of GRAWITA, I contributed to develop the image difference pipeline (diff-pipe) used for transient detection, and the related related analysis, such as the artificial star experiments to estimate the limiting magnitude and the light curve fitting for transient classification. I report the diff-pipe and analysis codes in the appendix.

Publications:

[a] Brocato, E.; Branchesi, M.; Cappellaro, E.; Covino, S.; Grado, A.; Greco, G.; Limatola, L.; Stratta, G.; **Yang, S.***.; Campana, S.; D'Avanzo, P.; Getman, F.; Melandri, A.; Nicastro, L.; Palazzi, E.; Pian, E.; Piranomonte, S.; Pulone, L.; Rossi, A.; Tomasella, L.; Amati, L.; Antonelli, L.*

A.; Ascenzi, S.; Benetti, S.; Bulgarelli, A.; Capaccioli, M.; Cella, G.; Dad-ina, M.; De Cesare, G.; D'Elia, V.; Ghirlanda, G.; Ghisellini, G.; Giuf-frida, G.; Iannicola, G.; Israel, G.; Lisi, M.; Longo, F.; Mapelli, M.; Mari-noni, S.; Marrese, P.; Masetti, N.; Patricelli, B.; Possenti, A.; Radovich, M.; Razzano, M.; Salvaterra, R.; Schipani, P.; Spera, M.; Stamerra, A.; Stella, L.; Tagliaferri, G.; Testa, V.; Grawita-Gravitational Wave Inaf Team, MNRAS 474, 411
[b] Grado, A.; **Yang, S**.; et al, in prep

2.1   GRAWITA observational strategy at the VST

GRAWITA [1] is the Istituto Nazionale di Astrofisica (INAF) colloboration, which is carrying out follow-up observational campaigns of the GW triggers in the whole EM domain. In particular for optical/NIR surveys, GRAWITA has access to a number of ground-based facilities, including the VST, VLT, LBT, TNG, REM, see Flg. 2.1. Reacting to a GW trigger released by LVC, GRAWITA activates follow-up of the interesting events with low latency. In figure 2.2 illustrates the flowchart of GRAWITA follow-up strategy. The process is initiated by a GW trigger and include three major components: a) the survey definition and execution; b) the image calibration and transient candidates detection and c) the candidate confirmation, classification and follow up. Details for each individual steps will be described in the following.

LVC carried out the first observing run (O1) from September 2015 to January 2016, providing three alerts for GW events (one subsequently not confirmed) that were reported to the observing groups participating in the LVC EM follow-up program.

The first GW event was identified after the real-time processing of data from LIGO Hanford Observatory (H1) and LIGO Livingston Observatory (L1) on 14 September 2015 at 09:50:45 UTC [LIGO/VIRGO Scientific Collaboration, 2015a]. An alert was issued on September 16. GW150914 was immediately considered an event of great interest because the false alarm rate (FAR) was largely smaller than the threshold of 1 per month adopted to send alert for O1 [2] . Further analysis showed that the GW event was produced by the coalescence of two black holes with rest frame masses of $29^{+4}_{-4} M_\odot$ and $36^{+5}_{-4} M_\odot$ at a luminosity distance of 410^{+160}_{-180} Mpc [Abbott et al., 2016b]. This information became available only months after the trigger, that is, after completion of the EM follow up campaign. Twenty-five teams of astronomers promptly reacted to

---

[1] https://www.grawita.inaf.it/
[2] FAR of GW150914 is $1.178 * 10^{-8}$ Hz, equivalent to 1 per 2.7 years.
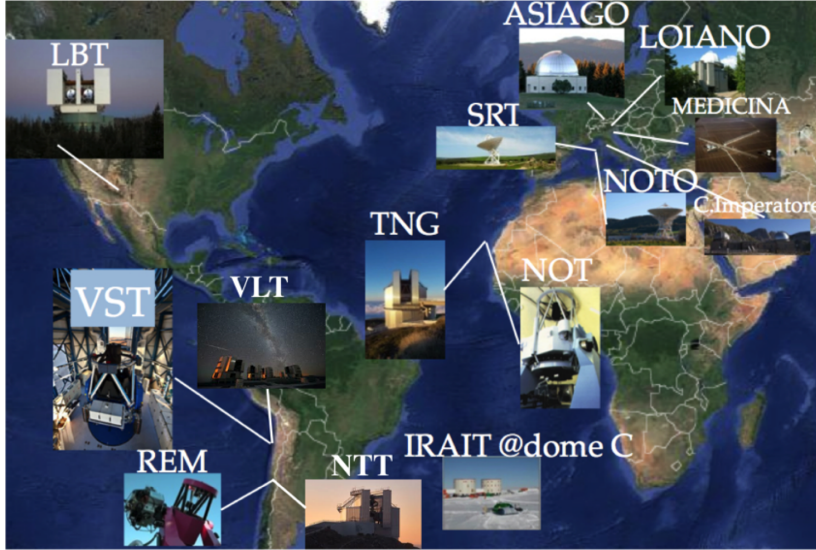
Figure 2.1: GRAWITA telescopes networks for GW follow-up. Credit by Enzo Brocato.

the alert and an extensive electromagnetic follow-up campaigns and archival searches were performed covering the whole electromagnetic spectrum [Abbott et al., 2016e; Abbott et al., 2016h].

On 26 December 2015, a second GW event (GW151226) was observed by LVC [LIGO/VIRGO Scientific Collaboration, 2015b]. Again, the GW event resulted from the coalescence of two black holes of rest frame masses of $14.2^{+8.3}_{-3.7}$ M$_\odot$ and 7.5 ± 2.3 M$_\odot$ at a distance of 440^{+180}_{-190} Mpc [Abbott et al., 2016c]. The EM transient search started on 27 December 2015, just 1 day after the GW trigger [LIGO/VIRGO Scientific Collaboration, 2015b], again with an excellent response from the astronomical community.

After interferometers upgrade, the LVC second observing run (O2) started in December 2016 and terminated in August 2017. In this run, VIRGO joined the global GW search from the early of August, 2017. GW170814 was the first GW event detected by both the two LIGO (H1, L1) and the Virgo (V1) detectors at 2017-08-14 10:30:43 UTC (GPS time: 1186741861.5268). The Advanced Virgo [Acernese et al., 2015] interferometer detected its first signal and the triangulation with the LIGO [Aasi et al. 2015] interferometers allowed to heavily improve the sky localization of the source, shrinking the area of the 90% credible region from 1160 deg^2, obtained using only the LIGO detectors, to 60 deg^2 using all three detectors Abbott et al. [2017b]. The GW170814
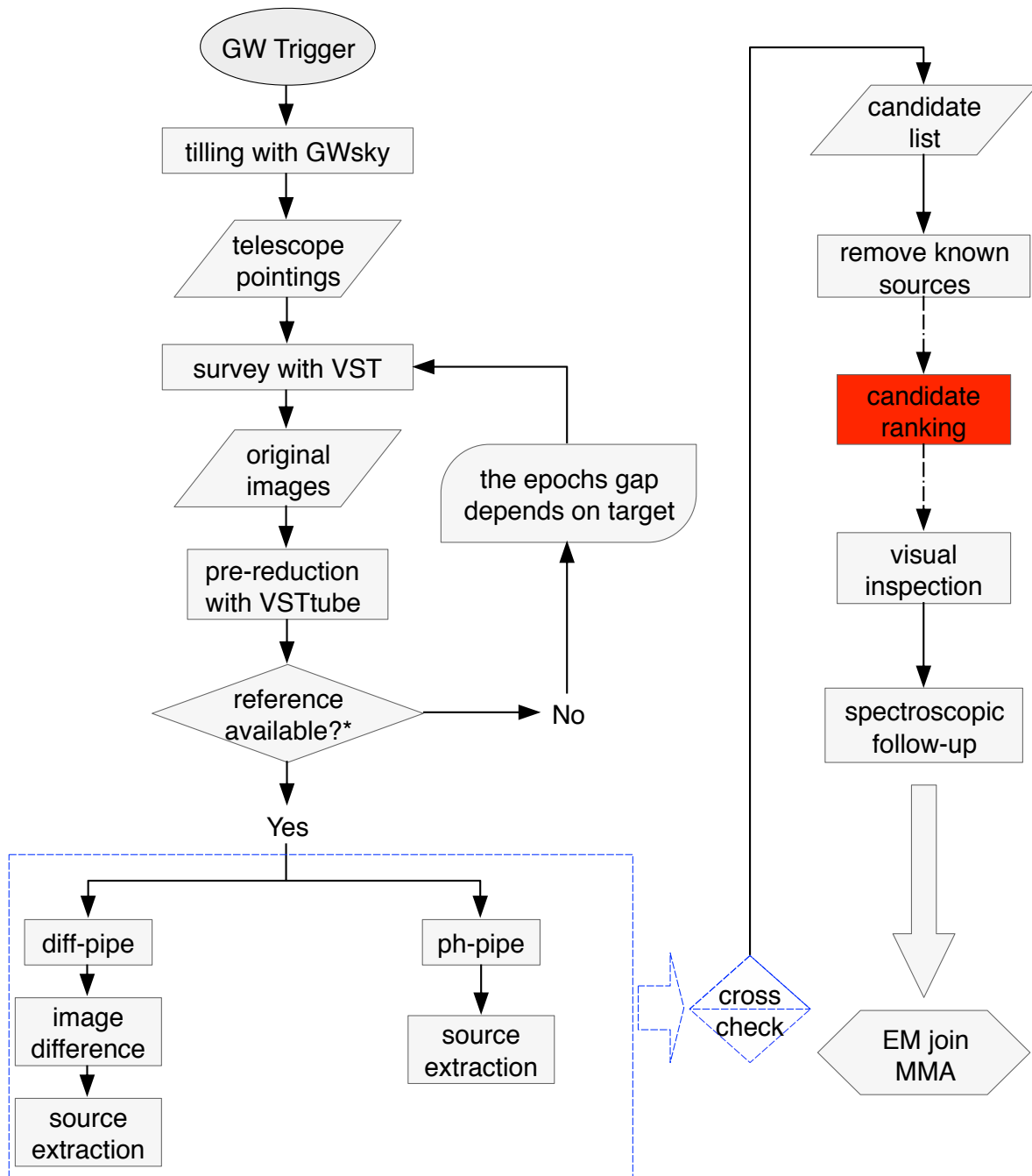
* At least 2 imges taken at different epochs of the same field are needed for transient detection.

Figure 2.2: Flowchart presents the GW's EM follow-up process.

event was produced by the merging of two black holes (BH) with a false-alarm rate of ≤ 1 in 27000 years. The estimated mass of the black holes are $30.5^{+5.7}_{-3.0}M_\odot$ and $25.3^{+2.8}_{-4.2}M_\odot$. The inferred luminosity distance is 540^{+130}_{-210} Mpc that corresponds to a redshift of z = $0.11^{+0.03}_{-0.04}$ Abbott et al. [2017b].

Binary BH events, such as GW 150914, 151226 and 170814, are not expected to produce bright EM counterpart. However, taking into account that exotic/optimistic models [De Mink et al. 2017] predict some EM radiation in the optical/near infrared spectrum, and the possibility of the unknown associated with such a new field, the GRAWITA collaboration decided to search for possible optical counterpart of these events with the VLT Survey Telescope (VST) [Capaccioli et al. 2003]. The ESO VST, a 2.6m, 1 deg^2 field of view (FoV) imaging telescope located at the Cerro Paranal Observatory in Chile [Capaccioli & Schipani, 2011; Kuijken et al., 2011]. The telescope optical design allows to achieve a uniform PSF with variation $< 4\%$ over the whole field of view. The VST is equipped with the OmegaCAM camera, which covers the field of view of 1 square degree with a scale of 0.21 arcsec/pixel, through a mosaic of 32 CCDs.

On 2017 August 17.528 UT, the LVC reported the detection of a GW nearly co-incident in time [2 seconds before, Goldstein et al., 2017b] the *Fermi* GBM trigger 524666471/170817529 located at RA=176.8° and DEC=-39.8° with an error of 11.6° (at 1σ). The LVC candidate had an initial localization of RA=186.62°, DEC=$-48.84°$ and a 1σ error radius of 17.45° [LIGO/Virgo Scientific Collaboration, 2017a]. The GW candidate was consistent with a binary NS with false alarm rate of $\sim 1/10,000$ years [LIGO/Virgo Scientific Collaboration, 2017a]. The GW was clearly detected in the LIGO detectors but was below threshold for the Virgo detector [LIGO/Virgo Scientific Collaboration, 2017b]. The Virgo data were crucial to constrain the localization of the event to only 31 deg^2 (90% credible region). The luminosity distance was constrained with LIGO data to be 40 ± 8 Mpc [LIGO/Virgo Scientific Collaboration, 2017b]. On 2017 August 17 23:49:55 UT (11.09 hours after the LVC event GW170817), the first EM counterpart of a GW event originated by the BNS, AT2017gfo, was independently detected by six groups, i.e. DLT40 group detected DLT17ck, at RA=13:09:48.09 and DEC=-23:22:53.4.6, 5.37W, 8.60S arcsec offset from the center of NGC 4993 [Yang et al., 2017a]. I will discuss the detection of DLT17ck in the following chapter.

The telescope time allocation was obtained in the framework of the Guarantee Time Observations (GTO) assigned by ESO to the teams in reward of their effort for the construction of the instrument. The planned strategy of the follow up transient survey foresees to monitor a sky area up to 100 deg^2 at 5/6 different epochs beginning soon after the GW trigger and lasting 8-10 weeks.

With the announcement of each trigger, different probability sky maps[3] were distributed to the teams of observers [LIGO/VIRGO Scientific Collaboration, 2015a,b]. For GW150914 at first, two initial sky maps were produced by un-modelled searches for GW bursts, one by the coherent Wave Burst (cWB) pipeline [Klimenko et al., 2016] and the other by the Bayesian inference algorithm LALInferenceBurst (LIB) [Essick et al., 2015]. The cWB and LIB sky maps encompass a 90% confidence region of 310 deg^2 and 750 deg^2, respectively. For GW151226, the initial localization was generated by the Bayesian localization algorithm BAYESTAR [Singer & Price, 2016]. The BAYESTAR sky map encompasses a 90% confidence region of 1400 deg^2. For GW170814, the initial localization was from BAYESTAR sky map spaning about 190 deg^2 in a 90% confidence region. The refined LALInference map covers about 13 and 62 square degrees with 50% and 90% confidence level respectively. For GW170817, the initial sky map was estimated by the BAYESTAR, and refined by LALInference, that the 50% and 90% credible regions span about 8 and 28 square degrees, respectively.

We choose the cWB skymap for GW150914, the BAYESTAR skymap for GW151226 and GW170817, the cWB and later on the refined skymap for GW170814, and planned our observing strategy to maximize the contained probability of GW localization accessible during the Paranal night. For the temporal sampling, we set up observations to explore different time scales able to identify day-weeks transients like short GRB afterglows and kilonovae, and slower evolving transients like supernovae or off-axis GRBs (cf. Tables 2.2, 2.3 and 2.4).

To prepare the Observing Blocks (OBs) we used a dedicated script named *GWsky*. *GWsky* is a `python`[4] tool devoted to effectively tile the sky localization of a gravitational wave signal and provide accurate sequences of pointings optimized for each telescope[5] (Greco et al. in preparation). To define the sequence of pointings, *GWsky* supplies information and descriptive statistics about telescope visibility, GW localization probability, presence of reference images and galaxies for each FoV footprint.

The sequence of the VST pointings for all GW events was defined optimizing the telescope visibility, maximizing the contained sky map probability accessible to the Paranal site, and excluding fields with bright objects and/or too crowded by galactic stars. The typical VST OB contains groups of nine pointings (tiles) covering an area

---

[3]FITS format files containing HEALPix (Hierarchical Equal Area isoLatitude Pixelization) sky projection, where to each pixel is assigned the probability to find the GW source in that position of the sky.

[4]http://www.python.org

[5] *GWsky* has a Graphical User Interface optimized for fast and interactive telescope pointing operations. The field-of-view footprints are displayed in real time in the Aladin Sky Atlas via Simple Application Messaging Protocol (SAMP) interoperability.
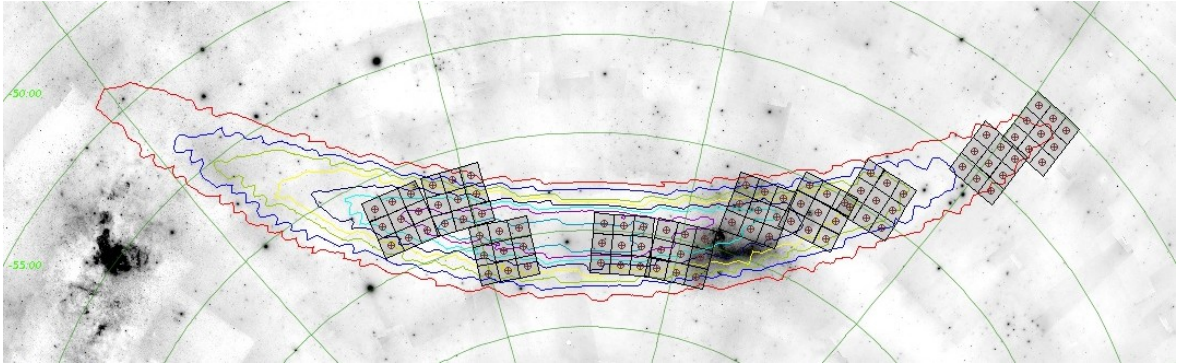
Figure 2.3: Footprints of the VST r band observations over the contours of the initially distributed cWB localization map of GW150914. Each square represents the VST Observing Block of 3×3 deg^2. The lines represent the enclosed probabilities from a 90% confidence level to a 10% confidence level in steps of 10%. The probability region localized in the northern hemisphere is not shown. The ten tiles enclose a localization probability of $\sim 29\%$. DSS–red image is shown in the background. An interactive skymap can be found in `https://www.grawita.inaf.it/highlights/`.
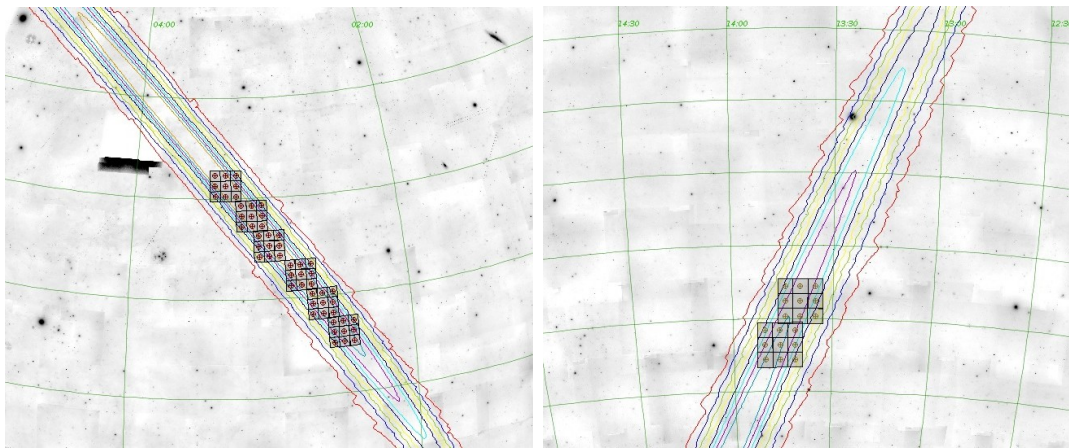
Figure 2.4: Footprints of the VST r band observations over the contours of the initially distributed BAYESTAR localization map of GW151226. From left to right, the VST coverage in the northern and southern hemispheres is shown. Each square represents the VST Observing Block of 3×3 deg^2. The lines represent the enclosed probabilities from a 90% confidence level to a 10% confidence level in steps of 10%. The eight tiles enclose a localization probability of $\sim 9\%$. DSS–red image is shown in the background. An interactive skymap can be found in `https://www.grawita.inaf.it/highlights/`.
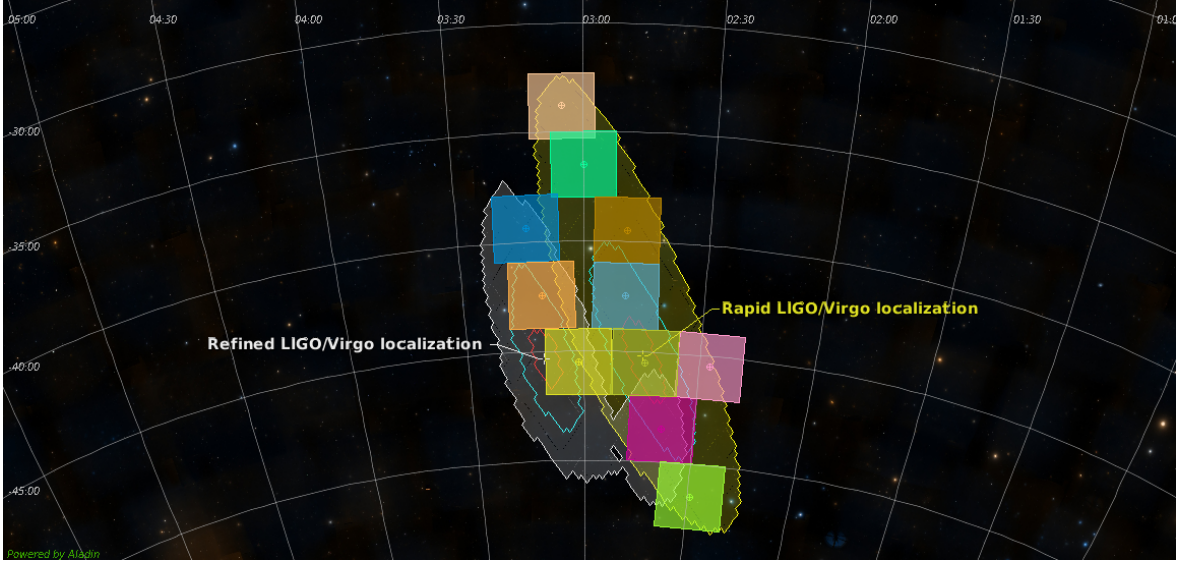
Figure 2.5: Footprints of the VST r band observations over the contours of both the initially distributed cWB localization map and refined map of GW170814. Each square represents a VST Observing Block of 3×3 deg^2. The yellow and white lines are the initial localization and refined map at 90% confidence level respectively. The tiles enclose a localization probability of $\sim 54\%$ of the refined sky map.

of 3×3 deg^2. For each pointing, we obtained two exposures of $40\,\mathrm{s}$ each dithered by $\sim 0.7 - 1.4$ arcmin. By doing this, the gaps in the OmegaCAM CCD mosaic are covered and most of the bad pixels and spurious events as cosmic rays are removed. The surveys of all events were performed in the r band filter. Summary of the VST follow-ups of GW 150914, 151226 and 170814 are reported in Tab. 2.2, 2.3 and 2.4, respectively. Also, the GRAWITA observing epochs and pointings of GW 150914, 151226 and 170814, together with the corresponding seeings, are shown in Fig. 2.6, 2.7 and 2.8, respectively. It should be mentioned that for the event GW170817 the initial sky map issued by LVC was offset of 2.5 degrees compared to the final sky map, a remarkable result. The VST observations, started very early, with 9.15 hours latency [Grado et al., 2017a], on August 17th at 23:18 using the initial map. The limited visibility of the area due to sun constraints, that allowed an observing time window sufficient to cover only nine deg^2, result on the fact that the optical transient AT2017gfo was not included in the search area. In the days after the discovery of AT2017gfo, new observations were executed pointing the telescope on its host galaxy NGC4993, as reported on the last three rows of the table 2.1, allowing us to secure

photometric measurements at the faint end of the kilonova light curve.

In table 2.1 is reported the summary of the observations for the four GW events followed by the VST (for details see table caption).

Table 2.1: Log of the VST observations for the GW events. The latency is the time between the start of the observations and the GW event alert, the coverage of the initial sky map is the fraction in percentage of the initial pycbc/bayestar 90% localization area covered with the VST. The coverage of the refined sky map is the fraction in percentage of the final LALInference 90% localization area covered with the VST. In column six are reported the number of epochs observed for the specified event and the last column report the 50% completeness for point like sources.

Event	Latency (hours)	Filter	Coverage Initial sky map (%)	Coverage refined sky map (%)	number of epochs	Completeness (AB mag)
GW150914	23	r	29	10	6	21
GW151226	7.6	r	9	7	6	21
GW170814	17.5	r	77	54	6	22 .5
GW170817	9.15	r	31	15	1	22.5
NGC4993	5.4d	g,r,i,z	-	-	1	23.6,23.5
						22.5,21.8
NGC4993	14.4d	i	-	-	1	22.5
NGC4993	145.7d	g,i	-	-	1	25.0, 24.5

GW150914

The VST responded promptly to the GW150914 alert by executing six different OBs on 17th of September, 23 hours after the alert and 2.9 days after the binary black hole merger [Brocato et al., 2015a]. In this first night observations covered 54 deg^2, corresponding approximately to the most probable region of the GW signal visible by VST having an airmass smaller than 2.5. The pointings projected over the central regions of the Large Magellanic Cloud (with a stellar density too high for our transient search) and the fields with bright objects were excluded. On 18th of September the sky map coverage was extended by adding a new set of four OBs, for a total coverage 90 deg^2. Monitoring of the 90 deg^2 region was repeated [Brocato et al., 2015b] over two months for a total of six observation epochs.

Fig. 2.3 shows the cWB sky locations of GW 150914 and the VST FoV footprints superimposed on the DSS-red image. The coloured lines represent the enclosed probabilities from a 90% confidence level to a 10% confidence level in step of 10%. For clarity, the probability region localized in the northern hemisphere is not shown. The VST observations captured a containment probability of 29%. This value dropped to 10% considering the LALinference sky map, which was shared with observers on 2016 January 13 [LIGO/VIRGO Scientific Collaboration, 2016a]. This sky map generated using Bayesian Markov-chain Monte Carlo [Berry et al., 2015], modeling the in-spiral and merger phase and taking into account the calibration uncertainty is considered the most reliable and provides a 90% credible region of 630 deg^2 [LALInf, Abbott et al., 2016e].

Table 2.2: Epochs and dates of the VST observations performed for the GW150914 event. The covered area and the night average seeing full width half maximum are reported in the last two columns.

GW150914			
Epoch	Date (UT)	Area deg^2	FWHM arcsec
1	2015-09-17	54	0.9
2	2015-09-18	90	0.9
3	2015-09-21	90	0.9
4	2015-09-25	90	1.1
5	2015-10-01	72	1.0
5	2015-10-03	18	1.0
6	2015-10-14	45	1.5
6	2015-11-16	9	1.2
6	2015-11-17	18	1.1
6	2015-11-18	18	1.5

GW151226

Also our response to GW151226 was rapid, 7.6 hours after the alert and 1.9 days after the merger event [Grado, 2015]. With eight OBs, we covered 72 deg^2 with the VST. Like for GW150914, the GW151226 survey consists of 6 epochs, spanning over one and
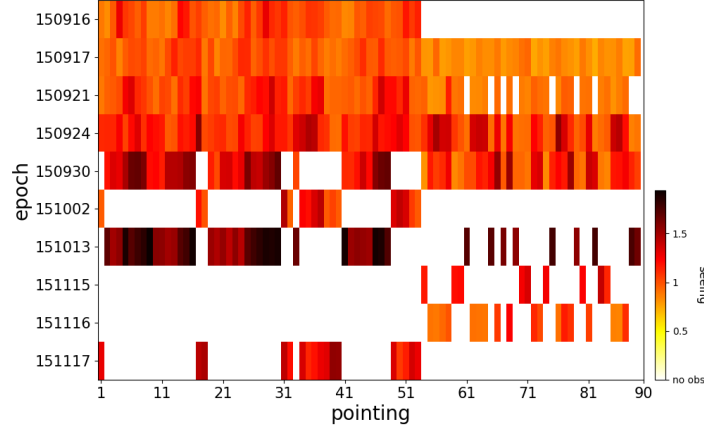
Figure 2.6: Epochs and dates of the VST observations performed for the GW150914 event. The colour represents the seeing.

a half month.

The two panels in Fig. 2.4 show the sequence of the VST pointings distributed across the BAYESTAR sky localization of GW151226 superimposed on the DSS-red image. The GW localization probability is concentrated in two long, thin arcs. Taking into account the characteristic ring-shaped region, the sequence of pointings runs along the inter-cardinal directions to maximize the integrated probability in each exposure. The VST observations captured a total probability of 9% of the initial BAYESTAR sky map and 7% of the LALinference sky map, which was shared on January 18 [LIGO/VIRGO Scientific Collaboration, 2015c] and and covered a 90% credible region of 1240 deg^2.

GW170814

Our response to GW170814 was relatively rapid, 17.5 hours after the alert [Greco et al., 2017], covering 81 deg^2 corresponding to 77% of the initial Bayestar sky map area and to 54% of the refined high probability region. The observations were repeated over nearly two months. The survey reached an average limiting magnitude of about 22.5 mag AB in the $r-$band.

Fig. 2.5 show the sequence of the VST pointings distributed across the cWB sky localization and refined map of GW170814 superimposed on the DSS-red image. The VST observations point both of the maps, captured a total probability of $\sim 31\%$ of the initial skymap and $\sim 15\%$ of the refined skymap.
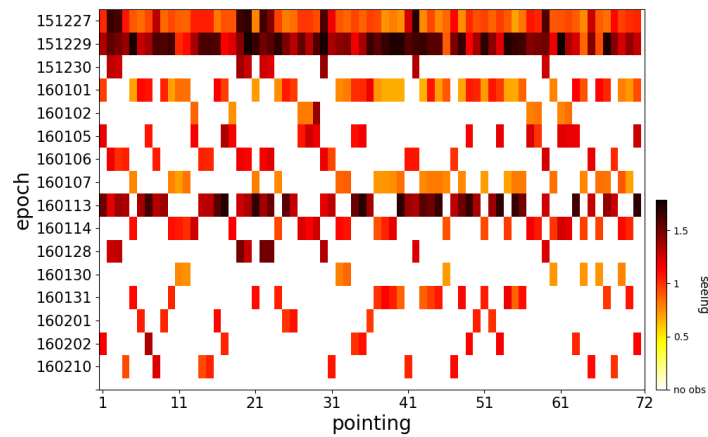
Figure 2.7: Epochs and dates of the VST observations performed for the GW151226 event. The colour represents the seeing.
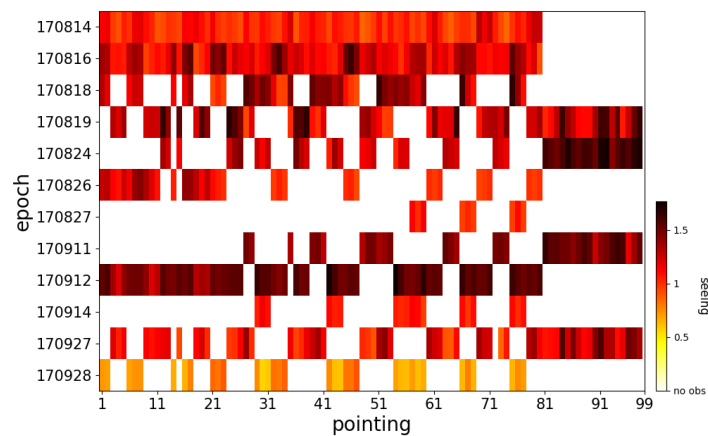
Figure 2.8: Epochs and dates of the VST observations performed for the GW170814 event. The colour represents the seeing.

Table 2.3: Epochs and dates of the VST observations performed for the GW151226 event. The covered area and the night average seeing full width half maximum are reported in the last two columns.

GW151226			
Epoch	Date	Area	FWHM
	(UT)	deg^2	arcsec
1	2015-12-27	72	1.0
2	2015-12-29	72	1.6
3	2015-12-30	9	1.3
3	2016-01-01	45	0.9
3	2016-01-02	9	0.9
4	2016-01-05	18	1.2
4	2016-01-06	18	1.1
4	2016-01-07	27	0.8
5	2016-01-13	45	1.5
5	2016-01-14	27	1.1
6	from 2016-01-28		
	to 2016-02-10	63	1.1

2.2   Data Processing

2.2.1   Pre-reduction

Immediately after acquisition, the images are mirrored to ESO data archive, and then transfered by an automatic procedure from ESO Headquarters to the VST Data Center in Naples. The first part of the image processing was performed using `VST-tube`, which is the pipeline developed for the VST-OmegaCAM mosaics [Grado et al., 2012]. It includes pre-reduction, astrometric and photometric calibration and mosaic production.

Images are treated to remove instrumental signatures namely, applying overscan, correcting bias and flat-field, as well as performing gain equalization of the 32 CCDs and illumination correction. The astrometric calibration is obtained using both positional information from overlapping sources and with reference to the 2MASS catalog. The absolute photometric calibration is obtained using equatorial photometric standard star fields observed during the night and comparing the measured magnitude of the

Table 2.4: Epochs and dates of the VST observations performed for the GW170814 event. The covered area and the night average seeing full width half maximum are reported in the last two columns.

	GW170814		
Epoch	Date	Area	FWHM
	(UT)	deg^2	arcsec
1	2017-08-14	81	1.0
2	2017-08-16	81	1.2
3	2017-08-18	45	1.3
3	2017-08-19	63	1.3
4	2017-08-24	45	1.4
4	2017-08-26	36	1.1
4	2017-08-27	9	1.0
5	2017-09-11	36	1.5
5	2017-09-12	63	1.5
6	2017-09-14	18	1.1
6	2019-09-27	62	1.2
6	2019-09-28	36	0.7

stars with the SDSS catalogue [6]. A proper photometric calibration is evaluated using the `Photcal` tool [Radovich et al., 2004] for each night. The relative photometric calibration of the images is obtained minimizing the quadratic sum of differences in magnitude between sources in overlapping observations. The tool used for both the astrometric and photometric calibration tasks is `SCAMP` [Bertin, 2006]. Finally the images are re-sampled and combined to create a stacked mosaic for each pointing. In order to simplify the subsequent image subtraction analysis, for each pointing the mosaics at the different epochs are registered and aligned to the same pixel grid. In this way, each pixel in the mosaic frame corresponds to the same sky coordinates for all the epochs. For further details on the data reduction see Capaccioli et al. [2015].

With the current hardware, the time needed to process one epoch of data of the VST follow-up campaigns here described, including the production of the *SExtractor* [Bertin & Arnouts, 1996] catalogs and all the quality control checks, amounts to about

---

[6]http://www.sdss.org

20 minutes per pointings.

2.2.2 Transient search

In order to search for variable and transient sources, the images were analysed by using two independent procedures. One is based on the comparison of the photometric measurements of all the sources in the VST field obtained at different epochs. The second is based on the analysis of the difference of images following the approach of the supernova (SN) search program recently completed with the VST [Botticella et al., 2016].

The two approaches are intended to be complementary, with the first typically more rapid and the latter more effective for sources projected over extended objects or in case of strong crowding. In the following, we report some details about both approaches. Taking into account the largely unknown properties of the possible EM gravitational wave counterpart we decided to not use model-based priors in the candidate selection. For both procedures, the main goal of our analysis is to identify sources showing a "significant" brightness variation, either raising or declining flux, during the period of monitoring, that can be associated to extra-galactic events.

2.2.2.1 The photometric pipeline (`ph-pipe`)

The photometric pipeline is intended to provide a list of "interesting" transients in low-latency to organise immediate follow-up activities. The computation time can be particularly rapid, e.g. just a few minutes for each epoch VST surveyed area. The weakness of this approach is that sources closer than about a Point Spread Function (PSF) distance or embedded in extended objects can be difficult to detect and therefore can possibly remain unidentified.

The procedure has been coded in `python` (version 3.5.1) language making use of libraries part of the `anaconda`[7] (version 2.4.1) distribution. The procedure includes a number of basic tools to manage the datasets, i.e. source extraction, classification, information retrieval, mathematical operations, visualization, etc. Data are stored and managed as `astropy`[8] (version 1.2.1) tables. I mentioned here that this ph-pipe package was developed by Stefano Covino from GRAWITA.

The analysis is based on the following steps:

---

[7]https://docs.continuum.io/anaconda/index
[8]http://www.astropy.org

1. The `SExtractor` package (Bertin & Arnouts 1996), as implemented in the python module `sep`[9] (version 0.5.2), was used for source extraction. This algorithm gives the best results considering the request of a rapid running time. The extraction threshold is set at 5σ.

2. The source list is then cleaned removing obvious artifacts by checking various shape parameters (roundness, full width at half maximum, etc.). Then a quality flag based on the "weight" maps generated by the VST reduction procedure [Capaccioli et al., 2015] is attributed to the detected objects. All the sources are processed but only those associated to the best exposed frame zones are used to tune the statistical analyses (described below) aimed at identifying transients or variable objects.

3. Aperture photometry is measured for all the sources at each epoch. Although at the expense of longer computation time, the more reliable algorithm `DAOPHOT` [Stetson, 1987], as coded in the `PythonPhot`[10] (version 1.0.dev) module, is used rather then other quicker alternatives. The magnitudes at each epoch are normalised to those of the reference epoch, typically but not necessarily the first in chronological order, computing the median difference of the magnitudes of objects with the highest quality flag. Finally, the angular distance and the magnitude difference from the closest neighbors are computed for each source to evaluate the crowding.

4. The source list is cross-correlated (0.5 arcsec radius) with the Initial GAIA source list [IGSL, Smart & Nicastro, 2014] and later, when it became available, with the GAIA catalogue (DR1 release)[11], saving the uncatalogued sources and sources catalogued as extended (possible GW host galaxies) for further analysis. This typically removes about 40% of the detected objects, depending on the depth of the observations and the Galactic coordinates of the observed field. The risk of erroneously remove the nucleus of some faint or far galaxy, wrongly classified in these catalogs as point-like sources, is of course present. We checked that within the magnitude limits of the considered catalogs (and considering the distance range of the counterparts to GW events we are looking for) most of the extended objects are indeed correctly identified and classified. The SDSS[12] and the Pan-

---

[9]https://sep.readthedocs.org/en/v0.5.x/
[10]https://github.com/djones1040/PythonPhot
[11]http://vizier.u-strasbg.fr/viz-bin/VizieR?-source=I/337
[12]http://www.sdss.org

STARRS[13] data releases are also used in case the analysed areas are covered by these surveys.

5. A "merit function" is derived taking into account several parameters as variability indices (i.e. maximum-minimum magnitude, χ^2 of a constant magnitude fit, proximity to extended objects, signal-to-noise ratio, crowding). The higher the value of the merit function the more interesting the variability of the transient object is.

6. The selection of the interesting objects, i.e. those showing a large variability and those with the higher merit (the merit also includes variability information although not necessarily large variability implies a high merit), including objects previously undetected or disappeared during the monitoring, is a multi-step process. First of all, the highest quality ranked objects are binned in magnitude to compute the sigma-clipped averages and the standard deviations of the magnitude difference for each available epoch. Then, all the objects showing variability larger than a given threshold (e.g. 5-7 σ, in our cases) between at least two epochs are selected (this practically corresponds to a magnitude difference larger than about 0.5 mag for good quality photometric information). The whole procedure is affected by some fraction of false positives due to inaccuracies of the derived photometry for sources with bright close companions since a seeing variation among the analyzed epochs can induce a spurious magnitude variation.

7. The list of (highly) variable objects is cross-correlated (2 arcsec radius) with the SIMBAD astronomical database [Wenger et al., 2000] to identify already classified sources and with the list of minor planets provided by the SkyBot[14] portal at the epoch of observation. This piece of information is stored but the cross-correlated objects are not removed from the list yet.

8. The last step of the analysis consists in the computation of PSF photometry for the selected objects again using `PythonPhot` module. The PSF is derived selecting automatically at least 10 isolated stars in a suitable magnitude range. In order to keep the computation time within acceptable limits, PSF photometry is derived only for the objects of interest without carrying out a simultaneous fit of the sources in the area of the target of interest. For moderate crowding this is already sufficient to derive reliable photometric information even in case of large seeing variation.

---

[13]http://panstarrs.stsci.edu
[14]http://vo.imcce.fr/webservices/skybot/

9. Then, by means of the PSF photometry, step 6 is repeated and the list of objects surviving the automatic selection is sent to a repository for a further final check via visual inspection. Stamps of these objects for each epoch are produced to aid the visual inspection and FITS files of any size around them can also be produced if needed. It is also possible to produce light-curves, to convert the list of candidates to formats suited for various graphical tools (e.g. the starlink GAIA FITS viewer[15]).

As an example, for the observations taken after the GW150914 trigger the number of extracted sources ranged from a few tens of thousands in high Galactic latitude fields, to about half a million for fields nearby the Large Magellanic Cloud. About three million sources per each epoch of our monitoring and a total of about nine million sources were extracted and analysed. The number of highly variable objects, satisfying our selection criteria and not present in the GAIA catalog, resulted to be 54239, about 0.6% of the initial list. Choosing only the sources with higher score we remain with about 5000 candidates. The last cleaning is carried out by visual check, candidates affected by obvious photometric errors due to crowding, faintness, or image defects are removed. Candidates showing good quality light-curves that can be classified basing on known variable class templates (RR Lyare, Cepheids, etc.) are also removed form the list, this step indeed allows us to clean the majority of the remaining candidates. Finally, candidates showing light-curves grossly consistent with the expectations for explosive phenomena as GRB afterglows, SNae and macronovae, or candidates laying nearby extended objects (i.e. galaxies) are saved for further processing defining a final list of 939 sources (cf. Sect. 2.3.1).

2.2.2.2   The image difference pipeline (`diff-pipe`)

A widely used, most effective approach for transient detection is based on the difference of images taken at different epochs. To implement this approach for the survey described in this paper we developed a dedicated pipeline exploiting our experience with the medium-redshift SN search done with the VST [SUDARE project, Cappellaro et al., 2015]. The pipeline is a collection of `python` scripts including specialized tools for data analysis, e.g. `SExtractor`[16] [Bertin & Arnouts, 1996] for source extraction and `topcat`[17]/`stilts`[18] for catalog handling. For optical images taken from the

---

[15]http://star-www.dur.ac.uk/ pdraper/gaia/gaia.html
[16]http://www.astromatic.net/software/sextractor
[17]http://www.star.bris.ac.uk/ mbt/topcat/
[18]http://www.star.bris.ac.uk/ mbt/stilts/

ground, a main problem is that the PSF is different at different epochs, due to the variable seeing. The PSF match is secured by the `hotpants`[19] code [Becker, 2015], an implementation of the Alard [1999] algorithm for image analysis. I mentioned here that this diff-pipe package was developed by my advisor, Enrico Cappellaro, and me. I show a detailed description of this pipeline in the appendix.

The analysis is based on the following steps:

1. For each image the VSTtube [Grado et al., 2012] pipeline produces a bad pixels mask with specific flags. The areas enclosing bright/saturated stars, that leave spurious residuals in the image difference, are also masked.

2. We compute the difference of images taken at different epochs. For PSF match, by comparing sources in common between the two images, the image with the best seeing is degraded to match the other image. In an ideal case one would like to use template images taken before the actual search epochs. Unfortunately, such templates are not always available for the specific area monitored in our survey and in that case we use as template the image taken at the latest epochs. With this approach we are able to detect as positive sources in the difference image all the transients that at the latest epoch disappeared or, in general, are fainter than in the previous epochs. On the contrary, sources that are brighter at the latest epoch leave a negative residual in the difference image and would not be detected. The latter ones can be detected by searching the "negative" difference image that is obtained by multiplying the regular difference by -1 (see next).

3. `SExtractor` is used to detect positive sources in the difference image (transient candidates). We also search for negative differences to guarantee completeness for raising or declining transients. The number of detected sources strongly depends on the adopted threshold, defined in unit of the background noise. In this experiment we use a $1.5\,\sigma$ threshold. From the list of detected sources we delete all sources occurring in a flagged area of the masked image.

4. The list of candidates contains a large number of spurious objects that can be related to small mis-alignment of the images, improper flux scalings, incorrect PSF convolution or to not well masked CCD defects and cosmic rays.

   To filter out the spurious candidates, we use a ranking approach. To each candidate we assign an initial score that is decreased/increased depending on different

---

[19]http://www.astro.washington.edu/users/becker /v2.0/hotpants.html

source parameters either provided by SExtractor or measured directly on the difference image. By using a combination of different parameters, we test whether the source detected in the difference image is consistent with being a genuine stellar source. The ranking scores are calibrated by means of artificial star experiments to ensure that good candidates obtain a positive score.

The main SExtractor parameters used to derive the ranking for each candidates are: FWHM, ISOAREA, FLUX_RADIUS and CLASS_STAR. In addition, we penalized transient candidates very close to a bright star of the reference image and/or those for which the ratio of positive/negative pixels in the defined aperture is below a specific threshold. In fact, in many cases small PSF variations produce positive/negative pairs in the difference image.

In this scheme, we also allow for positive attributes intended to promote specific type of sources. In particular, we promote transients found near galaxies with the idea that these are worth a second look.

5. The catalogs of sources detected at different epochs in each pointing are merged. In this final catalog we include only candidates with scores above a selected score threshold, though we also record the number of independent detections for each candidate regardless of the score.

6. We cross check our candidate list with the *SIMBAD* database using a search radius of 2 arcsec with the purpose to identify known variable sources. While we do not expect them to be the EM counterpart, known variable sources are useful to test the pipeline performance.

7. For each candidate we produce a stamp for visual inspection including the portion of the original images at the different epochs along with the same area in the respective difference images. If needed, one can also produce stamps for specific coordinates, not corresponding to detected transients. This is useful to check for candidates detected by other searches.

8. Finally, we perform detailed artificial star experiments with the aim to measure the search efficiency as a function of magnitude and provide rates or, in case, upper limits for specific kind of transients.

As an example, for the case of GW150914, the procedure produced a list of about 170000 transient candidates (with an adopted threshold of 1.5σ of the background noise) many with multiple detections. The scoring algorithm reduces this number by

one order of magnitude: the final list includes 33787 distinct candidates of which 11271 candidates with high score that are taken as bona-fide genuine transients. Finally, we performed a visual inspection concluding that $\sim 30\%$ are obvious false positive, not recognized by the ranking algorithm.

The image difference pipeline was definitely more time consuming than the photometric pipeline: e.g. the computing time for the typical case (90 deg^2, at six epochs) was around 2 days, that is fairly long for low-latency search. For future triggers we have implemented parallel version of the pipeline, using the `python` modulus `pp`[20]. This will reduce the required time by a factor ~ 5.

A comparison between the transients identified by the two pipelines shows that, as expected, the image-difference pipeline is more effective, in particular for objects very close to extended sources. However, the photometric pipeline is less affected by image defects as halos of very bright or saturated stars, offering a profitable synergy. Typically, a percentage ranging from 80 to 90% of the transients identified with the photometric pipeline are also recorded by the image-difference pipeline.

2.2.2.3   The detection efficiency

In order to measure our search performance and to tune the observing strategy, we performed extensive artificial star experiments. To this aim we use the `daophot` package to derive the PSF for each of the searched image and then we add a number of artificial stars of different magnitudes in random positions. Then, we run the image difference pipeline and count the number of artificial stars that are recovered with a score above the adopted threshold. The ratio of recovered over injected stars gives the detection efficiency as a function of magnitude. An example of the outcome of this procedure is shown in Fig. 2.9 for three different pointings following the GW151226 trigger. The detection efficiency vs. magnitude empirical relation is well fitted by a simple function [Cappellaro et al., 2015] and can be used to measure the parameter DE_{50}, defined as the magnitude at which the detection efficiency drops to 50% of the maximum value. This depends first of all on sky conditions, transparency and seeing, but also on field specific properties, in particular crowdedness and contamination by bright stars. In Fig. 2.10 we show the measurements of DE_{50} for all the pointings of the two GW triggers as a function of seeing. We notice that, for good sky conditions our survey can detect transients down to $r \sim 22$ though most observations are in the range $20 - 22$ mag. On the other hand, in case of poor seeing (FWHM> 1.5 arcsec) the magnitude limit is ~ 20 mag.

---

[20]https://github.com/uqfoundation/ppft
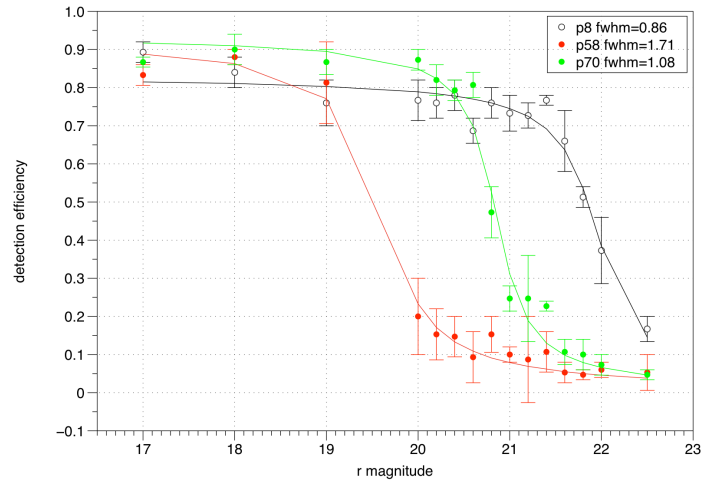
Figure 2.9: Example of the output of artificial star experiments. The detection efficiency (DE) is defined as the ratio between the number of detected stars and the number of injected stars in specific magnitude. The plot shows the correlation between DE and the magnitude for three pointings of GW151226 (p8, p58, p70).
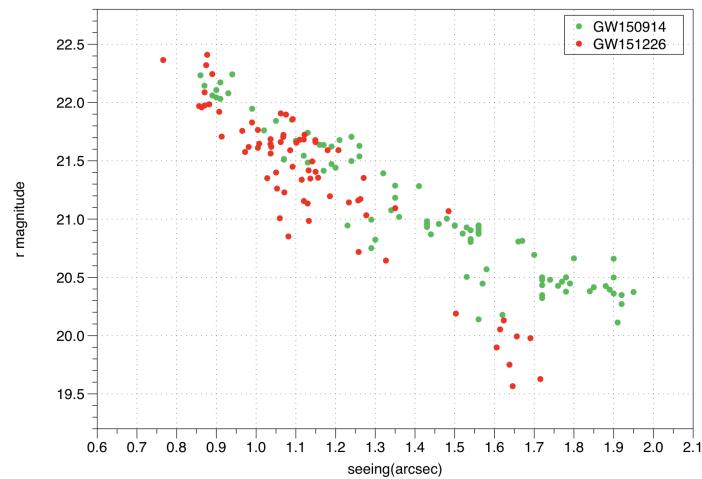
Figure 2.10: The limiting magnitude for transient detection (DE_{50}) as a function of seeing for the pointings of the two triggers discussed in this paper. The scatter is due to the fact that other factors are affecting the DE, first of all sky transparency.

2.3   Searching Results

In total, we have follow-up surveyed 4 GW triggers in the LVC O1 and O2 seasons, three events are generated by coalescence of black-holes, namely GW150914, 151226 and 170814, and one event, GW170817, is proved to be created by coalescence of binary neutron stars. We searched only one epoch for GW170817 since the EM counterpart was discovered very soon. I will present our detailed follow-up of the host galaxy of the counterpart in the following section. Here, we report the searching results for the other three BBH events. We now know that for the gravitational wave events generated by coalescence of black-holes, strong electromagnetic radiation is not expected to occur in the current scenario, and in fact none of the transients identified by the worldwide astronomical effort could be linked to the observed GW events. However, the analysis of the data obtained in response to the GW triggers is important both for evaluating the search performances and for tuning future counterpart searches. In the following we will give an overview of the results of our search and describe a few representative transients, typically candidate SNe, detected by our analyses with the purpose to illustrate pros and cons of our approach.

An important limitation for our analysis is that the sky areas surveyed after the three triggers were never observed before with the VST telescope and therefore we do not have access to proper reference images. The consequence is that for an efficient transient search we had to wait for the completion of the monitoring campaign and could not activate immediate follow up. For this reason, we only have few cases of candidate SNe associated with galaxies with known redshift, for which we can propose a plausible classification.

Finally, for an external check of our survey performances, we compared the candidate detected by our pipelines with those found by other searches, when available.

In table 2.5 are summarized the results found for the transients searches associated to the BBH events. In the table are shown the total number of sources summed all over the epochs, then for each pipeline are reported the number of transients found after removing all the known photometric and astrometric transients available in SIMBAD and GAIA databases. The last column shows the total number of supernovae candidates we found in the time window of interest. The list includes the known SNe that were also found in our search. A comparison between the transients identified by the two pipelines shows that, as expected, the image-difference pipeline is more effective, in particular for objects very close to extended sources.

Table 2.5: Results of the optical transients/variables search. The initial number of sources indicates the total number, summed over all the epochs, of the sources detected in the fields. The fourth columns indicates the number of transients found after removing the known photometric and positional variables sources. In the last columns, as by product, are reported the number of known and candidate supernovae found in the field.

Event	Pipeline	Initial number of sources	unknown optical transients	SNe
GW150914	ph-diff	9×10^6	2600	10
	ph-pipe		939	
GW151226	ph-diff	9×10^5	1113	21
	ph-pipe		305	
GW170814	ph-diff	1.5×10^6	55	24
	ph-pipe		37	

2.3.1   GW150914

As described in Section 2.1, the VST observations started 2.9 days after the occurrence of the GW150914 event and just 1 day after the alert. The 90 deg^2 observed sky area captured 29% of the initial cWB sky map probability and 10% of the more accurate LALInference sky map. Indeed, this latter sky map is more suitable for BBH mergers but it was made available only on January 2016, when most of the EM follow-ups on GW150914 were already over. Prompt response, survey area and depth make a unique combination of features of our VST survey (see Fig. 2.11) matched only by the DECam survey [Soares-Santos et al., 2017] at least for what concerns the combination of depth and area of the survey.

The total list of variable/transient objects selected by the `diff-pipe` consists of 33787 sources (of which 11271 with high score). The number of sources provided by the `ph-pipe` is 939. More than 90% of them are also detected by the `diff-pipe`. The smaller number of sources detected by the `ph-pipe` is due to i) the removal of all the "bright" and/or previously known variable sources after the match with the GAIA catalog and ii) the much higher adopted detection threshold. Most of the sources identified by the `ph-pipe` and not included in the catalog produced by the `diff-pipe` turned out to be real and were typically located in regions that needed to be masked for
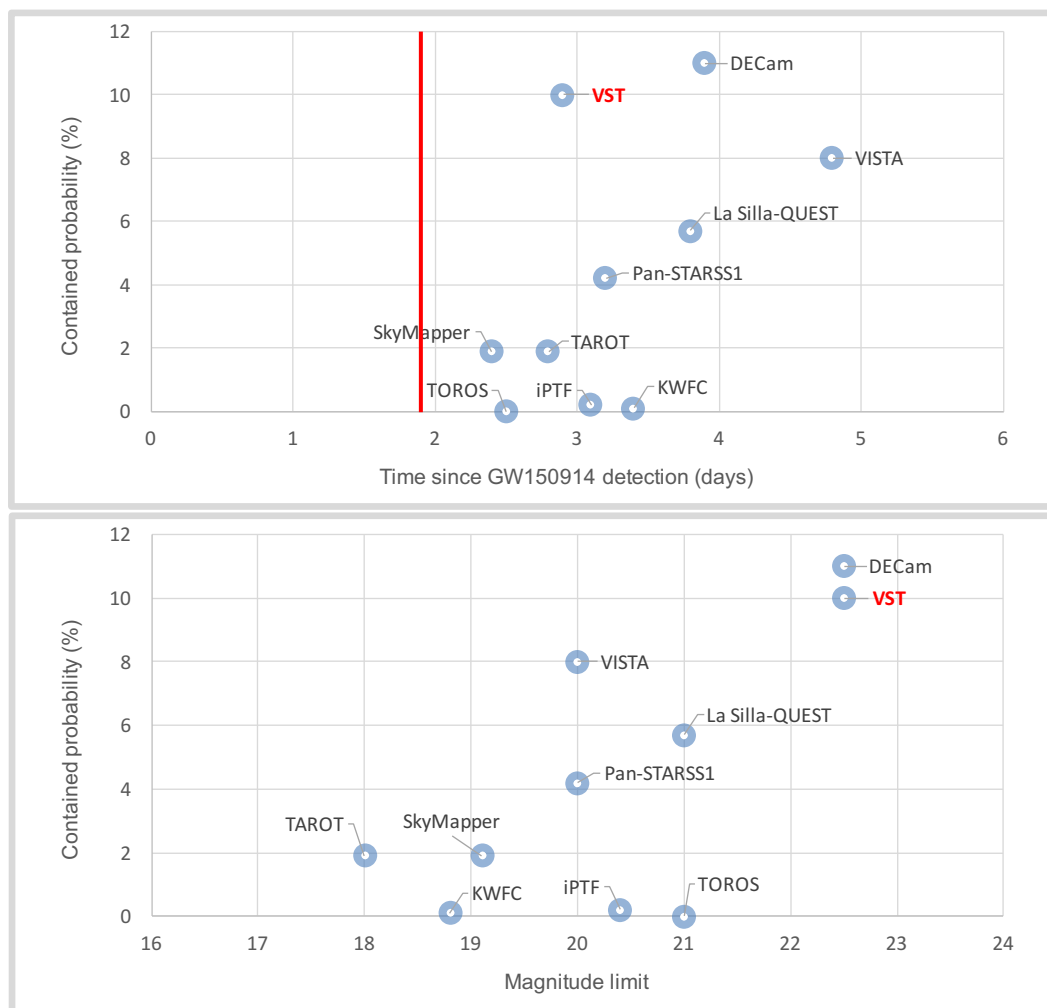
Figure 2.11: VST performance. In the top panel the time response of VST in terms of time and contained probability is compared to other facilities. The red vertical line marks the time of the LVC alert to the astronomical community. A similar comparison is plotted in the lower panel but in the abscissa the approximate magnitude limits are reported. The magnitude limits refer to different photometric bands. The data are from Abbott et al. [2016e]; Abbott et al. [2016h].

a reliable image subtraction. Many of the `diff-pipe` candidates are known variables. As a further test, we applied the same selection criteria of the `ph-pipe` to the list of the 33787 variable/transient sources identified by `diff-pipe`. The selection produces a list of about 3000 objects. This last sample still includes known variable sources (more than 400) or objects whose light-curves can be classified with known templates, or possible

Table 2.6: Number of variable and total detected sources (`diff-pipe`) within the 3×3 deg^2 areas covered by each of the 9 tiled observations. Those close to the LMC are clearly recognizable by the large number of sources.

RA J2000	Dec J2000	Num. var	Tot. sources
58.208846	−56.949515	196	34345
60.652964	−59.855304	430	36057
68.948300	−64.802918	645	69077
74.729746	−66.793713	6225	676621
82.166543	−67.952724	14590	1083748
91.163807	−71.180392	6337	720924
100.348601	−71.180473	1923	147827
118.562044	−71.090518	654	98150
122.909379	−67.971038	700	125286
131.090822	−67.972011	2087	183930

defects in the subtraction procedure. As expected, the `diff-pipe` is more effective in finding variable/transient objects than the `ph-pipe`, although the final cleaned lists also contain objects that are found by one pipeline only.

As it can be seen from Fig. 2.3, some of the VST fields overlap with the outskirt of the Large Magellanic Cloud (LMC) which contributes with a large number of relatively bright stars and many variable sources. This effect is clearly visible from the statistics of detected and variable sources in the fields as reported in Table 2.6. This represents a severe contamination problem in the search for the possible GW counterpart. On the other hand, the LMC has been the target of a very successful monitoring campaign by the Optical Gravitational Lensing Experiment (OGLE)[21]. The OGLE survey is fairly complete down to mag ~ 20 and has already identified many of the variable stars in the field. A cross-check of our `diff-pipe` candidate catalog against the SIMBAD database gave a match for 6722 objects of which 6309 identified with different type of variable sources, mainly RRLyrae (48%), eclipsing binaries (23%) and a good number of Long Period Variables, semi-regular and Mira (23%). The sky distribution of the matched sources reflects the LMC coverage by both our and the OGLE surveys. We notice that, as appropriate, the fraction of SIMBAD variable sources identified among our high score transient candidates is much higher (55%) than for the low score candidates

---

[21]http://ogle.astrouw.edu.pl

(26%).

2.3.1.1 Previously discovered Transients

Searching the list of recent SNe[22], we found that in the time window of interest for our search, three SNe and one SN candidate were reported that are expected to be visible in our search images, All these sources were detected in our images, and in particular:

- SN 2015F was discovered by LOSS in March 2015 [Monard et al., 2015] in NGC 2442 ($z \sim 0.0048$) and classified as type Ia with an apparent magnitude at peak of ~ 17.4. The object was detected by our pipeline in the radioactive declining tail.

- SN 2015J was discovered on 2015-01-16 [Brown et al., 2014; Scalzo et al., 2015] and classified as type IIn at a redshift $z \sim 0.0054$ [Guillochon et al., 2017]. In our images it was still fairly bright at $r \sim 17.8$, fading to $r \sim 18.5$ in a month (Fig. 2.12, right panel).

- OGLE15oa was discovered on 2015-10-16 (by OGLE-IV Real-time Transient Search, Wyrzykowski et al. [2014]) and was classified as a type Ia about 20 days after maximum on 2015-11-09 by Dennefeld et al. [2015]. Most of our images are pre-discovery and the pipeline detected the transient at mag $r \sim 18.8$ in the images obtained in the last epoch, 2015-11-16.

- A special case is OGLE-2014-SN-094, which was discovered on 2014-10-06 and initially announced as a SN candidate [Wyrzykowski et al., 2014]. The source showed a second outburst in May 2015 and again in Nov 2015 [Guillochon et al., 2017]. We detected the source at the end of our monitoring period at a magnitude similar to that at discovery ($r \sim 19.5$, Fig. 2.12, left panel). The photometric history indicates that this is not a SN but more likely an AGN. A UV bright source, GALEXMSC J044652.36-655349.9, was also detected at the same position[23].

2.3.1.2 Transient candidates

In addition to known sources, we also singled out a few objects that most likely are previously undiscovered SNe (Fig. 2.13).

---

[22]We used the update version of the Asiago SN catalog [http://sngroup.oapd.inaf.it/asnc.html, Barbon et al., 1999]

[23]http://ned.ipac.caltech.edu

Table 2.7: Coordinates of the known or newly identified sources (SNe or candidate SNe) derived from the GW 150914 follow-up campaign discussed in this section.

Id	RA J2000	Dec J2000	Alternate Id	Note
VSTJ54.55560-57.56763	3:38:13.34	-57:34:03.5		SN candidate
VSTJ56.28055-57.91392	3:45:07.33	-57:54:50.1		SN candidate
VSTJ57.77559-59.13990	3:51:06.14	-59:08:23.6		SN Ia or Ib/c candidate, $z \sim 0.11$
VSTJ60.54727-59.91890	4:02:11.34	-59:55:08.0		SN candidate
VSTJ61.20106-59.98816	4:04:48.25	-59:59:17.4		SN candidate
VSTJ69.10694-62.79775	4:36:25.67	-62:47:51.9	OGLE15oa	SN Ia.
VSTJ69.55973-64.47081	4:38:14.34	-64:28:14.9		SN candidate
VSTJ71.71864-65.89735	4:46:52.47	-65:53:50.5	OGLE-2014-SN-094	AGN candidate
VSTJ113.77187-69.13147	7:35:05.25	-69:07:53.3	SN 2015J	SN IIn, $z \sim 0.0054$
VSTJ114.06567-69.50639	7:36:15.76	-69:30:23.0	SN 2015F	SN Ia, $z \sim 0.0048$
VSTJ119.64230-66.71255	7:58:34.15	-66:42:45.2		SN Ia or Ib/c candidate, $z \sim 0.047$
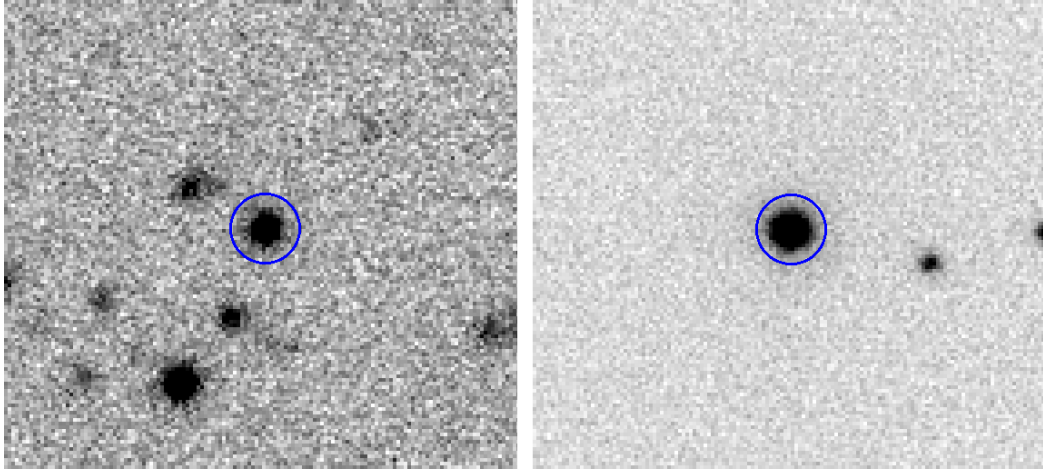
Figure 2.12: *Left:* The SN candidate OGLE-2014-SN-094 observed on 2015 Nov. 11. *Right:* The SN IIn SN 2015J at $z \sim 0.0054$ observed on 2015 Sept. 15. The blue annuli represent the position identified by our pipelines
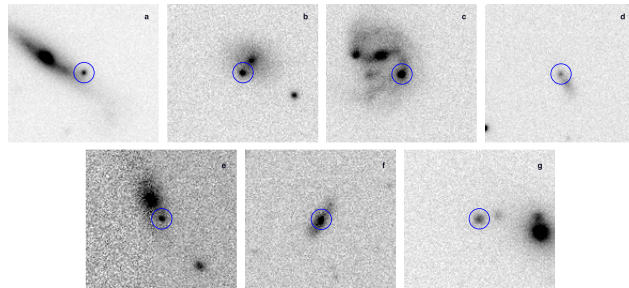
Figure 2.13: SN candidates identified in our survey after GW150914. *a.* VSTJ54.55560-57.56763 observed on 2015, Sept. 17. *b.* VSTJ56.28055-57.91392 observed on 2015, Oct.13. *c.* VSTJ57.77559-59.13990 observed observed on 2015, Sept. 18. The galaxy is at redshift $z \sim 0.11$. *d.* VSTJ60.54735-59.91899 observed on 2015, Sept. 30. *e.* VSTJ61.20106-59.98816 observed on 2015, Sept. 30. *f.* VSTJ69.55986-64.47089 observed on 2015, Sept. 17. *g.* VSTJ119.64244-66.71264 observed on 2015, Oct. 13. In all images the showed field sizes are 30×30 arcsec, North is up and East to the left. The blue annuli represent the position identified by our pipelines.

- VSTJ54.55560-57.56763: the source was fading after the detection during our first epoch observation. It is located close to an edge-on spiral galaxy PGC 145743 [HyperLEDA, Makarov et al., 2014]. No redshift is available.

- VSTJ56.28055-57.91392: this source was caught during brightening. It is located close to a spheroidal galaxy (2MASXJ03450711-5754466 in HyperLEDA). No redshift is available.

- VSTJ57.77559-59.13990 was likely detected close to peak ($r \sim 19.4$ mag). It was located in the arm of the face-on, barred spiral galaxy PGC 141969 at redshift $z \sim 0.11$ [The 6dF Galaxy Survey Redshift Catalogue, Jones et al., 2009]. The transient absolute magnitude was then brighter than ~ -19. In Fig. 2.14, top panel, we show our photometry (assuming the distance obtained from the redshift of the likely host galaxy, i.e. $z \sim 0.11$) superposed to the light-curve of SN 1998bw [Galama et al., 1998; Iwamoto et al., 1998; Patat et al., 2001]. SN 1998bw was associated with the long GRB 980425 [Pian et al., 2000] and it is the prototype of the broad-lined stripped-envelope SNe events SN Ib/c [Iwamoto et al., 1998; Mazzali et al., 2013]. From this comparison we estimate that the SN explosion occurred about three weeks before our first observation, that is in late August 2015. Interestingly, the *Fermi*-GBM online archive[24] shows that on 2015 August 27 a GRB (burst time 18:50:12.969 UT, $t_{90} \sim 10$ s, RA$_{J2000}$=04:33:12.0, DEC$_{J2000}$=-60:00:00) was detected at a distance of about 5.5°, consistent within the error with the SN position [the reported pointing error is $\sim 5.1°, 1\sigma$, to which we should add the systematic error of 2-3°, Singer et al., 2013].

  Fig. 2.14 shows the data simply plotted without any fitting and considering the GRB time as the SN explosion time. The agreement, within the limits of our sparse monitoring, is remarkable. Assuming these events are really associated, GRB 150827A would be a low-luminosity GRB, $E_{\mathrm{iso}} \sim 10^{49}$ erg, similar, in energy output, to the underluminous GRBs 980425 and 031203 [Amati, 2006; Ghisellini et al., 2006; Yamazaki et al., 2003], and to the X-ray flashes 060218 and 100316D [Campana et al., 2006; Starling et al., 2011].

  It would also be compatible with the luminosity function derived, e.g., in Pescalli et al. [2015].

  Although the connection of the *Fermi*-GBM event and the optical transient draws a credible scenario, we cannot rule out the possibility of a chance association. As

---

[24]https://heasarc.gsfc.nasa.gov

an example, in Fig. 2.14, the bottom panel shows the light-curves of a standard type Ia SN 1999ee [Stritzinger et al., 2012] or even with that of the peculiar type Ia SN 1991T [Cappellaro et al., 2001] are also consistent with our data.

- VSTJ60.54727-59.91890 was detected already during the raising phase in an uncatalogued galaxy probably of spiral morphology. Its light-curve is compatible with several different SN types at different redshift in the range $0.04 - 0.14$. The best fit is for a SN II at $z \sim 0.07$.

- VSTJ61.20106-59.98816 was detected during the raising phase. The transient appears to be located in the outskirt of PGC 367032 (from HyperLEDA), a spiral galaxy with a bright core. No redshift is available.

- VSTJ69.55973-64.47081 was detected in an uncatalogued spiral galaxy. The transient was at approximately constant magnitude ($r \sim 21.6$) for a couple of weeks after the GW 150914 alert and then it was below our detection threshold at the end of our campaign.

- VSTJ119.64230-66.71255 was also detected during the raising phase. It is located in the spheroidal galaxy 6dFJ0758321-664248 at redshift $z \sim 0.047$ [Jones et al., 2009]. The light-curve is consistent with both a SN Ia or a Ib/c.

Assuming all these objects are SNe and including the three other SNe first discovered in other surveys (we did not consider the likely AGN OGLE-2014-SN-094, Table 2.7), we count 10 SNe. This can be compared with the expected number of SNe based on the known SN rates in the local Universe, the survey area, the light curve of SNe, the time distribution of the observations, the detection efficiencies at the different epochs [c.f. Sect. 5.1 of Smartt et al., 2016a]. For this computation we used a tool specifically developed for the planning of SN searches [Cappellaro et al., 2015]. We estimate an expected number of 15-25 SNe that suggest that our detection efficiency is roughly 50%.

2.3.2 GW151226

The follow-up campaign for GW151226 was also characterized by a prompt response to the trigger and deep observations over a large sky area (see Section 2.1) Different from the follow-up campaign carried out for GW150914, the covered fields are at moderate Galactic latitude and close to the Ecliptic. In fact, the total number of analyzed sources was about an order of magnitude below the former case.
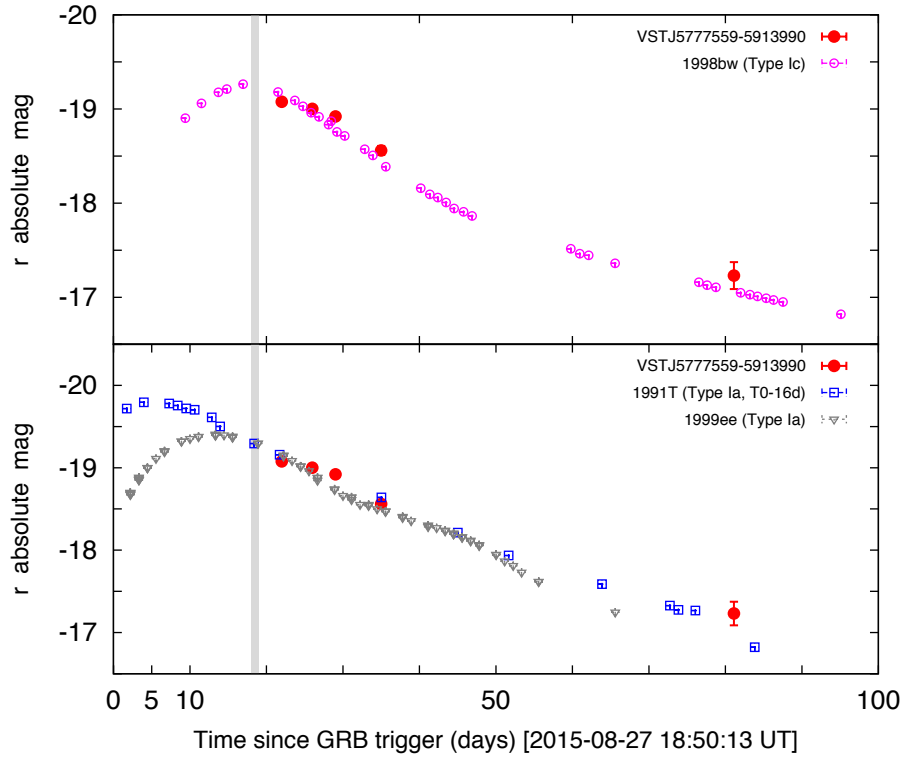
Figure 2.14: *Top:* The light-curve of the SN candidate VSTJ5777559-5913990 and superposed the light-curve of the hypernova prototype SN 1998bw [Iwamoto et al., 1998]. The explosion time is the *Fermi*-GBM GRB 150827A event time, and data for the SN are simply scaled to the redshift of the likely host galaxy at $z \sim 0.11$. The agreement with the observed data is quite good. The vertical grey line identifies the GW event time. *Bottom:* The same data plotted with the light-curves of two SNe of the Ia family, SN 1991T [Lira et al., 1998] and SN 1999ee [Stritzinger et al., 2012]. The SN 1999ee light-curve is also in reasonable agreement with the data. It is clear that without a spectroscopic confirmation, with only sparse photometric information, it is not possible to classify a SN reliably. If the *Fermi*-GBM event time and the optical transient are not associated even the light-curve of the peculiarly bright SN Ia as SN 1991T can be in agreement with the observations assuming that the explosion time was about 16 days before the (unrelated) high-energy event.

The `diff-pipe` procedure produced a list of 6310 candidates of which 3127 with high score. Performing a crosscheck of our candidate catalog with SIMBAD database gave 54 matches with known variable sources. The candidate list shows a large number of transients that appear only at one epoch. It turned out that this is due to a high contamination from minor planets, which was expected for the projection of the GW151226 sky area onto the Ecliptic. A query with Skybot[25] showed a match of 3670 candidates of our transients with known minor planets within a radius of 10 arcsec. The `ph-pipe` yielded 305 highly variable/transient sources (after removing the known sources reported in the GAIA catalogue and the known minor planets). 90% of them are also part of the list provided by the `diff-pipe`.

2.3.2.1 Previously discovered Transients

We searched in our candidate list the sources detected by the Pan-STARRS (PS) survey from Table 1 of Smartt et al. [2016b]. Of the 56 PS objects 17 are in our survey area. Out of these, 10 ($\sim 60\%$) were identified also by our pipelines as transient candidates. The main reason for the missing detections is the lack of proper reference images. As mentioned above, in the ESO/VST archive we could not find exposures for the surveys area of the two triggers obtained before the GW events. Therefore, we have an unavoidable bias against the detection of transients with slow luminosity evolution in the relatively short time window of our survey. The PS candidates detected in our survey are:

- PS16bqa is a SN candidate first announced by Smartt et al. [2016b].

- PS15csf was classified by the PESSTO team [Harmanen et al., 2015] as a SN II at $z \sim 0.021$.

- PS15dpn was classified by LIGO Scientific Collaboration [2016] as a SN Ibn at $z \sim 0.1747$.

- PSN J02331624+1915252 was tentatively classified by Shivvers et al. [2015] as a SN II at $z \sim 0.0135$ although the possibility it is an AGN in outburst or a tidal disruption event is not ruled out. In our images the transient was at $r \sim 20.6$.

- PS15dom was classified by Pan et al. [2016] as a SN II at $z \sim 0.034$.

- PS15don was classified by Smartt et al. [2016b] as a SN Ia at $z \sim 0.16$.

---

[25]http://vo.imcce.fr/webservices/
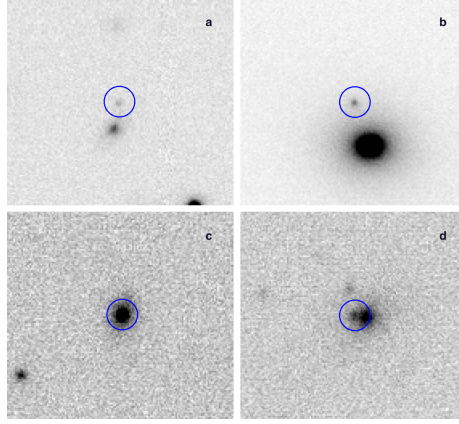
Figure 2.15: A few SN candidates identified in our survey after GW151226. *a.* VSTJ38.84617+19.33631 observed on 2016, Jan. 01. *b.* VSTJ39.14621+18.21061 observed on 2016, Jan. 01. *c.* VSTJ45.37163+28.6 observed observed on 2016, Jan. 05. *d.* VSTJ46.51175+2770492 observed on 2016, Feb. 02. In all images the showed field sizes are 30×30 arcsec, North is up and East to the left. The blue annuli represent the position identified by our pipelines.

- PS15dox was classified by the PESSTO team [Frohmaier et al., 2016] as a SN Ia at $z \sim 0.08$.

- PS16kx is a SN candidate proposed by Smartt et al. [2016b].

- PS15doy was classified by Smartt et al. [2016b] as a SN Ia at $z \sim 0.19$

- PS16ky is a SN candidate first announced by Smartt et al. [2016b].

2.3.2.2   Transient candidates

In addition, we also singled out a few objects that most likely are previously undiscovered SNe (Fig. 2.15).

- VSTJ38.84617+19.33631 is close to an unclassified galaxy, possibly a barred spiral seen almost edge-on. The transient was caught already in the decaying phase.

- VSTJ39.14621+18.21061 is close to the galaxy 2MASXJ02363494+1812327 (from HyperLEDA) of spheroidal shape. No redshift is known and the transient was already in the decaying phase.

Table 2.8: Coordinates of the known or newly identified sources (SNe or candidate SNe) derived from the GW 151226 follow-up campaign discussed in this section.

Id	RA J2000	Dec J2000	Alternate Id	Note
VSTJ39.73851+18.17786	2:38:57.24	18:10:40.4	PS16bqa	SN candidate
VSTJ36.50933+17.06122	2:26:02.24	17:03:40.4	PS15csf	SN II, $z \sim 0.021$
VSTJ38.24896+18.63528	2:32:59.75	18:38:07.0	PS15dpn	SN Ibn, $z \sim 0.1747$
VSTJ38.31767+19.25700	2:33:16.24	19:15:25.2	PSN J02331624+1915252	SN II?, $z \sim 0.0135$
VSTJ38.69008+18.34381	2:34:45.62	18:20:37.7	PS15dom	SN II, $z \sim 0.034$
VSTJ38.84617+19.33631	2:35:23.08	19:20:10.7		SN candidate
VSTJ39.14621+18.21061	2:36:35.09	18:12:38.2		SN candidate
VSTJ39.29767+19.05561	2:37:11.44	19:03:20.2	PS15don	SN Ia, $z \sim 0.16$
VSTJ40.06271+22.53669	2:40:15.05	22:32:12.1	PS15dox	SN Ia, $z \sim 0.08$
VSTJ41.17617+22.61097	2:44:42.28	22:36:39.5	PS16kx	SN candidate
VSTJ41.97567+21.77333	2:47:54.16	21:46:24.0	PS15doy	SN Ia, $z \sim 0.19$
VSTJ45.37163+28.65375	3:01:29.19	28:39:13.5		SN candidate
VSTJ46.51175+27.70492	3:06:02.82	27:42:17.7		SN candidate
VSTJ50.64421+30.60197	3:22:34.61	30:36:07.1	PS16ky	SN candidate

- VSTJ45.37163+28.65375 is at the center of an unclassified galaxy, apparently of spheroidal shape. The transient was possibly identified before the maximum and showed a slow evolution during our campaign.

- VSTJ46.51175+27.70492 is slightly off-center of the galaxy 2MASXJ03060262+2742176 (from HyperLEDA) of spheroidal shape. No redshift is available. The transient was brightening for the whole duration of our monitoring.

2.3.3 GW170814

The GRAWITA follow-up search for GW170814 started 17.5 hours after the merger , see Section 2.1. After analysis and removing known sources, the `ph-pipe` procedure produced a list of 37 candidates. The `diff-pipe` procedure produced a preliminary list of 5,550,951 transient candidates (with an adopted threshold of 1.5σ of the background noise) distributed over 99 pointings. After merging the duplicated sources, 2,481,201 candidates are left and the scoring algorithm reduces this number by further two order of magnitude. The final list includes 9,342 distinct candidates of which 1,687 with high score are taken as bona-fide genuine transients. The visual inspection for all these candidate sources leads to a list of 246 of preliminary candidates. We cross check the candidates with public datasets, e.g. Simbad, Ned, and Skybot, aiming for the discovery of unknown objects. This step helps to remove 2 RRLyr, 1 IG, 1 GinCl, and 21 asteroids, meanwhile, identified 63 galaxies. After cleaning the known sources, and a preliminary check of light curve trends and accompanied galaxies, a total number of 53 candidates were found by our transient identification system (among them 36 by both the pipelines and 17 only by the pipeline based on image subtraction), see figure 2.16. Since most of them are also located in the survey area of the Dark Energy Survey[26] (DES), we took DES images as references to investigate the variabilities. Details of the 53 candidate transients, namely, their light curve analysis, are reported in appendix in the table 2.9.

2.3.3.1 Previously discovered Transients

As shown in table 2.9, after light curve fitting and comparison, we identified several newly-burst candidate SNe. It is worth nothing that among them, there are three already reported in TNS:

- SN2017eni (Gaia17blw) was announced as a Gaia transient on 2017 June 6 with G=17.7 as a candidate SN in the galaxy 6dFGS gJ030511.0-453304 [Della Valle et

---

[26]https://www.darkenergysurvey.org/
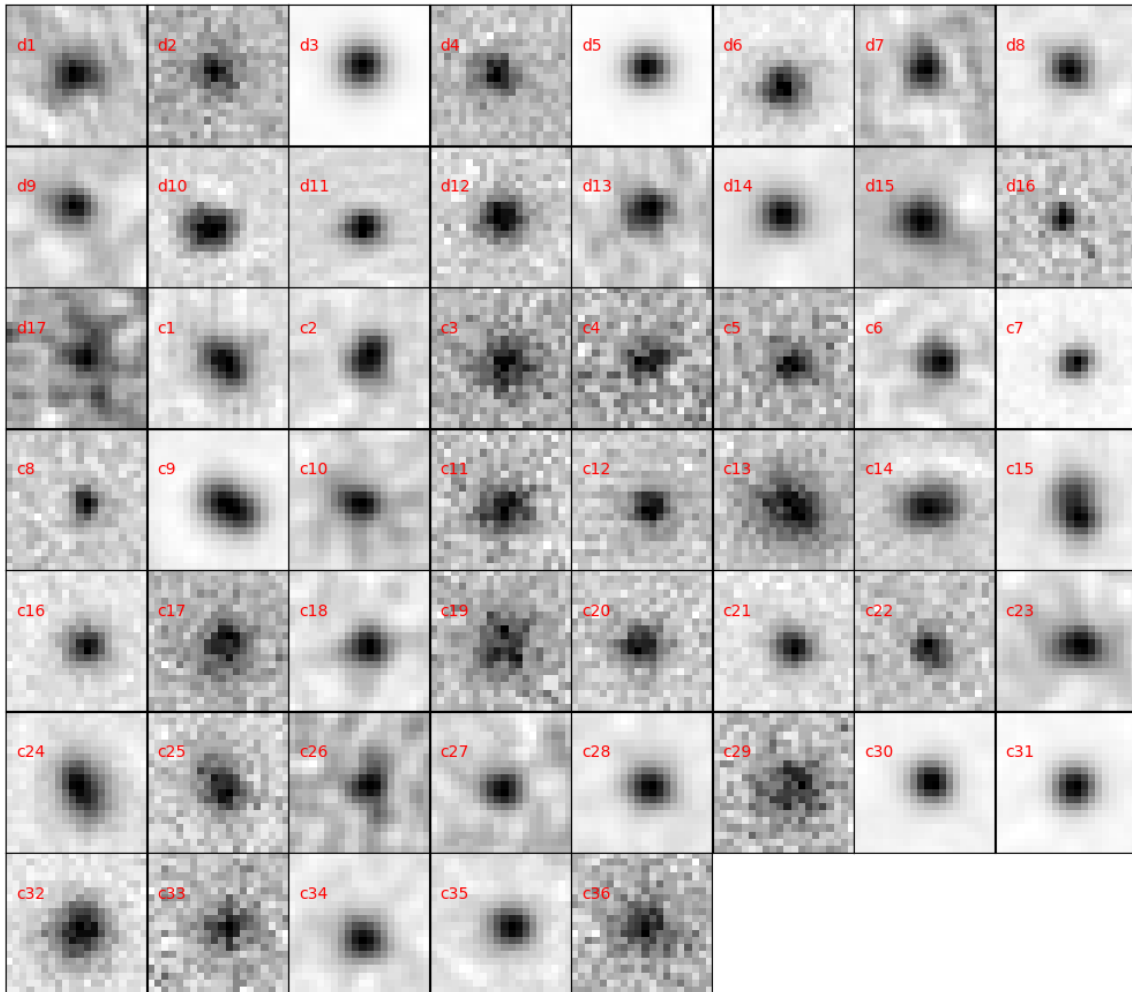
Figure 2.16: Detection frames of candidates in differencing images: 36 by both the pipelines and 17 only by the diff-pipe.

al., 2003]. It was continuously classified as a Type IIn superluminous supernova by ASAS-SN survey (ATel 10616). It's also mentioned that from the emission lines of its host galaxy give a redshift of 0.08165. Photometry from the ASAS-SN survey finds a peak at V=16.9 on 2017 Jun 6.44, implying an absolute magnitude of $M_V = -21.0$.

In Figure 2.17 is showing its differencing images by VST shots, revealing the existence of a transient, VST46.294752498-45.550898225. By light curve comparison with SN 2008es, we identified it as a super luminous type II SNe located at redshift 0.082. With a further check of TNS, We realize VST46.294752498-45.550898225 is detected before as a Gaia object. The VST source and redshift evaluation is very identical with the ASAS-SN.

- AT 2017gqz (Gaia17cgz) was announced as a Gaia transient on 2017-09-08 17:47:02 with G=18.79. Our light curve comparison suggest it as a Ia SN at redshift 0.05.

- AT 2017fat (Gaia17bqm) was announced as a Gaia transient on 2017-06-05 00:41:45 with G=18.18. Our light curve procudures suggested it as a Ia SN at redshift 0.08.

2.3.3.2 Transient candidates

In addition, we present a few objects that most likely are previously undiscovered transients in Tab. 2.9. We have distinguished the transients found by both the search pipelines (the prefix c in the Id) from the ones found only with the image subtraction pipeline (prefix d in the Id). Besides the coordinates we reported if the source was found in the NED (within 5 arcsec) or SIMBAD (within 3 arcsec) and the identification that come from the these database. Where possible a fit to the light curve was performed to derive a transient classification. Finally are reported notes about the identification. As shown, in 21 cases the photometric evolution is consistent with SNe, 9 are likely AGN, and for the remaining the photometric classification is unconclusive.

2.4 Detection limits for different type of GW counterparts

The artificial star simulations, which make use of the real objects images (PSF) and transparency taken during our VST surveys and take into account the cadence of the observations, allow us to derive the detection efficiency of our search for different types of possible optical counterparts of GW events. This can also be used to estimate the sensitivity distance of future VST surveys, and, in the case of non detections, can be turned into upper limits for the rate of specific kinds of events.

We took a number of proposed EM transients expected to be associated with GW sources from literature (cf. Fig. 2.18). We assumed as reference epoch the one of
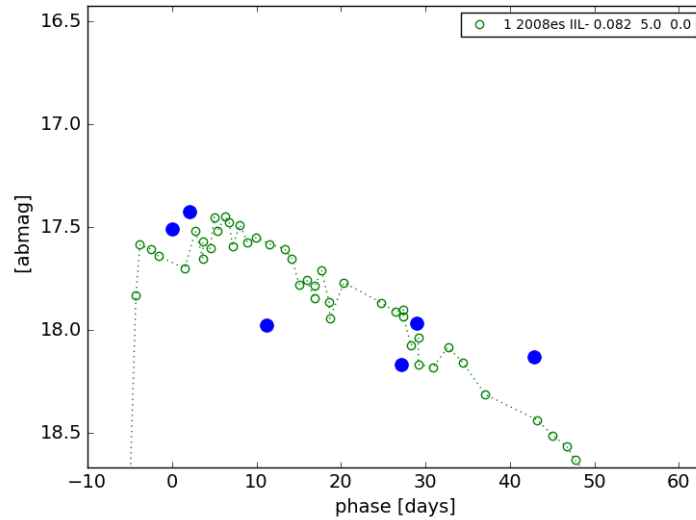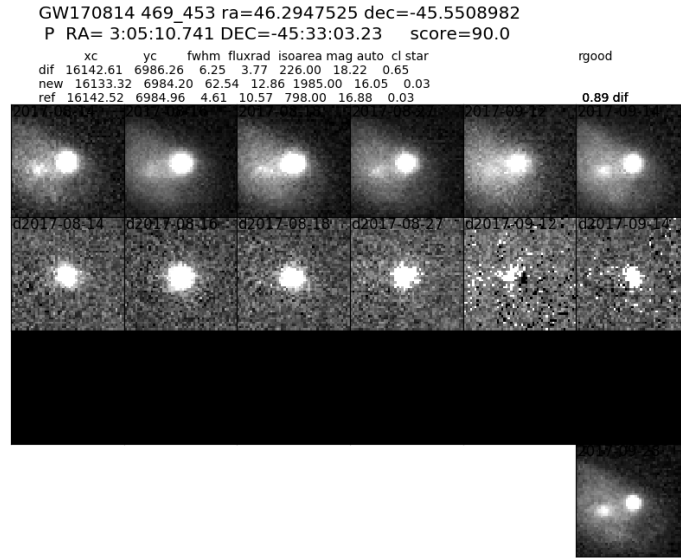
Figure 2.17: *Top:* Images of SN2017eni shown by our diff-pipe. Some parameters of the source are shown in the top (score equal to 90 means the highest priority). The first row show the original images. The second row show the differencing images. The third row show the masks (black stands for 1, which means good area). The last row shows the reference image. *Bottom:* Comparison between SN2017eni (blue points) and SN2008es (green dots) light curves. SN2008es is a super luminous type IIL SNe. I put its modelled light curve in redshift 0.082, shift 5 days in phase, and with no host galaxy extinction.

Table 2.9: Result of the transient search and identification. In column one the c indicates that the objects were found in both the image subtraction and catalogs pipelines, the d in the Id indicates that the transient were found only with the image subtraction pipeline. In columns two and three are Ra and Dec J2000, column 4 indicates if the object were found in NED database, the same in column 5 but against the SIMBAD database. Column six report the result of the light curve fit. In the last column, where applicable, are noted remarks about the identification

Id	RA	Dec	NED	SIMBAD	lc fit	Note
c1	47.93	-32.50	-	-	-	1
c2	41.12	-47.08	-	-	Ia 1990N z 0.12	-
c3	44.24	-36.10	-	-	-	2
c4	43.55	-46.05	-	-	AGN	-
c5	39.56	-45.53	-	-	IIP 1999em z 0.04	3
c6	44.29	-37.11	-	-	Ia faint 1991bg z 0.06	-
c7	36.37	-46.60	Y	-	-	4
c8	35.69	-43.94	-	-	Ia 1994D z 0.05 [5]	
c9	40.96	-39.09	-	-	-	6
c10	42.84	-46.75	Y	-	IcBL 1998bw z 0.09	-
c11	47.22	-33.98	Y	-	Iapec 2000cx z 0.08	-
c12	48.52	-42.08	-	-	1990N z 0.07	7
c13	40.71	-38.97	-	-	-	8
c14	36.19	-46.11	-	-	-	9
c15	49.44	-43.49	-	-	-	9
c16	43.33	-41.94	-	-	-	6
c17	42.54	-41.49	-	-	-	6
c18	47.20	-41.20	Y	-	AGN	-
c19	42.06	-49.45	-	-	-	6
c20	36.50	-43.98	-	-	Ia 1992A z 0.07	-
c21	41.17	-40.37	Y	-	Ia 2002bo z 0.055	-
c22	36.94	-49.98	-	-	-	10
c23	42.92	-45.71	-	-	-	11
c24	42.71	-42.51	-	-	-	6
c25	40.17	-46.87	-	-	-	6
c26	42.22	-38.25	-	-	Ia 1990N z 0.1	-
c27	40.63	-41.06	Y	-	Ia 1994D z 0.13	-
c28	36.88	-52.49	-	-	Ia 1990N z 0.095	-

Table 2.9: continue

c29	48.50	-42.58	-	-	-	[12]
c30	35.93	-44.02	Y	-	SNLC 2008es z 0.14	-
c31	47.23	-46.62	-	-	Ia 1992A z 0.05	[13]
c32	46.59	-38.23	-	-	Ia 1994D z 0.05	[14]
c33	46.09	-42.57	-	-	-	[4]
c34	38.97	-45.03	-	-	-	[9]
c35	38.86	-52.55	-	-	-	-
c36	39.28	-45.36	-	-	-	[6]
d1	42.24	-43.27	Y	-	Ia 1992A z 0.12	-
d2	44.27	-36.80	Y	-	IIP 1999em z 0.04	-
d3	46.29	-45.55	Y	Galaxy	SLSN 2008es z 0.08152	[15]
d4	44.32	-37.35	Y	-	AGN	-
d5	41.50	-46.85	Y	QSO	-	-
d6	45.05	-32.30	-	-	AGN	-
d7	37.81	-46.85	Y	-	Ia 1991bg z 0.05	-
d8	40.11	-46.33	-	-	Ic 2007gr z 0.07	-
d9	44.17	-42.58	-	-	Ia 1992A z 0.08	[16]
d10	41.56	-49.89	Y	AGN	AGN	-
d11	47.19	-33.94	Y	-	AGN	-
d12	39.78	-48.51	Y	-	Ia 1994D z 0.095	-
d13	45.63	-46.35	-	-	Ia faint 1991bg z 0.08	-
d14	45.75	-44.83	Y	-	Ia 1990N z 0.1	-
d15	44.42	-41.44	Y	-	AGN	-
d16	44.37	-42.12	Y	-	AGN	-
d17	45.45	-35.57	-	-	AGN	-

Note

[1]Nothing in DES and only one point in VST; [2]Flash star?; [3]nothing in DES, appears twice in the last 2 VST epochs; [4]associate with a galaxy, appears once in the last VST epoch; [5]appears in the last 2 VST epochs, weak signal in DES; [6]nothing in DES, only one point in VST; [7]appears twice in the last 2 VST epochs; [8]flash star? Appears in DES; [9]nothing in DES and only once in last VST epoch; [10]flash star? 'star' in DES, very bright in one VST images; [11]'star' in DES and VST, weak residual in last 2 diff epochs; [12]LPV or other variable star? appear in DES and the first VST epoch; [13] constant in DES and first 3 VST epochs, then become bright; [14] AT 2017gqz reported in TNS; [15] SN2017eni reported in TNS; [16] AT 2017fat reported in TNS.

the GW trigger and computed the expected light curve for each of the proposed EM counterparts, following two approaches: i) we adopted the distance derived from the GW analysis, the expected transient magnitudes are compared with the detection upper limits at the different epochs derived from the artificial star experiments; ii) we explored a range of distances regardless of the constraint from the GW trigger. We used the detection efficiency measured by artificial star experiments to compute the probability of detection for each of the transients as a function of distance.

Figure 2.18 shows the expected light curves assuming the distance derived from GW150914 data analysis (410 Mpc). On the same figure we show an example of our detection upper limits computed from the artificial star experiments for one of the pointings (field P31). Only three types of transients could have been detected, namely type Ic SNe-98bw like and the long GRB viewed from a slightly off-axis observer at all epochs, and within the first 2 epochs also a bright short GRB from a viewing angle that is equal to the jet opening angle [van Eerten & MacFadyen, 2011]. If we had reached a deeper threshold by one magnitude, we could have detected also a kilonova-like emission at a given distance [Kasen et al., 2015] during the first two epochs. All the other electromagnetic transients, at that distance, would have been far too faint to be detectable.

Figure 2.19 shows the detection efficiency as function of distance for all the models considered in figure 2.18 and using the P31 observations of GW150914 as representative of the average depth and cadence of the VST surveys. The majority of the models associated with the merger of binary systems containing a NS (kilonova models and bright short GRBs slightly off-axis) can be detected with a detection efficiency larger than 50% up to 100 Mpc. The expected detection rates of sightly off-axis short GRBs in associations with GW events seems also to be promising [Ghirlanda et al., 2016]. Instead, SNe can be detected up to distances many times larger than the few Mpc, that is the detectability range of a few tens of Mpc for core collapse of massive stars by the LIGO and Virgo network. We conclude that our search for optical counterparts of GW events goes in a promising direction for securing timely observations of light curves of the expected transients within distances of the order of ~ 100 Mpc.

2.5   Conclusions and Future Prospects

The search for EM counterparts is very challenging due to the large sky localization uncertainties of GW signals and the large uncertainties on EM emission that GW sources may produce. The improvement of sensitivity and sky localization will continue in the next years, when Virgo joined the network at the late phase of O2 run, KAGRA

will be completed, and possibly other interferometers will join the network in the future

The large number of GW events expected from future runs [Abbott et al., 2016b,c] will require an enormous EM observational effort. In case the optimistic rates (posted in recent literature) will be confirmed, the follow-up of all the GW detections will require a huge effort. At least for the transient identification wide field synoptic facilites like ZTP, and LSST [27] are expected to give a major contribution. On the other hand, the spectroscopic characterization of many transients remains the critical bottleneck. In this context the installation of efficient spectrograph at medium class telescopes is crucial, eg. SOXS, a fast optical/NIR spectrograph that will be mounted at ESO-NTT [Schipani et al., 2016].

At the same time, it will be important to perform a optimal selection of transient candidates, in order to follow the counterpart in real time. The main challenging is posted by the huge amount of candidates, meanwhile, the artificial intelligence, namely, the machine learning algorithms, are worth to be tested.

---

[27]https://www.lsstcorporation.org/science-collaborations
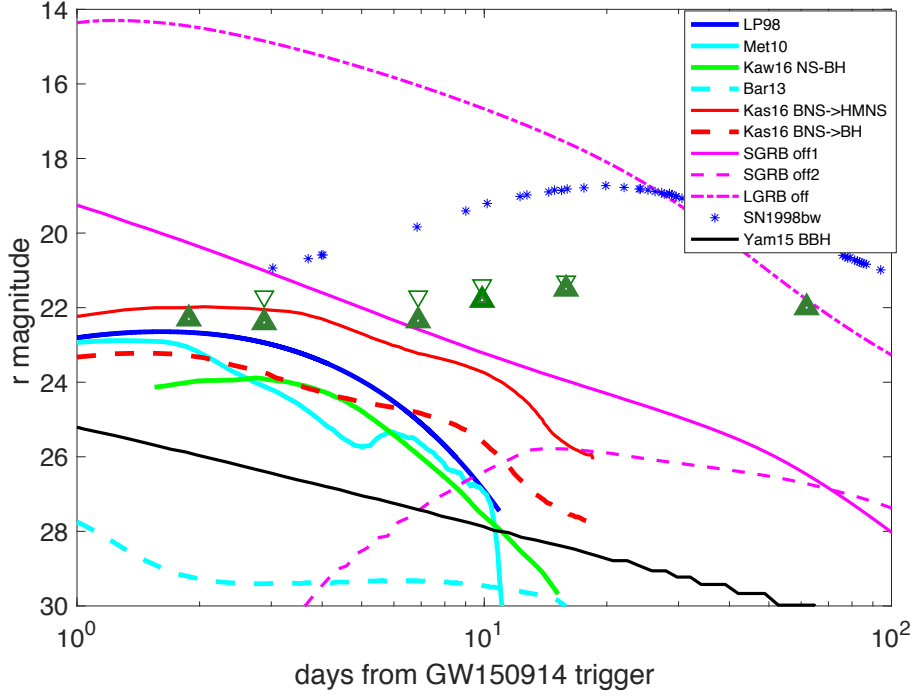
Figure 2.18: The expected fluxes (r band magnitudes) versus observed time from the GW150914 trigger, assuming several possible electromagnetic GW source emission models at the given distance of 410 Mpc, plotted against the 6 epochs VST observation 5σ limiting magnitude (*dark green triangles*) and the detection upper limits computed from artificial stars in frame P31 (*light green triangles*). *Blue and cyan solid line:* kilonova model from Metzger et al. [2010], assuming a radioactive powered emission for an ejecta mass 10^{-2} M$_\odot$, outflow speed of $v = 0.1c$, iron like opacities, and thermalization efficiency of 1 (cyan line) and a blackbody emission (blue line [Li & Paczyński, 1998]) with the same values of the mass and velocity. *Cyan dashed line:* kilonova model from Barnes & Kasen [2013] assuming an ejected mass of 10^{-3} M$_\odot$ and velocity of 0.1 c and lanthanides opacity. *Green solid line*: kilonova model from Kawaguchi et al. [2016] for a BH-NS merger with a BH/NS mass ratio of 3, ejected mass of 0.0256 M$_\odot$ and velocity $v = 0.237c$, hard equation of state for the NS, and BH spin of 0.75. *Red lines*: kilonova disk-outflow models from Kasen et al. [2015], assuming accretion disc mass of 0.03 M$_\odot$ and a remnant hyper-massive NS (solid) or a remnant NS collapsing into a BH within 100 ms (dashed). *Purple lines*: simulated off-axis afterglow light curve [van Eerten & MacFadyen, 2011], assuming a short GRB with ejecta energy of $E_{jet} = 10^{50}$ erg, interstellar matter density of $n \sim 10^{-3}$ cm^{-3}, jet half-opening angle of $\theta_{jet} \sim 0.2$ rad and an observed viewing angle of $\theta_{obs} \sim 0.2$ rad (solid) and $\theta_{obs} \sim 0.4$ rad (dashed) and a long GRB with ejecta energy of 2×10^{51} erg, $\theta_{jet} \sim 0.2$ rad and an observed viewing angle of $\theta_{obs} \sim 0.3$ rad (dot-dashed line). *Blue asterisks*: SN 1998bw associated with GRB 980425 [Clocchiatti et al., 2011]. *Black solid line* : R-band emission from a BBH merging according to the model by Yamazaki et al. [2016].
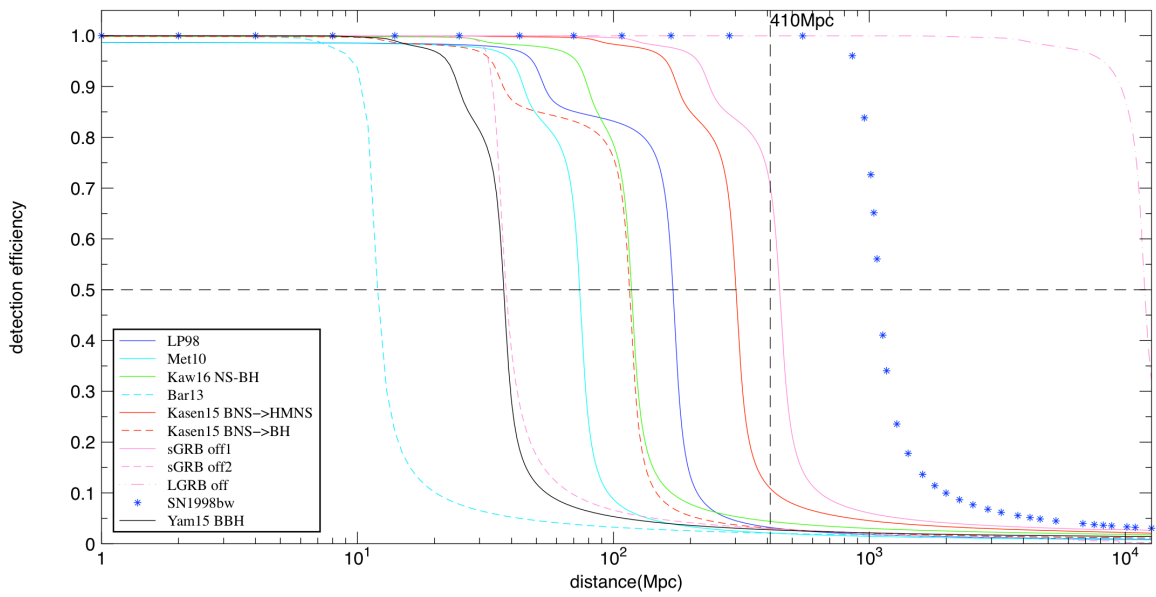
Figure 2.19: Detection limits for different counterpart models obtained by the artificial star experiments for the pointing P31 of GW150914. The models are described and shown as in Figure 2.18. The P31 field is representative of both the surveys of GW150914 and GW151226 and the curves in the figure can be considered as representative of the typical detection limit reached in the region of the sky observed for both the gravitational triggers.

Chapter 3

Electromagnetic counterpart searching of Gravitational Wave Sources with host galaxy monitoring strategy

In this chapter, I describe the galaxy monitoring strategy for searching GW optical counterparts as implemented in the DLT40 survey. During the LVC O2 season, DLT40 has followed ten GW triggers and identified two interesting transients, including the kilonova, AT 2017fgo/sss17a/DLT17ck. In section 3.1, some details of the DLT40 search are presented. Summary of the DLT40 GW follow-up receipe is described in section 3.2. And in section 3.3, the results of the DLT40 follow-up during O2 are described. A brief discussion will close the chapter in section 3.4.

As part of DLT40, I mainly contributed the galaxy priorization algorithms, which ranks the galaxies in our DLT40 samples, depending on specific informations, such as the GW uncertainty map, the galaxy luminosities, the sky visibility constrains, etc. I also developed a machine learning algorithms, that take previous DLT40 discoveries as training sample, to achieve a pre-filtering and classification of new candidates. I will describe the machine learning test in chapter 4 and present all related codes in the appendix.

3.1   DLT40 GW counterpart search

DLT40 is a one day cadence supernova search using a PROMPT 0.4m telescope located at Cerro Tololo Inter-American Observatory [CTIO; Reichart et al., 2005]. The survey goal is the early detection and characterization of nearby SNe. DLT40 has been operational since 2016, and observes ∼300–600 targeted galaxies on a nightly basis. A typical single-epoch integration of 45 s reaches a limiting magnitude of $r \approx 19$ mag with filterless observations. The field of view of the PROMPT camera is $10{\times}10$ arcmin^2, sufficient to map all but the nearest galaxies in the search.

The DLT40 galaxy sample is drawn from the Gravitational Wave Galaxy Catalogue [GWGC; White et al., 2011], with further cuts made on recessional velocity ($V <$ 3000 km/s, corresponding to $D \lesssim 40$ Mpc), declination (Dec$<+20$ deg), absolute magnitude ($M_B<-18$ mag), and Milky Way extinction ($A_V<0.5$ mag). For these galaxies, we strive for a one-day cadence between observations to constrain the explosion epoch of any potential SN. We maintained our original DLT40 galaxy samples even after The Galaxy List for the Advanced Detector Era (GLADE[1]) was made available because the completeness of the two catalogue is not significantly different within 40 Mpc [Dálya et al., 2018]. The physical properties of the ∼2200 galaxies in the DLT40 sample are shown in Figure 3.1 in comparison to the whole GWGC sample within D<40 Mpc. As shown, the DLT40 galaxy catalog is biased against low luminosity and small size galaxies but almost uniformly for Hubble type.

DLT40 operations are fully robotic. A schedule is submitted automatically every afternoon before the Chilean sunset, and targets are given a priority between one and five. A score of five is the highest priority, and is reserved only for the most important targets, such as the galaxies selected for GW follow-up. A score of four is assigned to galaxies that have been observed by the DLT40 survey over the last three days in order to maintain the program's cadence. A select few other galaxies are also given a native score of four – for instance, if they are within $D<11$ Mpc, or if one PROMPT field of view can capture more than one DLT40 galaxy. A score of three is assigned to other DLT40 galaxies not selected with higher priority, and which have $M_B<-20$ mag, while a score of two is assigned to those galaxies with $M_B<-19$ mag. The remaining galaxies are given a score of one. The Skynet scheduler observes targets from west to east within a priority category, so that all of the priority five galaxies are observed first (if visible), followed by the priority four galaxies, and so on. Galaxy priorities can not be assigned in a 'fine-grained' way beyond that described above, and so in this sense

---

[1]http://aquarius.elte.hu/glade
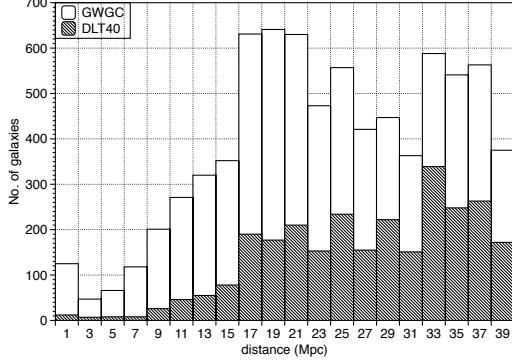
(a) the distance distribution for DLT40 galaxies (open histogram), GWGC galaxies within 40 Mpc (shaded histogram).
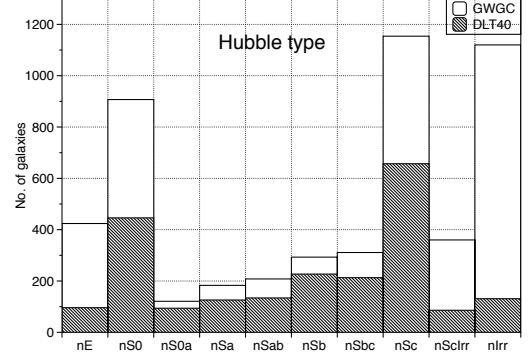
(b) the Hubble type distribution for DLT40 galaxies (shaded histogram) and for GWGC galaxies within 40 Mpc (open histogram).
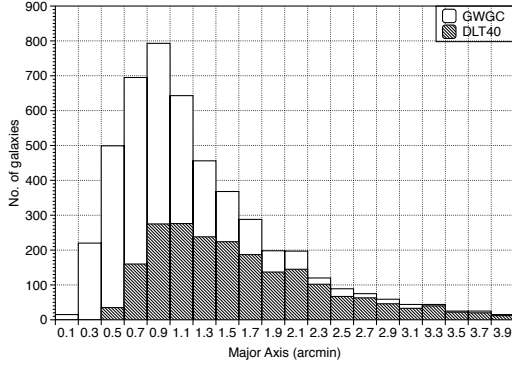
(c) the major axis distribution (in arcmin) for DLT40 galaxies (open histogram), GWGC galaxies within 40 Mpc (shaded histogram).
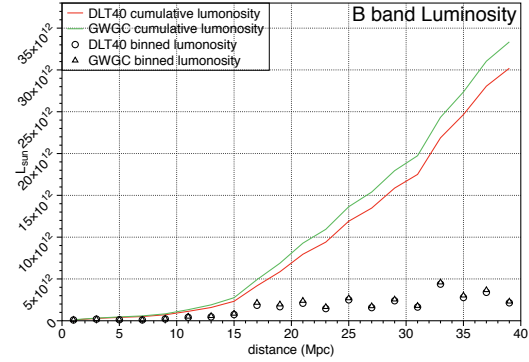
(d) the binned and integrated B band luminosity distribution for DLT40 galaxies, GWGC galaxies within 40 Mpc.

Figure 3.1: Some statistics regarding the DLT40 galaxy sample compared with the corresponding GWGC galaxies.

all of the galaxies targeted for the DLT40 GW search were observed with an equally high priority, observed from west to east.

After an exposure is completed, the Skynet Robotic Telescope Network system automatically detrends the data (i.e. applies bias and flat field corrections) and determines an astrometric world coordinate system solution before the image is ingested by the DLT40 pipeline. From there, image subtraction is performed with respect to a high quality template image using the publicly available `Hotpants` code [Becker,

2015]. `SExtractor`[2] [Bertin & Arnouts, 1996] is then used to extract all sources in the difference image above a specific signal to noise threshold. The difference image source catalog typically includes a large number of spurious objects due to stochastic processes, small misalignments between the images, improper flux scalings, imperfect PSF matching between the template and target image, and cosmic rays. In order to filter out spurious candidates, a scoring algorithm was developed based on catalog parameters returned by `SExtractor`. This approach still required visual screening of a significant number of candidates, most of which are rejected. For this reason we have tested and implemented a machine learning algorithm for the classification of candidate transients, which we discuss briefly along with our plans for the third observing run of the Advanced Detectors (Chapter 4). In order to manage our real time dataset, we have built a DLT40 database using `MySQL`[3] and visually inspect SN candidates through web pages powered by the `Flask`[4] tool. After eyeballing, we secure immediate follow-up photometry or spectroscopy from collaborating facilities, most notably Las Cumbres Observatory, which itself is operated robotically [Brown et al., 2013].

In Figure 3.2 shows that the DLT40 galaxy monitoring search with its automatic data processing system can rapidly detect and classify sources. The real time and quick response of the DLT40 SN search make it ideal for rapidly evolving transients including the electromagnetic counterparts to GW sources. As such, DLT40 joined the global search effort during the Advanced Detector O2 run. We discuss our GW follow-up strategy in more detail next.

Figure 3.3 shows the DLT40 working flowchart. The single step will be described in detail in the following sections.

3.2   GW follow-up strategy

Considering the average limiting magnitude of DLT40 images is r ∼ 19 mag [Yang et al., 2017], which is deep enough to reach most of the possible EM emission from BNS sources at 40 Mpc, see Fig. 3.4, the next step is to employ a galaxy prioritization tool that can ensure to observe the high probability fields as early as possible.

---

[2]http://www.astromatic.net/software/sextractor
[3]https://www.mysql.com/
[4]http://flask.pocoo.org/
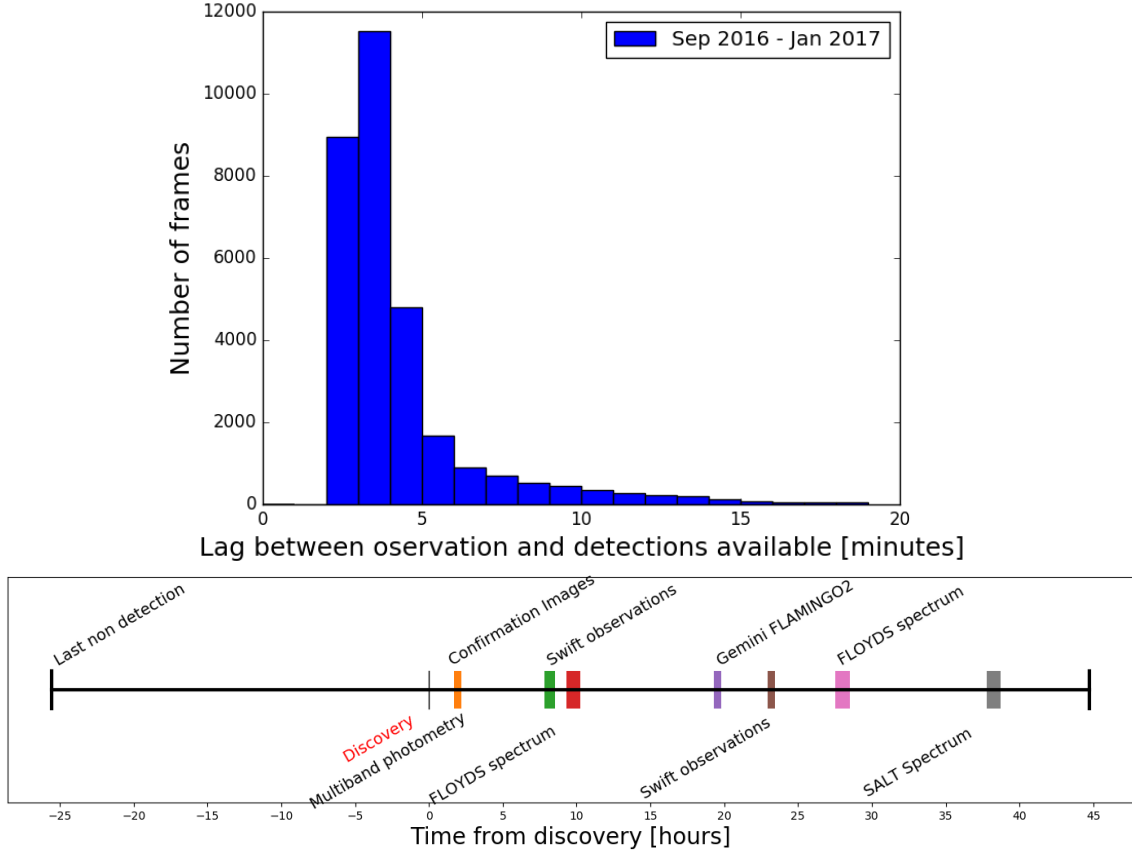
Figure 3.2: Top: Histogram of time lag between DLT40 observation and available detections. Data are taken from Sep. 2016 to Jan 2017; Bottom: Timeline of early followup for the DLT17ch. We collected UV-Optical and infrared observations within 24h of discovery.

3.2.1 Galaxy Prioritization

The DLT40 software suite ingested the GCN alerts employed during O2 for disseminating GW event information, and we downloaded the HEALPIX localization map with distance constraints [see Singer & Price, 2016, for further information on the generation of these maps]. From this GW-based data, we prioritize galaxies in the DLT40 catalog given the position and relative probability within the localization map, and the galaxy's inferred mass. The target prioritization process is implemented as follows (see also Figure 3.3):
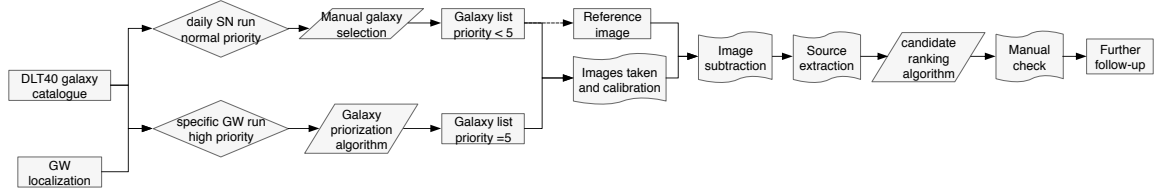
Figure 3.3: Flowchart presents the DLT40 working procedures, including the GW follow-up.

1. The DLT40 galaxy catalog is mapped with the Healpix tool. After weighting by the luminosity (we assume that the mass distribution follows the B band luminosity) and adopting a gaussian smoothing with the assumed galaxy size radius, we obtain the luminosity distribution map S_{lum} and the normalized map:

$$N_{lum} = \frac{S_{lum}}{\sum S_{lum}} \tag{3.1}$$

2. The GW probability map is normalized as S_{gw}.

3. The combined probability from each sky directions is obtained by convolving the two maps above as,

$$C = S_{gw} \times N_{lum} \tag{3.2}$$

4. For one specific galaxy i, the accumulated value over all pixels in C within the galaxy radius goves the metric of the prioritization,

$$s_i = \sum_j C_{ij} \tag{3.3}$$

where j is the index of the Healpix pixel within the specific radius.

It is shown in Tab 3.2 that NGC4993, that is the host galaxy of the kilonova AT17fgo, is ranked by our pipeline as the 7th in the list (see Score column). In principle, the prioritization can also account for the distance of the GW source (if given) and the detection efficiencies accounting for each galaxies [Arcavi et al., 2017]. For DLT40 in LVC O2 run, we didn't consider the distance since it was not always available in the early GW trigger announcement. However, we made a posteriori test for GW170817 assuming a distance with a normal distribution with mean value of 40 Mpc and standard deviation 8 Mpc. Including the distance information, NGC4993 is ranked as 6th (see Score2 column). Considering the distance estimation should be available early in O3, in DLT40 we will use this information later on.
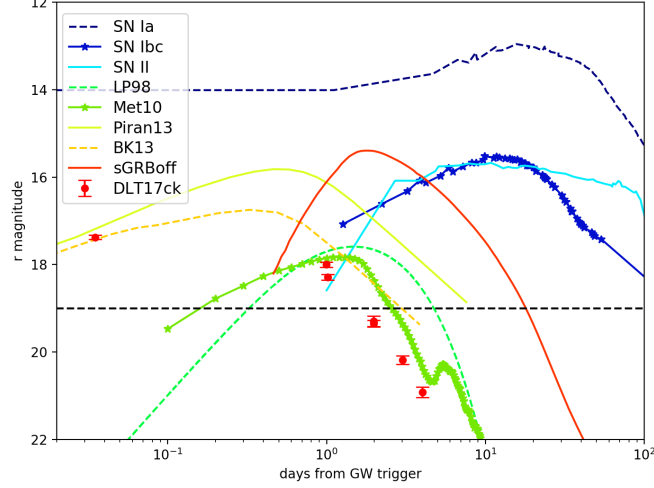
Figure 3.4: Several possible EM emission models of GW source, scaled to a distance of 40 Mpc, are plotted against the 6 epochs DLT17ck observation(red dots). Among these optical emission models, there are 4 kilonova models: LP98[Li & Paczyński, 1998], assuming a blackbody emission for an ejecta mass $10^{-2}M_\odot$, outflow speed of $v = 0.1c$; Met10[Metzger et al., 2010], assuming a radioactive powered emission with the same values of the mass and velocity, iron like opacities; B&K[Barnes & Kasen, 2013], assuming an ejected mass of $10^{-3}M_\odot$ and velocity of $0.1c$ and lanthanides opacity; Piran13[Piran et al., 2013], assume a BH-NS merger with $NS = 1.4M_\odot$, $BH = 10M_\odot$; 2 sGRB off axis models: sGRBoff1[van Eerten & MacFadyen, 2011], simulated off-axis afterglow light curve assuming a short GRB with ejecta energy of $E_{jet} = 10^{50}erg$, interstellar matter density of $n = 10^{-3}cm^{-3}$, jet half-opening angle of $\theta_{jet} = 0.2rad$ and an observed viewing angle of $\theta_{obs} = 0.2rad$. For comparison, we also show some SN light curve, including SN 2009dc as SN1a, SN2002ap as SN1bc and one type IIP SN as SNII.

Galaxies with high score have a high priority in the DLT40 observing schedule. If the number of galaxies is over what we can observe per night, a cut based on this ranking algorithm would be employed.
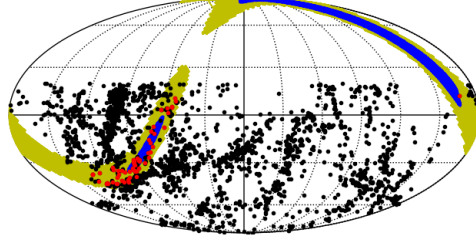
Figure 3.5: Illustration for description of DLT40 ranking algorithm. The full galaxy samples are smoothed into a healpy map, which was then combined with the LVC probability map. After normalization, the score of galaxy is defined as the accumulated pixel values inside the galaxy area. After ranking, the top ranked galaxies would be selected, shown in the last plot, which is the DLT40 selected galaxy samples based on LIGO trigger G275404. Black and yellow region presents the 95% and 68% GW probability region. Red dots shows the selected galaxies while the black ones illustrate the full DLT40 galaxy catalogue.

3.2.2   Monitoring Timescale

The cadence of monitoring is selected depending on the type of GW trigger as reported by LVC. For burst type GW events possibly related to core-collapse, the time scale of the optical transient is tens to hundreds of days and then we adopt a monitoring cadence of 3 weeks. For the GW merging of BNS in particular, an r-process kilonova [Li & Paczyński, 1998] and anisotropic short Gamma-ray Burst (GRBs) afterglow emission are expected. Fig 3.4 shows different kilonova models and GRB afterglow emissions, scaled to a distance of 40 Mpc which is the DLT40 searching boundary in O2. It shows that DLT40 could detect transients predicted by most of the models. We then put the modelling light curves at different distances and we define the limiting distance as the maximum distance at which the transient can be detected. Considering that the limiting magnitude of DLT40 is 19 mag [Yang et al., 2017], Fig.3.7 shows that most kilonova or GRB afterglow emission are within the limit of DLT40 for about 10 days. Therefore, we plan to monitor merger events for a period of 2 weeks.
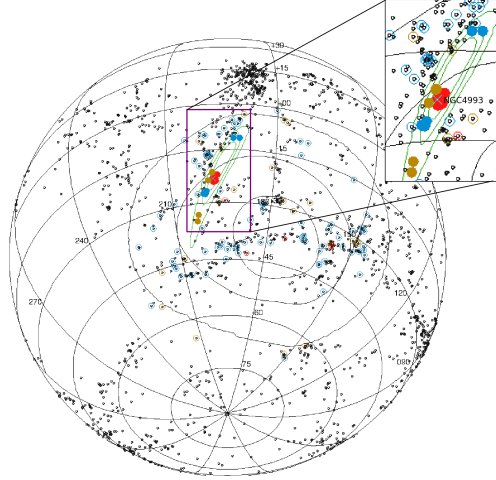
Figure 3.6: Localization region (contours) and the matched galaxies (circles) for GW170817/G298048(solid circles) and GRB170817a(filled circles). The contours indicate 50%, 90%, and 99% confidence bounds while GW trigger is shown in green and GRB trigger is shown in black. The colors of the circles denote the priority of the galaxies (high priority in red, normal priority in yellow and low priority in blue). All the DLT40 galaxy samples are shown in black dot. After ranking, we decided to follow all 20 GW galaxies(9 high + 5 normal + 6 low) and the top 31 GRB galaxies(5 high + 26 normal).

3.2.3   Triggering Process

This galaxy prioritization process produces a list of galaxies that are sent automatically to the DLT40 scheduler. Soon after observations with the Prompt telescope, DLT40 pipeline performs image calibration, image difference and source extraction for all selected galaxy frames. After filtered with the ranking algorithm (now with the machine learning algorithm), the candidates are visually inspected. If an interesting transient is found, a GCN is issued to allow for spectroscopic follow up.
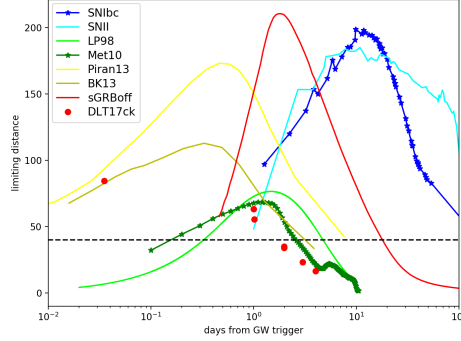
Figure 3.7: Limiting distance measurement for different counterpart models obtained by the artificial star experiments. With the Assumption that the limiting magnitude for DLT40 measurements is r=19 mag, we scale modelling light curves into different distances while the limiting distance is defined as the distance where the specific model cannot reach the limiting magnitude in any epochs. The models are described and shown as in Figure 3.4.

3.3 Searching results in O2

LIGO O2 ran from 2016 November 30 to 2017 August 25, with Virgo joining the network of GW detectors, starting on 2017 August 01. Several triggers were issued by LVC for follow-up to the EM community among which we followed the ten triggers listed in Tab.3.1 with their localization shown in Fig. 3.8. Notably, in LVC O2 run we decided to follow all the GW triggers (if possible), to probe the uncertain emission from BBH. It should be noticed that the typical distance of BBH is relatively large compared with the DLT40 counterpart search. For instance, the luminosity distance of G275697 estimated by LVC has a mean value of 181 Mpc and standard deviation 55 Mpc. The cumulative probability within the 40 Mpc volume is only 1%, however, we activated our follow-up search. The main reason is that the distance informations of burst candidates are not always available in the early announcement in the LVC O2 run, which need an assumption on the emitted energy which is unknown. In respect of CBC events in the second run, whose distance information is always available, especially in these early triggers we were not sure if the distance estimation from GW channel was reliable or not [5]. Therefore, we decide to monitor all those possible GW triggers, even

---

[5]Now we learn from GW170817 that the distance predicted by GW is accurate. The estimated distance from GW signal of the BNS merger is 40 Mpc where there's a galaxy, NGC4993 hosted the
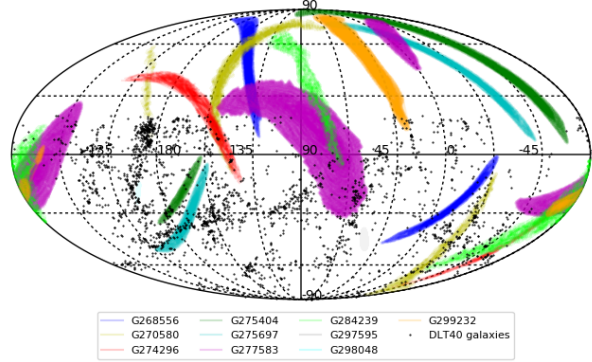
Figure 3.8: The ~ 2000 DLT40 galaxy samples over-imposed on the 1 sigma localization of the ten LVC trigger which has been followed by DLT40 during O2.

most of them are later proved to place in much further region, compared with 40Mpc. Here we introduce our follow-up observations for these ten GW triggers.

3.3.1 G275404

G275404 was identified as marginal GW candidate by the two LIGO interferometers, Hanford (H1) and Livingston (L1) using the pyCBC analysis [Usman et al., 2016] at 2017-02-25, 18:20:21.374 UTC (GPS time: 1172082639.374). The false-alarm rate is $1.89 \times 10^{-7} Hz$, corresponding to ~ 1 in 0.17 years. Following the early released bayestar localization map [Singer et al., 2016], the 50% (90%) credible region spans about 460 (2100) deg^2. We selected and observed 50 galaxies within the LVC error region from 2017-2-26 to 2017-3-9. At 2017-08-08 22:30:50 UTC, the LALInference localization map [Veitch et al., 2015] was issued by LVC with the 50% (90%) credible region increasing to about 2000 (17000) deg^2. Meanwhile, LVC announced that the mass estimates are consistent with a BNS or NS-BH binary. Starting from 2017-3-9 (until 2017-3-12) we observed 84 galaxies based on the update GW localization map. Both these galaxy samples were prioritized. The DLT40 limit magnitude, for these observations is 19.2 (open filter scaled to r band). We found one SN Ia, SN2017cbv/DLT17u in NGC5642 in the observations of 2017-3-8 (distance is 16 Mpc). Our follow-up observations of SN2017cbv/DLT17u with Las Cumbres Observatory telescopes show that

accompanied optical kilonova, see Sec. 3.3.2.

Table 3.1: Summary table of LIGO O2 triggers

LIGO trigger	False Alarm Rate (per year)	90% sky erea (deg^2)	luminosity distance (Mpc)	number of galaxies selected	observation window (JD)	transient detected
GW170104 G268556	2	1600		18	2457759-2457766	
G270580	5	3100		25	2457774-2457796	
G274296	6			25	2457802-2457825	
G275404	6	2100 17000	280±80	50 84	2457815-2457821 2457821-2457825	SN2017cbv/DLT17u (SN Ia)
G275697	6	1800 3890	181±55 193±61	59 114	2457812-2457820 2457820-2457825	
G277583	3	12140		55	2457826-2457847	
G284239	4	3593		58	2457877-2457892	
GW170814 G297595	1/82800	97	550±130	24	2457980-2457982	
GW170817 G298048	1/9100	33.6	40 ± 8	20 (LVC) 31 (Fermi)	2457983-2457985	AT17fgo/DLT17ck (KN)
G299232	5.3	2040	339 ± 110	20	2457991-2458005	

We cover 20 Mpc for the first two triggers and 40 Mpc for the rest.

SN2017cbv/DLT17u reached its maximum luminosity (Bmag ~ 11.79) 17.7 days after discovery. Giving the typical rise time of SNe Ia [18.98 ± 0.54 days; Firth et al., 2015], we deduced that SN2017cbv was discovered very close to the explosion epoch and we can then exclude that SN2017cbv is related to the GW event that occurred ~ 2 weeks before the explosion epoch of SN2017cbv. Futher LVC analysis indicated that it was not a trigger of interest.

3.3.2 GW170817/G298048

GW170817 [Abbott et al., 2017b,e] was identified by the LIGO H1 at Aug,17, 2017 12:41:04 UTC (GPS time: 1187008882.4457), as likely BNS merger GW event according to the mass estimation. The false alarm rate is $3.478 \times 10^{-12} Hz$, equivalent to ~ 1 bogus in 9100 years on average, which is significantly low. In addition, the gravitational-wave signal was found in coincidence with the Fermi GBM trigger 524666471/170817529 [GRB170817a; Goldstein et al., 2017b] registered about 2 seconds later on Aug, 17, 2017 12:41:06 UTC (GPS time: 1187008884.47). With the constraint of the upper limit from VIRGO, the LVC joint sky area is reduced to 8.6 (33.6) deg^2 with 50% (90%) credible regions. The 90% confidence area of the GW localization includes 23 galaxies based on the DLT40 selection. We selected 20 of them which cover 99% of the cumulative luminosity, and we added we added the 31 most luminous galaxies in the Fermi error-box region. About 11 hours later the GW trigger, at the beginning of the Chilean night, DLT40 reported the detection of DLT17ck at RA=13:09:48.09 and DEC=-23:22:53.4.6, 5.37W, 8.60S arcsec from the centre of NGC 4993 [Valenti et al., 2017]. We were one of the six optical groups which independently detected this kilonovae, named 2017 gfo/sss17a [Abbott et al., 2017e; Arcavi et al., 2017; Coulter et al., 2017; Lipunov et al., 2017; Soares-Santos et al., 2016; Tanvir et al., 2017; Valenti et al., 2017]. No other transient was found in the other surveyed galaxies. The follow-up data obtained for DLT17ck are described in Valenti et al. [2017]. Yang et al. [2017] used the observed light curve of DLT17ck to constrain the rate of BNS mergers to less than 0.50 SNuB [6] and we conclude that DLT40 would need to be operated for ~ 18.4 years in order to discover a kilonova without GW trigger.

I specify that here in the section discuss briefly the discovery process while a full discussion of this GW trigger, and the associated kilonova, is presented later in chapter 6.

---

[6]SNuB $= 1$ SN per 100 yr per $10^{10} L_{B_\odot}$
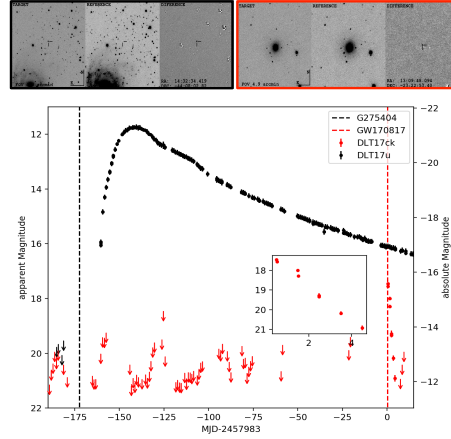
Figure 3.9: Top: SN and KN identified in our survey during O2. Black: SN Ia, 2017cbv/DLT17u discovered after G275404. Red: KN, AT17fgo/DLT17ck discovered after GW170817/G298048. In all images the showed field sizes are 10×10 arcsec, North is up and East to the left. The cross represent the position identified by our pipelines. Bottom: The light curves of DLT17u and DLT17ck while the data before the GW discovery(dashed line) represents the magnitude upper limit of the the host galaxy.

3.3.3   Others GW trigger

GW170104/G268556 [Abbott et al., 2017a] was identified by L1 and H1 at 2017-01-04 10:11:58.599 UTC (GPS time: 1167559936.599). GW170104 is a BBH event with a very low false-alarm rate, 6.1e-08 Hz (about one in 6 months). This GW event was the first identified LVC trigger in O2 run, and the first GW event followed by DLT40. As a test run, we monitored 18 galaxies within 20 Mpc. No obvious counterpart candidates were found.

G270580 was identified by L1 and H1 at 2017-01-20 12:30:59.350 UTC (GPS time: 1168950677.350). The false alarm rate is 1.6e-07 Hz (about one in 2.4 months). The 50% credible region spans about 600 deg2 and the 90% region about 3100 deg2. We selected 33 galaxies from the DLT40 catalogue within 99% of the trigger error region, within a distance of 20 Mpc and 25 of those galaxies have been observed. We started to observe these sample of galaxies on 2017-01-23 and monitored them for 3 weeks after the GW trigger. No interesting transients have been identified down to a limit magnitude of 19.2.

G274296 was identified by LIGO Hanford Observatory (H1) and LIGO Livingston

Observatory (L1) at 2017-02-17 06:05:55.050 UTC (GPS time:1171346771.050) as a burst GW candidate, with false alarm rate 1.7e-07 Hz or about one in 2 months. We selected 46 galaxies from our DLT40 galaxy catalogue within 80.0% of the trigger error region, within a distance of 40.0 Mpc while 25 of those galaxies have been observed by us. We started to observe these sample of galaxies on 2017-2-17 and monitored them for 3 weeks after the GW trigger. No interesting transients have been identified down to an average limit magnitude of 18.5.

G275697 was identified as marginal candidate by L1 and H1 at 2017-02-27 18:57:31.375 UTC (GPS time: 1172257069.375), with a false alarm rate of 1.43e-07 Hz or about one in 2 months. Based on preliminary analysis, LVC reported that the less massive companion in the binary had a mass less than 3 M_{sun} and there is a 100% chance that the system ejected enough neutron-rich material to power an electromagnetic transient. The 50% credible region spans about 480 deg2 and the 90% region about 1800 deg2. The luminosity distance is estimated to be 181 ± 55 Mpc. We observed 59 galaxies from the LVC localizarion from 2017-2-27 to 2017-3-7. After the update of LVC localization map, we updated the galaxy sample and observed 114 galaxies from 2017-3-7 to 2017-3-12. No interesting transients have been identified down to a limit magnitude of 19.0. Further LVC analysis indicated that G275697 was not a trigger of interest.

G277583 was identified by L1 and H1 as a burst GW candidate at 2017-03-13 22:40:09.593 UTC (GPS time:1173480027.593). Its false alarm rate is 8.4e-08 Hz (one in 4 months). We selected 112 galaxies from our galaxy samples within 80.0% of the trigger error region, within a distance of 40.0 Mpc. 55 of them have been observed from 2017-3-13 and lasted for 2 weeks after the GW trigger. No interesting transients have been identified down to a limit magnitude of 19.5 mag.

G284239 was identified by L1 and H1 at 2017-05-02 22:26:07.910 UTC (GPS time: 1177799185.910). G284239 is a low-significance short-duration burst candidate, whose false alarm rate is 1.26e-07 Hz (4 per year). The 50% confidence region covers 1029 squares degrees and the 90% confidence region covers 3593 square degrees. We selected 85 galaxies within 95.0% of the trigger error region, within a distance of 40.0 Mpc and observe 58 of them. We started to observe these sample of galaxies on 2017-5-2 and monitored them for 2 weeks after the GW trigger. No interesting transients have been identified down to a limit magnitude of 19.

G297595/GW170814 was the first GW event detected by both two LIGO (H1, L1) and the Virgo (V1) detectors at 2017-08-14 10:30:43 UTC (GPS time: 1186741861.5268). The Virgo detection helped to decrease the 50% (90%) localization region from 333 (1158) deg^2 to 22(97) deg^2. GW170814 was predicted to have a very low false alarm rate $3.83 \times 10^{-13} Hz$, equivalent to ~ 1 fake reported in every 82800 years. LVC re-

ported that the event was most likely a BBH merger at $\sim 550 \pm 130$ Mpc. Despite the lack of expected optical outcomes and the large distance, we have triggered follow up because of the small localization region. We monitored 24 galaxies within the LVC error region with an average limit magnitude of 19.0. No obvious optical counterparts were detected. All selected galaxies from this trigger were reset to normal priority on 2017 August 17 in order to aggressively pursue the next trigger GW170817.

G299232 was identified by L1 and H1 at 2017-08-25 13:13:31 UTC (GPS time: 1187702035.9831). G299232 is a low-significance candidate with a false alarm rate, 1.68e-07 Hz (about 5.3 per year). The 50% credible region spans about 450 deg2 and the 90% region about 2040 deg2. We selected and observed 41 galaxies within 95.0% of the trigger error region, within a distance of 40.0 Mpc from 2457991.48 (JD) to 2458005.21 (JD). No obvious transient was found.

3.3.4 Upper Limit Estimation For Different Type Of GW Counterparts

With the aim to evaluate the detection egficiency of the DLT40 survey I performed artificial star experiment, using the Daophot [Stetson, 1987] for PSF modeling and source simulation [Yang et al., 2017]. These measurements can also be used to estimate the performances of DLT40 for future GW counterpart searches and also to different observing strategy. In Fig. 3.10, we derive the sensitive distance for all the considered models and DLT17ck. It shows that DLT17ck could be detected using the DLT40 imaging facility and strategy up to 81^{+16}_{-13} Mpc. After completion of the ongoing interferometers updated, the BNS range (the range is the volume- and orientation-averaged distance at which a compact binary coalescence consisting of a particular mass gives a matched filter signal-to-noise ratio (SNR) of 8 in a single detector in the best position and face-on orientation the limiting distance is range * 2.26) of LVC in the O3 is to increase to 120-170 Mpc for LIGO, while reaching 65-85 Mpc from VIRGO [Abbott et al., 2016j]. If we assume that all kilonovae are as bright as DLT17ck and neglect that the galaxy catalog is incomplete, with the current DLT40 observing strategy we have the reference images for all targets, in principle we could detect all kilonovae in the Virgo volume in O3 season. Therefore, we decide to maintain the current observing strategy for the upcoming LVC O3 GW search but extent DLT40 galaxy samples from 40 Mpc to 60 Mpc.
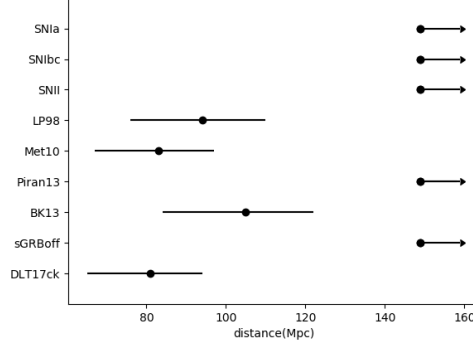
Figure 3.10: Limiting distance estimation for different emission models(details described in Figure 3.4). When scaling a EM model to distance D_i, the single detection efficiency[a] is denoted as DE_j for each DLT17ck observing epochs j[b] while the total detection efficiency for the model is derived as $DE_{D=D_i} = 1 - \Sigma_j(1 - DE_j)$. The limiting distance estimation would take the distance where $DE_{D=D_i}$ equals to 50%.

[b] The footnote-like comment under the caption

[a] recorded in the DLT40 log database towards NGC 4993

3.4 Conclusions and Future Prospects

The research on kilonovae could enrich our understanding on the astrophysics during high energy phenomenon, however for optical surveys alone, it's difficult to discover and classify such high cadence transients. The success with GW170817 is a lesson highligthening the importance of GW informations for kilonova study in the multimessenger astronomy era. For the upcoming LVC O3 run, DLT40 observing strategies have been designed taking into account the performance of DLT40 for kilonova search and the sensitivity expected for the LIGO and Virgo network. The machine learning algorithm is now applied into DLT40 ongoing search, and it would be used for transient validation when following GW triggers.

Table 3.2: Galaxies observed after trigger GW170817/G298048 while the information shows name, coordinates, distance, magnitude, observing window and the score from our ranking algorithm.

Name	RA (J2000)	DEC (J2000)	Dist (Mpc)	BMAG	KMAG	OBS WINDOW (JD)	Score	Score2

NGC4968	196.77	-23.68	33.42	-19.44	-23.14	2457983.41-2457985.17	1.850e-01	1.32e-01
IC4180	196.74	-23.92	33.65	-19.98	-23.04	2457983.41-2457985.17	1.773e-01	1.29e-01
IC4197	197.02	-23.80	34.10	-20.24	-23.39	2457983.41-2457985.17	1.518e-01	1.16e-01
ESO576-003	197.65	-21.75	28.44	-18.94	-20.65	2457983.41-2457985.17	5.278e-03	1.00e-01
ESO508-019	197.47	-24.24	38.55	-19.33	-21.16	2457983.41-2457985.17	5.854e-02	5.76e-02
ESO508-015	197.33	-24.38	33.42	-18.77	-18.79	2457983.41-2457985.17	6.547e-02	5.67e-02
NGC4993	197.45	-23.38	33.81	-20.20	-23.42	2457983.41-2457985.17	4.784e-02	4.78e-02
ESO508-024	197.69	-23.87	33.42	-19.98	-21.59	2457983.41-2457985.17	3.430e-02	2.45e-02
ESO575-053	196.27	-22.38	30.48	-18.44	-21.31	2457983.41-2457985.17	2.832e-02	1.40e-02
ESO576-001	197.60	-21.68	35.47	-19.18	-22.00	2457983.41-2457985.17	5.563e-03	4.74e-03
NGC5188	202.87	-34.79	28.84	-20.20	-23.78	2457983.41-2457985.17	8.945e-03	3.38e-03
ESO508-003	196.60	-24.16	33.43	-19.20	-21.23	2457983.41-2457985.17	1.408e-01	1.86e-03
NGC5161	202.31	-33.17	18.53	-19.84	-22.71	2457983.41-2457985.17	4.561e-04	1.24e-05
NGC5042	198.88	-23.98	12.65	-18.70	-21.11	2457983.41-2457985.17	3.534e-03	1.02e-05
IC0874	199.75	-27.63	29.06	-19.29	-22.64	2457983.41-2457985.17	5.020e-06	1.97e-06
NGC5078	199.96	-27.41	27.67	-21.24	-25.09	2457983.41-2457985.17	4.617e-06	1.41e-06
NGC5061	199.52	-26.84	24.21	-20.82	-24.63	2457983.41-2457985.17	5.615e-06	8.01e-07

NGC4680	191.73	-11.64	29.92	-19.12	-22.61	2457983.41-2457985.17	7.624e-07	3.45e-07
NGC5101	200.44	-27.43	24.21	-20.68	-24.76	2457983.41-2457985.17	1.926e-06	2.75e-07
NGC4594	190.00	-11.62	9.77	-21.43	-24.99	2457983.41-2457985.17	1.539e-06	1.22e-09

Chapter 4

Machine learning for transient selection

In this chapter, I discuss multiple machine learning (ML) algorithms that can assist in transient classification into real objects and artefacts, strongly reducing the need for human visual inspection. I review the usage of ML algorithms in the modern transient survey in chapter 4.1. In chapter 4.2, I introduce a ML tool, `asml`*, developed by me for transient identification, by exploiting the differencing images.* `asml` *is now employed for DLT40 ongoing SN search, and ready for both DLT40 and GRAWITA in the coming LVC O3 run. Testing different approaches, I found that with a random forest classifier we can reach a completeness of 90% for real sources, while incorrectly classifying 8% of bogus detections as real. The classifier has already been implemented into DLT40 daily search from the end of April, 2018, with excellent results. Till the end of June, during two months, we identified 5 transients with ML approach, resulting in a rate consistent with what we expected. Details of* `asml` *is shown in the appendix.*

4.1 Machine learning in the modern transient search

Modern synoptic surveys aimed at detecting the variability of astronomical sources, monitoring large sky areas with high cadence. When images are acquired, the most effective approach for transient detection involves the subtraction between search images with reference images taken previously. The candidates extracted from the residual images are contaminated by large number of artefacts (typically there can be 100 bogus

for 1 real candidate) and human visual inspection is often the bottleneck for a rapid target identification. However, the readiness is a significant and crucial factor for transient research: a) early discovery is important for those fast transients, in particular an r-process kilonovae [Li & Paczyński, 1998] associate with GW/sGRB [Abbott et al., 2017e]; b) even for transients with relative long timescale, early spectroscopy taken hours to days after explosion can be used to measure various physical properties of the environment, as well as constrain, e.g. the flash spectroscopy of SNe progenitors [Khazov et al., 2016]. Therefore, any tool that can rapidly help with real-bogus classification is important in the time domain astronomy researches.

So far, for automatic transient selection, most surveys adopt a ranking method. The "Traditional" ranking method (TR) uses photometric and geometric features of candidate sources measured in the difference image by some tool (`Sextractor` in our case). Thresholds on the acceptable value of selected parameters based on evaluation of training set and/or artificial star experiments are set. This approach is able to reduce the number of candidates left to visual inspection by a factor 10 which however is not enough since in wide field survey they may still count several hundreds candidates. Because of the amount of data, artificial intelligence algorithm, e.g. the ML and deep learning (DL) techniques, are worth to be tested.

ML algorithms uses statistical techniques to give machine the ability to learn from the features [1] extracted from training set, which is some known or simulated samples. ML could be divided into three classes: supervised/classification with label information, unsupervised/clustering without label information and semi-supervised which is a mixture. Supervised Learning would train the machine with a set of features together with labels that enable machine to classify the unknown features. For unsupervised Learning, there is no outcome variable to predict but the goal is clustering the samples into a number of sub-clusters based on the features only. We adopt the ML for the preliminary classification of DLT40 transient candidates, and the input for the ML is collection of measured parameters or an image section (stamp). We use the evaluation merit described in Brink et al. [2013] to compare different ML classification performances. After performance comparison, we decide to use a specific supervised learning for transient classification, and, we employ clustering algorithms to experiment on the proper way for label assignments. Once a suitable classifier is found, it can be employed to predict the class of any future object from its observed data.

---

[1]Features refer to digital numbers, that is representative for a training sample.

4.2 Machine learning with DLT40

In this section, I present the construction of DLT40 ML classifiers, and their performance comparison.

4.2.1 Training Set and Label Assignment

For ML, firstly, we need a number of known objects with some measured features, as an input for training the machine.

On DLT40, there are a few thousand of visually validated candidates together with ten times more artefacts which have already been cataloged over the past two survey years, which can be used for ML training. The real transients are labelled as SN, AGN, variable star, minor planet and so on, while the artefacts can be many different things, e.g. bright star which exceeds the threshold, bad subtraction due to the mismatched convolution, etc. Some representative real/bogus candidate examples are shown in Fig. 4.1 (see also Wright et al. [2015], section 2.1).

For the current DLT40 classifier, I use supervised ML for a 2-class division, namely real/bogus classification. Further comparison and discussion with multi-class division is shown in section 4.2.5.1. The training set are taken from the `MySQL` database at UC Davis, sometimes with a pre-ingest cuts based on our TR algorithms in order to rule out the very bad stamps.

4.2.2 Feature Representation

After obtaining a training sample, the next crucial step is the mathematical modelling process, namely, to find a set of reasonable and representative features to characterize the specific objects. A well selected feature set can provide a sententious representation of the training stamps that captures the salient class information encoded in the observed data.

For transient detection, there are several ways for feature construction, and I tested three approaches in this work:

- M1: The first approach is to use the stamp itself, namely the pixel matrix around the source [Wright et al., 2015] extracted from the image frame. It is noteworthy that, we use only the informations from the differencing image as input to ML experiments for transient detection. In the future works, We plan to explore also the information from the target and reference images.

(a) supernova

(b) variable star

(c) real transient

(d) bright star

(e) dipole

(f) edge

(g) artifact

(h) very low SNR
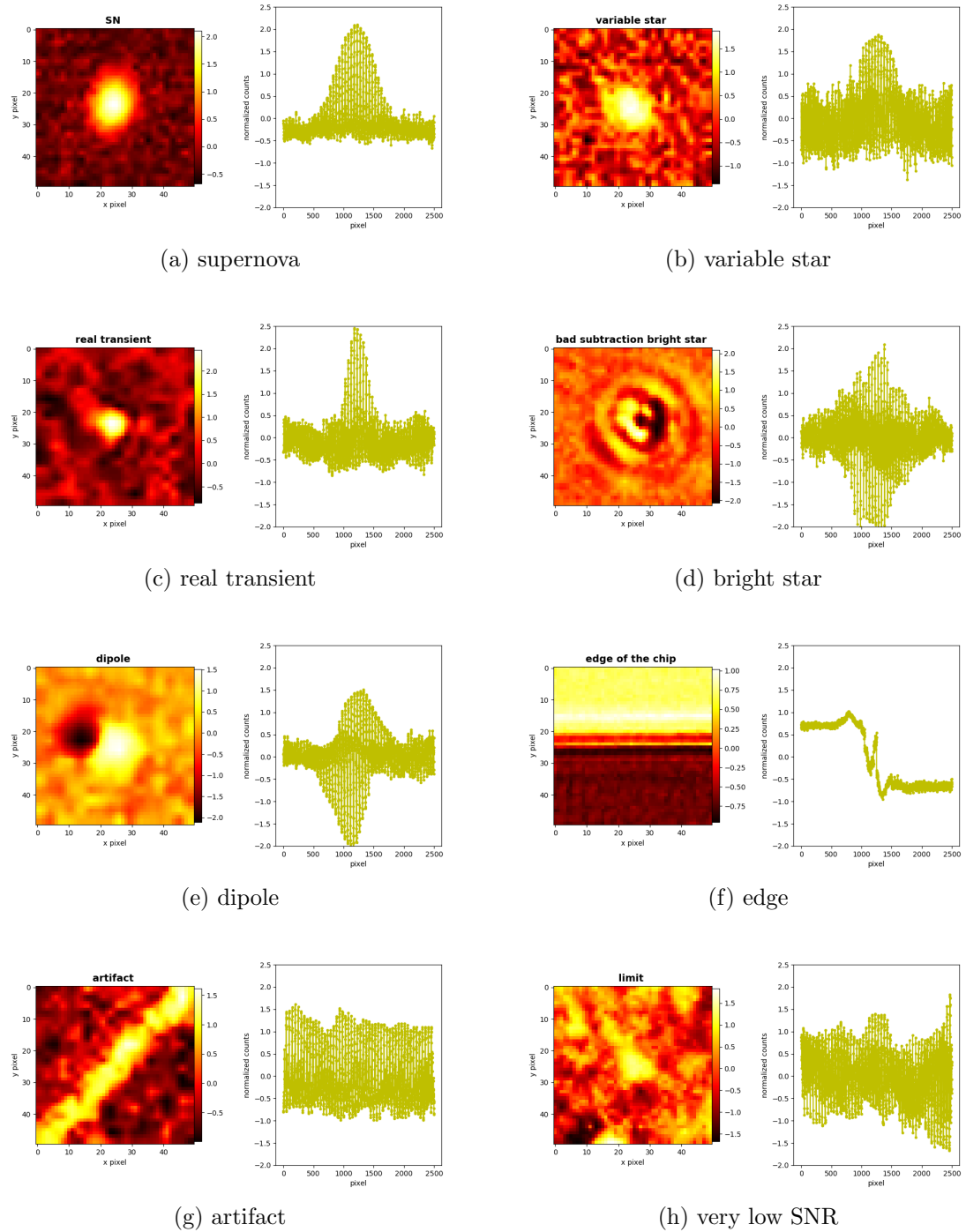
Figure 4.1: Visualisation of DLT40 ML feature vectors which are constructed by the stamp image of a 20×20 pixel matrix on the left and appending them together to produce the 400 element 1-D feature vector depicted on the right.
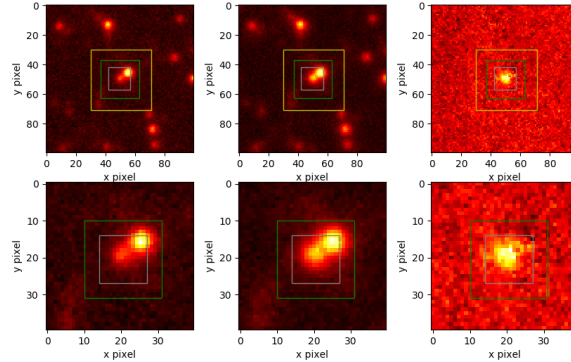
Figure 4.2: Visualisation of a DLT40 sample with different stamps size. Upper: the targeting image, reference image and difference image are shown in the left, middle and right correspondingly. The yellow, green and gray rectangle presents a view with stamp size equal to 40, 20 and 10 pixels. The lower panel are the zoom in plots of the upper stamps.

- M2: Following du Buisson et al. [2015], we use principal component analysis (PCA) along with linear discriminant analysis (LDA) to reconstruct the pixel matrix. This approach is supposed to run faster and then be useful for the future with much larger amount of data.

- M3: We also tested ML as a tool to aggregate Sextractor parameters, much similar to the TR [M3; Brink et al., 2013; Romano et al., 2006].

I compare the performances of the different approaches in section 4.2.5.3, explaining the reason for the selection of M1 as the current DLT40 classifier.

4.2.2.1   Feature Construction

By adopting approach M1, I collect the pixel array of individual counts around the centre for every candidate as the ML input features. The size of the array should be representative and well chosen: if the stamp is to too small, it cannot cover the full features of candidates, and vice versa, the stamps would be contaminated by nearby sources, especially for the crowded fields. Fig. 4.1 shows the visualizations of these feature vectors. Fig. 4.2 illustrates the 3, 5 and 7 times the median seeing full width at FWHM (5 pixel on average). The size selection process is described in section 4.2.5.2.
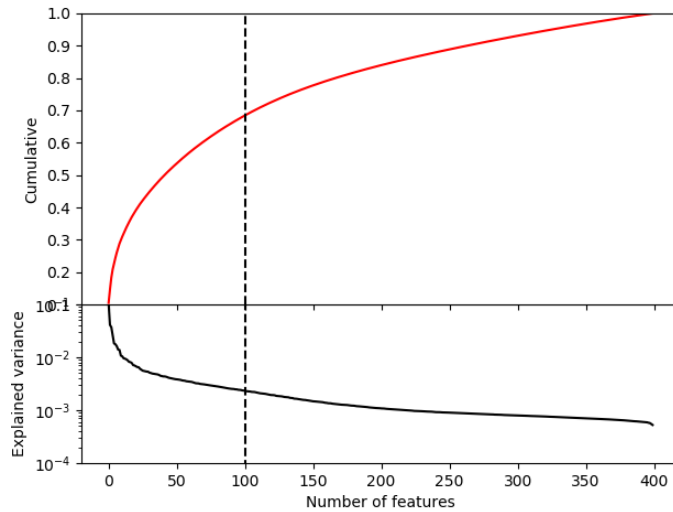
Figure 4.3: PCA variance spreading for a 20*20 size stamps. The y axis of lower panel is the amount of variance explained by each of the selected components, while in the upper case shows the cumulative variance. The result shows that PCA with the top 100 PCs cover 70% of the variance.

M2 introduces a PCA approach, which applies a dimensionality reduction for data sets. PCA adopts an orthogonal transformation to convert a set of uncorrelated variables into a set of values of linearly uncorrelated variables called principal components (PCs) with the requirement that most of the variance present in the original data set is preserved in the first few PCs. It is suggested by du Buisson et al. [2015] that considering a component generated from Linear Discriminant Analysis (LDA) along with PCA features can help to alleviate the so-called decision boundary alignment problem. The PCA+LDA approach is faster at the cost of variance. In Fig. 4.3 shows a PCA experiment for DLT40 training sample, that is a list of 20×20 pixel matrices. As shown, the top 100 PCs can explain 70% variance, and we verified that this decreases the calculation time by a factor of five. As a consequence, I will test this approach using 100 PCs along with one LDA feature to construct the feature vectors in M2 approach.

M3 is to some extent similar to M2, sacrificing variance to gain time. Like what TR method do, in M3, I organise the feature matrix with a set of Sextractor parameters: *class_star*, *flux_rad*, *ellipticity*, *FWHM*, *BKG*, *flux_max*, *flux_psf*, *flux_auto*, *flux_autoerr*, *mag_abs*. The meaning of thses parameters are defined in `https://www.astromatic.net/pubsvn/software/sextractor/trunk/doc/sextractor.pdf`.

4.2.2.2   Feature Preprocessing

In order to remove the contribution from background brightness, and allow ML classifiers to focus on relative pixel intensities, we have to apply feature normalization. It is shown in Romano et al. [2006] Fig. 4 that ML with normalization performs better than the one without normalization. In this work, I employ the modified log-normalization, suggested by Romano et al. [2006]; Wright et al. [2015], for all the three ML construction approaches:

$$f(x) = \frac{x}{|x|} log(1 + \frac{|x|}{\sigma})$$

(4.1)

where x is the feature vector and σ is the standard deviation.

4.2.3   Classification System

I developed a dedicated pipeline, `asml`, collection of `python` scripts to exploit the ML functions. These scripts call scikit-learn [2] and TensorFlow [3] modulus to implement ML and DL functions correspondingly.

In this section, I introduce several ML and DL classifiers.

4.2.3.1   Supervised Classifier

In this work, I tested the following supervised machine learning approaches:

a) K-Nearest Neighbors (KNN) [Cover et al., 1967] is among the simplest of all ML algorithms, which classify or regress samples by calculating the distance between different features. The main disadvantage of this approach is that the algorithm spend lots of time in distance computation and sorting, which can be slow if there are a large number of training examples. Further, KNN is a "lazy" ML algorithm without learning anything from the training data, which is expected to have some potential defects, e.g. not robust to noisy data. b) Decision Tree (DT) [Loh, 2014] is a non-parametric supervised learning method hiring a tree-like model of decisions that map possible outcomes of a series of related choices. DT usually works top-down in the tree structure and at each node of the tree, some metrics, e.g. Gini impurity, are used for measuring the best choice in order to best split the set of items. DT is simple and well designed to classify the training samples, however, puzzled by the so-called overfitting problem. c) In order to correct for the DT's habit of overfitting, Random Decision Tree or Random

---

[2]`http://scikit-learn.org/`
[3]`https://www.tensorflow.org/`

Forest (RF) [Breiman, 2001] is then designed aiming to classify examples by building multiple decision trees and applying bootstrap aggregation. Each individual tree is grown by randomly sampling n features from the m input ones ($n \leq m$) and the feature that best separates samples are selected as informed by the Gini function. This step would be repeated N times cloning N decision trees while each randomly created decision tree takes the selected features to predict an outcome. The high voted predicted outcome is considered as the final prediction from the RF algorithm. d) Adding one further step of randomization yields ExtraTree (extremely randomized trees, ET) [Geurts et al., 2006] classifier, which splits the trees randomly whereas deterministic in RF. e) Support Vector Machines (SVM) [Cortes et al., 1995] constructs an optimal hyperplane in the input feature space that is used to categorizes samples. For instance as the linear SVM classifier, a sample of p-dimensional vectors can be separated by a (p-1)-dimensional hyperplane. The best hyperplane is the one that represents the largest separation, or margin, between the two classes. SVM can efficiently perform a non-linear classification using what is called the kernel trick, implicitly mapping their inputs into high-dimensional feature spaces. In this work, we use Radial Basis Function (RBF) as the input SVM kernel. f) Naive Bayes (NB) [Friedman et al., 1997] classifier is a probabilistic classifiers based on Bayes' theorem with naive independence assumptions between the features. g) AdaBoost (Adaptive Boosting, AB) [Freund et al., 1997] is a meta-algorithm that can be used in conjunction with many other types of learning algorithms to improve performance. In this work, we take decision trees as the weak learners for AB.

4.2.3.2   Unsupervised Classifier

Besides supervised learning classifiers, unsupervised learning is also adopted to explore the inherent properties of DLT40 training samples. In this work, I use K-means as for the unsupervised classifier:

K-means aims to cluster the training data into K groups through finding the best centroids in the parameter space. The basic procedure of K-means classifier is as followed: 1. initial K cluster centroids in Monte Carlo way; 2. assign data points to clusters based on the current K random centroids; 3. update K new centroids based on the current assignment of data points to clusters. After a number of iterations, the centroids would converge to K constant points which cluster the training set into K groups.

4.2.3.3   Deep Learning Classifier

I have also tested a DL approach on the DLT40 samples, since, DL is well designed for image recognition and considered a very powerful categorizing tool in big data era. DL using Convolution Neural Networks (CNNs) has shown great success in the field of machine learning and computer vision and hence in this work, we decide to implement the inception CNN network [Szegedy et al., 2015] as DLT40 DL classifier:

CNN are a set of algorithms inspired by the biological neural networks, that comprise a number of interconnected nodes arranged into a series of layers: an input and an output layer, as well as multiple hidden layers, which include some convolution layers for CNN classifier. A node combines input with a set of weights, that either amplify or dampen that input, thereby assigning significance to inputs. These weighted inputs are summed and passed through an activation function, to determine whether and to what extent that signal progresses further to affect the ultimate outcome. In DL networks, each layer of nodes trains on input features from the previous layer's output, which means the more layers one classifier advance, the more complex features it can recognize.

4.2.4   Evaluation of Machine Learning Performance

The classifiers trained with the training sample can be used to further classify new objects, predicting its classes. To test the different methods and options, a cross validation process, that adopt a trained classifier to predict known features, is subsequent designed to evaluate their performances, in order to find the most suitable one for the ongoing DLT40 search. For the the cross validation process, it is important to make sure that the candidates to be predicted have not been inspected during the training phase, otherwise the overfitting result would be overly optimistic. To mitigate this effect we split our data randomly into two parts, training set (T1) and testing set (T2). After ML training phase with T1, the ML classifier is used to predict for T2 set, whose real label is known by human, however, not known by the machine.

For a two-class classification problem, the trained classifier output a predicted variable for each new feature, namely the hypothesis, that is defined as the probability of the candidate belong to one class. As an example case, I randomly separate the DLT40 training sample, 80% as T1 and the rest, 20%, for T2. Hypothesis on T2 can be plotted as a distribution histogram, Fig. 4.4 where red line is for the real candidates while black line is for the bogus. It appears that a threshold of 0.2, can be adopted to set a boundary for new candidates: if the ML hypothesis of a candidate larger than 0.2, the candidate is considered to be more similar to the real sources. We may notice
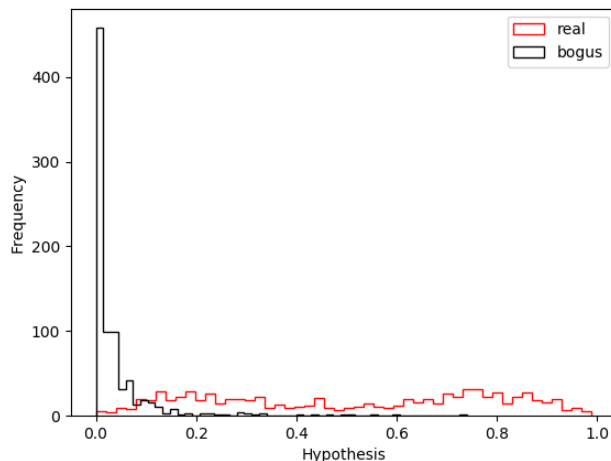
Figure 4.4: DLT40 machine learning classification results, with RF algorithm using n_estimator=100, max_features=25 and min_sample_leaf=1. The DLT40 training samples, namely the 4159 real and 63666 bogus stamps, are divided randomly into 2 parts, 80% as the training set and 20% as the testing set. As shown, the threshold can be set close to 0.2.

that the threshold is far from to 0.5 due to the imbalanced data problem (the ratio bogus/real is large), which is discussed later in section 4.2.5.5.

A commonly used figure of merit (FoM) for judging a ML classifier is the so-called "receiver operating characteristic" (ROC) curve, which is created by plotting the missed detection rate (MDR) against the false positive rate (FPR) at various threshold in the hypothesis histogram. After running of decision boundary in Fig. 4.4, we get the ROC curve, as shown in Fig. 4.5. The classifier whose ROC curve has a smaller AUC (Area Under the ROC Curve) value, is considered as the better one. Furthermore, I define a metric, f_{10}, as the False Positive Rate (FPR) that gives a Missed Detection Rate (MDR) of 10%, which means that we accept to discard 10% of the real sources, meanwhile, what fraction of the bogus candidates are deemed real by the classier, see Fig. 4.5. In particular, this metric would be modified to f_5, f_1, or even less, when f_{10} is saturated at some point.
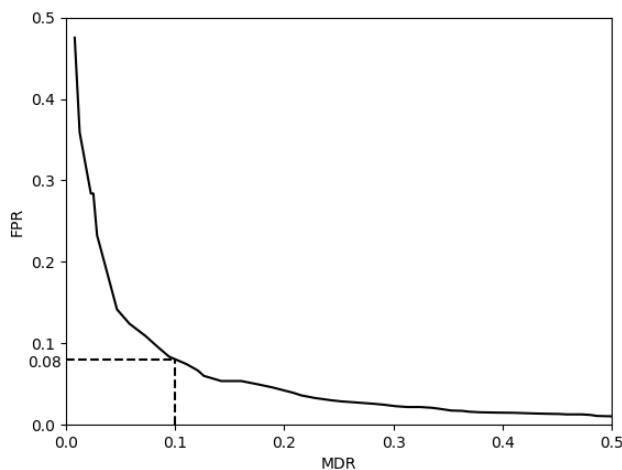
Figure 4.5: ROC curve: FPR as a function of the MDR. The merit can be defined as the FPR where MDR=0.1

4.2.5   Machine Learning Optimization

In this section, I use the merit defined in section 4.2.5 to compare performances achieved with different options.

4.2.5.1   Why two-class classification

As an preliminary exploratory test, I set up an unsupervised learning experiments from the DLT40 training sample, to verify how well the candidates could be clustered into classes with different clustering number. As discussed in section. 4.2.5, a two-class clustering outputs a ROC curve through varying the threshold settings in the hypothesis histogram. With more clustering number, instead of the hypothesis, the clustering algorithm predict the class directly, therefore, we obtain a single ROC instead of a curve. Fig. 4.6 is showing the unsupervised ROC points for different number of classes, together with a supervised ROC curve. It turns out that the ROC value with more than 5 clusters is significantly lower, suggesting at least 5 sub-classes are required by the intrinsic properties of training samples. On the other hand, as it can be seen from the figure, the performances of the supervised approach is much better. This is likely due to the asymmetry of the cluster population, with a small number of real candidates compared with bogus (imbalance problem, see section 4.2.5.5). Therefore in this work, I use two-cluster supervised learning algorithms.
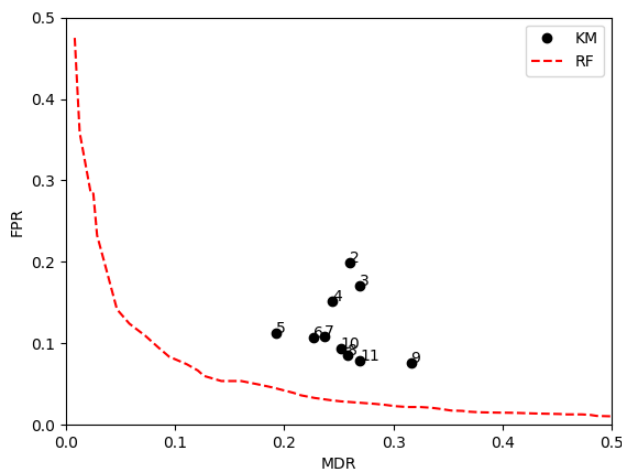
Figure 4.6: ROC curve comparison between different unsupervised learning cases of various clustering number, with the supervised learning case. The result shows that supervised is better that unsupervised as expected, and also, dividing the candidates into at least 5 is preferred.

4.2.5.2   How to select the stamp size

In general, the optimal stamp size depends on the telescope scale and average seeing. To choose the optimal value for the DLT40 survey, in Fig. 4.7, I plotted the comparison between ROC curves for different stamp size. As shown, ML with stamp size of 20 and 30 pixel have the best performance, so I decide to adopt 20×20 pixel matrix as input feature vectors for M1.

4.2.5.3   Why choose M1 for feature construction

For TR, to each candidate we assign an initial score that is then increased/decreased depending on parameters provided by SExtractor or measured directly on the difference image. This score is then considered as the hypothesis to output the ROC curve. It's shown in Fig. 4.8 that ML performs much better than TR, and this is why we need a ML approach.

For DLT40 ML selection, Fig. 4.8 shows that M1 gives better result than M2 and M3. Meanwhile, the time requested to run M1 on the current DLT40 samples and computers is acceptable for us after we implemented a parallel computing mode. M2, that is faster and not that worse than M1, can also be an alternative in the future big
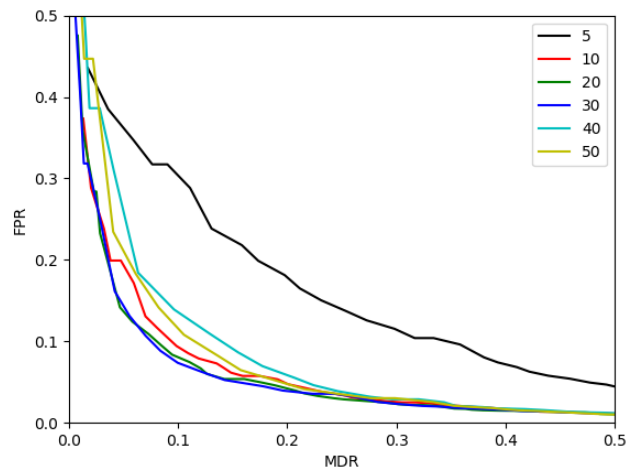
Figure 4.7: ROC curve comparison between different stamp size using DLT40 RF classifier. As shown, cut stamp with size to 20 pixel, or 30 pixel, obtain the best performance.
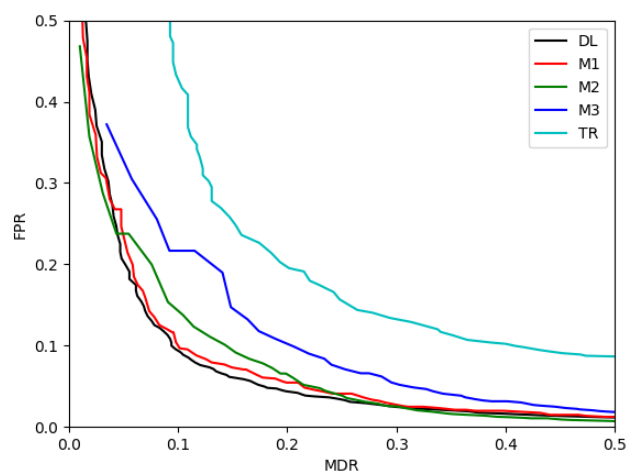
Figure 4.8: ROC curve comparison between different ML methods. As shown, the DL performs better than ML, while TR is the worst case. Among ML, M1, namely ML with matrix, is better than the other two.
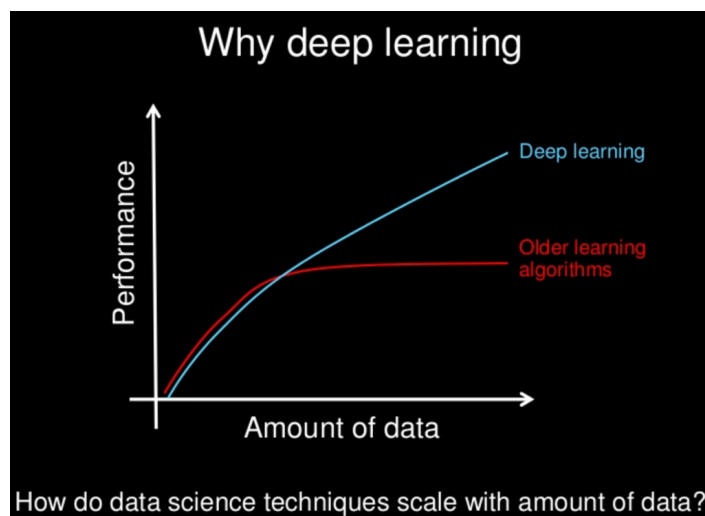
Figure 4.9: DL is expected to be more powerful than ML with big data. Credit by Andrew. NG.

data era.

4.2.5.4 Why choose RF for ML classifiers

Fig. 4.8 shows that DL is very similar to M1. DL is supposed to work better than standard ML, with very large data size (cf. figure 4.9). We set up DL classifiers with different steps, and their comparison with M1 is presented in figure 4.10. It appears that with the current data size of DLT40 training samples, namely $\sim 10^4$ objects, DL is not significantly better than M1. However, DL takes much more computing resources. As a consequence, I decide to use M1 at the current stage, while continuing to test DL performances in future experiments.

In Fig. 4.11 we present a number of ROC curves representing the DLT40 ML classifiers for different algorithm all with the M1 approach. As shown, the RF and SVM classifiers give the best results. Considering again the computing resource required we selected RF as the DLT40 ML classifier.

In Fig. 4.13 we show ROC curves of RF classifiers with various parameter settings changing in particular n_estimators, max_features and min_samples_leaf, which are specific input scikit-learn parameters, also following Wright et al. [2015]. After the tests, we find that n_estimators, defined as the number of decision trees, is the dominant factor. Selecting a value of 100 for n_estimators produces the best merit, namely, 0.08, which means with a cost of 10% wrong detections, we missed only 8% the real sources.

(a) f_{20}

(b) f_{10}

(c) f_5

(d) f_1
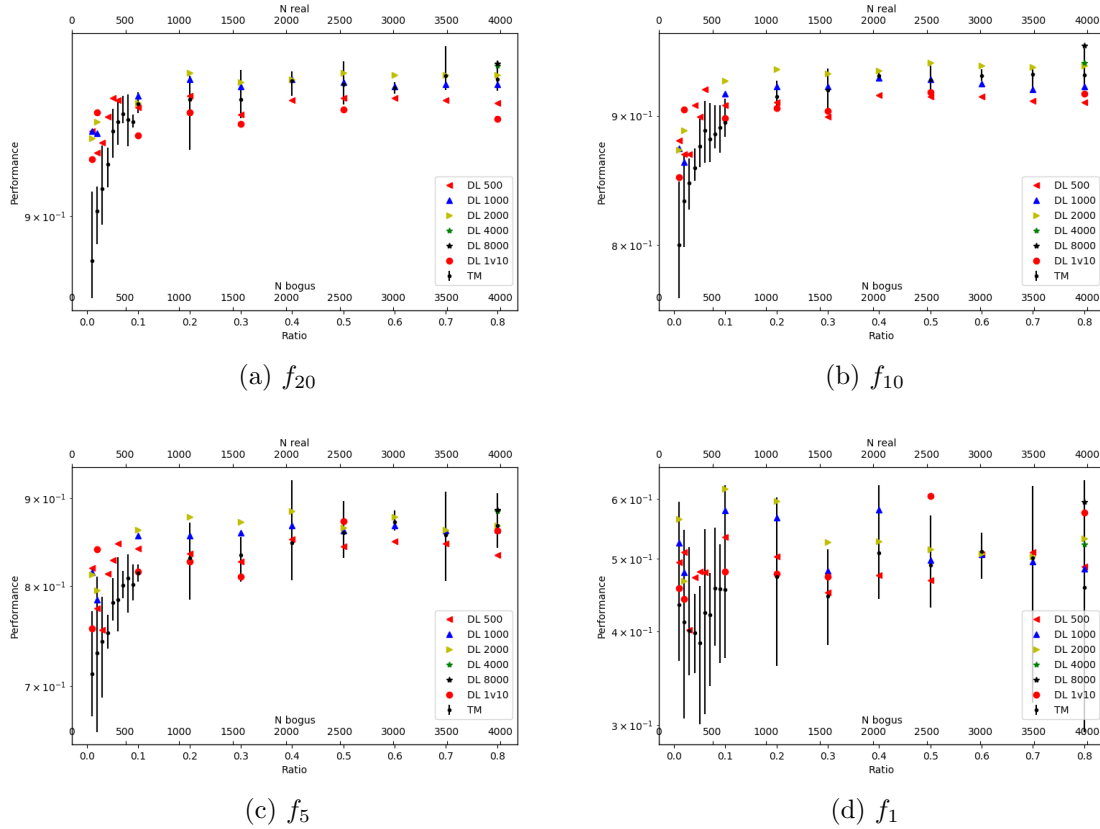
Figure 4.10: Performance comparison between TM (trend of machine learning) with different depth of DLs. In each sub-plot, TM is weighted by 10 random ML results, while different colored symbols are DL results, with different steps.

In this first DLT40 ML implementation, we decided to apply RF algorithm with $n\_estimators = 100$ as DLT40 classifier.

4.2.5.5 Imbalance data problem

During a real transient survey, the number of bogus detection is much larger than the real sources, even after the pre-cut with TR which somehow alleviate the imbalanced data problem. To exam how the data imbalance affects the prediction, I trained ML classifiers with different real/bogus ratio. The result, showing in Fig. 4.13, suggest that when both real and bogus objects are above 1000 we get the more consistent result with a just a few percent of real candidates lost.

The current DLT40 training samples consist of 4159 real and 63666 bogus stamps.
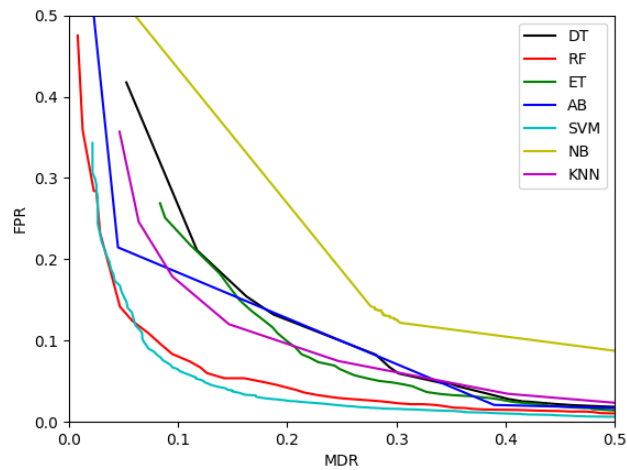
Figure 4.11: ROC curve comparison between different supervised learning algorithms with specific input parameters. As shown, the RF and SVM are two of the best, explained why DLT40 choose RF.
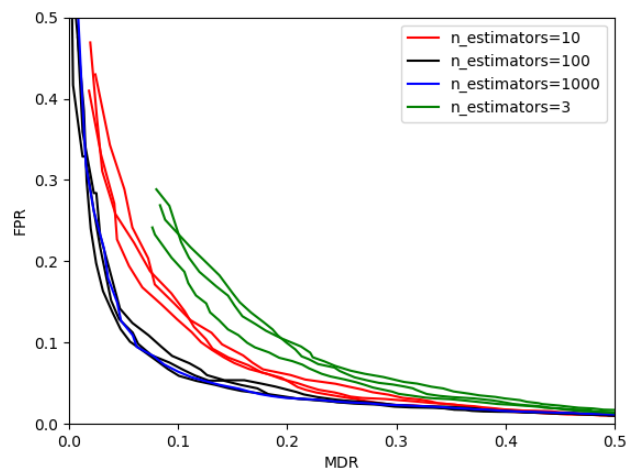
Figure 4.12: ROC curve comparison of RF classifiers with different input parameters. As shown, the main parameters that make an affect for performance is the n_estimators, which is assigned as 100 and 1000, for the best performance.
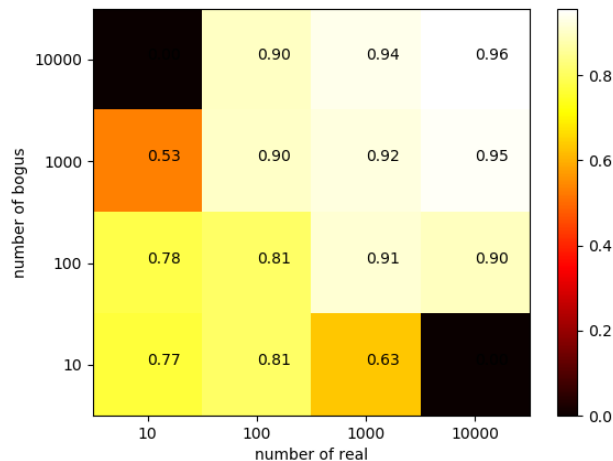
Figure 4.13: A ML test designed for the imbalanced data problem, by manual varying ratio of training candidates. The number shown in each square is f_{10}, by averaging 10 experiments. The two black squares stands for null values, since too imbalanced training dataset cannot be used divide testing samples, so that it failed to output the ROC curve and the ML hypothesis. The resampling technic is applied for cases with number of real objects greater that 4159.

Fig. 4.4 is showing the classification result by using these imbalanced sample, that, for a 10% FPR prompts for a threshold around 0.2. As a test, I applied a random selection of the bogus stamps, resulting with a set of 4159 real and 4159 bogus stamps as ML training phase. The resulting hypothesis histogram is shown in Fig. 4.14, where the threshold is now adjusted to 0.5.

A further test was made altering the size of the training sample, as shown in Fig. 4.15, by a random selection of the DLT40 training stamps. The figure shows that there is no much loss if the sample is reduced by a factor 2/3, suggesting that based on current sample size is close to ML saturation (cf. Fig. 4.9). Therefore it appears that a balanced sample of few thousands events is sufficient for this stage of the analysis. On the other hand there may be cases where the sample is relatively small and strongly unbalanced. In these cases one may adopt some remedies to increase the sample size, as well as alleviating the imbalance data problem. Meanwhile, increasing sample size can provide abundant training samples for deep learning in the future. Therefore two approaches are tested:
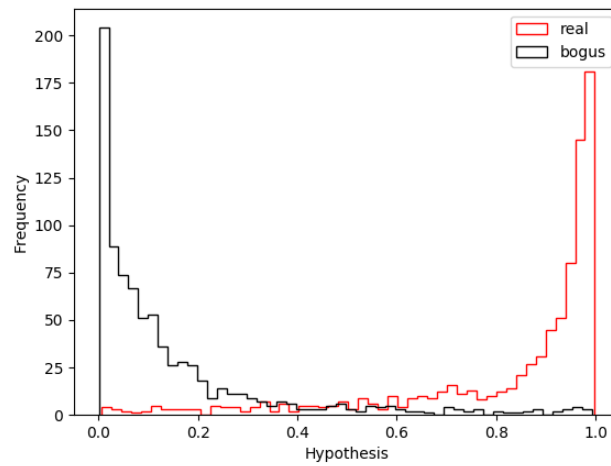
Figure 4.14: The same histogram as figure 4.4, while the DLT40 training samples are pre-cut to the 4159 real and 4159 bogus stamps. As shown, the threshold can be set close to 0.5.
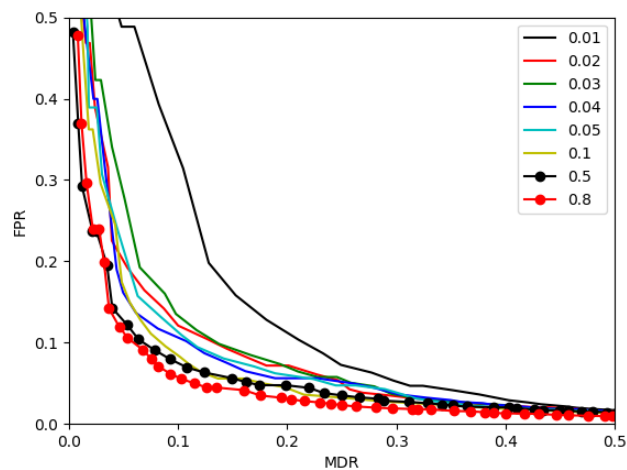
Figure 4.15: How much number of data might be needed to construct the training set? Different lines represent for different fraction of data adopted for training the machine, with the total number of 4159 real and 4159 bogus.

- One method suggested in Romano et al. [2006] to increase the fraction of real stamps, is merely a modification of the individual weights ('resampling').

- Another approach is to use artificial star experiment. In Yang et al. [2017] we used `Daophot` to inject a number of simulated sources into raw images. The raw images are then input to the difference image pipeline, and the simulated candidates increase the sample of real objects in the training set. In this case the main problem is to assure that the simulated sources have the same properties of the real source in particular with reference to the noise components.

4.2.6 Further Analysis

In this section, I investigate some specific problem of ML, by using the RF ML classifier, together with the DLT40 training samples.

4.2.6.1 Label contamination

In the process of sample identification, label contamination, namely, candidates classified with incorrect labels, is inevitable. In order to investigate how label contamination affects the process of training and testing for the optimal RF model, we design an artificial pollution experiment: where the labels for a specific number of candidates in the training and training sets are switched from real to bogus and vice-versa. After varying the fraction of label contamination, the trained classifiers are used to predict the classification for the T2 test set. As shown in Fig. 4.16, the identification performance is robust to around 95%, up to 10% contamination of T1 training set, suggesting the DLT40 ML classifier is not too sensitive to the incorrectly training data. As reference we show the result of the artificial pollution experiment contaminating the T2 dataset.

4.2.6.2 Feature Importance

The tree classifier, e.g. RF, split data into subsets which most heavily belong to one class, and continue to build the lower level subsets, until to figure out the relationship between the features and the labels. The feature importance could be then estimated by the classifier through mathematically determining which split will most effectively help distinguish the classes. Scikit-learn RF classifier, which is applied as the current DLT40 classifier, provide a built-in method to estimate the relative importance of each feature [Breiman, 2001].

As shown in Fig. 4.17, most weight of the classification relies on the central pixels. Actually, edge pixels are expected to be important for identifying bogus candidates,
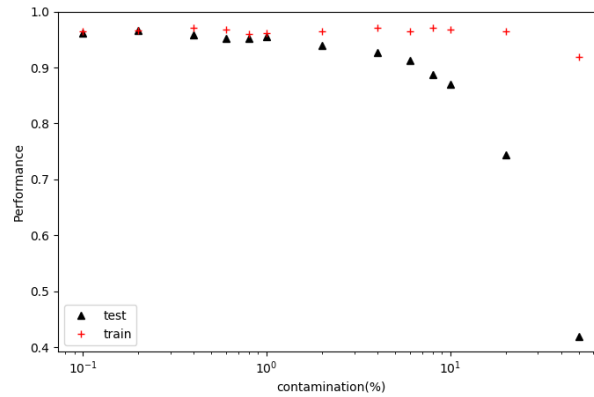
Figure 4.16: The artificial pollution experiment is designed to investigate the influences of label contamination. As shown of red plus symbols, pollution in the training set affects less to the performance, up to $\sim 10\%$.

however, the weight from artefact on the edge pixel is random, so that the average value is relatively low.

4.2.6.3 Classification as a Function of Signal-to-Noise

To investigate the classifier performance as a function of Signal-to-Noise (S/N), I also performed a specific test following Wright et al. [2015]. I used the DLT40 classifier to make a prediction for the T2 examples and plotted the result in the left panel of Fig. 4.18 as a function of the source magnitude (that, for a given observing configuration is a proxy of the SNR). Then, I calculated the fraction of real candidates classified as bogus which I take as an estimate of the classifier performance for objects at that magnitude. In Fig. 4.18 right panel shows that the MDR rapidly increases with sources getting close to the observing limit.

4.2.6.4 Classification as a Function of Ellipticity

Apart from the brightness, another significant factor that I can imagine is the ellipticity of sources. In Fig. 4.19 is showing a similar analysis as S/N, suggesting that MDR increase with sources getting more and more elongate.
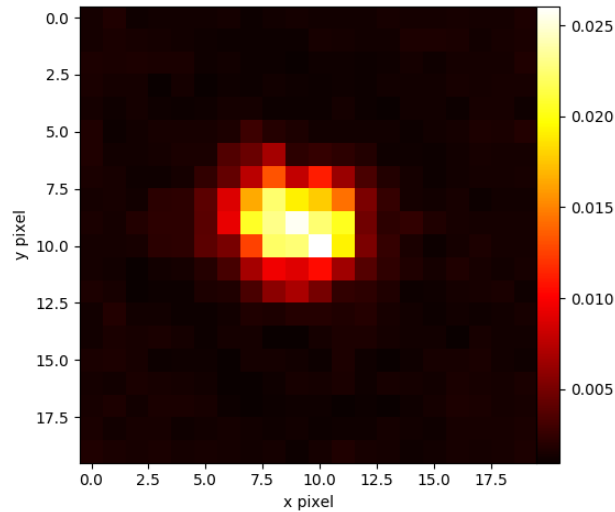
Figure 4.17: Feature importance of DLT40 RF classifier on a number of stamps with size of 20 pixels. The relative importance is normalized, so that the sum of all pixel number is equal to 1.
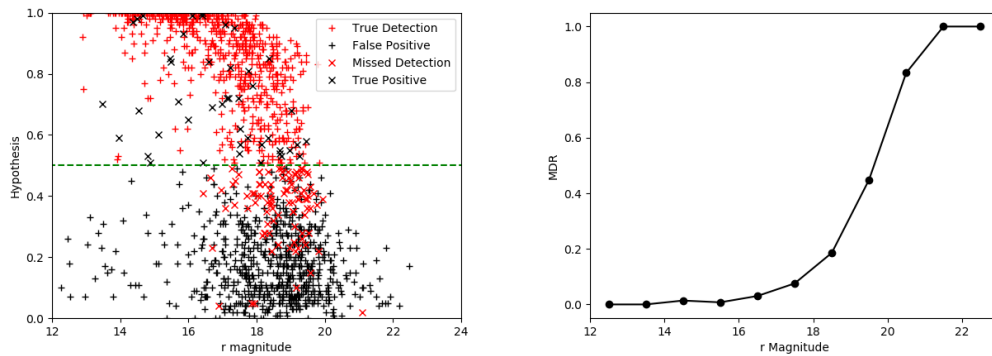
Figure 4.18: Left: ML hypothesis as a function of apparent magnitude. Red symbols denote the real candidates while black ones are bogus. Crosses are for the wrong classification while plus are correct cases. Right: MDR as a function of apparent magnitude. As shown, more detection would be missed when they're more fainter.
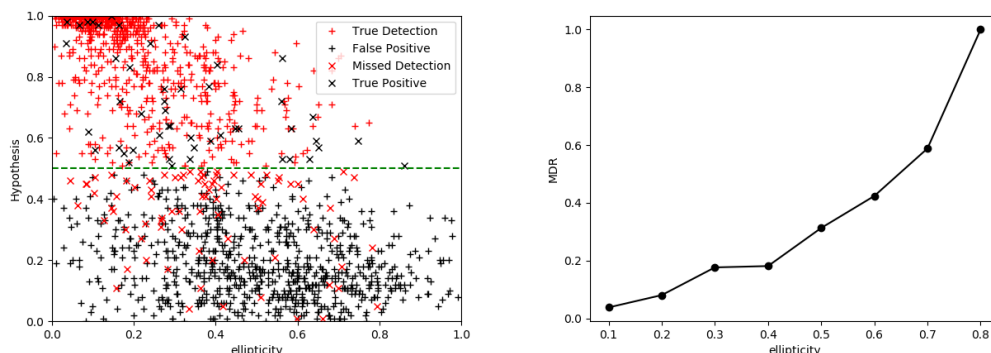
Figure 4.19: Ellipticity is a Sextractor parameter, defined as $1 - \frac{B}{A}$, where A and B are semi-major and semi-minor axis lengths of the extracted source, respectively. Left: ML hypothesis as a function of ellipticity. Red symbols denote the real candidates while black ones are bogus. Crosses are for the wrong classification while plus are correct cases. Right: MDR as a function of ellipticity. As shown, more detection would be missed when they're more elongated.

4.2.6.5   Incorrect ML Classifications

I visually inspected all objects incorrectly classified in the test set, and select twenty examples shown in Fig. 4.20 and 4.21, as for the missed detections and false positives, correspondingly. In particular, there're ~ 100 wrong classifications in respect of a few thousand candidates in total.

Of the ten missed detected objects, three, i.e. 5, 6, 7, are clear wrong labels in the test set (in large sample a fraction of errors in visual inspection is unavoidable). The first four cases are close to the detection limit and in this case as shown before there can be a large fraction of misclassification by ML should be expected. In the remaining cases, their FWHMs are small so that their features are similar to those cosmic rays, and even manual check cannot easily classify them.

Of the ten false positive objects, mostly are instead clear wrong, except the first one, which is excluded by human inspection using informations from all the three images, while the currently ML classifier is only trained with difference images. For the rest examples, I conclude a point of them in common, is that, showing a good Gaussian profile in the centre, however, contaminated in the edge.

These incorrect ML classifications reveal the properties of our current training sample, point out the direct for the training sample constructions in future ML test.
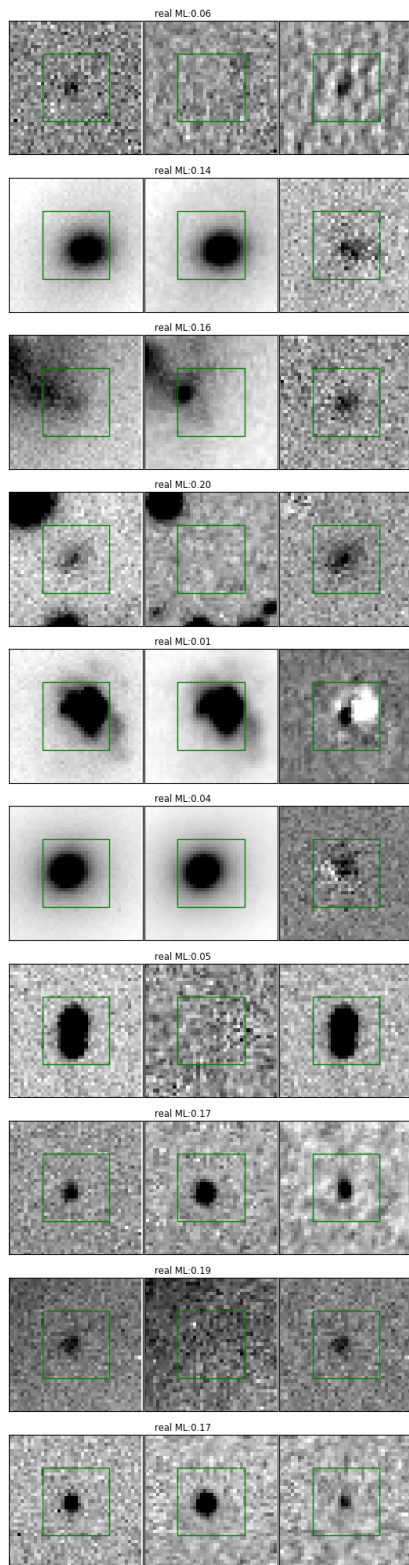
Figure 4.20: 10 examples candidates were classified as real, however obtain a low ML score. In each subplot shows the eyeballed result, ML score, together with two target image, reference image, and their difference.
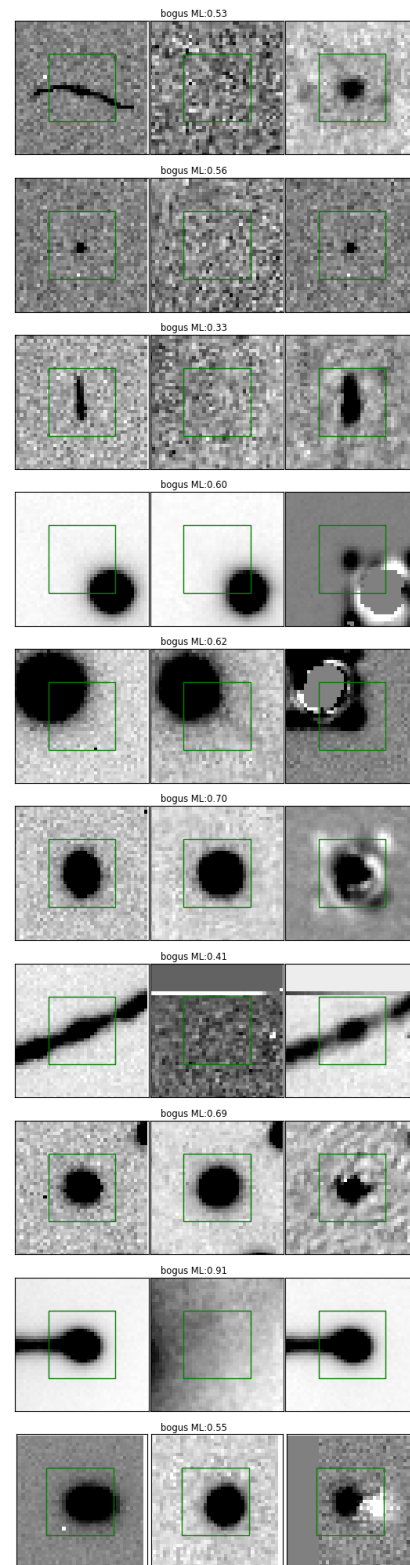
Figure 4.21: 10 examples candidates were classified as bogus, however obtain a high ML score.
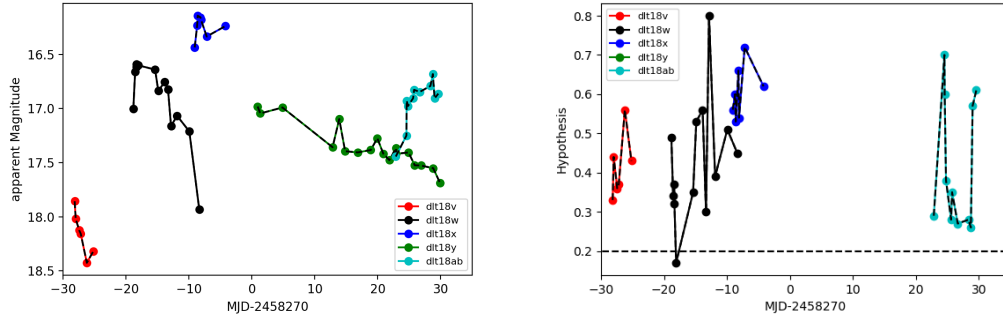
Figure 4.22: The ML has been applied into the daily DLT40 search from the the end of April, 2018. Till the end of June, there're 5 transients discovered. In left panel is showing their light curves, while their hypothesis curves are shown in the right. As shown, the hypothesis at majority epochs of these candidates are below threshold, 0.2, suggesting the existence of a real source, despite only the fifth epoch of DLT18w.

4.3   Machine learning performance in the on-going DLT40 search

After completion of performance test, at the end of April, 2018, I proceeded in the implementation of the RF classifier in the ongoing DLT40 search. At the test stage, we adopted all DLT40 classified objects as training sample, which is imbalanced, and as a consequence, the threshold is set to 0.2, which means objects with ML score less than 0.2 is ignored automatically. During the first two months, the ML performs well and help DLT40 discovering 5 interesting transient sources. Details on these transients, together with the corresponding ML hypothesis are shown in Tab. 4.1. Fig. 4.22 shows their light curves and hypothesis values at the different epochs showing that in most cases the values are above threshold, suggesting a existence of real source as expected, despite only the fifth epoch of DLT18w.

The transient rate during these two months is consistent with the previous estimation [Yang et al., 2017], suggesting that using ML instead of eyeballing all candidates does not significantly miss real transients. While, it strongly relieving the burden of visual inspection. Indeed, the number of candidates to be eyeballed per night which was up to thousand without ML, with the ML implementation decreased by a factor 50 to 100.

Table 4.1: Machine learning searching results of DLT40 daily search, from the end of April, 2018 to the end of June

Transient Name	Disc Time	Disc Mag	Disc ML hypothesis	Host Galaxy	Classification
DLT18v/AT2018beg (ATEL #11600)	2018 May 03.35	17.9	0.37	ESO 221-G 013	Variable (ATEL #11613)
DLT18w/AT2018bko (ATEL #11638)	2018 May 12.67	17.0	0.18	ESO 126-001	Galactic (ATEL #11639)
DLT18x/AT2018bwo (ATEL #11665)	2018 May 22.42	16.4	0.44	NGC45	ILRT (ATEL #11669)
DLT18y/AT2018cdc (ATEL #11678)	2018 June 01.42	16.9	0.27	NGC 274	SN II (ATEL #11704)
DLT18ab/AT2018cuf (ATEL #11770)	2018 June 23.36	17.4	0.47	IC 5092	SN II (ATEL #11777)

4.4 Conclusions and Future Prospects

In this work, I have presented the DLT40 ML classifier for transient identification, which is employed in the DLT40 ongoing transient survey. I am currently working to improve the training sample purity, also through artificial star experiment. Also, I am testing the ML implementation in the VST data obtained in O1/2 by the GRAWITA collaboration. The goal is to have this in operation for the incoming O3 run.

Chapter 5

Follow up observations of selected candidates

In a few cases, selected transients found in our search or by other groups show characteristics that may suggest a possible link with the GW event. We then activate dedicated photometric and spectroscopic follow-up to investigate this possibility. GRAWITA triggered follow-up analysis of iPTF15dld, ATLAS17aeu, besides the kilonova AT17fgo (cf. chapter 6), during the LVC two runs. In this chapter, I present the GRAWITA follow-up secured for these transients. The observation and analysis reported were published in [a] and [b].

Publications:

[a] Pian, E.; Tomasella, L.; Cappellaro, E.; Benetti, S.; Mazzali, P. A.; Baltay, C.; Branchesi, M.; Brocato, E.; Campana, S.; Copperwheat, C.; Covino, S.; D'Avanzo, P.; Ellman, N.; Grado, A.; Melandri, A.; Palazzi, E.; Piascik, A.; Piranomonte, S.; Rabinowitz, D.; Raimondo, G.; Smartt, S. J.; Steele, I. A.; Stritzinger, M.; **Yang, S**.*; Ascenzi, S.; Della Valle, M.; Gal-Yam, A.; Getman, F.; Greco, G.; Inserra, C.; Kankare, E.; Limatola, L.; Nicastro, L.; Pastorello, A.; Pulone, L.; Stamerra, A.; Stella, L.; Stratta, G.; Tartaglia, L.; Turatto, M., MNRAS 466, 1848*

[b] Melandri,...,Yang,...,et al, submitted to A&A

5.1 iPTF15dld after G194575

On 22 October 2015, a low probability event [false alarm rate of 1/1.5 per days, LIGO/VIRGO Scientific Collaboration, 2016b] was detected by the Advanced LIGO interferometers [named G194575, LIGO/VIRGO Scientific Collaboration, 2015d]. Because of the low probability GRAWITA did not activate a search campaign for this event, but other groups were instead more active and a number of multi-wavelength transients were detected during the wide field optical searches of the huge sky localization uncertainty area of the gravitational wave. The majority of them were immediately recognised as unrelated with the GW event (see Corsi et al. 2016; Palliyaguru et al. 2016, and references therein). There was however an interesting case which deserved further analysis, iPTF15dld.

SN iPTF15dld [Singer et al., 2015] was detected by the 48inch Oschin telescope at Mount Palomar during the intermediate Palomar Transient Factory (PTF) survey [Kulkarni, 2013; Law et al., 2009; Rau et al., 2009] on 23 October, 08:15 UT at coordinates RA = 00:58:13.28, Dec = -03:39:50.3 with a magnitude of 18.50 [Mould R filter, AB system, Ofek et al., 2012]. The initial identification as a Seyfert 2 galaxy at $z = 0.046$ [Tomasella et al., 2015a], based on a preliminary spectral analysis, was later revised to the classification as a broad-lined type Ic SN [Benetti et al., 2015]. The redshift was also slightly revised to $z = 0.047$ based on accurate analysis of the host galaxy emission lines. This corresponds to a distance of 200 Mpc using $H_0 = 73 \, \mathrm{km \, s^{-1} \, Mpc^{-1}}$ [Riess et al., 2016], and a flat cosmology with $\Omega_m = 0.31$ [Planck Collaboration et al., 2015]. The Galactic extinction along the SN line of sight is $A_V = 0.085$ mag [Schlafly & Finkbeiner, 2011]. The SN was also independently discovered as LSQ15bfp on 5 October 2015 with $V = 19.5$ mag during the La Silla QUEST survey [LSQ, Baltay et al., 2013; Walker et al., 2015] by Rabinowitz et al. [2015] who also report a pre-discovery detection on 3 October 2015 at $V = 20.2$ mag and a brightening of 0.7 mag in 2 days suggesting that this date must be very close to explosion time. The object was also detected by Pan-STARRS as PS15crl in 6 separate exposures on 23 October 2015 (see Smartt et al. 2016, and Huber et al. 2015 for a description of the current Pan-STARRS surveys[1]). The Pan-STARRS reference images show a very blue starburst region that is superimposed on a larger spiral galaxy. Corsi et al. [2016], who reported early optical photometry and a spectrum on 7 November 2015, detected no significant X-ray or radio emission for this SN (see also Evans et al. 2015; 2016).

Here we present the *Swift*/UVOT and ground-based optical observations of the

---

[1]http://star.pst.qub.ac.uk/ps1threepi/
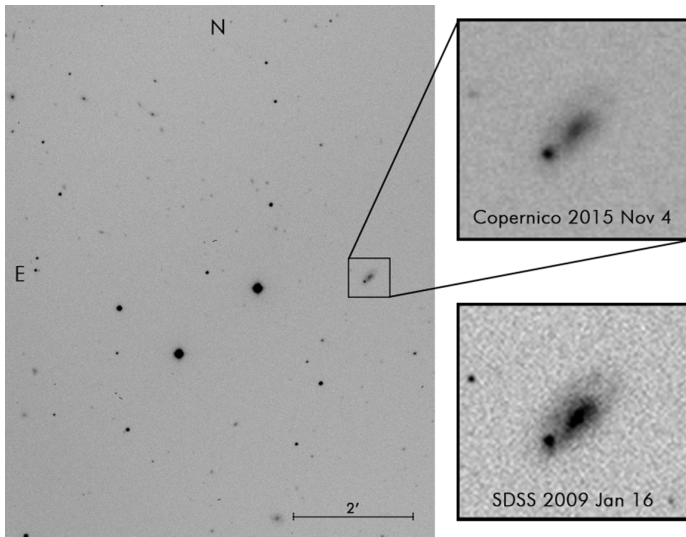
Figure 5.1: Images of the field of iPTF15dld in r-band (exposure time of 120 seconds) taken on 4 November 2015 with the 1.82m *Copernico* telescope (larger panel on the left and enlargement centered on the host galaxy on the top-right smaller panel) and from the SDSS prior to explosion (smaller bottom-right panel, covering the same area as the small top-right panel).

SN, including those preliminarily reported in Tomasella et al. [2015b] and Steele et al. [2015], and additional spectra acquired within the PESSTO program [Smartt et al., 2015]. We adopt 3 October 2015 as the date of explosion, with an uncertainty of one day.

5.1.1   Observations and Data Analysis

Optical photometry and spectroscopy of the SN were acquired at the 1.82m *Copernico* telescope at Cima Ekar (Asiago, Italy), at the Telescopio Nazionale Galileo (TNG), Nordic Optical Telescope (NOT) and Liverpool Telescope (LT, Steele et al. 2004) at the Canary Islands (Spain), at the ESO NTT and 1m Schmidt telescope as part of the PESSTO and LSQ surveys, respectively. UV photometry was taken with the UVOT instrument onboard the *Swift* satellite. The logs of optical photometric and spectroscopic observations are reported in Tables 5.1 and 5.2, respectively. The exposure times were typically 5-10 minutes for the photometry and 20-40 min for spectroscopy. These data were reduced following standard tasks within the IRAF[2] reduction package.

---

[2]IRAF is distributed by the National Optical Astronomy Observatory, which is operated by the Association of Universities for Research in Astronomy (AURA) under a cooperative agreement with

5.1.1.1 Photometry

The *r*-band image of the SN field obtained at the *Copernico* telescope is presented in Figure 5.1. The SN exploded in the outskirts of a spiral galaxy, in a starburst region that is marginally resolved both in our and in the SDSS images ($\sim 2.5''$ angular size) and contaminates dramatically the measurements of the SN in the bluer bands (see Sect. 5.1.2.1).

Given the complex background, the SN magnitudes were measured via template subtraction. For this purpose we used the SNOoPY package[3] developed by one of us (E. Cappellaro): this is a collection of python scripts based on publicly available tools. In particular, for template subtraction we used the "hotpants" package[4]. For the LSQ observations we used images of the field taken by the LSQ in 2012 as subtraction templates; while for the *ugriz* photometry we used SDSS images, which provide a solid estimate of the pre-explosion background. SN magnitudes in the template-subtracted images were measured by PSF fitting. We found PSF fitting is less sensitive to background fluctuations compared with standard aperture photometry. The LSQ images are unfiltered, but close to the *r* filter, therefore the magnitudes resulting from the photometry were converted to this band using a calibrating sequence of field stars.

Starting on 6.97 November 2015, UT and ending on 7.43 November 2015, UT the *Swift* satellite observed the target (see observing log in Table 5.3). The UVOT camera measurements in the optical and UV were reduced according to Brown et al. (2015) and calibrated following Poole et al. (2008) and Breeveld et al. (2010). Aperture photometry with a radius of $5''$ with background estimated from a nearby sky area yielded the magnitudes reported in Table 5.3.

5.1.1.2 Spectroscopy

After bias and flat-field correction, the SN spectra were extracted and wavelength-calibrated through the use of arc lamp spectra. Flux calibration was derived from observations of spectrophotometric standard stars obtained, when possible, on the same night as the SN. Corrections for the telluric absorption bands were derived using telluric standards. In some cases, non-perfect removal can affect the SN features that overlap with the strongest atmospheric features, in particular with the telluric O2 A band at 7590-7650 Å.

In order to subtract the starburst contribution from the SN spectra, we used the

---

the National Science Foundation.

[3]SNOoPy: a package for SN photometry, http://sngroup.oapd.inaf.it/snoopy.html

[4]http://www.astro.washington.edu/users/becker/v2.0/hotpants.html

Table 5.1: Ground-based photometry[a] of iPTF15dld.

MJD	UT	Tel.+instr./Survey	r	i
57284.17	2015 Sep 19.17	LSQ[b]	> 18.8	...
57298.29	2015 Oct 3.29	LSQ	20.2 ± 0.4	...
57300.20	2015 Oct 5.20	LSQ	19.0 ± 0.4	...
57306.17	2015 Oct 11.17	LSQ	18.4 ± 0.4	...
57312.16	2015 Oct 17.16	LSQ	18.4 ± 0.3	...
57318.17	2015 Oct 23.17	LSQ	19.4 ± 0.5	...
57318.98	2015 Oct 23.98	PS[c]	...	18.80 ± 0.04
57319.15	2015 Oct 24.15	LSQ	19.2 ± 0.4	...
57324.13	2015 Oct 29.13	LSQ	20.1 ± 0.5	...
57330.94	2015 Nov 4.94	1.82m+AFOSC	19.9 ± 0.1	19.9 ± 0.2
57332.11	2015 Nov 6.11	LSQ	20.5 ± 0.4	...
57332.87	2015 Nov 6.87	1.82m+AFOSC	20.2 ± 0.09	20.5 ± 0.2
57332.92	2015 Nov 6.92	TNG+LRS	20.0 ± 0.1	...
57333.85	2015 Nov 7.85	1.82m+AFOSC	19.9 ± 0.2	20.4 ± 0.1
57334.10	2015 Nov 8.10	LSQ	20.6 ± 0.4	...
57334.87	2015 Nov 8.87	1.82m+AFOSC	20.0 ± 0.2	20.4 ± 0.1
57338.84	2015 Nov 12.84	1.82m+AFOSC	20.1 ± 0.2	20.7 ± 0.3
57341.92	2015 Nov 15.92	1.82m+AFOSC	20.3 ± 0.2	20.8 ± 0.4
57342.85	2015 Nov 16.85	1.82m+AFOSC	20.4 ± 0.2	20.8 ± 0.2
57344.90	2015 Nov 18.90	1.82m+AFOSC	20.5 ± 0.2	21.1 ± 0.3
57358.82	2015 Dec 2.82	1.82m+AFOSC	20.6 ± 0.2	21.1 ± 0.3
57361.83	2015 Dec 5.83	1.82m+AFOSC	20.8 ± 0.3	> 21.1
57363.83	2015 Dec 7.83	1.82m+AFOSC	20.5 ± 0.3	> 20.7
57366.77	2015 Dec 10.77	1.82m+AFOSC	20.7 ± 0.1	21.5 ± 0.2
57373.76	2015 Dec 17.76	1.82m+AFOSC	21.0 ± 0.2	21.5 ± 0.3
57374.72	2015 Dec 18.72	1.82m+AFOSC	20.8 ± 0.2	> 21.1
57399.83	2016 Jan 12.83	NOT+ALFOSC	21.1 ± 0.1	21.9 ± 0.3

[a] The magnitudes are galaxy-subtracted and not corrected for Galactic extinction.

[b] The La Silla QUEST survey uses the 1m ESO Schmidt telescope at the La Silla Observatory with the 10 square degree CCD camera.

[c] This value was reported in Rabinowitz et al. (2015) from the Pan-STARRS Survey for Transients (Huber et al. 2015).

Table 5.2: Ground-based spectroscopy of iPTF15dld.

MJD	UT	Phase[a]	Telescope	Instrument	grism
57330	2015 Nov 4	19.1	1.82m	AFOSC	gm4
57332	2015 Nov 6	21.0	TNG	LRS	LRS-B
57332	2015 Nov 6	21.0	LT	SPRAT	red
57333	2015 Nov 7	22.0	NTT	EFOSC2	gr13
57342	2015 Nov 16	30.6	1.82m	AFOSC	gm4
57344	2015 Nov 18	32.5	1.82m	AFOSC	gm4
57360	2015 Dec 4	47.8	NTT	EFOSC2	gr13
57373	2015 Dec 17	60.2	LT	SPRAT	red
57374	2015 Dec 18	61.2	LT	SPRAT	red

[a] Phase is given in days with respect to light curve maximum and in rest frame.

template spectra of star-forming galaxies by Kinney et al. [1996]. The best fitting template was chosen by matching the colours of the starburst region as measured on the pre-explosion SDSS images (Table 5.4): this indicated a preference for a template with moderate intrinsic absorption ($0.11 < E_{B-V} < 0.21$, Kinney et al. 1996), as independently indicated also by the UVOT detections in the UV filters. The spectral template was fitted with a low order polynomial (to reduce noise in subtraction); the relative contributions of the starburst and SN components were then determined based on the starburst archival magnitudes and on the template-subtracted SN photometry simultaneous with the spectra, respectively. Finally, the template was reduced to the SN redshift and subtracted from the SN spectra in rest-frame. With this procedure the spectra show some variation in the residual continuum of the blue spectral region, which we attribute to uncertainties in the flux calibration. We allowed for a small adjustment in the template continuum slope (corresponding to ± 0.1 mag variation in E_{B-V}) to ensure all spectra show a similar overall continuum.

5.1.2 Results

5.1.2.1 Host galaxy

The SN is hosted by a compact starburst galaxy/region that, in turn, appears projected over the disc of a spiral galaxy. The narrow emission lines we detected in our spectra (see Sect. 5.1.2.3) indicate that the two objects, starburst and spiral galaxy, are located at the same redshift, although we cannot assess whether they form a unique structure

Table 5.3: *Swift*/UVOT observations of the region of iPTF15dld on 6-7 November 2015[a].

Filter	Expotime (s)	Vega mag[b]	AB mag[b]
v	508.36	17.82 ± 0.08 (stat) ± 0.01 (sys)	17.81 ± 0.08 (stat) ± 0.01 (sys)
b	706.64	18.24 ± 0.05 (stat) ± 0.02 (sys)	18.12 ± 0.05 (stat) ± 0.02 (sys)
u	706.65	17.72 ± 0.05 (stat) ± 0.02 (sys)	18.74 ± 0.05 (stat) ± 0.02 (sys)
$uvw1$	1415.24	17.55 ± 0.04 (stat) ± 0.03 (sys)	19.08 ± 0.04 (stat) ± 0.03 (sys)
$uvm2$	2576.14	17.51 ± 0.03 (stat) ± 0.03 (sys)	19.10 ± 0.03 (stat) ± 0.03 (sys)
$uvw2$	2576.14	17.51 ± 0.03 (stat) ± 0.03 (sys)	19.20 ± 0.03 (stat) ± 0.03 (sys)

[a] Note that these measurements refer entirely to the emission of the starburst region underlying the SN, while the SN itself is undetected at these wavelengths.

[b] Not corrected for Galactic extinction.

or a galaxy pair. The starburst nucleus is a luminous UV source which was detected by GALEX on 8 October 2008 (GALEX source J005813.0-033946) with AB magnitudes FUV = 18.89, and NUV = 18.38, (Kron aperture; note that the NUV band, $\sim$2300 Å, is similar to the uvm2 band of *Swift*/UVOT).

The SDSS magnitudes of the starburst region at the location of the SN are reported in Table 5.4. Note that the half-magnitude offset in the measurements obtained with different photometric apertures does not affect significantly the colours. The u-band magnitude obtained with the $5''$ radius aperture, $u = 19.1$ mag, is consistent with the AB magnitude measured by UVOT in the U-band (Table 5.3). This and the lack of UV flux variability suggest that the source detected by UVOT is dominated by the emission of the starburst region, so that the UV emission of the SN is undetectable. At a distance of 200 Mpc, the starburst component has an absolute magnitude in g-band of -18.5 mag, which places it at the bright end of the blue compact dwarf luminosity function [Tolstoy et al., 2009].

Figure 5.2 shows a stellar population synthesis model to estimate the age of the stellar population in the vicinity of the SN from the observed colours [Brocato et al., 2000; Raimondo, 2009]. The model assumes solar metallicity and ages comprised between 1 and 500 Myr. By correcting the starburst colours – adopting the circumstellar Large Magellanic Cloud extinction law of Goobar [2008] as in Brown et al. [2010] – for moderate values of intrinsic extinction (from null to $E_{B-V} = 0.35$, i.e. somewhat higher than the maximum intrinsic extinction of the assumed star-forming galaxy template, $E_{B-V} = 0.21$), in addition to the Galactic one ($E_{B-V} = 0.027$), we obtain the intrinsic colours reported in Figure 5.2 as filled blue squares. The colour resulting from maximum correction is consistent with a population age of 10 Myr, which corresponds to the evolution time of a 20 M$_\odot$ star. The use of an extinction curve more suitable for hot stars [Siegel et al., 2014] leads to a similar conclusion.

This satisfactory match indicates the presence of a young massive star population, consistent with the explosion of a massive stellar core that has evolved from a main sequence mass of $\sim$20 M$_\odot$ (see Section 5.1.3). We note that a Milky Way extinction curve only provides a match with the starburst colors if the intrinsic extinction is as high as $E_{B-V} = 0.8$, which is inconsistent with the observed colours of the starburst and indicates that this region presents the characteristics of a more rapidly star-forming, lower metallicity, less evolved environment than our Galaxy. In fact, the star-formation rate of $\sim$1 M$_\odot$ yr^{-1} derived by Palliyaguru et al. [2016] from radio excess detection within a region a few kpc across, spatially compatible with the UVOT source, points to an explosion site of high star formation rate per unit mass. This is typical for stripped-envelope SNe [Anderson et al., 2012; Crowther, 2013], expected to be predominantly
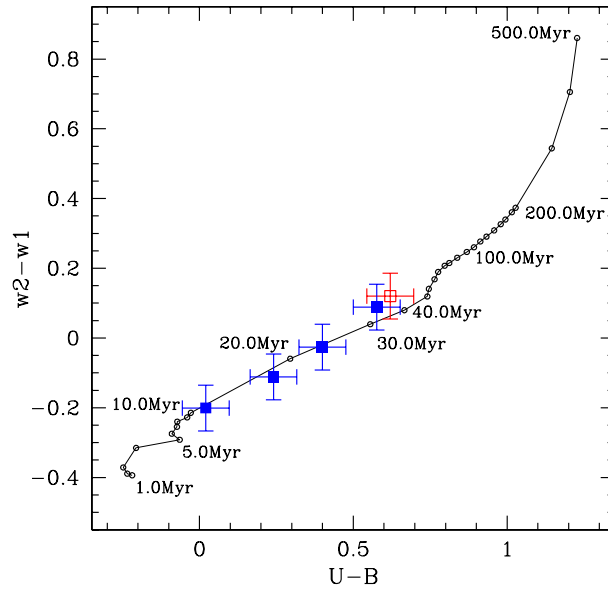
Figure 5.2: Stellar synthesis diagram for the starburst region underlying iPTF15dld.
Ages of the stellar populations along the diagram are indicated. The squares represent
the observed (empty red) and de-reddened (filled blue) colours of the starburst, ob-
tained from the magnitudes reported in Table 5.3 by correcting for different amounts
of internal absorption (E_{B-V} = 0.027, 0.137, 0.237, 0.377 mag) and using the circum-
stellar Large Magellanic Cloud extinction law with no red-tail-corrected coefficients of
Brown et al. (2010; see their Table 1). For maximum extinction (E_{B-V} = 0.377 mag),
the starburst is compatible with an age of 10 Myr, equivalent to the lifetime of a 20
$M_\odot$ star.

associated with bright regions of massive and rapid star formation, which could make
their detection systematically more arduous at large distances even with the biggest
telescopes.

Table 5.4: Magnitudes[a] of the starburst region.

Filter[a]	5″-radius	3″-radius
u	19.09	19.60
g	18.03	18.59
r	17.77	18.43
i	17.50	18.26
z	17.46	18.22

[a] in the SDSS system, not corrected
for Galactic extinction.

5.1.2.2 Light curves

The r- and i-band magnitudes of the point-like SN source, derived with PSF fitting from the background-subtracted images (see Section 5.1.1.1), are reported in Table 5.1 and, after correction for Galactic absorption (using $A_V = 0.085$, Schlafly & Finkbeiner 2011, and the extinction curve of Cardelli, Clayton & Mathis 1989), in Figure 5.3. We have not corrected for intrinsic extinction within the starburst region because we cannot estimate how much this influences the SN emission (it depends on the relative position of the SN and starburst with respect to the observer) and we have no evidence that iPTF15dld is significantly absorbed in its rest-frame. In fact, its $R - I$ color, computed from the r- and i-band light curves, is comparable to that of well-monitored SNe Ic close to maximum luminosity [Ferrero et al., 2006; Foley et al., 2003; Galama et al., 1998; Hunter et al., 2009; Patat et al., 2001; Richmond et al., 1996; Taubenberger et al. , 2006; Valenti et al. , 2008a,b], and possibly bluer at later times, likely owing to significant background still affecting the weaker r-band flux. No detection of iPTF15dld was obtained with the ugz filters in individual exposures. The magnitudes from the co-added exposures in these filters are consistent with the SDSS measurements.

The r- and i-band light curves of iPTF15dld were compared with those of SN 2007gr, a type Ic SN of "classical" spectral appearance, i.e. with no broad absorption lines [Hunter et al., 2009; Valenti et al. , 2008b]. At $z = 0.047$, the central wavelengths of the r- and i-band filters correspond to 5980 Å and 7328 Å, respectively. From the VRI light curves of SN 2007gr we have constructed template light curves at those two reference wavelengths and reported them in Figure 5.3, after brightening the template at 5980 Å by 0.7 magnitudes. With the exception of the first i-band point, which is significantly brighter, the match with the templates is generally satisfactory, and it indicates that iPTF15dld is a factor of $\sim$2 brighter at $\sim$6000 Å and therefore bluer
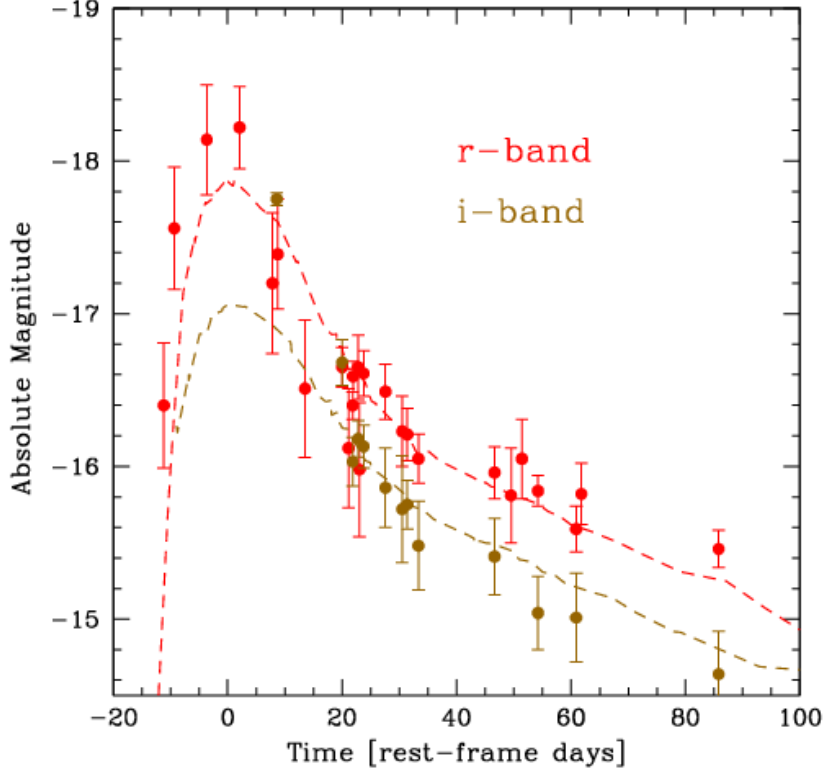
Figure 5.3: Light curves of iPTF15dld in r-band (red circles) and i-band (brown circles), corrected for Galactic extinction ($A_V = 0.085$). At $z = 0.047$, the central wavelengths of these bands correspond to 5980 Å and 7328 Å, respectively. The time origin corresponds to the maximum of the r-band light curve. For comparison, we overlaid the light curves of the type Ic SN 2007gr at identical reference wavelengths (dashed curves; see text for the construction of these templates). The "r-band"-equivalent template of SN 2007gr was brightened by 0.7 magnitudes for best match with iPTF15dld.

than SN 2007gr in the 6000-8000 Å range.

Although the available photometry (r- and i-band only) is not sufficient to construct a proper pseudo-bolometric light curve, the total spectral flux is a rough proxy of the bolometric behavior. For each spectrum, we integrated the flux-calibrated, dereddened spectral signal in the rest-frame, approximately corresponding to the range 3800-7800

Å (see Fig. 5.5) and obtained a bolometric light curve that is similar in shape to those of the faintest stripped-envelope SNe that were monitored long enough to allow a comparison with iPTF15dld (SNe 1994I, 2002ap) and in particular to that of SN 2007gr (see Hunter et al. 2009). Since our pseudo-bolometric estimate does not include the near-UV and near-infrared contributions, we have estimated this using other SNe Ic that have good photometric coverage in these bands simultaneous with the optical. At epochs comparable to those of the iPTF15dld photometry, the near-UV and near-infrared fluxes of type SNe Ic combined represent about 40-50% of the total flux in 3000-24000 Å (e.g. SN 1998bw, Patat et al. 2001; SN 2004aw, Taubenberger et al. 2006; SN 2007gr, Hunter et al. 2009). Even taking this into account, iPTF15dld is still less luminous than the average of stripped-envelope SNe (Fig. 5.4).

5.1.2.3   Spectra

The two spectra taken at the 1.82m *Copernico* telescope on 16 and 18 November 2015 were averaged, owing to their closeness in time and similarity, and so were the two spectra acquired at the LT with SPRAT on 17 and 18 December 2015. Six final spectra, corrected for Galactic extinction and redshift, are reported in Figure 5.5. The SPRAT spectrum of November 6 was not shown because it is very close in time to the TNG spectrum and of lower signal-to-noise ratio. The starburst dominates the spectral emission with a blue continuum and narrow emission lines. However, when its contribution is removed (see Section 5.1.1.2), the broad lines typical of SNe Ic become visible in the visual/red spectral regions. No hydrogen nor helium absorption lines are seen, indicating a high degree of envelope stripping and leading to type Ic classification of the SN. The narrow emission lines from the underlying starburst region were removed.

In search of a close spectral analogue of iPTF15dld, we compared its spectra with those of eight type Ic SNe, both broad- and narrow-lined (SN 1994I, Filippenko et al. 1995; Richmond et al. 1996; Millard et al. 1999; SN 1997ef, Iwamoto et al. 2000; Mazzali et al. 2000; SN 1998bw, Patat et al. 2001; SN 2002ap, Gal-Yam et al. 2002; Mazzali et al. 2002; Foley et al. 2003; SN 2003jd, Valenti et al. 2008a; SN 2004aw, Taubenberger et al. 2006; SN 2006aj, Mazzali et al. 2006; SN 2007gr, Hunter et al. 2009). With the partial aid of a χ^2-minimization routine we selected the spectra of our SN templates that best-matched, in the 4000-7500 Å wavelength range, those of iPTF15dld at comparable phases after light curve maximum.

SNe 1998bw and 2006aj, that were associated with GRBs [Campana et al., 2006; Galama et al., 1998; Pian et al., 2000; Pian et al., 2006], do not compare well with
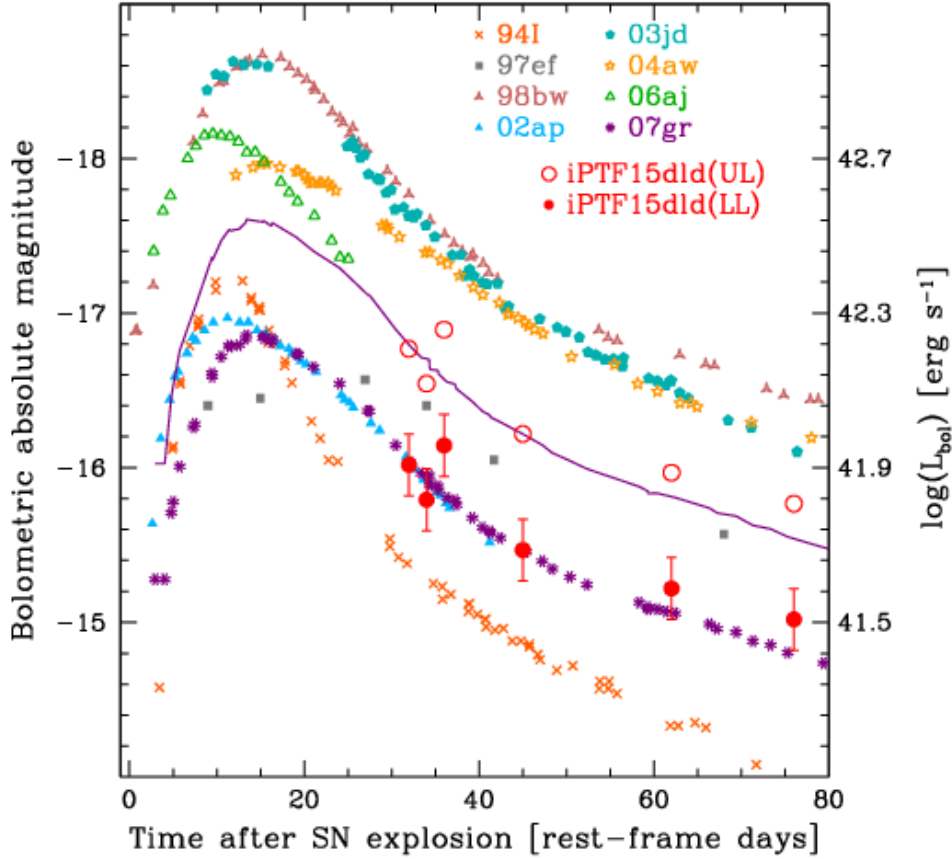
Figure 5.4: Pseudo-bolometric (UVOIR) light curves of stripped-envelope SNe. The curve of iPTF15dld was obtained by integrating the spectral flux in its rest-frame (filled red points). Since this covers a limited wavelength range ($\sim$3800-7800 Å), it is likely a lower limit (LL) on the UVOIR light curve, and a correction of a factor of 2 was applied to take into account the flux in a broader range (3300-24000 Å), based on the ratio of broad-band optical and near-infrared fluxes in SNe 1998bw, 2004aw, 2007gr. These corrected pseudo-bolometric luminosities, that can be considered an upper limit (UL) on the UVOIR light curve, are reported as open red circles. The errors on the iPTF15dld luminosities are estimated to be $\sim$20%. For clarity, the errors on the bolometric luminosities of all other SNe were omitted (the data for these are from Iwamoto et al. 2000; Ferrero et al. 2006; Hunter et al. 2009, and references therein; the data of SN 1997ef were corrected for the different value of the Hubble constant adopted here). The purple curve represents the bolometric light curve of SN 2007gr brightened by 0.75 mags.
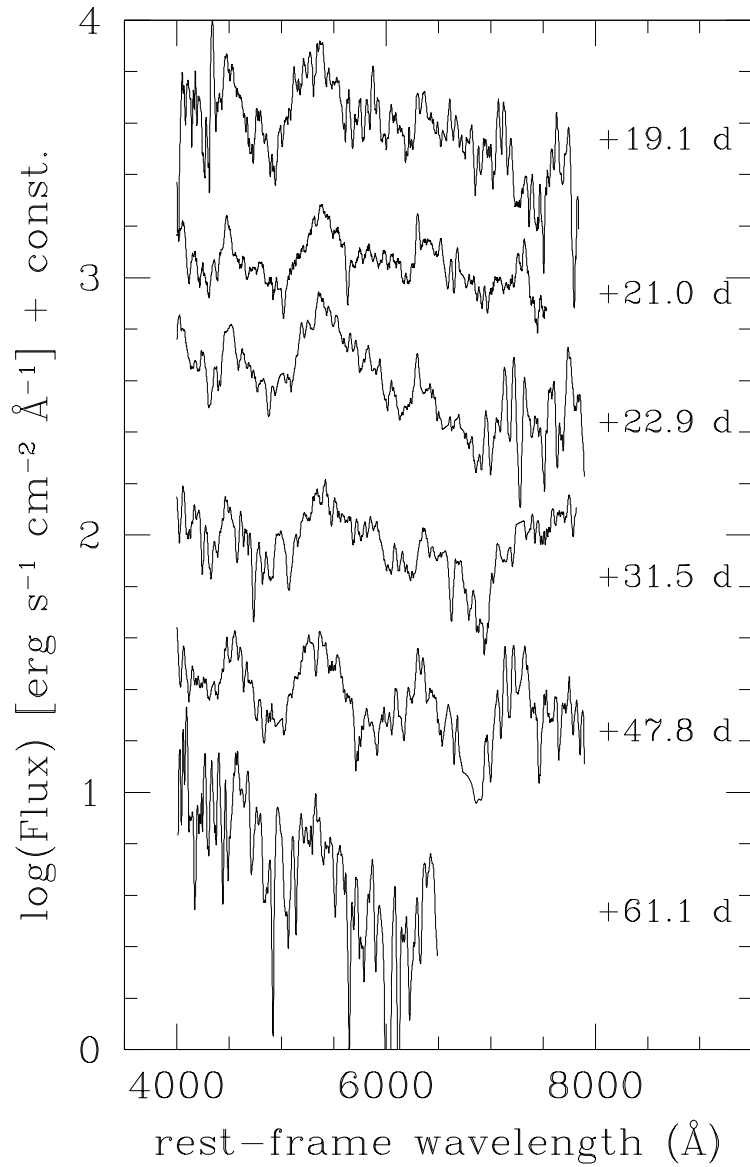
Figure 5.5: Spectra of iPTF15dld in rest frame, corrected for Galactic extinction ($A_V =$ 0.085), smoothed with a boxcar of 50 Å and arbitrarily scaled in flux. The phases are given in rest-frame, with respect to maximum luminosity.

iPTF15dld because their spectra have significantly broader absorption lines (although in the case of SN2006aj only one spectrum overlaps in phase). On the other hand, the classical SNe 1994I and 2007gr represent an equally unsatisfactory match because they have narrower lines than our target. The first four spectra of iPTF15dld are more similar to those of SNe 1997ef, 2002ap, 2003jd and 2004aw, that are broad-lined Ic SNe with no accompanying GRB (see also Corsi et al. 2016). These have kinetic energies higher than seen on average in SNe Ic, although they are not as massive nor as luminous as GRB SNe. The last spectra (December 2015) resemble both broad- and narrow-lined Ic SN spectra, presumably because they are more noisy and at those epochs (∼50-60 rest-frame days after maximum), the photospheric velocities have significantly decreased also in broad-lined SNe. In Fig. 5.6 and 5.7 we show two examples of spectral comparison.

While the signal-to-noise ratio of the spectra and the partial blending of absorption lines, due to their width, makes it difficult to isolate the chemical species and measure their associated velocities, the similarity with broad-lined SNe suggests higher-than-normal photospheric velocities.

5.1.3 Discussion

The light curve of iPTF15dld resembles that of normal, narrow-lined type Ic SNe, with SN 2007gr (Hunter et al. 2009) providing an excellent match (Fig. 5.3). However, the photospheric absorption lines are broad, so this is classified as a broad-lined Ic SN, rather similar to well-monitored broad-lined SNe Ic at comparable epochs after light maximum (SNe 1997ef, 2002ap, 2003jd, 2004aw). Since spectra were taken only starting 20 days after maximum, we cannot make an assessment of the photospheric velocity before and around maximum; similarly, the photometric information does not allow us to construct a pseudo-bolometric light curve covering the epoch of maximum luminosity. As a consequence, our estimates of the physical parameters are only approximated.

In absence of synthetic light curve and spectra based on a detailed radiative transfer model obtained from observed quantities, the basic SN physical parameters can be derived by rescaling those of other well studied SNe using the fundamental relationships of Arnett [1982], as done for instance in Corsi et al. [2012]; D'Elia et al. [2015]; Mazzali et al. [2013]; Walker et al. [2014]. However, iPTF15dld lacks an estimate of both its light curve width, τ, and its photospheric velocity at maximum luminosity, v_{ph}. Therefore, our estimate of its kinetic energy and ejecta mass can only be based on an average of these parameters for the five SNe that provide the best light curve and spectral match
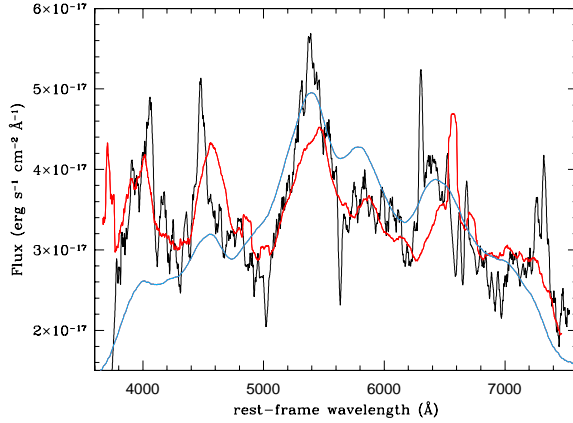
Figure 5.6: Spectrum of iPTF15dld of 6 November 2015 (black) dereddened with $A_V = 0.085$ compared with those of SN 1997ef (red) and SN 1998bw (blue) at comparable rest-frame phases. The spectrum of SN 1998bw was dereddened with $A_V = 0.16$, while that of SN 1997ef needs no absorption correction. All spectra were smoothed with a boxcar of 50 Å. The absorption lines of SN 1998bw are significantly broader than those of iPTF15dld, while those of SN 1997ef represent a better match.

(see Section 5.1.2.3).

From the physical parameters estimated for SNe 1997ef, 2002ap, 2003jd, 2004aw and 2007gr, [Hunter et al., 2009; Iwamoto et al., 2000; Mazzali et al. , 2000, 2002; Taubenberger et al. , 2006; Valenti et al. , 2008a] we derive ranges of [1-18] $\times 10^{51}$ erg and [2-10] $M_\odot$ for the kinetic energy and ejecta mass of iPTF15dld, respectively. Since the shape and luminosity of the bolometric light curve suggest that iPTF15dld could have been similar to SN 2007gr or up to a factor of 2 more luminous at peak,
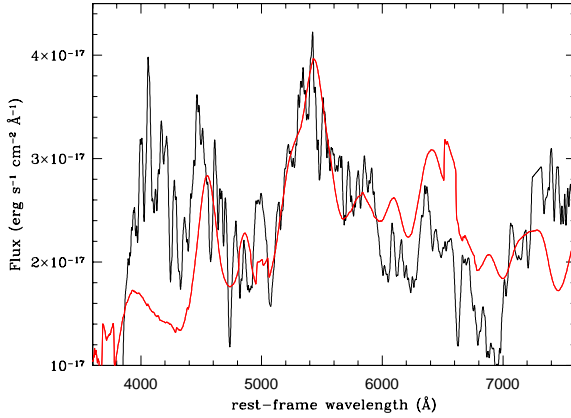
Figure 5.7: Spectrum of iPTF15dld of 17 November 2015 (black) dereddened with $A_V = 0.085$ compared with that of SN 2003jd (red) at comparable rest-frame phase, dereddened with $A_V = 0.43$. All spectra were smoothed with a boxcar of 50 Å.

we accordingly estimate that the mass of radioactive ^{56}Ni synthesized in the explosion may be in the interval [0.08-0.2] $M_\odot$. These values are consistent with a progenitor of main sequence mass of the order of $\sim$20-25 $M_\odot$. A dedicated accurate model is not completely justified by the limited quality of these data.

Broad-lined Ic SNe of modest luminosity are a rather uncommon and poorly known class, and have started to be detected in larger numbers thanks to dedicated surveys. As GRB SNe, that are significantly more massive and luminous, they may be partially powered by an inner engine, i.e. an unusual type of remnant, like a magnetar or a black hole. The prototype of this sub-class is SN 2002ap [Mazzali et al. , 2002], for which evidence had been found of a small fraction of ejected material accelerated to velocities

larger than 30000 km s^{-1}. Since these objects have low ejecta mass (their synthesized ^{56}Ni mass is small), the total kinetic energy is also not extremely large ($\sim 10^{51}$ erg), but the high photospheric velocities suggest a powerful engine. Whether these are the progenitors of GRBs that are misaligned with respect to the line of sight and therefore go undetected, or they represent a population of intermediate properties between classical, narrow-lined SNe Ic and GRB SNe, is matter of controversy [Maeda et al., 2008; Mazzali et al., 2005; Pignata et al., 2011; Soderberg et al., 2010]. Clarification of this issue [e.g., through late-epoch radio observations, van Eerten & MacFadyen, 2011] may lead to a simplification of the apparent diversity of stripped-envelope SNe. We note that the opposite, i.e. low photospheric velocities in highly luminous SNe are never observed [e.g., Mazzali et al., 2013].

The case of iPTF15dld shows how optical surveys that cover large areas of the sky with good cadence using classical facilities can improve dramatically the study of a broad range of transients. Early detection and decent monitoring of objects with a variety of properties will fill gaps present in the current information and unify seemingly different phenomena.

5.2 ATLAS17aeu and GW 170104/GRB 170105A

On January 4, 2017 at 10:11:58.6 UTC the Advanced LIGO detectors revealed the signal from a binary black-hole coalescence, GW 170104 [Abbott et al., 2017a]. The system was made of two black-hole of masses $31.2^{+8.4}_{-6.0}$ M$_\odot$ and $19.4^{+5.3}_{-5.9}$ M$_\odot$ (at the 90% confidence level) at a luminosity distance of 880^{+450}_{-390} Mpc corresponding to a redshift of $z = 0.18^{+0.08}_{-0.07}$ [Abbott et al., 2017a]. An alert with an initial source localization ($\sim$ 1600 deg^2 at the 90% confidence level) was distributed to collaborating astronomers [LIGO/Virgo Scientific Collaboration, 2017c]. During the electromagnetic counterpart follow-up search, the ATLAS and Pan-STARRS surveys discovered ATLAS17aeu [Tonry et al., 2017], 23.1 hr after GW 170104, which was a rapidly fading transient within the inner 16% sky-localization probability contour (see Fig. 5.8). The transient, with a decay similar to a GRB afterglow, was also detected in X-rays by *Swift* and in the radio at 6 and 15 GHz by the VLA and the AMI large array, respectively Corsi et al. [2017]; Evans et al. [2017a,b]; Mooley et al. [2017a].

By fitting a power law to the optical decay, the time zero was found consistent with the gamma-ray burst GRB 170105A [Kasliwal et al. , 2017] detected by the POLAR instrument onboard the Chinese space laboratory Tiangong-2 [Marcinkowski et al., 2017], *AstroSat*-CZTI [Sharma et al., 2017], *Konus*-Wind, and *INTEGRAL*-SPIACS [Svinkin et al., 2017] 20.04 hr after GW 170104. Temporal and spatial consistency led to

the conclusion that ATLAS17aeu was the afterglow of GRB 170105A and unrelated to GW 170104 [Bhalerao et al., 2017b]. Considering all the multi-wavelength observations of ATLAS17aeu, Stalder et al. [2017] concluded that the GRB 170105A is compatible with a classical long-GRB at redshift $1 \lesssim z \lesssim 2.9$ and that ATLAS17aeu is statistically likely the associated afterglow. However, they evaluated a small but non-negligible probability of association of ATLAS17aeu and the GW signal, which only a direct redshift measurement of the host galaxy of ATLAS17aeu could exclude.

We present optical observations of ATLAS17aeu transient and its possible host galaxy taken with the 1.8-m Asiago Copernico telescope, the 3.6-m Telescopio Nazionale Galileo (TNG), the 8.4-m Large Binocular telescope (LBT), the 10.4-m Gran Telescopio Canarias (GTC), and the *Hubble Space Telescope* (*HST*) over 230 days from the GRB 170105A trigger time. Together with the radio and X-ray observations, the connection between the transient ATLAS17aeu and the long gamma-ray burst GRB 170105A is discussed.

Throughout the section, distances are computed assuming a Λ CDM-Universe with $H_0 = 71$ km s^{-1} Mpc^{-1}, $\Omega_m = 0.27$, and $\Omega_\Lambda = 0.73$ [Komatsu et al., 2011; Larson et al., 2011]. Magnitudes are in the AB system and errors are at a 1σ confidence level.

5.2.1   ATLAS17aeu

The rapidly fading transient ATLAS17aeu [Tonry et al., 2017], identified within the localization of GW 170104 [LIGO/Virgo Scientific Collaboration, 2017c], was only $20''$ away from the SDSS galaxy J091312.36+610554.2, with a spectroscopic redshift ($z \sim 0.2$) consistent with the distance inferred for GW 170104. Considering this galaxy as possible host of ATLAS17aeu, the position and distance consistency of ATLAS17aeu and GW 70104 led to many multi-wavelength observations to probe the possible association of ATLAS17aeu with the gravitational signal.

Within the GRAWITA[5] framework, we monitored the light curve of the source between 1.65 and 88.7 days after the GRB trigger with the Asiago and TNG telescopes. In addition, we obtained two multi-filters epochs ($griz$) with the GTC telescope between 3.92 and 78.7 days after the GRB trigger. Finally, we observed the field with the LBT telescope in imaging mode (gri) at ~ 104 days after the gamma-ray burst trigger, GRB 170105A. Image reduction was carried out following standard procedures and the optical data were calibrated using a common set of selected catalogued stars of the SDSS catalog present in the field of view.

Two spectra were also acquired with the GTC telescope, one at ~ 3 days and a

---

[5]GRAvitational Wave Inaf TeAm: https://www.grawita.inaf.it/
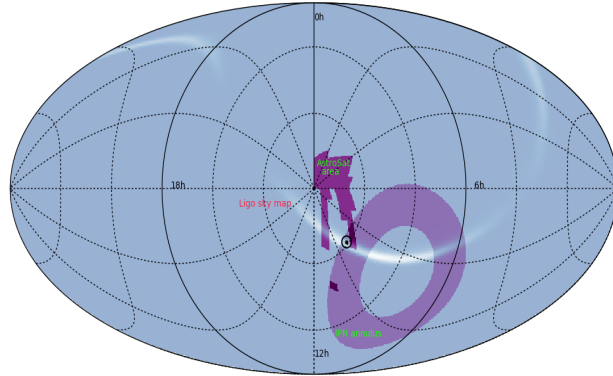
Figure 5.8: The mollweide projection for localisation area of ATLAS17aeu (black circle). We report the AstroSat CZTI localisation area (dark purple) at 1σ confidence level and the IPN triangulation annulus (light purple) at 3σ confidence level for GRB 170105A. The final LVC sky map for GW 170104 is shown in white.

second one secured at ~ 116 days after the burst event. GTC spectroscopy was carried out using the OSIRIS camera in slit mode, with the R1000B ($R = 1000$, spectral range $3630 - 7500$ Å) and R2500I ($R = 2500$, spectral range $7330 - 10000$ Å) grisms. The slit width was set to $1''$. The data were optimally extracted [Horne , 1986] and reduced following standard procedures using ESO MIDAS[6] and IRAF[7] software.

In addition, three further optical spectra were collected on April 14, 2017, on January 25, 2018, and on March 19, 2018 with LBT, using the two Multi-Object Double Spectrograph [MODS, Pogge et al., 2010]. All observations were obtained in the spectral range $3200 - 9500$ Å with a $1''$ slit ($R \sim 2000$). MODS uses two red- and blue-optimized channels with a spectral range of $3500 - 6500$ Å and $5000 - 10000$ Å, respectively. The first two epochs were taken with the one grating for each channel which has the advantage to avoid a gap at ~ 5650 Å between the two channels but doubles the observing time. Therefore, the last epochs were taken with the dual grating mode in which the light is separated by a dichroic into red- and blue-channels. A 2x2 binning was set in the second epoch, but it caused read-out artifacts and thus in the final epoch we adopted a 1x2 binning. The last observation was obtained under the best conditions (seeing ~ 0.7 arcsec, airmass $1.1 - 1.2$) for a total exposure time of 4800 s. Data reduction was performed at the Italian LBT Spectroscopic Reduction

---

[6]http://www.eso.org/projects/esomidas/

[7]http://iraf.noao.edu/

Center[8] by means of scripts optimized for LBT data. Steps of the data reduction of each two-dimensional spectral image are the correction for dark and bias, bad-pixel mapping, flat-fielding, sky background subtraction, and extraction of one-dimensional spectrum by integrating the stellar trace along the spatial direction. Wavelength calibration was obtained from the spectra of arc lamps, while calibration was obtained using catalogued spectrophotometric standards.

The location of ATLAS17aeu was subsequently observed with the *HST*-WFC on August 22, 2017 (~ 229 days after the burst event). At this point, observations were obtained in the UVIS arm F390W, F606W and the IR arm with F140W[9]. Observations were reduced by `astrodrizzle` in the standard fashion. At the location of ATLAS17aeu, we clearly detect a source in both F606W and F140W, but there is no detection in F390W (Fig. 5.10). The position of the ATLAS17aeu transient is RA = 09:13:13.89, Dec = +61:05:32.54 with an error of 0.06 arcsec .

For our UVIS observations, we measure the AB magnitudes (or upper limits) within a 0.1 arcsec aperture and correct them with the published encircled energy curves[10]. We determine that F390W> 28.1 mag (3σ) and F606W$=27.64 \pm 0.21$ mag. In the IR we use a 0.2 arcsec aperture due to the poorer PSF, and measure F140W$=25.87 \pm 0.14$ mag. There is no sign of extension in the images, and the sources appear point-like. However, at this faint magnitude the detection of extension is challenging. We consider the source located S-E with respect to ATLAS17aeu as its host galaxy. The separation between the two objects is ~ 1.8 arcsec (Fig. 5.10).

The summary of our photometric and spectroscopic observations is reported in Tables 5.5 and 5.6, respectively. Data have not been corrected for Galactic extinction [$E_{B-V} = 0.028$ mag, Schlafly & Finkbeiner, 2011].

5.2.2   GRB 170105A

GRB 170105A was detected at 06:14:07.0 UT (T_0, corresponding to MJD=57758.259803) with a total duration $T_{90} = 2.0 \pm 0.5$ s. The burst event was also detected by *INTEGRAL*-SPIACS, *Konus*-Wind, and *AstroSat*-CZTI [Sharma et al., 2017] with a measured duration $T_{90} \sim 2.9$ s. Its fluence derived from the *Konus*-Wind observation is $S_{[0.02-10 \text{ MeV}]} \sim 2.5 \times 10^{-6}$ erg cm^{-2} and it displayed longer emission (with a duration

---

[8]http://www.iasf-milano.inaf.it/Research/lbt_rg.html

[9]HST observations have been cross-calibrated with the g, r, and J bands, respectively.

[10]`http://www.stsci.edu/hst/wfc3/phot_zp_lbn`
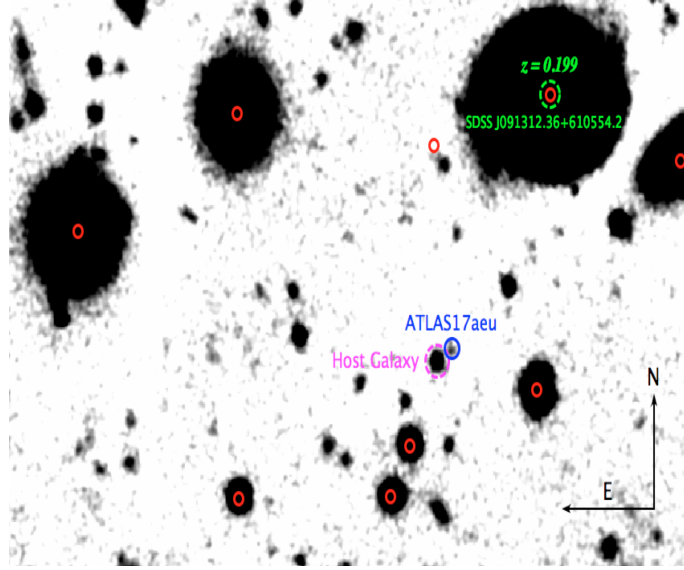
Figure 5.9: TNG image (field of view $\sim 1' \times 1'$) acquired at $\Delta t \sim 56$ days, in the r filter. The ATLAS17aeu position (blue circle) is $\sim 2''$ away from the centre of its host galaxy (magenta circle). The cataloged SDSS objects (red circles), including the J091312.36+610554.2 galaxy at $z \sim 0.2$ (green circle), are shown.

of about 20 seconds) in the 18-70 keV soft channel of *Konus*-Wind [Stalder et al., 2017; Svinkin et al., 2017].

In Fig. 5.8 we show the localisation areas (*AstroSat* and IPN) for this event, together with the LVC sky map for GW 170104 and the most accurate position for ATLAS17aeu. As it can be seen ATLAS17aeu is slightly outside the 1σ *AstroSat*/CZTI localisation area, well within the LVC probability contours. The temporal and spatial coincidence between ATLAS17aeu and GRB 170105A indicated that the two events were most likely associated [Bhalerao et al., 2017a,b; Kasliwal et al. , 2017] while it remained unclear the association with the GW 170104 due to the lack of a firm ATLAS17aeu distance determination.

The GRB 170105A fluence is consistent with a long-soft, under-energetic GRB. In fact, assuming the distance inferred for GW 170104 ($z \sim 0.1$) the estimated isotropic energy of the GRB event would be $E_{iso} \sim 5.8 \times 10^{49}$ erg, and at larger distances up to $z \approx 1$, the isotropic energy remains still consistent with the faint end of the E_{iso} distribution for long GRBs [D'Avanzo et al., 2012; Nava et al., 2012].
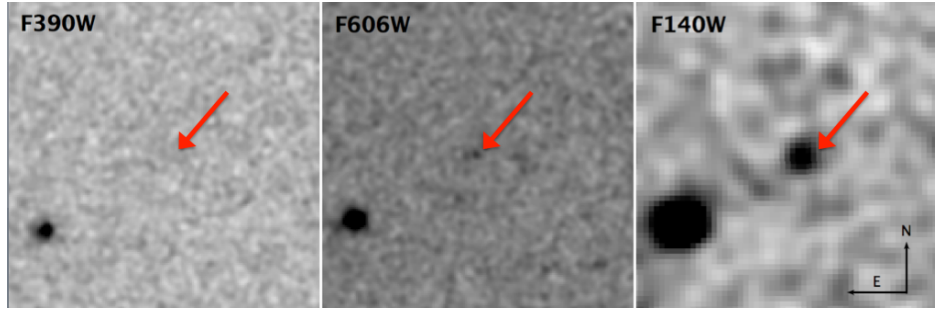
Figure 5.10: HST observations of the field of ATLAS17aeu (field of view = 5arcsec ×
5arcsec). The red arrow indicates the location of the optical transient. The other object
visible in that image is what we consider the host galaxy of ATLAS17aeu, reported
also in Fig. 5.9. The offset between the two objects is ∼ 1.8 arcsec.

5.2.3   Temporal analysis

The early time optical light curve of ATLAS17aeu (Fig. 5.11) can be described by a
single power-law decay ($\alpha_r = 1.38 \pm 0.02$). At a later time (> 10 days) a significant
deviation from that decay is detected, unveiling the presence of a possible supernova
component (Fig. 5.11).

   Many known under-energetic long-duration gamma-ray bursts and X-ray flashes
have an associated highly stripped-envelope core-collapse supernova (Type Ib/c). At
low redshifts ($z \lesssim 0.3$) the supernova component is well identified both photometrically
and spectroscopically [Bufano et al., 2012; Cano et al., 2011a; D'Elia et al., 2015; Ferrero
et al., 2006; Galama et al., 1998; Hjorth et al., 2003; Malesani et al., 2004; Melandri et
al., 2012, 2014; Patat et al., 2001; Pian et al., 2006; Schulze et al., 2014], while at higher
redshifts ($0.3 \lesssim z \lesssim 1$) the presence of the supernova is inferred from the detection
of a re-brightening in the late afterglow light curve [Bloom et al., 1999; Cano et al.,
2011b; Castro-Tirado & Gorosabel, 1999; Castro-Tirado et al., 2001; Della Valle et al.,
2003, 2006; Galama et al., 2000; Greiner et al., 2003; Jin et al., 2013; Soderberg et al.,
2010; Sparre et al., 2011; Zeh et al., 2004]. The supernova origin for the re-brightening
observed in the afterglows of high-z GRBs is further sometime enhanced by sporadic
spectroscopic observations of the "bumps" which reveal supernova features [e.g. Jin et
al., 2013]. Our Fig. 5.11 shows a faint optical light curve of ATLAS17aeu suggesting
$z > 0.3$ and the signature of an emerging supernova which starts to outshine the GRB
afterglow from ∼10-12 days.

   In order to have additional information about the possible SN component we
rescaled the absolute r-band magnitudes of ATLAS17aeu to the distance of several

well-known Type Ib/c SNe, and compared our data with their light curves that cover a wide range of brightness (Fig. 5.12). This results in a possible range of distances that can explain the observed late time afterglow re-brightening ($0.28 \leq z \leq 0.72$) of ATLAS17aeu. The best match is obtained with SN 1998bw (a typical Type Ib/c SN associated with the sub-luminous gamma-ray burst GRB 980425) assuming a redshift of $z \sim 0.6$ (see Fig. 5.11). We note that even in the case of the match with the brightest known SN associated with a GRB (SN 2003lw) we obtain $z \sim 0.7$. The hypothesis of a higher redshift would require a much more luminous SN, that has never been observed in association with a long GRB.
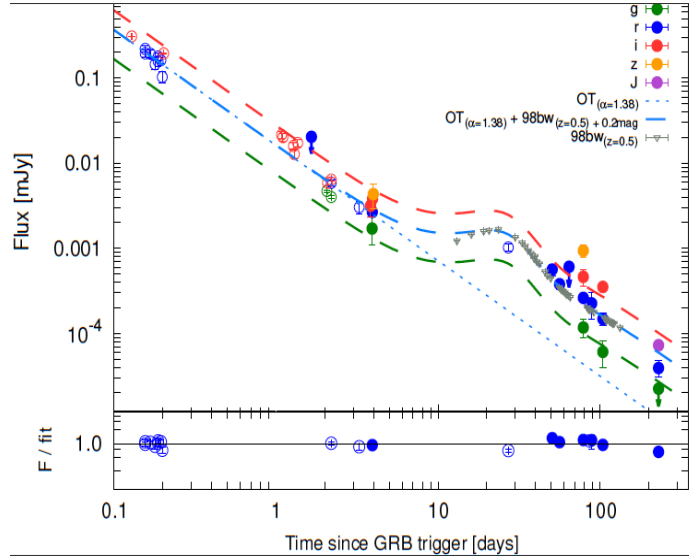
Figure 5.11: The optical light curve for ATLAS17aeu. Filled points identify our data while empty symbols are data from the literature. The power-law decay of the optical afterglow (blue dashed line) and the SN 1998bw (gray open triangles) template at z=0.5 are shown. The overall fit to the light curve, assuming SN 1998bw as a template (fainter by 0.2 mag) is shown with blue solid dashed line. The overall fit is then shifted arbitrarily to guide the eye and match the g (green solid dashed line) and i (red solid dashed line) band data.

5.2.4 Spectral analysis

To investigate the possible connection between ATLAS17aeu and GRB 170105A, the early time spectrum obtained with GTC was compared with several Type Ib/c supernova templates. A good match is found with the Type Ic SN 2003jd [Valenti et al. ,

2008a], reproducing well the overall shape of the spectrum. A satisfactory comparison is also obtained with SN 2006aj [Mirabal et al., 2006; Pian et al., 2006; Sollerman et al., 2006], a well-studied supernova (Fig. 5.13) associated with an under-energetic long-duration GRB 060218 [Campana et al., 2006]. Our analysis showed a possible supernova (SN) signal if a redshift $z \sim 0.6$ is assumed.

A similar value for the redshift is also found when comparing the late time LBT spectrum of the host galaxy with the template of a star-forming galaxy, by identifying several Balmer transitions at redshift $z \sim 0.623$. The red region of the spectrum (which is the one with the higher signal-to-noise ratio) shows a correspondence between the observed lines (Hη, H&K, Hδ and Gband+Hγ+Fe4383 Å) and the model. These spectral comparisons indicated a plausible redshift for ATLAS17aeu of $z \sim 0.6 \pm 0.1$.
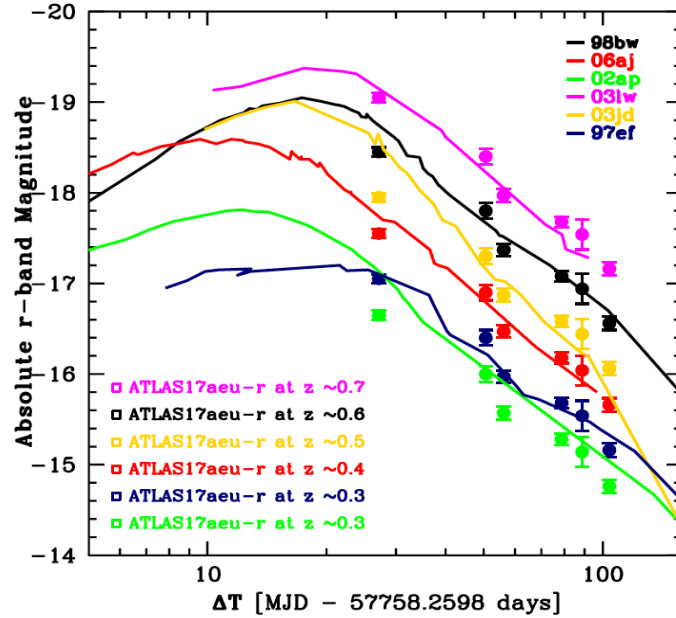
Figure 5.12: Comparison between the absolute r-band magnitudes of several well known Type Ib/c SNe and ATLAS17aeu observations. Times are days since GRB 170105A trigger time and magnitudes have been k-corrected. From the match with each SNe light curve we estimated the possible distance modulus (DM) of ATLAS17aeu and infer the possible range of redshifts ($0.3 \leq z \leq 0.7$) for the transient.
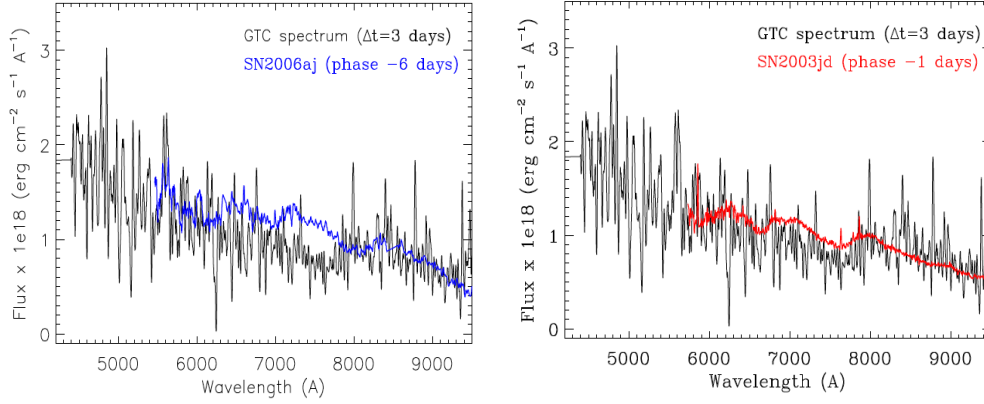
Figure 5.13: *Left*: Comparison between the early time GTC spectrum of ATLAS17aeu and the template (assuming a redshift $\sim 0.6 \pm 0.1$) of the well-studied Type Ib/c SN 2006aj [Pian et al., 2006], at a phase of about six days before B-maximum light. *Right*: Same assumption as for the left panel, using the template of the Type Ic SN 2003jd [Valenti et al. , 2008a], at a phase of about one day before B-maximum light.

5.2.5   Spectral energy distribution of the afterglow

In order to study the transient, we modeled and investigated the data-set separately at different wavelength ranges: radio, optical and X-rays. We then interpolate the data to two common epochs and performed a broad band analysis.

We first fitted the radio light curve, for which there are observations at different frequencies, with most of the data at 15.5 GHz and only a couple of detections at 7.4 and 5.0 GHz [Bhalerao et al., 2017b]. The light curve has a different behaviour in the different bands, and it is decaying more rapidly at higher frequencies (Fig. 5.14, left panel). When we modeled the data with a power-law fit, we obtained decaying indices of $\alpha_{15.5\mathrm{GHz}} = 0.66 \pm 0.04$, $\alpha_{7.4\mathrm{GHz}} = 0.4$ and $\alpha_{5.0\mathrm{GHz}} = 0.05$ at 15.5, 7.4 and 5.0 GHz, respectively. Note that for the latter two indexes the data points are as many as the parameters, and no uncertainty can be provided. The different decays in the radio bands might be due to colour evolution, which can only be explained by the presence of a spectral break moving from higher to lower frequencies.

Then, to study the behaviour in the optical band, we considered the data up to 5 days after the trigger, when only the afterglow is contributing to the observed flux. Data were corrected for foreground Galactic extinction. The light curve is best followed up in the r and i filters, with g and z bands data starting only 2 days after the trigger. We studied the $griz$ spectral energy distribution of the afterglow at 3.93 days for which

we have detections in all the optical bands. We find that the data are best modeled by a power-law with spectral index $\beta_{\mathrm{opt}} = 1.21 \pm 0.01$ and negligible dust extinction along the line of sight. Afterwards, we modeled all optical light curves together and sampled the time and wavelength plane with a two variable power-law $F(\nu, t) \propto t^{-\alpha_{\mathrm{opt}}} \nu^{-\beta_{\mathrm{opt}}}$, and fixed β_{opt} to the value reported above. This approach is only possible given the negligible dust extinction. In this way, we find an optical decay common to all optical bands of $\alpha_{opt} = 1.38 \pm 0.02$.

Afterward, we studied the *Swift*-XRT data. The data span the interval between ~ 1 and ~ 15 days and can be best modeled by a single power-law model with a decay $\alpha_{\mathrm{X}} = 0.87 \pm 0.24$. The X-ray spectrum is rather poor and can be fitted using `Xspec v12.9.0` with a simple power-law with $\beta = 0.7 \pm 0.1$, fixed foreground Galactic absorption $(0.66 \times 10^{21}$ cm^{-2}; Willingale et al. 2013) and negligible host gas absorption.

Finally, we modeled all optical, radio and X-ray spectral energy distribution (SED) at the logarithmic-mean time of the XRT observations, i.e. ~ 3.28 days. We also selected another epoch at 2.14 days, for which we have optical *gri* detections. We interpolated radio and optical data to the first epoch, and radio and XRT data to the second epoch. In the following we fixed the optical spectral slope to the value $\beta_{\mathrm{opt}} = 1.21$ found above. We modeled the SED at 3.28 days with a double broken power-law, and we find two spectral breaks: a first spectral break in the radio bands at $(0.7 \pm 0.1) \times 10^{10}$ Hz and a second break between radio and optical bands at $(1.0 \pm 0.1) \times 10^{12}$ Hz. Following the standard synchrotron theory under slow cooling regime [Sari et al., 1998], we identify the first break in the radio to be the absorption frequency ν_a and the break between optical and radio to be the injection frequency ν_m. The slope between ν_a and ν_m is fixed to the value of 1/3. It is important to note here that the first break ν_a is evolving with time and that the decay below the break is almost negligible. This behaviour can be interpreted within the jet scenario [Sari et al., 1999] and the slow cooling regime, which indeed predicts $\alpha = 0$ for $\nu < \nu_a$ and $\nu_a \propto t^{-1/5}$. Thus, to obtain the model at 2.14 days we followed Sari et al. [1999] and used the relations $\nu_a \propto t^{-1/5}$ and $\nu_m \propto t^{-2}$.

In Fig. 5.15 we show the radio, optical and X-ray SEDs at different epochs. The fit is acceptable, but we must note that the model does not perfectly match the optical data at the first epoch and the jet scenario would predict more rapid decay in optical and X-rays bands. This suggests the presence of a second break between optical and X-rays and thus a more sophisticated analysis is needed to fully understand the afterglow behaviour. This can be seen in Fig. 5.14 (right panel) which shows radio, optical, and X-rays light curves. In particular, while the radio and the X-rays light curves agree within 1σ (due to the large uncertainty of α_{X}), the optical light curve is not

consistent with the others. We interpret this as the presence of another spectral break between optical and X-ray bands. An evolving break between optical and X-rays can be seen in the jet scenario without sideways expansion if the circumburst medium has a wind profile, and the synchrotron cooling frequency ν_c lies in between optical and X-rays bands implying $\beta_X - \beta_{opt} = 0.5$, consistent with the values reported above [e.g., Racusin et al., 2009; Schulze et al., 2011]. It is also expected that $\alpha_{opt} - \alpha_X = 0.25$, and indeed doing so the two decay indexes are consistent within 2σ.
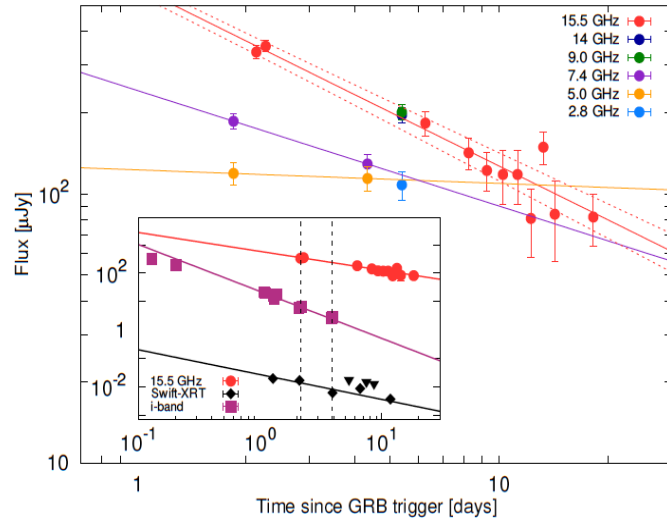
Figure 5.14: Radio band light curves of ATLAS17aeu at different frequencies. The data at 5.0 (gold), 7.4 (purple) and, 15.5 (red) GHz are fitted with simple power-laws. *Inset plot*: radio (red), optical (plum) and X-rays (black) light curves. Black triangles represent upper limits in the X-rays band. They can all be modeled with simple power laws. Dashed vertical lines represent the selected times for the spectral energy distribution fitting shown in Fig. 5.15.

5.2.6   Spectral energy distribution of the host galaxy

We used the photometric SED-fitting code LePHARE[11] [Arnouts, et al., 1999; Ilbert et al., 2006] to determine host-galaxy parameters from the detections. After fixing the redshift to the most plausible value found in our spectral and temporal analysis ($z \sim 0.62$, see Sections 4.1 and 4.2), we found that the host is a low-mass ($M = 10^{8.2^{+0.2}_{-0.2}}\,M_\odot$), galaxy with low global extinction ($E_{B-V} \sim 0.2$ mag using Calzetti et al. 2000 extinction

---

[11]http://www.cfht.hawaii.edu/~arnouts/LEPHARE.
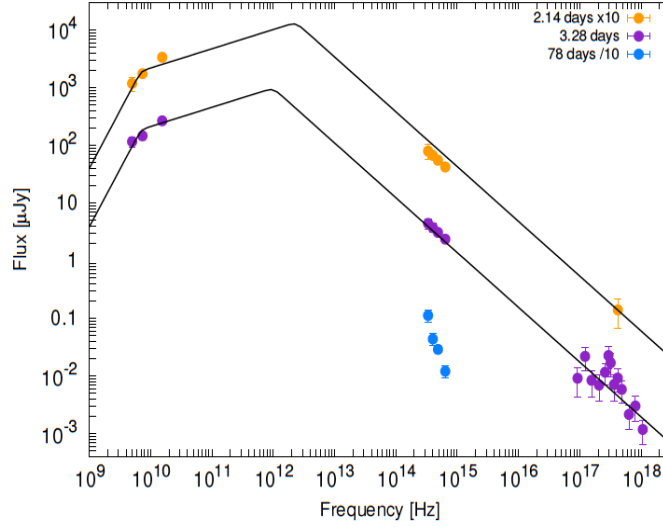
Figure 5.15: Radio, optical and X-rays data at 3.28 (purple) and 2.14 days (gold) of ATLAS17aeu. The model described in the text is also shown at both epochs. Data at 78 days (cyan) are clearly dominated by the supernova emission and we show them only for comparison with previous epochs.

law), and low star-formation rate (SFR = $0.9^{+1.5}_{-0.4} \, M_\odot \, yr^{-1}$). The inferred low mass is in agreement with the mass of typical long GRB hosts at these redshifts [Vergani et al., 2015].

Despite the low SFR, the low mass does not qualify this galaxy as an early type, which would be very unusual for the host of a long GRB [but see Rossi et al., 2014]. In fact, the main stellar population is moderately young (age = $0.3^{+0.6}_{-0.2}$ Gyr) and the galaxy has a high specific SFR of $10^{-8.3^{+0.5}_{-0.4}} \, yr^{-1}$ in agreement with other GRB hosts and star-forming galaxies [Hunt et al., 2014; Japelj et al., 2016]. The result of our fit is shown in Fig. 5.16. It is worth noting that if we do not fix the redshift we can use photometric data to constraint it between $0.4 < z < 2.8$, which is well expected given the featureless SED and still inconsistent with the inferred distance of GW 170104.

To give some indications on the properties of the host galaxy, in Fig. 5.17 we also plot the (F390-F140W) colour versus the (F606-F140W) colour of the host galaxy, together with stellar population models. The integrated colour predictions shown in the figure are based on the Stellar Population Tools (SPoT) code for single-age, single-metallicity stellar population (SSP) models [Brocato et al., 1999; Raimondo, 2009], updated for this study using higher total stellar masses, and new spectral libraries for cool and hot stars. Models suggest that the main component of the stellar population

in the galaxy is as young as few ten of Myr or younger, in agreement with a high specific SFR [e.g. Feulner et al., 2005]. This is mildly in agreement with the results of our photometric host-galaxy SED-fitting. The model and data uncertainties do not permit clear indications on the chemical composition of the stellar content.
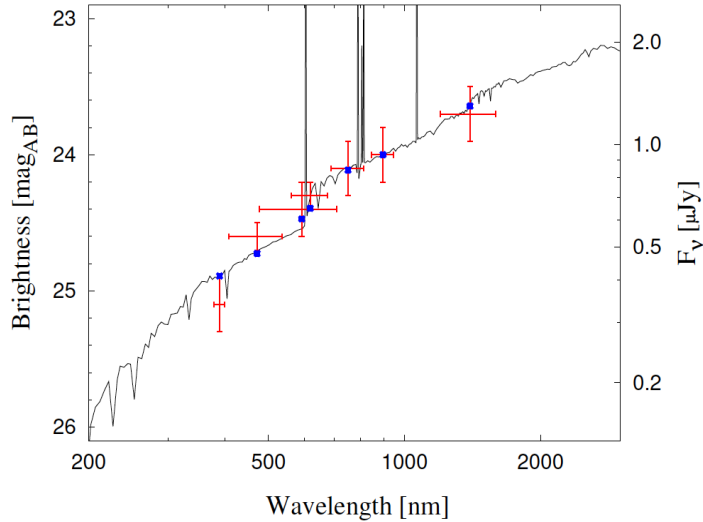
Figure 5.16: LePHARE fit to the magnitudes of the host galaxy of ATLAS17aeu/GRB 170105A with the redshift fixed to be the same as the spectroscopic one. The photometric points are highlighted in red and the blue marks represent the photometry values as determined by the synthetic SED. The fit is acceptable with $\chi/N_{filters} = 2.97/7$. For specific values, see text.

5.2.7   Conclusion

Our optical observations allowed us to comprehensively describe the temporal behaviour of the unusual transient ATLAS17aeu from early to very late phases. The detection of spectral absorption features reminiscent of broad-lined Ic supernova confirms that ATLAS17aeu is indeed the optical afterglow of the long-duration underenergetic GRB 170105A, and definitely not associated with the gravitational wave signal GW 170104, which was due to a binary BH merger [Abbott et al., 2017a].

The presence of the supernova is in fact confirmed at early times in our first spectrum (~ 3 days after the burst event) and at later times by the typical bump in the light curve already seen in many other light curves of GRBs connected SNe. Despite the fact that the redshift for this event is not strongly constrained by the data, we
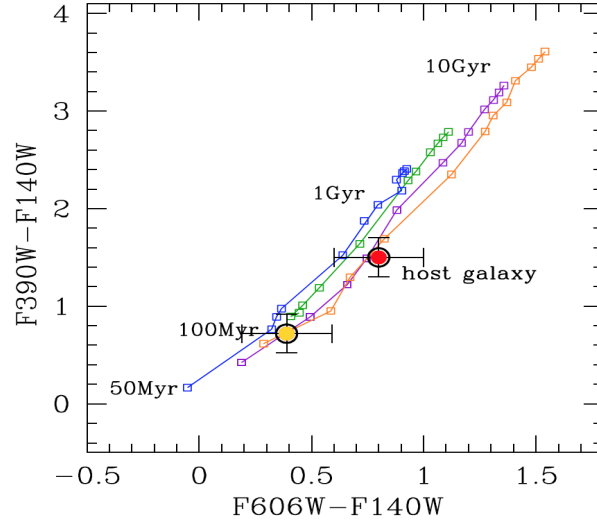
Figure 5.17: Distance-independent two-colour diagram. Simple stellar population colours from the SPoT code are compared to the measured host-galaxy colors (filled yellow circle). Lines and small squares refer to models with metallicity [Fe/H]=-0.7 (blue), [Fe/H]=-0.4 (green), [Fe/H]=0.0 (violet), [Fe/H]=+0.4 (orange), respectively. Indicative ages are also labeled, from 50 Myr to 14 Gyr. The host galaxy is plotted as a filled red (observed) and yellow (de-reddened) circle. The last value is obtained by applying the value E(B-V)=0.2). No k-correction is applied.

can confidently define a small range of possible values, that is $z \simeq 0.5 \pm 0.2$. The temporal behaviour of such a supernova is similar to the observed evolution of the prototype supernova associated with long GRBs (SN 1998bw), peaking at similar time after the burst event (~ 20 days). In fact, as for SN 1998bw, that was associated with a sub-luminous gamma-ray burst (GRB 980425), also ATLAS17aeu resulted to be associated with a long under-energetic event (GRB 170105A). All our observations including the host galaxy ones point to the scenario of a long GRB at $z \sim 0.5$ unrelated to gravitational wave signal.

By assuming the fluence measured by *Konus*-WIND and, based on the soft spectrum inferred from the measurements by *Konus*-WIND, POLAR and *AstroSat*-CZTI, a rest-frame spectral peak energy E_p of 50 ± 25 keV, we find that GRB 170105A would be consistent with the E_p-E_{iso} correlation of long GRBs [Amati et al., 2002; Amati, 2006] only for $z > 0.4$-0.5 (implying an isotropic energy for this event of $E_{iso} \gtrsim 2 \times 10^{51}$ erg). This finding further supports the above conclusion that this event came from a larger distance with respect to GW 170104, and is well consistent with its association with a

Table 5.5: Imaging log for ATLAS17aeu. Different columns correspond to: modified Julian date (1) and Δt corresponding to the mid time of the observation (2), total exposure time (3), filter identification (4), calibrated AB magnitude not corrected for Galactic extinction (5), and Telescope used for the observation (6).

MJD [d]	Δt^a [d]	t_{exp} [min]	Filt.	Mag (err)	Tel.
57762.179	3.92	8	g	23.53 (0.08)	GTC
57836.964	78.7	10	g	26.34 (0.26)	GTC
57862.194	103.9	60	g	27.05 (0.31)	LBT
57987.330	229.1	45.6	F390W	> 28.1	HST
57820.050	61.8	80	V	>22.6	TNG
57759.914	1.65	15	r	>20.7	Asiago
57762.187	3.93	10	r	23.13 (0.06)	GTC
57808.852	50.6	70	r	24.65 (0.18)	TNG
57814.436	56.2	65	r	25.03 (0.15)	TNG
57822.567	64.3	90	r	> 25.0	TNG
57836.973	78.7	10	r	25.43 (0.12)	GTC
57846.960	88.7	140	r	25.48 (0.29)	TNG
57862.194	103.9	60	r	26.05 (0.15)	LBT
57987.330	229.1	24.4	F606W	27.64 (0.21)	HST
57761.093	3.84	16	I	22.52 (0.32)	TNG
57762.197	3.94	10	i	22.85 (0.10)	GTC
57836.953	78.7	12	i	24.98 (0.26)	GTC
57862.178	103.9	60	i	25.13 (0.12)	LBT
57762.205	3.94	7	z	22.67 (0.13)	GTC
57836.980	78.7	8	z	24.01 (0.24)	GTC
57987.330	229.1	16.8	F140W	25.87 (0.14)	HST

^{a}This time is estimated from T_0.

supernova at $z \sim 0.5$.

Table 5.6: Spectroscopic log for ATLAS17aeu.

MJD [d]	Δt^a [d]	t_{exp} [min]	grism	seeing ['']	Tel.
57761.110	2.89	2x20	R1000B	1.5	GTC
57761.153	2.93	2x20	R2500I	1.5	GTC
57858.210	99.99	3x30	blue	0.9	LBT
57858.210	99.99	3x30	red	0.9	LBT
57873.903	115.68	2x20	R1000B	0.8	GTC
57873.924	115.70	1x20	R2500I	0.8	GTC
58142.431	384.21	4x10	blue	1.2	LBT
58142.431	384.21	4x10	red	1.2	LBT
58196.273	438.05	8x10	dual-grating	0.7	LBT

^{a}This time is estimated from T_0.

Table 5.7: Multi-band photometry of the host galaxy. Columns are: filter identification (1), calibrated AB magnitude not corrected for Galactic extinction (2), and Telescope used for the observation (3)

Filter	Magnitude (error)	Telescope
F390W	25.2 ± 0.2	HST
g	24.69 ± 0.11	LBT
F606W	24.5 ± 0.2	HST
r	24.38 ± 0.08	LBT
i	24.14 ± 0.06	LBT
z	24.02 ± 0.04	GTC
F140W	23.7 ± 0.2	HST

Chapter 6

Kilonova AT 2017gfo/DLT17ck, the electromagnetic counterpart of GW170817

During the second observing run of the LIGO and Virgo campaign, a gravitational-wave signal consistent with a binary neutron star coalescence was detected on 2017 August 17th (GW170817), quickly followed by a coincident short gamma-ray burst trigger by the Fermi satellite. As mentioned in the previous chapter, the DLT40 performed pointed follow-up observations of a sample of galaxies regularly monitored by the survey which fell within the combined LIGO+Virgo localization region of GW170817, and the larger Fermi gamma ray burst, GRB170917a's error box.

In section 6.1.2, I present the discovery of a new optical transient (DLT17ck, also known as SSS17a; it has also been registered as AT 2017gfo) by DLT40 spatially and temporally coincident with GW170817. The observation and analysis were published in [a]. In this work, I developed a galaxy prioritization tool, for selecting galaxies, that are possibly hosting the source of GW, and the GRB. I sent the GCN after we realize DLT17ck is unusual Yang et al. [2017a,b] and contribute to all the statistic works and figures.

Soon after, GRAWITA use a series of spectra from ground-based observatories covering the wavelength range from the ultraviolet to the near-infrared, find the source as a kilonova, which is characterized by rapidly expanding ejecta with spectral features similar to those predicted by current modelsKasen et al. [2015]; Tanaka et al. [2017]. Comparison with spectral models suggests that the merger ejected 0.03–0.05 solar masses of mate-

rial, including high-opacity lanthanides. The observation and analysis are presented in section 6.2, which were also published in [b]. In this work, I contributed to the data analysis, with particular reference to ISM spectral features.

Afterwards, the kilonova discovery AT 2017gfo/DLT17ck gives us several astrophysical and cosmological implications. In section 6.3 and 6.4, I present the constrain of DLT40 on the rate of binary neutron star mergers using the light curve of DLT17ck, and the limit of Hubble constant using both the GW and EM informations. They were published in [c] and [d], correspondingly.

Publications:

[a] Valenti, Stefano; David; Sand, J.; **Yang, Sheng***; Cappellaro, Enrico; Tartaglia, Leonardo; Corsi, Alessandra; Jha, Saurabh W.; Reichart, Daniel E.; Haislip, Joshua; Kouprianov, Vladimir, APJL, 848, L24*

[b] Pian, E.; D'Avanzo, P.; Benetti, S.; Branchesi, M.; Brocato, E.; Campana, S.; Cappellaro, E.; Covino, S.; D'Elia, V.; Fynbo, J. P. U.; Getman, F.; Ghirlanda, G.; Ghisellini, G.; Grado, A.; Greco, G.; Hjorth, J.; Kouveliotou, C.; Levan, A.; Limatola, L.; Malesani, D.; Mazzali, P. A.; Melandri, A.; Mller, P.; Nicastro, L.; Palazzi, E.; Piranomonte, S.; Rossi, A.; Salafia, O. S.; Selsing, J.; Stratta, G.; Tanaka, M.; Tanvir, N. R.; Tomasella, L.; Watson, D.; **Yang, S.***; Amati, L.; Antonelli, L. A.; Ascenzi, S.; Bernardini, M. G.; Bor, M.; Bufano, F.; Bulgarelli, A.; Capaccioli, M.; Casella, P.; Castro-Tirado, A. J.; Chassande-Mottin, E.; Ciolfi, R.; Copperwheat, C. M.; Dadina, M.; De Cesare, G.; di Paola, A.; Fan, Y. Z.; Gendre, B.; Giuffrida, G.; Giunta, A.; Hunt, L. K.; Israel, G. L.; Jin, Z.-P.; Kasliwal, M. M.; Klose, S.; Lisi, M.; Longo, F.; Maiorano, E.; Mapelli, M.; Masetti, N.; Nava, L.; Patricelli, B.; Perley, D.; Pescalli, A.; Piran, T.; Possenti, A.; Pulone, L.; Razzano, M.; Salvaterra, R.; Schipani, P.; Spera, M.; Stamerra, A.; Stella, L.; Tagliaferri, G.; Testa, V.; Troja, E.; Turatto, M.; Vergani, S. D.; Vergani, D., Nature, 551, 67*

[c] **Yang, Sheng***; Valenti, Stefano; Cappellaro, Enrico; Sand, David J.; Tartaglia, Leonardo; Corsi, Alessandra; Reichart, Daniel E.; Haislip, Joshua; Kouprianov, Vladimir, APJL, 851, L2*

*[d] Abbott, B. P. [LIGO],...,***Yang, S.** *[DLT40],...,et al, Nature, 551, 85*

6.1   DLT40 discovery

In this section I present the observations of the DLT40 team of the kilonova DLT17ck. The DLT40 team was one of the groups reporting the independent discovery of the kilonova (Section 6.1.1), and based on our light curve and an early spectrum, I show that DLT17ck resembles the expected observables of a kilonova.

6.1.1   Discovery of DLT17ck

On 2017 August 17.528 UT, the LVC reported the detection of a gravitational-wave nearly coincident in time [2 seconds before, Goldstein et al., 2017b] with the *Fermi* GBM trigger 524666471/170817529 located at RA=176.8° and DEC=-39.8° with an error of 11.6° (at 1σ). The LVC candidate had an initial localization of RA=186.62°, DEC=-48.84° and a 1σ error radius of 17.45° [LIGO/Virgo Scientific Collaboration, 2017a]. The GW candidate was consistent with a neutron star binary coalescence with false alarm rate of $\sim 1/10,000$ years [LIGO/Virgo Scientific Collaboration, 2017a]. The gravitational wave was clearly detected in the LIGO detectors but was below threshold for the Virgo detector [LIGO/Virgo Scientific Collaboration, 2017b]. Despite this, the Virgo data were still crucial to further constrain the localization of the event to only 31 deg^2 (90% credible region). The luminosity distance was constrained with LIGO data to be 40 ± 8 Mpc [LIGO/Virgo Scientific Collaboration, 2017b]. In Figure 6.1 we show a map of both the LIGO+Virgo and *Fermi* GBM localizations, which overlapped on the sky. As part of the DLT40 search, we prioritized observations of 20 galaxies within the 99% confidence area of the LVC error-box and with a cut in luminosity. Among the 23 galaxies within the LIGO/Virgo error box, we selected the 20 galaxies within 99% of the cumulative luminosity distribution. At the same time, we also selected the 31 most luminous galaxies in the *Fermi* region of the coincident short GRB (see Figure 6.1). The 51 DLT40 galaxies selected were then observed at high priority. In this work, we present the only transient we detected within either the LVC or *Fermi* localizations: AT 2017gfo/DLT17ck (detected in in NGC 4993).

On 2017 August 17 23:49:55 UT (11.09 hours after the LVC event GW170817), we detected DLT17ck, at RA=13:09:48.09 and DEC=-23:22:53.4.6, 5.37W, 8.60S arcsec offset from the center of NGC 4993 [Yang et al., 2017a, see Figure 6.2]. At the same time, DLT17ck was detected by Coulter et al. [2017], Allam et al. [2017], Melandri et al. [2017a] and Arcavi et al. [2017]. Before reporting to the internal (collaboration-wide) GCN, I secured a second confirmation image which was obtained on August 18 00:40:38 UT Yang et al. [2017b]. After announcement of the discovery of an interesting

optical transient, the LVC GW region of GW170817 was also observed in the whole EM spectrum, from radio to X-ray wavelengths. It was soon recovered in the UV, and near infrared. Deep X-ray follow-up observations conducted with the *Chandra* observatory revealed X-ray emission from a point source at a position consistent with that of the optical transient DLT17ck [Bartos et al., 2017b; Fong et al., 2017; Troja et al., 2017]. A radio source consistent with the position of DLT17ck [Adams et al., 2017] was detected with the Karl G. Jansky VLA [Corsi et al., 2017; Mooley et al., 2017b], at two different frequencies ($\approx 3\,\mathrm{GHz}$ and $\approx 6\,\mathrm{GHz}$). Marginal evidence for radio excess emission at the location of DLT17ck was also found in ATCA images of the field at similar radio frequencies [$\approx 5\,\mathrm{GHz}$; Bartos et al., 2017b]. Finally, neutrino observations report one neutrino candidate within the preliminary LVC localization [Bartos et al., 2017a], which was established to be consistent with the background and unrelated to GW170817/DLT17ck [Bartos et al., 2017b].

6.1.2 DLT17ck: a new type of transient

Our discovery magnitude $r = 17.46\pm0.03\,\mathrm{mag}$ at the distance of $39.5\pm2.6\,\mathrm{Mpc}$ [distance modulus, μ=32.98$\pm$0.15 mag using the Tully-Fisher relation Freedman et al., 2001] and Milky Way reddening $E(B-V) = 0.109\,\mathrm{mag}$ [Schlafly & Finkbeiner, 2011] brings DLT17ck to an absolute magnitude of $M_r = -15.8 \pm 0.1\,\mathrm{mag}$. This magnitude is consistent with what it is typically observed in faint CC SNe [Spiro et al., 2014] and brighter than some kilonova models. However, in the hours after the discovery, it became clear that DLT17ck was a unique event. DLT17ck was indeed cooling down and getting dimmer, much faster than any other SN we ever observed. About 35 hours after GW170817, DLT17ck had dimmed by almost a magnitude [Yang et al., 2017b]. Five days after the merger, DLT17ck was already ~ 4 magnitudes fainter than at the discovery and disappeared below our DLT40 magnitude limit the day after. At the same time, DLT17ck remained detectable in the near-infrared for a longer time. In Figure 6.3 (right panel), we compare the DLT40 light curve of DLT17ck with those of the most rapid transients available in the literature. DLT17ck evolves faster than any other known SN (gray points) and peaked probably between our discovery images and our third detection (respectively 11 and 35 hours after GW170817)[1].

Regardless of the energy source powering them, the light curves of astronomical transients like supernovae and kilonovae are regulated by the same physics. At early times, the photons can not immediately escape due to the high optical depth. The

---

[1]The possibility that DLT17ck is not related to GW170817, and exploded prior to the event, is discussed in Sec.6.1.3

photon *diffusion time* depends on the ejecta mass, the opacity and the ejecta velocity [Arnett , 1982]. For kilonovae, the ejected mass has been predicted to be between 10^{-4} and 10^{-2} $M_\odot$ depending on the lifetime of the hypermassive neutron star that forms at the moment of coalescence. A longer lifetime corresponds to a larger ejected mass and a brighter and longer-lasting optical electromagnetic counterpart [Kasen et al., 2013; Metzger, 2017].

Because of the high neutron fraction the nucleosynthesis in the ejected material is driven by the r-process, producing a significant fraction of lanthanide that dominates the opacity. Because of a large uncertainty in lanthanide opacity, the ejecta opacity is not well constrained; it should be between 1 and 100 cm^2 g^{-1} [closer to 1 for ejecta with a small amount of lanthanide elements; Metzger, 2017]. Finally, velocities in the range 0.1-0.3 times the speed of light are also expected [see Metzger, 2017, and reference therein]. Using equation 5 from Metzger [2017],

$$t_{peak} \equiv (\frac{3Mk}{4\pi\beta vc})^{1/2} \approx 1.6d(\frac{M}{10^{-2}M_\odot})^{1/2}(\frac{v}{0.1c})^{-1/2}$$

$$(\frac{k}{1cm^2g^{-1}})^{1/2} \tag{6.1}$$

where $\beta \approx 3$, M is the ejected mass, v is the expansion velocity, k the opacity and t_{peak} is the time of the peak, we can give a a rough estimate of the ejected mass. Soon after our first detection (11 hours after explosion), a few groups reported a flattening or slightly increase of the luminosity [Arcavi et al., 2017; Wolf et al., 2017], but our second detection (35 hours after explosion) shows the object fading. We then assume Aug. 18.528 UT (24 hours after GW170817) as the epoch of the peak. We use an opacity of 1-10 cm^2/g since the early blue peak should not contain large amounts of lanthanide [Metzger, 2017] and an expansion velocity of 0.2 × c. With these values, we obtain an ejected mass of $\approx 3 \times 10^{-3}$ - 10^{-2} $M_\odot$. However, the equation we used is an approximation and more careful models are needed. Comparing the DLT40 light curve with several kilonova models (see Figure 6.3), we found two models evolving as fast as DLT17ck which we describe below: The model by Metzger et al. 2010 (Met10) which assumes a radioactive powered emission and an ejected mass of 10^{-2} $M_\odot$, outflow speed of $v = 0.1c$ and iron like opacity; the model by Barnes & Kasen 2013 (B&K) which assumes an ejected mass of 10^{-3} $M_\odot$, velocity of 0.1 c and a typical lanthanide opacity. Both models are consistent with the ejected mass we computed above, and support the kilonova interpretation.

Further evidence for the kilonova hypothesis comes from the analysis of DLT17ck spectra. Spectroscopic observations were performed by Shapee et al. [2017] about 12

hrs after GW170817, showing a blue and featureless continuum. This supports the idea that DLT17ck was discovered young, although a blue and featureless continuum is also common for young SNe II and GRB afterglows. The fast cooling of DLT17ck (and hence the small ejected mass) became evident as more spectra were collected. The extended-Public ESO Spectroscopic Survey for Transient Objects [ePESSTO Smartt et al., 2015] observed DLT17ck $\sim$ 35 hours after GW170817, reporting a featureless spectrum, with a much redder continuum than that observed in SN spectra at similar phases [Lyman et al., 2017, see Figure 6.4]. A black-body fit to the spectrum revealed a temperature of ≈ 5200 K. Considering a spherically symmetric explosion and a black body emission, the radius of the kilonova should have expanded from the radius of a neutron star (few tenth 10^5 cm) to $\sim 7.3 \times 10^{14}$ cm. Under homologous expansion this requires a velocity expansion of $0.2\,c$.

6.1.3   Search for pre-discovery outbursts in historical data.

In the standard kilonova model, we only expect a bright electromagnetic signature after coalescence. We can test this by looking at DLT40 observations taken before 2017 August 17. NGC 4993 is one of the galaxies monitored by the DLT40 supernova search, observed on average every 3 days from February 2017 to July 2017 (see Table 6.1). Our images show no sign of an optical transient down to a limit of $m_r \sim 19$ mag (see Figure 3), corresponding to $M_r \sim -14$ mag at the adopted distance of NGC 4993. Similarly, the field was also observed from 2013 to 2016 from La Silla QUEST on the ESO 1.0 meter telescope with no detection to a limit of $R \sim 18$ mag [Rabinowitz & Baltay, 2017].

The last DLT40 non-detection at the position of DLT17ck is on 2017 July 27th (21 days before the LVC event) down to $m_r = 19.1$ mag. Combining this limit with the extremely fast timescale of the transient, its blue continuum in the early spectra, its rapid cooling, and its photometric consistency with some kilonova models makes it extremely unlikely DLT17ck can be explained by any kind of supernova unrelated to the GW/GRB event. Rather, all the evidence favors that DLT17ck was discovered young, and is the optical counterpart of GW170817 and GRB 524666471/170817529.

6.1.4   Summary and Future Prospects

We described the discovery of DLT17ck in the error region of the LVC event GW170817 and the *Fermi* short GRB 524666471/170817529. DLT17ck is characterized by a very fast optical evolution, consistent with some kilonova models and with a small ejecta

mass (10^2 - 10^{-3} M$_\odot$). Spectroscopic observations conducted about 35 hrs after the explosion show a featureless continuum with blackbody temperature of 5200 K, confirming the fast evolution of DLT17ck compared to the evolution of other transients like classical supernovae. In addition, it is also surprising that at such a low temperature, no features are visible. We may speculate that this is the result of blending due to the high velocity of the expanding ejecta. Given the coincidence with the LVC event and the short *Fermi* GRB, it is likely the optical counterpart of the merging of two neutron stars in a binary system. This event represents a milestone for astronomy, being the first multimessenger event from which both photons and gravitational waves have been detected.

The unprecedented characteristics of DLT17ck raise a question as to the rates of such objects. The daily cadence of the DLT40 search can help constrain the rates of kilonovae and other rapidly-evolving transients. Details of rate measurements was presented in the following of this thesis, while here we report some of the results related to kilonovae. Using the galaxies within 40 Mpc that we have observed in the last two years, and under the simplifying assumption that all kilonovae have a light curve similar to DLT17ck, we find an upper limit (at 95% confident level) to the rate of kilonovae of $0.48^{+0.9}_{-0.15}$ binary neutron stars (BNS) SNu[2]. For a Milky Way luminosity $\sim 2 \times 10^{10}$ $L_\odot$, this translates to an upper limit of 9 Galactic kilonovae per millennium. This limit is not too stringent since it is two orders of magnitude larger than the Galactic rate of binary neutron star coalescence of 24 Myr^{-1} estimated by Kim et al. [2015] from known neutron-star binaries.

We can convert our luminosity-based kilonova rate to a volumetric rate using the local luminosity density from Blanton et al. [2003]. This gives a limit of $9.4 \pm 0.8 \times 10^{-5}$ kilonovae Mpc^{-3} yr^{-1}. This is consistent with previous limits [<0.05 Mpc^{-3} yr^{-1}; Berger et al., 2013b], that however were based on hypothetical parameters for the BNS optical light curve, and is comparable to the volumetric rate of fast optical transients, 4.8 - 8.0 $\times 10^{-6}$ Mpc^{-3} yr^{-1} found by Drout et al. [2014].

Looking forward to the O3 LVC run, in 2018, it is useful to explore strategies to detect EM counterparts of NS-NS mergers. DLT17ck was discovered independently by several groups (eg. SWOPE and DLT40; Coulter et al. 2017 and Yang et al. 2017a), using the approach of targeting nearby galaxies within the LVC region with small field-of-view instruments [Gehrels et al., 2016]. Several wide-field searches were also able to identify the transient [Allam et al., 2017; A. Mller, 2017; Chambers et al., 2017; Lipunov et al., 2017], but only after reports from the targeted searches. This was likely due to the challenge of analyzing a large amount of data in a short period of time.

---

[2]SNu = $(100 \; yr)^{-1}$ $(10^{10} L_\odot^B)^{-1}$
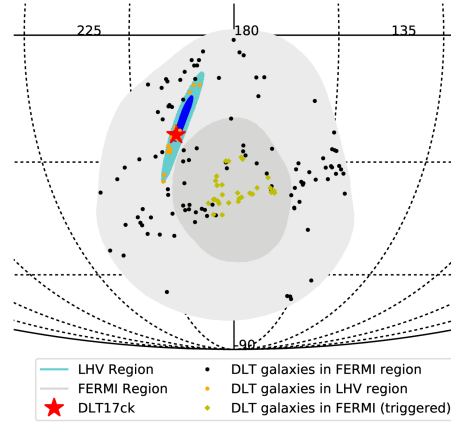
Figure 6.1: The sky map region of the GW170817 LVC event using all three gravitational-wave observatories (H1, L1, and V1) over-imposed on the *Fermi* localization of GBM trigger 524666471/170817529. The DLT40 galaxies observed the first Chilean night after the LVC trigger are marked in orange (galaxies within the LVC region) and in olive green (galaxies within the *Fermi* localization). The remaining black points are those DLT40 galaxies which were within the *Fermi* localization but were not observed by our program. The red star marks the location of DLT17ck and the host galaxy NGC 4993.

The small field-of-view strategy, and certainly our discovery, was successful because GW170817/DLT17ck was extremely nearby. The short *Fermi* GRB associated with DLT17ck is the closest ever discovered [see Berger, 2014, for a review of short GRBs]. However, with the expected increase in sensitivity of the LVC detectors, in O3 the volume where NS-NS mergers can be detected will reach 150 Mpc, increasing further to 200 Mpc at full sensitivity [2019+; Abbott et al., 2016j]. At these distances galaxy catalogs are incomplete [Smartt et al., 2016b] and the sheer number of galaxies will likely favor wide-field strategies. Nonetheless, because the Virgo horizon distance during O3 is predicted to be $65 - 115 \, \mathrm{Mpc}$ [Abbott et al., 2016j], the small field-of-view strategy may still be important for the best-localized sources. DLT40 reaches a limiting magnitude of $r \sim 19$ mag in 45 to 60 second exposures. Taking a more conservative limit of 18.5 mag, we would expect to be able to see sources like DLT17ck out to 70 Mpc. Increasing the exposure time to reach a depth of ~ 20 mag would allow us to observe binary neutron star mergers in the full range of the Virgo interferometer.
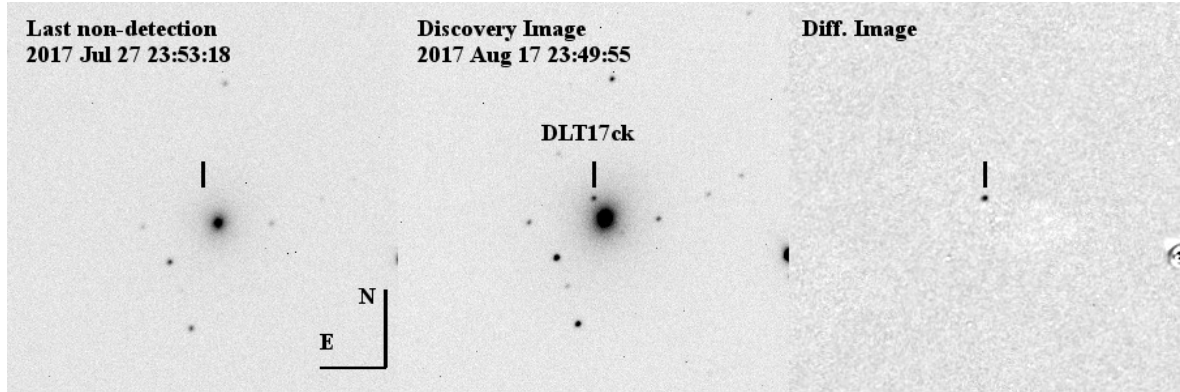
Figure 6.2: Last non-detection (on the left), discovery image of DLT17ck observed on 2017-08-17 at 23:49:55 UT. The difference image is shown on the right, where DLT17ck is clearly visible.
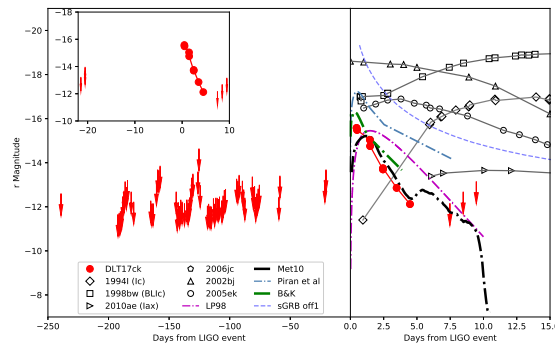
Figure 6.3: **Right panel:** DLT40 light curve of DLT17ck (in red) over plotted with normal or fast-evolving SNe (in gray). Several NS-NS merger models, scaled to a distance of 40 Mpc, are shown as comparison from Li & Paczyński 1998 [LP98]; Metzger et al. 2010 [Met10]; Barnes & Kasen 2013 [B&K] and Piran et al. 2013 [Piran et al]. **Left panel:** We show the detection limits in the position of DLT17ck in the 6 months before GW170817 and an inset with the detected light curve

Table 6.1: Photometric Data for DLT17ck

Date	JD	mag^{a,b}	Filter^c	telescope	Date	JD	mag^{a,b}	Filter^c	telescope
2017-08-17	2457983.493	17.46 0.03	r	Prompt 5	2017-03-07	2457819.772	> 20.90	r	Prompt 5
2017-08-18	2457983.528	17.56 0.04	r	Prompt 5	2017-03-10	2457822.595	> 19.97	r	Prompt 5
2017-08-18	2457984.491	18.00 0.06	r	Prompt 5	2017-03-11	2457823.592	> 19.37	r	Prompt 5
2017-08-19	2457984.510	18.29 0.06	r	Prompt 5	2017-03-12	2457824.594	> 19.39	r	Prompt 5
2017-08-19	2457985.476	19.34 0.08	r	Prompt 5	2017-03-13	2457825.586	> 19.20	r	Prompt 5
2017-08-19	2457985.478	19.29 0.12	r	Prompt 5	2017-03-26	2457838.881	> 20.37	r	Prompt 5
2017-08-21	2457986.503	20.18 0.10	r	Prompt 5	2017-03-27	2457839.714	> 21.14	r	Prompt 5
2017-08-22	2457987.504	20.92 0.12	r	Prompt 5	2017-03-28	2457840.717	> 20.86	r	Prompt 5
2017-07-27	2457961.599	> 19.84	r	Prompt 5	2017-03-29	2457841.720	> 21.03	r	Prompt 5
2017-07-27	2457962.495	> 19.36	r	Prompt 5	2017-03-30	2457842.666	> 20.74	r	Prompt 5
2017-05-15	2457888.762	> 19.79	r	Prompt 5	2017-03-31	2457843.713	> 20.83	r	Prompt 5
2017-05-16	2457889.751	> 19.88	r	Prompt 5	2017-04-02	2457845.704	> 20.90	r	Prompt 5
2017-05-17	2457890.796	> 19.61	r	Prompt 5	2017-04-04	2457847.695	> 20.73	r	Prompt 5
2017-05-20	2457893.500	> 19.88	r	Prompt 5	2017-04-05	2457848.700	> 20.87	r	Prompt 5
2017-05-21	2457894.562	> 20.27	r	Prompt 5	2017-04-06	2457849.857	> 20.63	r	Prompt 5
2017-05-22	2457895.545	> 20.65	r	Prompt 5	2017-04-07	2457850.699	> 20.24	r	Prompt 5
2017-05-28	2457901.715	> 19.69	r	Prompt 5	2017-04-08	2457851.695	> 19.74	r	Prompt 5
2017-05-29	2457902.548	> 20.16	r	Prompt 5	2017-04-09	2457852.679	> 19.56	r	Prompt 5
2017-05-30	2457903.547	> 20.12	r	Prompt 5	2017-04-13	2457856.861	> 19.45	r	Prompt 5
2017-05-31	2457904.544	> 20.70	r	Prompt 5	2017-04-14	2457857.678	> 18.41	r	Prompt 5
2017-06-01	2457905.542	> 20.45	r	Prompt 5	2017-04-15	2457858.666	> 20.07	r	Prompt 5
2017-06-02	2457906.511	> 20.24	r	Prompt 5	2017-04-21	2457864.654	> 21.01	r	Prompt 5
2017-06-02	2457907.498	> 20.06	r	Prompt 5	2017-04-22	2457865.642	> 20.93	r	Prompt 5
2017-06-19	2457923.645	> 20.61	r	Prompt 5	2017-04-23	2457866.760	> 21.02	r	Prompt 5
2017-06-19	2457924.481	> 19.65	r	Prompt 5	2017-04-24	2457867.652	> 21.04	r	Prompt 5
2016-12-21	2457743.834	> 20.44	r	Prompt 5	2017-04-26	2457869.631	> 20.67	r	Prompt 5
2017-02-06	2457790.858	> 21.39	r	Prompt 5	2017-04-27	2457870.626	> 20.92	r	Prompt 5
2017-02-07	2457791.823	> 21.34	r	Prompt 5	2017-04-28	2457871.622	> 20.65	r	Prompt 5
2017-02-08	2457792.826	> 21.26	r	Prompt 5	2017-04-29	2457872.694	> 20.66	r	Prompt 5
2017-02-09	2457793.835	> 21.10	r	Prompt 5	2017-04-30	2457873.618	> 20.71	r	Prompt 5
2017-02-10	2457794.824	> 20.58	r	Prompt 5	2017-05-01	2457874.615	> 20.60	r	Prompt 5
2017-02-11	2457795.825	> 20.33	r	Prompt 5	2017-05-03	2457876.665	> 20.76	r	Prompt 5
2017-02-12	2457796.756	> 19.90	r	Prompt 5	2017-05-04	2457877.594	> 20.55	r	Prompt 5
2017-02-13	2457797.747	> 20.16	r	Prompt 5	2017-05-05	2457878.606	> 20.30	r	Prompt 5
2017-02-14	2457798.692	> 19.85	r	Prompt 5	2017-05-06	2457879.577	> 20.25	r	Prompt 5
2017-02-17	2457801.725	> 20.37	r	Prompt 5	2017-08-25	2457990.504	> 20.89	r	Prompt 5
2017-02-19	2457803.828	> 20.83	r	Prompt 5	2017-08-26	2457991.504	> 20.37	r	Prompt 5
2017-03-05	2457817.886	> 20.78	r	Prompt 5	2017-08-26	2457992.489	> 19.90	r	Prompt 5
2017-03-06	2457818.784	> 20.91	r	Prompt 5	—	—	—	—	—

(a) : Data has not been corrected for extinction.

(b) : Limit magnitude are 5 σ detection limit.

(c) : *Open* filter calibrated to r.
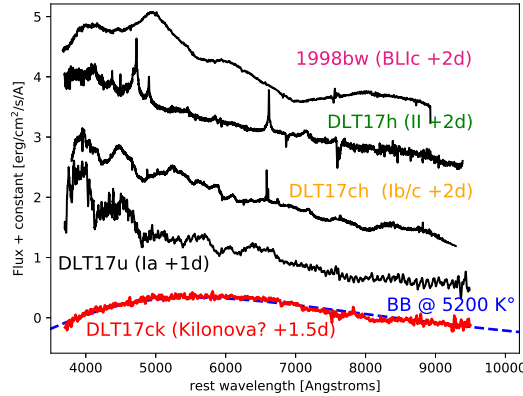
Figure 6.4: DLT17ck spectrum at 35 hours after the GW170817 compared with spectra of young SNe at similar epochs. DLT17ck is cooling much faster than any previously observed explosive transient. A blackbody fit indicates a temperature of $\approx$5200 K. Data from: DLT17u (FLOYDS), DLT17ch (SALT), DLT17h (SALT), DLT17ck (NTT), SN1998bw (Danish 1.54 telescope + DFOSC). The presence of an emission feature at $\sim$7800 Å is suspicious due to the presence of telluric lines close its position.

6.2 First Spectroscopic identification of a kilonova by GRAWITA

The merger of two neutron stars is predicted to give rise to three major detectable phenomena: a short burst of γ-rays, a gravitational wave signal, and a transient optical/near-infrared source powered by the synthesis of large amounts of very heavy elements via rapid neutron capture (the r-process)Eichler et al. [1989]; Lattimer et al. [1977]; Li & Paczyński [1998]. Such transients, named "macronovae" or "kilonovae" [Kulkarni et al., 2005; Rosswog et al., 2017; Tanaka et al., 2013; Wollaeger et al., 2017], are believed to be centres of production of rare elements such as gold and platinumMetzger [2017]. The most compelling evidence so far for a kilonova was a very faint near-infrared rebrightening in the afterglow of a short γ-ray burstBerger et al. [2013a]; Tanvir et al. [2013] at $z = 0.356$, although findings indicating bluer events have been reportedJin et al. [2016]. Here we report the spectral identification and describe the physical properties of a bright kilonova associated with the gravitational wave source GW 170817LIGO/Virgo Collaboration [2017c] and γ-ray burst GRB 170817AGoldstein et al. [2017b]; Savchenko et al. [2017] associated with a galaxy at a distance of 40 Mpc

from Earth. Using a series of spectra from ground-based observatories covering the wavelength range from the ultraviolet to the near-infrared, we find that the kilonova is characterized by rapidly expanding ejecta with spectral features similar to those predicted by current modelsKasen et al. [2015]; Tanaka et al. [2017]. The ejecta is optically thick early on, with a velocity of about 0.2 times light speed, and reaches a radius of ~ 50 astronomical units in only 1.5 days. As the ejecta expands, broad absorption-like lines appear on the spectral continuum indicating atomic species produced by nucleosynthesis that occurs in the post-merger fast-moving dynamical ejecta and in two slower (0.05 times light speed) wind regions. Comparison with spectral models suggests that the merger ejected 0.03–0.05 solar masses of material, including high-opacity lanthanides.

6.2.1   DLT17ck and GW170817

GW170817 was detected on Aug 17, 12:41:04 UTLIGO/Virgo Collaboration [2017c]. A weak short duration ($t \sim 2s$) GRB in the GW error area triggered the Fermi-GBM about two seconds laterGoldstein et al. [2017b], and was detected also by the INTEGRAL SPI-ACSSavchenko et al. [2017]. A significantly improved sky localization was obtained from the joint analysis of LIGO and Virgo data of the GW event, with a 90% error region of 33.6 square degreesLIGO/Virgo Collaboration [2017c]. Following this joint GW/GRB detection, a world-wide extensive observational campaign started, using space and ground-based telescopes to scan the sky region were the events were detected. A new point-like optical source (coordinates RA(J2000) = 13:09:48.09, Dec(J2000) = -23:22:53.3) was soon reportedCoulter et al. [2017]; Valenti et al. [2017], located at 10 arcsec from the center of the S0 galaxy NGC 4993 ($z = 0.00968$Jones et al. [2009]) in the ESO 508-G018 group at a distance of 40 Mpc from Earth, consistent with the luminosity distance of the GW signal. It was first named "SSS17a" and "DLT17ck", but here we use the official IAU designation, AT 2017gfo.

6.2.2   Observations and results

We carried out targeted and wide field optical/NIR imaging observations of several bright galaxies within the reconstructed sky localization of the GW signal with the Rapid Eye Mount (REM) telescope and with the ESO VLT Survey Telescope (ESO-VST). This led to the detection of SSS17a in the REM images of the field of NGC 4993 obtained 12.8 hours after the GW/GRB event. Following the detection of this source, we started an imaging and spectroscopic follow-up campaign at optical and

NIR wavelengths. Imaging was carried out with the REM, ESO-VST and ESO-VLT telescopes. A series of spectra was obtained with the VLT/X-shooter, covering the wavelength range 3200–24800 Å with VLT/FORS2, covering 3500–9000 Å, and with Gemini-S/GMOS covering 5500-9000 Å (see ref 20 for GMOS reduction and analysis details). Overall, we observed the source with an almost daily cadence during the period Aug 18 – Sep 03, 2017 ($\sim$ 0.5–17.5 days after the GW/GRB trigger; details are provided in the Methods section). We present here the results of the observations carried out until late August 2017.

As described in the following, the analysis and modelling of the spectral characteristics of our dataset, together with their evolution with time, result in a good match with the expectations for kilonovae, providing the first compelling observational evidence for the existence of such elusive transient sources. Details of the observations are provided in the Methods.

We adopted a foreground Milky-Way extinction of $E(B - V) = 0.1$ mag and the extinction curve ofCardelli et al. [1989], and used this to correct both magnitudes and spectra (see Methods). The extinction within the host galaxy is negligible, based on the absence of substaintial detection of characteristic narrow absorption features associated with its interstellar medium. The optical light curve resulting from our data is shown in Figure 1 and the sequence of X-shooter, FORS2, and GMOS spectra in Figure 2. Apart from Milky Way foreground lines the spectrum is otherwise devoid of narrow features that could indicate association with NGC 4993. In the slit, displaced from the position of the transient from $3''$–$10''$ (0.6–2.0 kpc in projection), we detect narrow emission lines exhibiting noticeable structure, both spatially and in velocity space (receding at 100–250 km/s with respect to the systemic velocity) likely caused by the slit crossing a spiral structure of the galaxy (see Methods).

6.2.3 Methods

6.2.3.1 Optical/NIR imaging

Our first observations of the field of SSS17a were carried out with the 60-cm robotic telescope REMChincarini et al. [2003] located at the ESO La Silla Observatory (Chile) in the g, r, i, z and H bands starting on 2017 Aug 18 at 01:29:28 UT (i.e. 12.8 hours after the GW event). The field was included in the selection we made to carry out targeted observations of catalogued galaxies in the LVC skymap aimed at searching for an optical/NIR counterpart of the GW event starting on 2017 Aug 17 at 23:11:29 UT (i.e. 10.5 hours after the GW event)Melandri et al. [2017a,b]. Following this

first detection, we started an extensive follow-up campaign of optical/NIR imaging carried out with an almost daily cadence from about 1.5 to 15.5 days after the time of the GW trigger. These observations were performed using the ESO VLT telescopes equipped with the X-shooter acquisition camera, the FORS2 instrument, and the ESO VST equipped with OmegaCam instrumentD'Avanzo et al. [2017]; Grado et al. [2017a,b]; Pian et al. [2017]. The complete log of our photometric observations is reported in Extended Data Table 1. The optical/NIR light curves are shown in Figure 1. Concerning REM and FORS2 imaging, data reduction was carried out following the standard procedures: subtraction of an averaged bias frame and division by a normalized flat frame. The astrometric solution was computed against the USNO-B1.0 catalogue (`http://www.nofs.navy.mil/data/fchpix/`). Aperture photometry was performed using SExtractorBertin & Arnouts [1996] and the PHOTOM package part of the Starlink software distribution (`http://starlink.eao.hawaii.edu/starlink`). The photometric calibration was achieved by observing Landolt standard fields and the Pan-STARRS catalogue (`https://panstarrs.stsci.edu`). In order to minimize any systematic effect, we performed differential photometry with respect to a selection of local isolated and non-saturated reference stars. As shown in Extended Data Figure 1, the transient is embedded in the host galaxy light, so that the background around the transient position is highly inhomogeneous, making accurate photometry measurements arduous. In order to minimize the effect of flux contamination from the host light, we fitted it with an analytical profile. The result obtained from the fit was then subtracted from the image in a neighborhood of the transient. This procedure was repeated for each frame. After this subtraction, the background around the transient position is much more uniform, enabling accurate photometric measurements. A dedicated procedure was applied for the reduction and analysis of the wide-field images obtained with the VLT Survey Telescope (VSTCapaccioli & Schipani [2011]). The telescope is equipped with OmegaCam Kuijken et al. [2011], a camera with one square degree field of view (FOV) matched by 0.21 arcsec pixels scale. Data have been processed with a dedicated pipeline for the VST-OmegaCAM observations (dubbed VST-tubeGrado et al. [2012]). The pipeline searches for new data in the ESO Data archive and, if available, automatically downloads and processes them performing the following main steps: pre-reduction; astrometric and photometric calibration; mosaic production. The OT magnitude, in the AB system, is the PSF fitting magnitude measured on the image after subtracting a model of the galaxy obtained fitting the isophotes with the IRAF/STSDAS task ELLIPSE Tody et al. [1993]. The reference catalog used for the absolute photometric calibration is the APASS DR9.

6.2.3.2 FORS2 spectroscopic observations

FORS2 spectra were acquired with the 600B and 600RI grisms, covering the 3500–8600 Å wavelength range. We used in all cases a $1''$ slit, for an effective resolution of $R \sim 800 - 1000$. Spectral extraction was performed with the IRAF software package (IRAF is the Image Reduction and Analysis Facility made available to the astronomical community by the National Optical Astronomy Observatories, which are operated by AURA, Inc., under contract with the US National Science Foundation. It is available at http://iraf.noao.edu.). Wavelength and flux calibration of the spectra were accomplished using helium-argon lamps and spectrophotometric stars. A check for slit losses was carried out by matching the flux-calibrated spectra to our simultaneous photometry (see Extended Data Table 1 and Extended Data Table 2). This shows that the derived spectral shape is robust.

6.2.3.3 X-shooter spectroscopic observations

The cross-dispersed echelle spectrograph, X-shooterVernet et al. [2011], mounted on the VLT, was used to observe the optical/near-infrared counterpart of GW170817. The observing campaign started on the night following the discovery and continued until the source had faded below the detection limit (see Extended Data Table 2) of X-shooter. The observations were carried out using a standard ABBA nodding pattern. Similar position angles of the slit were used for all observations. The position of the slit on the source is shown in Extended Data Figure 1.

The spectroscopic data obtained with X-shooter were managed with the Reflex interfaceFreudling et al. [2013] and reduced using version 2.9.3 of the X-shooter pipelineModigliani et al. [2010]. The reduction cascade consists of bias subtraction, order tracing, flat fielding, wavelength calibration, flux calibration using the spectrophotometric standard EG274 Moehler et al. [2014], background subtraction and order rectification – all carried out using the nightly obtained calibration files. A refinement to the wavelength solution was obtained by cross correlating the observed sky spectra with a synthetic sky spectrumJones et al. [2013]; Noll et al. [2012], leading to a wavelength solution more accurate than 1 km s^{-1}. Because X-shooter is a cross-dispersed echelle spectrograph, the individual echelle orders are curved across each detector and a rectification algorithm, which correlates neighboring pixels, must be employed. A sampling of 0.2/0.2/0.6 Å per pixel (in the UVB, VIS, and NIR arms, respectively) in the rectified image was chosen to minimize this correlation while conserving the maximal resolving power. The effective resolving power, R, of each observation was obtained from fits to unsaturated telluric absorption lines and yielded mean values of 4290/8150/5750 in

the UVB/VIS/NIR arms, respectively. This is better than nominal values, owing to a seeing PSF being narrower than the slit width. Immediately following the observations each night, telluric standard stars were observed at an airmass comparable to the target from which the atmospheric transmission spectrum was obtained using MolecfitKausch et al. [2015]; Smartt et al. [2015]. Host continuum contamination is visible as a faint background gradient along the slit. An effort has been made to minimize this contamination by using the background regions closest to the target. The images are combined in nightly sets using a weighting scheme based on a moving background variance measure wide enough to avoid it being pixel based and therefore unsuitable for Poisson-noise dominated images. For a subset of the observations, the signal-to-noise (S/N) in the spectral trace is large enough to build a model of the spectral line-spread function to employ an optimal extraction algorithm Horne [1986], but for the majority of the data, an aperture covering the entire trace is used. To establish an accurate flux calibration, slit loss corrections were calculated using the average seeing FWHM of the nightly observations along with the theoretical wavelength dependence of seeing Fried et al. [1966]. The slit losses are obtained by integrating a synthetic 2D PSF over the width of the slits and corrections are made accordingly.

6.2.3.4   Foreground dust extinction

We have estimated the intervening dust extinction toward the source using the Na I D line doublet at 5896 Å. Based on the strength of the line in our Galaxy we derive $E(B-V) = 0.09$ mag using component D1, $E(B-V) = 0.05$ mag using component D2, and $E(B-V) = 0.06$ mag using the sumPoznanski et al. [2012]. The Galactic extinction is thus limited to $E(B-V) < 0.1$ mag. Similar upper limits on $E(B-V)$ are obtained from the upper limits on the equivalent widths of the undetected K I 7699 Å absorption lineMunari et al. [1997] (EW < 0.025 Å) and undetected 8620 Å diffuse interstellar bandMunari et al. [2008] (EW < 0.04 Å). These estimates and limits are marginally consistent with the value of $E(B-V) = 0.11$ mag obtained from COBE/DIRBE maps covering that sky regionSchlafly & Finkbeiner [2011].

6.2.3.5   Spectrum analysis and interpretation

The first epoch X-shooter spectrum was fit with a black-body with temperature of 5000±200 K. The main deviations from this fit are two absorption-like lines at 8100 and 12300 Å, that evolve with time and become more pronounced in the second spectrum. Altogether, all deviations from a black-body in the first spectrum are below ∼10% from 3500 Å to 20000 Å, indicating that the fit is very satisfactory. Moreover, the

expansion speed of $0.2c$ we derive from the black-body radius at the epoch of the first spectrum (1.5 days) is compatible with the width of the absorption lines we observe in the second spectrum ($\Delta\lambda/\lambda \sim 0.1 - 0.2$), confirming that the black-body emission in the first spectrum is highly efficient.

The first 4 X-shooter spectra were compared with kilonova models from Tanaka et al. (2017). The model uses atomic structure calculations for Se ($Z = 34$), Ru ($Z = 44$), Te ($Z = 52$), Ba ($Z = 56$), Nd ($Z = 60$), and Er ($Z = 68$) to construct the atomic data for a wide range of r-process elements. By using two different atomic codes, they confirmed that the atomic structure calculations returned uncertainties in the opacities by a factor of up to ~ 2. Thereafter, they apply multiwavelength radiative transfer simulations to predict a possible variety of kilonova emission. For each model, the abundance is assumed to be homogeneous in the ejecta, However, a high-Y_e component should preferentially dominate near the polar region and low-Y_e/dynamical component develops in the equatorial region. For each model, the energy release is similar to a power-law ($t^{-1.3}$) owing to the sum of the radioactive decays of various nuclei with different lifetimes. The efficiency of the energy deposition is also taken into account, and the energy deposition rate is somewhat steeper than $t^{-1.3}$ because the gamma-rays can escape without depositing energy.

We emphasize that we have not attempted a real fit of this model to our X-shooter spectra, but have rather looked into an interpretation that was in reasonable agreement. The match is satisfactory only for the first X-shooter spectrum, and not completely satisfactory for the following three. For this reason, we refrained from deriving a light curve model. Infact, in principle, one may fold the synthetic spectral model with the sensitivity curve of any given broad-band filter and integrate the flux in the corresponding band to compare with the observed one. However, the result may be misleading independent of how persuasive it is at face value. The spectral comparison allows one to appreciate in which wavelength ranges the model is effective and in which ones it fails. Integration of the model over a broad wavelength interval cancels the spectral "memory" and prevents a critical judgment. In other words, since the spectral model is not completely satisfactory, the comparison of synthetic and observed photometry is not significant, although it may appear good.

6.2.3.6   Description of the spectral evolution

The first X-shooter spectrum obtained at $t = 1.5$ d after the GW trigger shows an almost featureless, moderately blue continuum. The overall spectral energy distribution is similar to that of early, broad line core collapse SNe. While in general at this

relatively low temperature ($\sim$5000 K) SNe typically show strong broad features using the supernova spectral classification tool GELATO Harutyunyan et al. [2008] a good match is obtained with the early spectra of the type Ib SN2008D/XRF080109Mazzali et al. [2008]. As shown in Extended Data Figure 2, the X-shooter extended spectral range displays, by comparison with the black-body fit (dotted line) the presence of some large scale modulations that are suggestive of multi-component contributions already suggestive of a kilonova event.

In the next two days the spectrum shows a very rapid evolution. The continuum temperature rapidly drops to about 3300K and broad features emerges, with peaks at 10700 Å and 16000 Å. The broad features point to very high expansion velocity and the rapid evolution to a low ejected mass. The combined spectral properties and evolution are unlike those of any known SN types and instead they are very similar to the predicted outcomes of kilonova models.

In the following week the temperature derived from the optical continuum seems to remain roughly constant while the peak at 10700 Å drifts to longer wavelengths (11200 Å at day 6) and decreases in intensity until, at ten days from discovery, the dominant feature in the spectrum is a broad emission centered at about 21000 Å.

6.2.3.7   Host emission analysis

Extending 3–10″ (0.6 – 2.0 kpc in projection) from the position of the GW counterpart are emission lines formed in the host. The lines are identified as [O II]$\lambda 3726, 3729$, Hβ, [O III]$\lambda 4959, 5007$, Hα, [N II]$\lambda 6549, 6583$ and [S II]$\lambda 6717, 6731$, and they exhibit both spatial and velocity structure along the extent of the slit, as shown in Extended Data Figure 3.

From the brightest blob of emission, centered at 6″ (1.2 kpc in projection) from the source, we measure a receding velocity of $247 \pm 15\,\mathrm{km\,s^{-1}}$ relative to the host nucleus (adopting a systemic velocity of NGC 4993 of $2916 \pm 15\,\mathrm{km\,s^{-1}}$). Along the spatial direction of the slit, closer to the source, the emission line centroids become more blue-shifted, approaching a recession velocity of $100\,\mathrm{km\,s^{-1}}$ relative to the NGC 4993 systemic velocity. The velocity range ($150\,\mathrm{km\,s^{-1}}$) of the line emission along the slit indicates coherent motion of the gas along the slit. This is further supported by the dust lanes superposed on the host nucleusCoulter et al. [2017]; Pan et al. [2017]. The presence of spiral arms was also noted byLevan et al. [2017b]. A strong [N II]$\lambda 6583$ relative to Hα combined with a weak Hβ relative to [O III]$\lambda 5007$ indicates a radiation field dominated by AGN activity, as also reported previouslyCooke et al. [in prep]; Hallinan et al. [2017]; Kasliwal et al. [2017] and supported by the presence of a central radio

sourceAlexander et al. [2017]. Using the Balmer decrement, the inferred extinction at the position of the line emission is $E(B - V) = 0.21 \pm 0.21$.

6.2.3.8 Off–beam jet scenario

GRB170817A had a fluence of 2.2×10^{-7} erg cm^{-2} in the 10-1000 keV energy range as observed by the GBM which, at a distance of 40 Mpc, corresponds to a γ–ray isotropic equivalent energy $E_{\mathrm{iso}} \sim 4.3 \times 10^{46}$ erg. The peak energy is $E_{\mathrm{peak}} = 128 \pm 48$ keVGoldstein et al. [2017a]; Goldstein et al. [2017b]. The observed E_{iso} is three to four orders of magnitude smaller than the average energy of short GRBs with known redshiftBerger [2014]; D'Avanzo et al. [2014].

For illustration let us consider a very simple model: a uniform conical jet of semi-aperture angle θ_{jet} observed off–beam, i.e at a viewing angle $\theta_{\mathrm{view}} > \theta_{\mathrm{jet}}$. In this case larger bulk Lorentz factors Γ correspond to larger de–beaming factors $b = E_{\mathrm{iso}}(0°)/E_{\mathrm{iso}}(\theta_{\mathrm{view}})$ for a fixed θ_{view}Ghisellini et al. [2006]; Salafia et al. [2016]. Given the small distance of 40 Mpc, and a likely luminosity function decreasing with increasing luminosity (e.g. Ghirlanda et al. [2016]; Wanderman et al. [2015]), we can assume that the on–axis luminosity of this burst belongs to the low–luminosity tail. For this reason we assume $E_{\mathrm{iso}}(0°) = 10^{50}$ erg. Therefore $b = 2500$. The probability of a jet oriented at an angle $< \theta_{\mathrm{view}}$ is $P(< \theta_{\mathrm{view}}) = 1 - \cos\theta_{\mathrm{view}}$. A probability of at least $P > 10\%$ implies $\theta_{\mathrm{view}} > 26°$. An off-axis viewing angle larger than $\sim 30°$ is also suggested by the expected rate of joint GW and Fermi-GBM detectionPatricelli et al. [2016] rescaled to the actual observations. Combining Eq. 2 and 3 fromGhisellini et al. [2006] it is possible to estimate the observed energy E_{iso} and peak energy E_{peak} as a function of θ_{view} and Γ for a given θ_{jet}. With $\theta_{\mathrm{view}} = 30°$, $b = 2500$ ($E_{\mathrm{iso}}(0°) = 10^{50}$ erg) requires $\Gamma = 10$ for $\theta_{\mathrm{jet}} = 10°$. The latter is within the currently few estimates of short GRB opening anglesFong et al. [2016] and $\Gamma \sim 10$ is within the dispersion of the $\Gamma - E_{\mathrm{iso}}$ relationGhirlanda et al. [2012]; Liang et al. [2013] for $E_{\mathrm{iso}}(0°) \sim 10^{50}$ erg. With these values $E_{\mathrm{peak}}(0°)$ turns out to be ~ 2 MeV. The corresponding comoving frame peak energy would be ~ 100 keV. If photons with much larger energies are absorbed by pair production we should expect (as observed at $30°$) a spectral cutoff at ~ 650 keV which is larger than the observed peak energy reported by the GBM. Though these values of $E_{\mathrm{peak}}(0°)$ and $E_{\mathrm{iso}}(0°)$ are consistent with those observed in short GRBs, they locate this burst relatively far from the possible spectral-energy correlations of short GRBs.

Extended Data Figure 4 shows the predicted afterglow light curves at 6 GHz, R band and 1 keV. The filled circle shows the X–ray flux at 15 daysHaggard et al. [2017];

Troja et al. [2017]. The arrows show two representative radio upper limits: at 8.65 days (obtainedMoldon et al. [2017] by co-adding six e-MERLIN observations at 5 GHz) and at 20 days (obtainedMooley et al. [2017c] with MeerKAT at 1.5 GHz). For the model curves the assumed parameters are: $\theta_{\text{jet}} = 10°$, $\theta_{\text{view}} = 30°$, isotropic equivalent kinetic energy $E_{\text{k,iso}} = 10^{50}$ erg, $\Gamma = 10$, a uniform density ISM with $n = 2 \times 10^{-3}$ cm^{-3} and standard micro-physical parameters at the shock i.e. $\epsilon_{\text{e}} = 0.1$, $\epsilon_{\text{B}} = 0.01$ and electrons' energy injection power law index $p = 2.1$. Standard afterglow dynamics and radiation codesVan Eerten et al. [2010] are used. As can be seen the R flux is always below 2×10^{-5} mJy, corresponding to R>28, and therefore orders of magnitude lower than the kilonova emission.
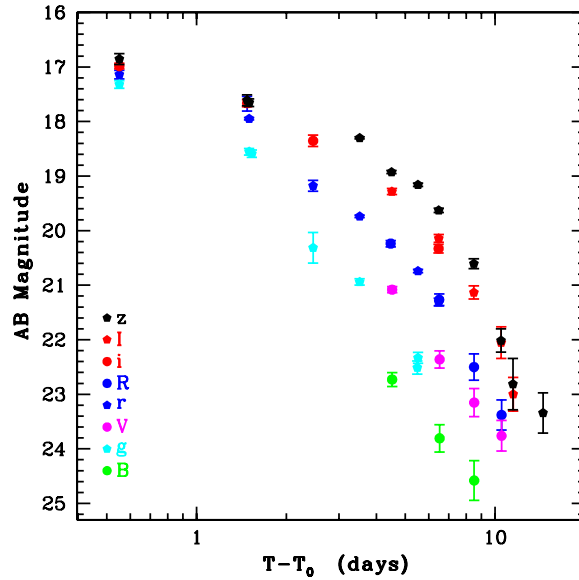
Figure 6.5: **Multiband optical light curve of AT 2017gfo.** The data shown for each filter (see legend) are listed in Extended Data Table 1. Details of data acquisition and analysis are reported in Methods. The x axis indicates the difference in days between the time at which the observation was carried out T and the time of the gravitation-wave event T_0. The error bars show the 1σ confidence level. The data have not been corrected for Galactic reddening.

6.2.4 Kilonova

The first X-shooter spectrum of the transient shows a bright, blue continuum across the entire wavelength coverage – with a maximum at $\sim$6000 Å and total luminosity of
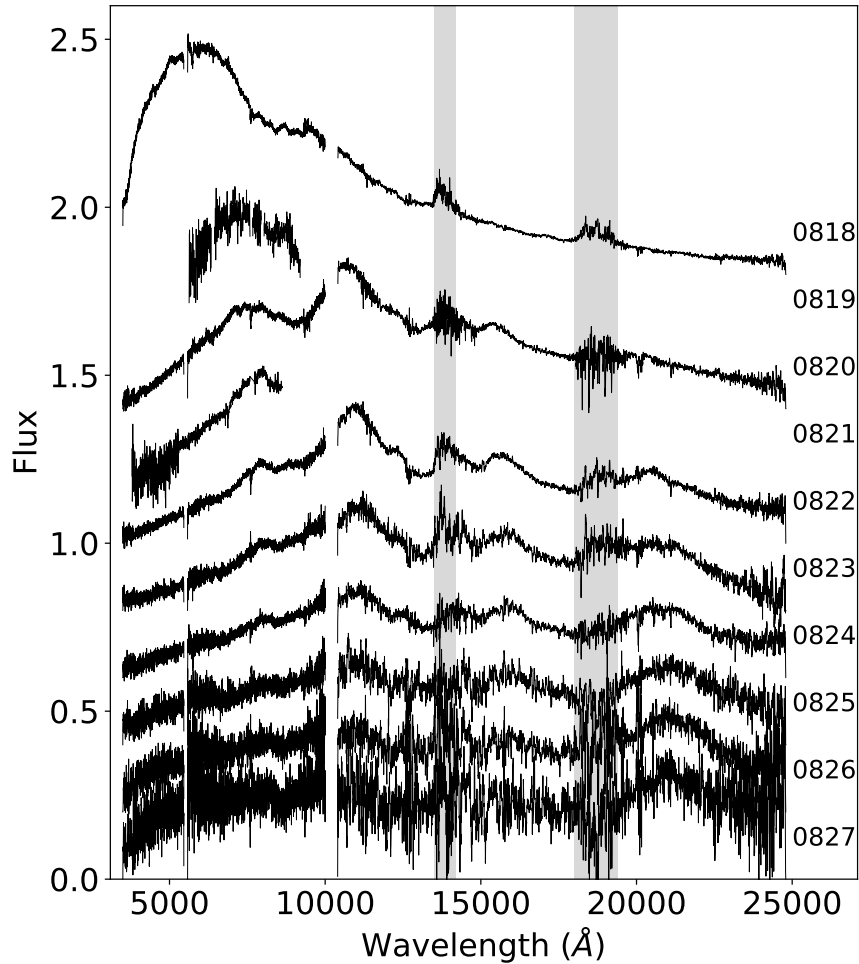
Figure 6.6: **Time evolution of the AT 2017gfo spectra.** VLT/X-shooter, VLT/-FORS2 and Gemini/GMOS spectra of AT 2017gfo. Details of data acquisition and analysis are reported in Methods. For each spectrum, the observation epoch is reported on the left (phases with respect to the gravitation-wave trigger time are reported in Extended Data Table 2; the flux normalization is arbitrary). Spikes and spurious features were removed and a filter median of 21 pixels was applied. The shaded areas mark the wavelength ranges with very low atmospheric transmission. The data have not been corrected for Galactic reddening.
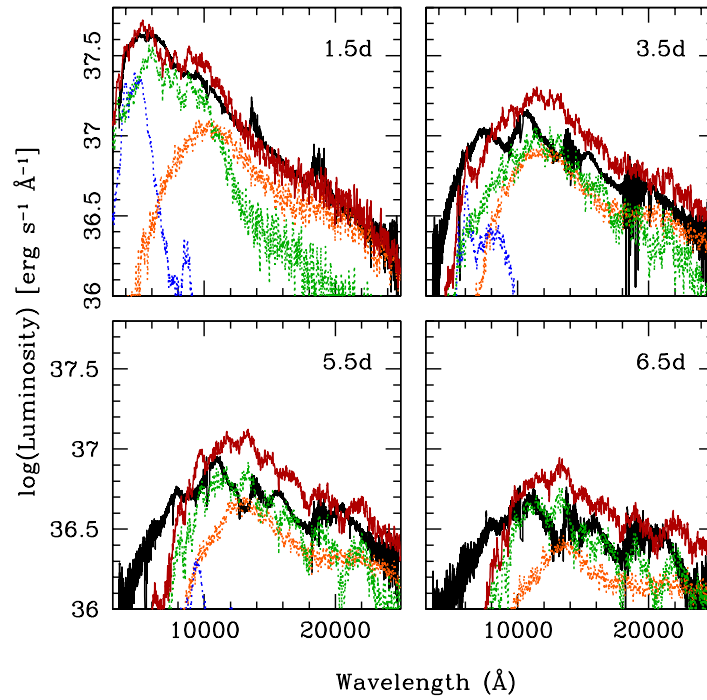
Figure 6.7: **Kilonova models compared with the AT 2017gfo spectra.** X-shooter spectra (black line) at the first four epochs and kilonova models: dynamical ejecta ($Y_e = 0.1 - 0.4$, orange), wind region with proton fraction $Y_e = 0.3$ (blue) and $Y_e = 0.25$ (green). The red curve represents the sum of the three model components.

3.2×10^{41} erg s^{-1} – that can be fit with a black-body of temperature 5000 ± 200 K, and a spherical equivalent radius of $\sim 8 \times 10^{14}$ cm. At a phase of 1.5 days after the GW/GRB trigger, this implies an expansion velocity of the ejected material of $\sim 0.2c$. The temperature is considerably lower than that inferred from photometric observations

MID[a]	Phase[b] (days)	Telescope	Instrument	Exposure (seconds)	Filter	Mag[c]
57987.02	4.5	VLT	FORS2	480	B	22.729 ± 0.128
57989.02	6.5	VLT	FORS2	600	B	23.807 ± 0.251
57991.01	8.5	VLT	FORS2	600	B	24.581 ± 0.363
57983.05	0.55	REM	ROS2	720	g	17.320 ± 0.070
57984.00	1.5	VLT	XS	90	g	18.553 ± 0.060
57984.01	1.5	REM	ROS2	720	g	18.591 ± 0.068
57984.96	2.5	REM	ROS2	720	g	20.314 ± 0.282
57986.02	3.5	VLT	XS	90	g	20.940 ± 0.060
57987.99	5.5	VST	OmegaCam	200	g	22.507 ± 0.122
57988.02	5.5	VLT	XS	90	g	22.332 ± 0.100
57987.02	4.5	VLT	FORS2	240	V	21.082 ± 0.054
57989.02	6.5	VLT	FORS2	600	V	22.361 ± 0.158
57991.01	8.5	VLT	FORS2	600	V	23.152 ± 0.256
57993.01	10.5	VLT	FORS2	840	V	23.761 ± 0.280
57983.05	0.5	REM	ROS2	720	r	17.140 ± 0.080
57983.98	1.5	REM	ROS2	720	r	17.675 ± 0.134
57984.00	1.5	VLT	XS	90	r	17.951 ± 0.020
57984.96	2.5	REM	ROS2	720	r	19.178 ± 0.100
57986.02	3.5	VLT	XS	90	r	19.740 ± 0.020
57986.97	4.5	VLT	FORS2	240	R	20.238 ± 0.058
57988.02	5.5	VLT	XS	90	r	20.740 ± 0.030
57988.98	6.5	VST	OmegaCam	200	r	21.310 ± 0.075
57989.00	6.5	VLT	FORS2	240	R	21.268 ± 0.106
57991.00	8.5	VLT	FORS2	240	R	22.501 ± 0.240
57993.01	10.5	VLT	FORS2	360	R	23.379 ± 0.277
57983.05	0.55	REM	ROS2	720	i	16.984 ± 0.050
57983.98	1.5	REM	ROS2	720	i	17.664 ± 0.064
57984.96	2.5	REM	ROS2	720	i	18.354 ± 0.105
57987.01	4.5	VLT	FORS2	300	i	19.284 ± 0.055
57988.97	6.5	VST	OmegaCam	200	i	20.329 ± 0.089
57988.98	6.5	VLT	FORS2	300	I	20.142 ± 0.072
57990.99	8.5	VLT	FORS2	300	I	21.133 ± 0.119
57992.99	10.5	VLT	FORS2	300	I	22.052 ± 0.289
57994.00	11.5	VLT	FORS2	630	I	23.000 ± 0.309
57983.05	0.55	REM	ROS2	720	z	16.854 ± 0.100
57983.98	1.5	REM	ROS2	720	z	17.611 ± 0.098
57984.00	1.5	VLT	XS	90	z	17.654 ± 0.070
57986.02	3.5	VLT	XS	90	z	18.300 ± 0.020
57987.00	4.5	VLT	FORS2	300	z	18.927 ± 0.027
57988.02	5.5	VLT	XS	90	z	19.160 ± 0.030
57988.98	6.5	VLT	FORS2	300	z	19.627 ± 0.039
57990.99	8.5	VLT	FORS2	300	z	20.606 ± 0.092
57992.98	10.5	VLT	FORS2	600	z	22.014 ± 0.214
57993.98	11.5	VLT	FORS2	720	z	22.815 ± 0.471
57996.98	14.5	VLT	FORS2	1350	z	23.342 ± 0.368

Figure 6.8: **Extended Data Table 1: Log of photometric observations.** [a]JD - 2,400,000.5; [b]After GW trigger time; [c]AB magnitudes, not corrected for Galactic extinction (E_{B-V}=0.11).

about 20 hours earlier ($\sim$ 8000 K)Malesani et al. [2017], suggesting rapid cooling. On top of this overall black-body shape are undulations that may represent very broad absorption features similar to those suggested in merger ejecta simulationsTanaka et al. [2017]. We refrain from connecting these to expansion velocity as they may be blends of many lines with poorly known properties.

In the second epoch, one day later, where the spectrum only covers the optical range, the maximum has moved to longer wavelengths, indicating a rapid cooling. At

the third epoch, when information is again available also at NIR wavelengths, the peak has shifted still to 11000 Å, and the overall spectral shape is quite different, indicating that the photosphere is receding, the ejecta are becoming increasingly transparent, and more lines become visible. The NIR part of the spectrum evolves in flux and shape much less rapidly. Spectrally broad absorption features are observed ($\Delta\lambda/\lambda \sim 0.1 - 0.2$). We exclude that these rapid changes can be compatible with supernova time evolution and are instead consistent with a kilonova (see Methods and Extended Data Figure 2).

Unlike in the case of supernova absorption lines, the identification of kilonova atomic species is not secure. The neutron-rich environment of the progenitors suggests r-process nucleosynthesis as the mechanism responsible for the elemental composition of the ejecta. Lacking line identification, various plausible nuclear reaction networks are considered and included in models of radiative transfer of kilonova spectrum formation. A fraction of the synthesized atoms are radioactive: while decaying they heat the ejecta, which then radiate thermally. All atomic species present in the ejecta with their various degrees of excitation and ionization absorb the continuum and cause the formation of lines. The models aim at reproducing these lines assuming a total explosion energy, a density profile and an ejecta abundance distribution. In kilonovae it is often envisaged that nucleosynthesis takes place in different regions with different neutron excesses and ejecta velocities, typically a post-merger dynamical ejecta region and a disk-wind region.

Various models predict different components and different synthesized masses. Tanaka et al. (2017) presented three models with different electron/proton fractions Y_e (see Methods). We compare our spectra with a scenario where these three components contribute to the observed spectra (Figure 3): a lanthanide-rich dynamical ejecta region with a proton fraction in the range $Y_e = 0.1$–0.4 and a velocity of 0.2c (orange in Fig. 3), and two slow (0.05c) wind regions of which one has $Y_e = 0.25$ and mixed (lanthanide-free and lanthanide-rich) composition (green) and one has $Y_e = 0.30$ and is lanthanide-free (blue). Each of these spectra falls short of the observed luminosity by a factor of ~ 2, while for other predictionsKasen et al. [2015]; Tanaka et al. [2013] the discrepancy is an order of magnitude. In order to investigate the applicability of the model to the present, more luminous, case we have assumed that the involved ejecta mass is larger. By decreasing the high Y_e (0.3) wind component to 30% of the value in the original model, and increasing both the intermediate Y_e (0.25) wind component and the contribution of the dynamical ejecta nucleosynthesis by a factor of 2 we obtain a satisfactory representation of the first spectrum (Figure 3).

Although direct rescaling of these models is not in principle correct (for larger masses we can expect that the spectrum of each ejecta could change) we can estimate

that the ejected mass was $\sim 0.03 - 0.05$ M$_\odot$, and that the high Y_e wind ejecta (blue line) are significantly suppressed, possibly because of viewing angle away from the GRB or a narrow jet angle or both. It is also suggestive that a wide range of Y_e values are realised in the ejecta, possibly as a function of latitude.

At successive epochs, the same components represent in a less satisfactory way the observed spectral features, which indicates that the set of adopted opacities is not completely adequate, as the cooling of the gas is not properly followed by lines of different ionization states, and that the radioactive input may also not be accurately known.

6.2.5   Off-axis jet and afterglow

Because a short GRB was detected in association with a GW trigger, we evaluated the expected contribution of its afterglow at the epochs of our observations. Nine days after GW170817 trigger time, an X-ray source was discovered by Chandra at a position consistent with the kilonova, at a flux level of $\sim 4.5 \times 10^{-15}$ erg cm^{-2} s^{-1} (0.3–8 keV). This source could be delayed X-ray afterglow emission from GRB170817A, produced by an off-beam jetTroja et al. [2017]. This may account for the otherwise small probability of having an aligned short GRB jet within such a small volumePatricelli et al. [2016]. The X-ray emission is compatible with different scenarios: a structured jet with an energy per solid angle decreasing with the angular distance from the axis, viewed at large angles (e.g.Salafia et al. [2015]), a cocoon accelerated quasi–isotropically at mildly relativistic velocities by the jetLazzati et al. [2017]; Nakar et al. [2017] or a simple uniform jet observed at large angles. All these scenarios predict an optical afterglow much fainter than the kilonova (see Methods). On the other hand, if we assume that the early (0.45 days) optical flux we measured is afterglow emission, we estimate, at the same epoch, an X-ray flux $> 10^{-12}$ erg cm^{-2} s^{-1} and a 6 GHz radio flux density of ≈ 10 mJy. These estimates are not consistent with the absence of X-ray and radio detections at the corresponding epochsBannister et al. [2017]; Evans et al. [2017c].

6.2.6   Conclusions

Our long and intensive monitoring and wide wavelength coverage enabled the unambiguous detection of time-dependent kilonova emission and sampled fully its time evolution. This not only confirms the association of the transient with the GW, but, combined with the short GRB detection, also proves beyond doubt that at least a fraction of short duration GRBs are indeed associated with compact star mergers.

Furthermore, this first detection provides important insights on the environment of merging NSs. The counterpart's location is only ~ 2 kpc (projected distance) away from the center of an early-type galaxy. This is a quite common offset for short GRBs (e.g.Fong et al. [2010]) and is consistent with predictions from theoretical models of merging NSs (e.g.Belczynski et al. [2006]). Moreover, the counterpart's location does not appear to coincide with any globular cluster, which suggests a field origin for this NS binary. The nearest possible globular clusters are at $> 2.5''$ (corresponding to 500 pc) from the source positionLevan et al. [2017a]. The formation channel of this event would be best explored with future modeling and simulations. Finally, since this GRB was rather under-energetic (isotropic gamma-ray output of $\sim 10^{46}$ erg) and likely off-axis with respect to the line of sight, we conclude that there may be a large number of similar nearby off-axis short bursts that are not followed up at frequencies lower than gamma-rays. These are also GW emitter candidates and the present event has demonstrated how the search of the randomly oriented parent population of short GRBs can be made effective via coordinated gravitational interferometry and multi-wavelength observations.

6.3   An astrophysical implication - Kilonova rate estimation

Binary neutron star (BNS) systems [Hulse & Taylor, 1975] have been studied with great interest by the astronomical community because of their connection with many open problem of astrophysics, from short GRB to r-process element production, from the physics of very high density matter to gravitational waves. The number of known BNS today is limited to a dozen systems [Lattimer, 2012] and the rate of BNS coalescences is known with order of magnitudes of uncertainty[Abadie et al., 2010; Abbott et al., 2017c; Berger et al., 2013b; Coward et al., 2012; Dominik et al., 2015; Drout et al., 2014; Fong et al., 2015; Jin et al., 2015; Kim et al., 2015; Petrillo et al., 2013; Siellez et al., 2014; Vangioni et al., 2016; de Mink & Belczynski, 2015]. The rate of BNS coalescences can be constrained from the population of galactic pulsars [Kalogera et al., 2004], from modeling the evolution of binary system [Dominik et al., 2015; de Mink & Belczynski, 2015], from the cosmic abundance of r-process elements [Vangioni et al., 2016] or measuring the rate of short Gamma-Ray Bursts (GRBs), most likely produced at the moment of the coalescence [Berger et al., 2013b].

An alternative method to constrain the rate of BNS mergers is to constrain the rate of kilonovae detected in supernova (SN) search surveys. Kilonovae are thought to be

the ubiquitous, isotropically emitting counterparts to neutron star mergers. They are expected to eject at very high velocity a small mass (0.01-0.05 M_{sun}) mainly made of high opacity r-process heavy elements, hence are predicted to have a 'red' spectrum, to be faint at maximum light ($M_V \sim -16 \, \text{mag}$) and declining quickly over the course of 1-2 weeks[e.g. Kasen et al., 2013; Metzger et al., 2010; Piran et al., 2013]. This is in contrast to the most common SNe, which evolve of $0 - 100 \, \text{day}$ timescales [e.g. see Figure 1.1 of Kasliwal et al., 2011].

One clear hindrance to calculate the kilonova rate has been the lack of observed kilonova events [with possible exceptions, see Jin et al., 2016, for a compilation] in ongoing transients searches. Some progress has been made by using theoretical kilonova light curves to calculate the upper limit of their rate in programs like the Dark Energy Survey [Doctor et al., 2017]. Additionally, there have been several recent attempts to estimate the rate of fast optical transients that evolve on sub-day timescales [$\tau \sim 0.5$ hours to 1 day; Berger et al., 2013b] all the way up to $\sim 10 \, \text{day}$ timescales [Drout et al., 2014].

With the discovery of AT 2017gfo [Abbott et al., 2017c; Abbott et al., 2017e], we can directly constrain the rate of kilonovae by using its light curve as a templatewhile allowing for possible diversity in kilonova light curves and a range of extinction values. Here we present the rate estimate for kilonovae using our observed light curve of AT 2017gfo and the data from the ongoing Distance less then 40 Mpc (DLT40) Supernova search [Tartaglia et al., 2017]. DLT40 is a SN search that points galaxies within $D \lesssim 40 \, \text{Mpc}$ with a one day cadence [3]. Given the magnitude limit of the program ($r \sim 19 \, \text{mag}$) DLT40 is well suited to detect nearby kilonova event.An advantage of DLT40, is that we can directly use the light curve of AT 2017gfo obtained with the same instrumental set-up[Valenti et al., 2017] to get a direct limit for similar transients in the DLT40 program.

This section is organized as follows. In Section 6.3.1 I describe the DLT40 survey operation during the O2 run. In Section 6.3.2 I will highlight the steps necessary to measure the rates, while in Section 6.3.3, I will compare our results with previous rate estimates and discuss the future prospects on how the improve the rates with or independently from LIGO/Virgo next observing run.

6.3.1   The DLT40 search

The DLT40 search, its design, galaxy samples and pipelines, are described in detail, in section 3.1.

---

[3]see next section for the detail on DLT40 cadence

Since the beginning of the search (September 2016), we have discovered 26 SNe, twelve of which were first announced by DLT40. Seven were discovered within 48 h of explosion (see Table 6.3 for a list of transients discovered by DLT40). The late discovery of the remaining transients by DLT40 was due to poor weather conditions.

While searching for SNe, DLT40 also reacted to LIGO/Virgo triggers during the O2 observing run, prioritizing the galaxies from the DLT40 catalog within the LIGO/Virgo localization region for each trigger. Following the LIGO/Virgo trigger of GW170817 [Collaboration, 2017a,b], DLT40 independently discovered and monitored the evolution of the kilonova AT 2017gfo/DLT17ck [Valenti et al., 2017]. Given the daily cadence of the search, DLT40 is well suited to discover similar fast kilonova-like transients. In the particular case of DLT17ck, we did have to revise our target priority list because the GW localization placed it near the horizon at sunset in Chile. During the course of the normal survey, however, any other kilonova-like transient would have been visible in the DLT40 search fields, given that DLT17ck itself was ∼1.5 magnitudes brighter than our typical detection limit, out to the border of our $D\sim40$ Mpc pointed search.

6.3.2 Rate Measurement

One approach to measuring the rate of an astronomical transient makes use of the *control time* concept [Cappellaro et al., 1993, 1997; Zwicky, 1942]. For each i-th galaxy, the control time (ct_i) is defined as the time during which a hypothetical transient is above the detection limit. It depends on the magnitude limit of each observation and the light curve of the transient. The total control time per unit luminosity of our search is computed by multiplying the ct_i control time by the luminosity of the i-th galaxy, and then summing over all of the galaxies in our sample:[4]

$$ct = \sum_{i=1}^{n} L_i * ct_i$$

The ratio between the number of transients detected and the sum of the control times for all galaxies observed gives immediately the rate as:

$$r = \frac{N}{ct}$$

---

[4]The control time ct_i depends also on the absolute magnitude of the transient (brighter transients will remain visible for a longer time above threshold). To account for the transient luminosity function, we use a monte carlo approach, simulating a number of transients for each galaxy following an adopt distribution

In order to measure the control time, the first step is evaluate the transient detection efficiency for each image or, in other words, to measure the apparent magnitude limit for transient detection. In order to do that, we performed artificial star experiments for a subset of frames, implanting stars with different magnitudes using the proper point-spread functions (PSFs), and registering the fraction of artificial stars automatically identified by our pipeline on the difference images.

Hereafter we will adopt the magnitude corresponding to a 50% detection efficiency as the limiting magnitude for the DLT40 survey, while we use the 16% and 84% detection efficiencies as lower/upper limits to determine its uncertainty. We found that the magnitude limit of our search is in the range $M_r \sim 18 - 20$ mag (see left panel of Figure 6.15) depending on weather and seeing conditions of the specific observation. Since artificial star experiments are time consuming, instead of repeating the simulation for all of the $\sim 120,000$ frames observed so far, we exploited a linear relation between the limiting magnitude for transient detection computed through artificial star experiments and the limiting magnitude for stellar source detection computed for each target frame (i.e. not the difference image). The latter was derived through an analytic equation using information on the noise and photometric calibration for each image. The comparisons between the two limiting magnitudes is shown in the right panel of Figure 6.15. In general, the limiting magnitude computed with the analytic function on the target image (y axes) is $\sim$1 magnitude deeper than the limit magnitude from artificial stars experiment (x axes). This is expected since the difference imaging technique effectively adds the template image noise to that of the target image.

The second ingredient to measure the control time is simulation of kilonova light curves in the time window each galaxy was observed. The time that the transient is above our detection limit contributes to the control time. The observed light curve of AT 2017gfo/DLT17ck was used as a reference, scaled to the distance of each galaxy with an explosion epoch randomly distributed in the observed time window. We took into account that kilonovae may have a range of absolute magnitudes, and that they may experience a variety of host galaxy extinction due to dust. For the range in kilonova magnitudes, we varied the absolute magnitude of the kilonova using a Gaussian distribution centered on the absolute magnitude of AT 2017gfo/DLT17ck and a sigma of 0.5 magnitudes (e.g. 95% of simulated light curves have an absolute magnitude within ± 1 mag of AT 2017gfo/DLT17ck). For the extinction distribution, we notice that the host environment of neutron stars mergers is often compared to the host environment of SNe Ia since both types of systems are found in early-type and star-forming galaxies [Fong et al., 2013]. For this reason, we adopted for the extinction distribution $P(A_V) = e^{-A_V/\tau_V}$, with $\tau_V = 0.334 \pm 0.088$ mag[Kessler et al., 2009], which

we label 'SN Ia extinction' scenario. We also computed the control time using either no extinction (low extinction scenario) or an extinction distribution with a τ value inflated by a factor 2 (high extinction scenario). We want to stress that, giving that DLT17ck is the first clear case of a kilonova, any choice of absolute magnitude range and reddening law is somehow arbitrary and those quantities will be better constrained when a larger number of kilonovae was discovered.

In summary, for each galaxy, we have simulated 20,000 light curves randomly distributed in the 13 months of the search, with a range of absolute magnitudes and reddening. If at any epoch of observation, the simulated light curve was brighter than our detection limit, the simulated transient would have been detected. The fraction of detected simulated transients, multiplied by the time window each galaxy was observed, gives the control time. The uncertainty on the detection limits (right panel of Figure 6.15), are reported as systematic errors, while the three extinction distributions used (low, similar to SNe Ia and high extinction) are reported separately.

During the 13 months of the search, the average number of observed frames per galaxy was 64, while the average control time per galaxy was 80 days. This means that any fast evolving transient like AT 2017gfo/DLT17ck would likely not be detected a second time if the survey cadence was 2 days or larger. Our strategy of triggering a confirmation image for each new target within a few hours of first detection well fits the need for these fast transients. Excluding AT 2017gfo/DLT17ck, which was discovered only thanks to the LIGO/Virgo trigger, no other transient with a similar fast evolution was detected. We infer a limit to the rate of kilonovae of $< 0.47^{+0.04}_{-0.03}$ SNuB[5] (low extinction), $< 0.50^{+0.05}_{-0.04}$ SNuB (SNe Ia extinction) and $< 0.55^{+0.07}_{-0.05}$ SNuB (high extinction), where the rate has been normalized to the galaxy integrated luminosity. This translates to a limit in our Galaxy of $< 0.94^{+0.38}_{-0.37}$ (low extinction), $< 1.00^{+0.43}_{-0.36}$ (SN Ia extinction), $< 1.10^{+0.51}_{-0.40}$ (high extinction) per 100 years. These limits and the systematic error are reported in Table 6.3. As a cross check, we have also computed from DLT40 the SN rates for SNe Ia, Ibc and II that will be reported in a dedicated paper (Yang et al in preparation). We stress that our SN rates estimates are consistent with previous measurements [Cappellaro et al., 1993, 1997; Leaman et al., 2011], despite the poor statisitcs a few simplifications in the calculation of the control time.

6.3.3 Summary and Future Prospects

In this paper, we have used the observed light curve of a kilonova to constrain the rate of BNS mergers to less than $0.47^{+0.04}_{-0.03}$ SNuB (low extinction), $0.50^{+0.05}_{-0.04}$ SNuB (SNe Ia

---

[5]SNuB = 1 SN per 100 yr per $10^{10} L_{B_\odot}$

extinction) and $0.55 \, ^{+0.07}_{-0.05}$SNuB (high extinction). Since some published measurements of the BNS coalescence rates are expressed in units of co-moving volume, we convert SNu rates to volumetric rates similarly to Botticella et al. [2012], that is multiplying the SNuB rate by the galaxy $B-$band luminosity density reported in Kopparapu et al. [2008] $(1.98 \pm 0.16) \times 10^{-2} \times 10^{10} \, L_\odot^B \, Mpc^3$. The kilonova volumetric rate upper limit is $0.93 \, ^{+0.16}_{-0.18} \, 10^{-4} \, \mathrm{Mpc^{-3} \, yr^{-1}}$, $0.99 \, ^{+0.19}_{-0.15} \, 10^{-4} \, \mathrm{Mpc^{-3} \, yr^{-1}}$ or $1.09 \, ^{+0.28}_{-0.18} \, 10^{-4} \, \mathrm{Mpc^{-3} \, yr^{-1}}$ (depending on the extinction law used) and is compared with previous measurements in Figure 6.16. Our rate is one order of magnitude higher than the BNS merger rate limit obtained by LIGO/Virgo during the observing run O1 [Abadie et al., 2010] and two order of magnitude higher than the optimistic rates of short Gamma-ray bursts [Coward et al., 2012; Petrillo et al., 2013].

We can also investigate how long it would on average take for our search to discover (independently from LIGO/Virgo) a kilonova. During the LIGO O2 run ($\sim 1\,\mathrm{yr}$), $117\,\mathrm{d}$ of simultaneous LIGO-detector observing time has been used to discover one BNS coalescence [Abbott et al., 2017c], which means there are $1/(117/365)=3.12$ BNS sources in the LIGO searching volumn, while our control time for kilonovae in the same period (monitoring galaxies within $40\,\mathrm{Mpc}$) is $0.22\,\mathrm{yr}$ (on average 80 days per year per galaxy). Comparing the total luminosity of the DLT40 galaxy sample and the total luminosity of the GWGC catalog, within 40 Mpc, gives 60% of the GWGC catalog sample monitored by the DLT40 survey. In order to independently discover a kilonova we would need to run the DLT40 for 3.12 / (control time * completeness) $\times$ the volume ratio of the two surveys aLIGO/aVirgo and DLT40. During the O2 run, aLIGO/aVirgo were sensitive up to a volume of $78.5\,\mathrm{Mpc}$ [Abbott et al., 2016i] and taking into account the different volumes of the two surveys $(78.5/40)^3$, we would need to run DLT40 for $\sim 18.4\,\mathrm{years}$ in order to independently discover a kilonova. This explains why historical optical searches [like the Lick SN search; Leaman et al., 2011] never detected a kilonova.

Given that it is quite unlikely to independently discover a kilonova with a search like DLT40, we may at least understand what a DLT40-like search may be able to do during the O3 aLIGO/aVirgo run. During O3, LIGO will be able to detect BNS coalescences out to $150\,\mathrm{Mpc}$, while Virgo should be sensitive out to $65 - 85$ Mpc [Abbott et al., 2016j]. If all kilonovae would be as bright as DLT17ck, with the current DLT40 observing strategy, we could detect kilonovae within a distance of $70\,\mathrm{Mpc}$. In order to cover the full Virgo volume ($85\,\mathrm{Mpc}$), we would need to go $\sim 0.4\,\mathrm{mag}$ deeper (to a limiting magnitude $\sim 19.4\,\mathrm{mag}$), hence increasing the exposure time by a factor of 2.2 (100 seconds per exposure, instead of the current 45 seconds). As DLT40 currently observes 400-600 galaxies per night with $45\,\mathrm{s}$ exposures, increasing

the exposure time to 100 seconds would still allow us to observe ~ 230 galaxies during a single night. Randomly selecting galaxies within 85 Mpc from the GLADE[6] catalog in typical aLIGO/aVirgo regions (30 sq degrees) the average number of galaxies is ~ 230 – almost exactly the same number of galaxies observable by DLT40 each night with an exposure time of 100 seconds. Here we neglect that the GLADE catalog is only $\sim 85 - 90\%$ complete in the integrated luminosity up to 85 Mpc (GLADE catalog).

Therefore, within 85 Mpc, small telescopes can still play a useful role (unless DLT17ck turns out to be a particularly bright kilonova), but the incompleteness of the available catalogs, especially for faint galaxies, may suggest that a wide-field of view strategy to directly tile the full aLIGO/aVirgo localization region may be preferred to avoid possible biases in sampling of the stellar population. In this respect the association of GRBs [Savaglio et al., 2009] and SLSN [Perley et al., 2016] with dwarf galaxies is a lesson learned.

6.4 A cosmological implication - Hubble constant constrain

The detection of GW170817 [Abbott et al., 2017b] in both gravitational waves and electromagnetic waves heralds the age of gravitational-wave multi-messenger astronomy. On 17 August 2017 the Advanced LIGO [LIGO Scientific Collaboration et al., 2015] and Virgo [Acernese et al., 2015] detectors observed GW170817, a strong signal from the merger of a binary neutron-star system. Less than seconds after the merger, a gamma-ray burst (GRB 170817A) was detected within a region of the sky consistent with the LIGO-Virgo-derived location of the gravitational-wave source [Abbott et al., 2017e; Goldstein et al., 2017b; Savchenko et al., 2017]. This sky region was subsequently observed by optical astronomy facilities [Abbott et al., 2017e], resulting in the identification of an optical transient signal within ~ 10 arcsec of the galaxy NGC 4993 [Arcavi et al., 2017; Coulter et al., 2017; Lipunov et al., 2017; Soares-Santos et al., 2016; Tanvir et al., 2017; Valenti et al., 2017]. These multi-messenger observations allow us to use GW170817 as a standard siren [Dalal et al., 2006; Holz & Hughes, 2005; Nissanke et al., 2010, 2013; Schutz, 1986], the gravitational-wave analog of an astronomical standard candle, to measure the Hubble constant. This quantity, which represents the local expansion rate of the Universe, sets the overall scale of the Universe and is of fundamental importance to cosmology. Our measurement combines the distance to the source inferred purely from the gravitational-wave signal with the recession

---

[6]http://aquarius.elte.hu/glade/

Table 6.2: Summary table of the supernovae detected with DLT40. Their light curves are shown in Figure 6.14. Supernovae detected in background galaxies are marked as BKG.

RA	DEC	DLT NAME	TNS NAME	SN TYPE	HOST GALAXY
278.63	-58.53	DLT16b	2016bmi	SN IIp	IC4721
170.08	12.98	DLT16c	2016cok	SN IIp	NGC3627
329.77	18.19	DLT16d	2016coi	SN Ic	UGC11868
328.62	-57.66	DLT16w	2016fjp	SN Ia	BKG
23.56	-29.44	DLT16z	2016gkg	SN IIb	NGC0613
20.55	0.95	DLT16ac	2016hgm	SN II	NGC0493
140.87	-23.17	DLT16ad	2016gwl	SN Ia	NGC2865
63.02	-32.86	DLT16al	2016iae	SN Ic	NGC1532
63.03	-32.85	DLT16am	2016ija	SN II	NGC1532
114.29	-52.32	DLT16bw	2016iyd	SN II	BKG
159.32	-41.62	DLT17h	2017ahn	SN II	NGC3318
218.14	-44.13	DLT17u	2017cbv	SN Ia	NGC5643
193.46	9.70	DLT17ag	2017cjb	SN II	NGC4779
200.52	-13.14	DLT17ah	2017ckg	SN II	BKG
144.15	-63.95	DLT17ar	2017cyy	SN Ia	ESO091-015
263.11	7.06	DLT17aw	2017drh	SN Ia	NGC6384
192.15	-41.32	DLT17bk	2017ejb	SN Ia	NGC4696
349.06	-42.57	DLT17bl	2017bzc	SN Ia	NGC7552
344.32	-41.02	DLT17cr	2017bzb	SN II	NGC7424
227.31	-11.33	DLT17cc	2017erp	SN Ia	NGC5861
20.06	3.40	DLT17bx	2017fgc	SN Ia	NGC0474
114.11	-69.55	DLT17cx	2016jbu	SN IIn	NGC2442
95.39	-27.21	DLT17cd	2017fzw	SN Ia	NGC2217
71.46	-59.25	DLT17ch	2017gax	SN Ibc	NGC1672
88.27	-17.87	DLT17cl	2017gbb	SN Ia	IC0438
38.88	-9.35	DLT17cq	2017gmr	SN II	NGC0988
197.45	-23.38	DLT17ck	2017gfo	kilonova	NGC4993

Table 6.3: DLT40 rate estimation results

Type	extinction (mag)	control time (days)	lums rate[a] (SNuB)	vol rate[b] $(10^{-4}Mpc^{-3}yr^{-1})$	Milky Way rate[c] $((100yr)^{-1})$
no reddening	$P(A_V) = 0$	$79.67^{+4.51}_{-5.53}$	$< 0.47^{+0.04}_{-0.03}$	$< 0.93^{+0.16}_{-0.18}$	$< 0.94^{+0.38}_{-0.37}$
Ia reddening	$P(A_V) = e^{-A_V/0.334}$	$75.07^{+5.35}_{-6.56}$	$< 0.50^{+0.05}_{-0.04}$	$< 0.99^{+0.19}_{-0.15}$	$< 1.00^{+0.43}_{-0.36}$
high reddening	$P(A_V) = 2 \times e^{-A_V/0.334}$	$69.46^{+6.15}_{-7.28}$	$< 0.55^{+0.07}_{-0.05}$	$< 1.09^{+0.24}_{-0.18}$	$< 1.10^{+0.51}_{-0.40}$

(a) : DLT40 only detected DLT17ck because of the LIGO detection and subsequent localization, therefore it is not considered in our rate calculations, which we report here as 95% confidence level Poisson single-sided upper limits, given zero events [Gehrels, 1986].

(b) : We converted the rates in units of SNuB to volumetric rates with luminosity density: $(1.98 \pm 0.16) \times 10^{-2} \times 10^{10} L_\odot^B Mpc^3$ [Kopparapu et al., 2008].

(c) : The total B-band luminosity of the MW is quite uncertain; we adopt $(2.0 \pm 0.6) \times 10^{10} L_\odot^B$ [van der Kruit, 1987].

velocity inferred from measurements of the redshift using electromagnetic data. This approach does not require any form of cosmic "distance ladder" [Freedman et al., 2001]; the GW analysis can be used to estimate the luminosity distance out to cosmological scales directly, without the use of intermediate astronomical distance measurements. We determine the Hubble constant to be $70.0^{+12.0}_{-8.0} \, \mathrm{km \, s^{-1} \, Mpc^{-1}}$ (maximum a posteriori and 68% credible interval). This is consistent with existing measurements [Planck Collaboration et al., 2016; Riess et al., 2016], while being completely independent of them. Additional standard-siren measurements from future gravitational-wave sources will provide precision constraints of this important cosmological parameter.

The Hubble constant H_0 measures the mean expansion rate of the Universe. At nearby distances ($d \lesssim 50 \, \mathrm{Mpc}$) it is well approximated by the expression

$$v_H = H_0 d, \tag{6.2}$$

where v_H is the local "Hubble flow" velocity of a source, and d is the distance to the source. At such distances all cosmological distance measures (such as luminosity distance and comoving distance) differ at the order of v_H/c where c is the speed of light. As $v_H/c \sim 1\%$ for GW170817 we do not distinguish between them. We are similarly insensitive to the values of other cosmological parameters, such as Ω_m and Ω_Λ.

To obtain the Hubble flow velocity at the position of GW170817, we use the optical identification of the host galaxy NGC 4993 [Abbott et al., 2017e]. This identification is based solely on the 2-dimensional projected offset and is independent of any assumed

value of H_0. The position and redshift of this galaxy allow us to estimate the appropriate value of the Hubble flow velocity. Because the source is relatively nearby the random relative motions of galaxies, known as peculiar velocities, need to be taken into account. The peculiar velocity is $\sim 10\%$ of the measured recessional velocity (see Methods).

The original standard siren proposal [Schutz, 1986] did not rely on the unique identification of a host galaxy. By combining information from ~ 100 independent GW detections, each with a set of potential host galaxies, a $\sim 5\%$ estimate of H_0 can be obtained even without the detection of any transient optical counterparts [Del Pozzo, 2012]. This is particularly relevant, as gravitational-wave networks will detect many binary black hole mergers over the coming years [Abbott et al., 2016d], and these are not expected to be accompanied by electromagnetic counterparts. Alternatively, if an EM counterpart has been identified but the host galaxy is unknown, the same statistical method can be applied but using only those galaxies in a narrow beam around the location of the optical counterpart. However, such statistical analyses are sensitive to a number of complicating effects, including the incompleteness of current galaxy catalogs or the need for dedicated follow-up surveys, as well as a range of selection effects [Messenger & Veitch, 2013]. In what follows we exploit the identification of NGC 4993 as the host galaxy of GW170817 to perform a standard siren measurement of the Hubble constant [Dalal et al., 2006; Holz & Hughes, 2005; Nissanke et al., 2010, 2013].

Analysis of the GW data associated with GW170817 produces estimates for the parameters of the source, under the assumption that general relativity is the correct model of gravity [Abbott et al., 2017b]. We are most interested in the joint posterior distribution on the luminosity distance and binary orbital inclination angle. For the analysis in this paper we fix the location of the GW source on the sky to the identified location of the counterpart [Coulter et al., 2017]. See the Methods section for details.

An analysis of the GW data alone finds that GW170817 occurred at a distance $d = 43.8^{+2.9}_{-6.9}$ Mpc (all values are quoted as the maximum posterior value with the minimal width 68.3% credible interval). We note that the distance quoted here differs from that in other studies [Abbott et al., 2017b], since here we assume that the optical counterpart represents the true sky location of the GW source instead of marginalizing over a range of potential sky locations. The $\sim 15\%$ uncertainty is due to a combination of statistical measurement error from the noise in the detectors, instrumental calibration uncertainties [Abbott et al., 2017b], and a geometrical factor dependent upon the correlation of distance with inclination angle. The GW measurement is consistent with the distance to NGC 4993 measured using the Tully-Fisher relation, $d_{\mathrm{TF}} = 41.1 \pm$

5.8 Mpc [Freedman et al., 2001; Sakai et al., 2000].

The measurement of the GW polarization is crucial for inferring the binary inclination. This inclination, ι, is defined as the angle between the line of sight vector from the source to the detector and the orbital angular momentum vector of the binary system. For EM phenomena it is typically not possible to tell whether a system is orbiting clockwise or counter-clockwise (or, equivalently, face-on or face-off), and sources are therefore usually characterized by a viewing angle: $\min(\iota, 180° - \iota)$. By contrast, GW measurements can identify the sense of the rotation, and thus ι ranges from 0 (counter-clockwise) to 180 deg (clockwise). Previous GW detections by LIGO had large uncertainties in luminosity distance and inclination [Abbott et al., 2016d] because the two LIGO detectors that were involved are nearly co-aligned, preventing a precise polarization measurement. In the present case, thanks to Virgo as an additional detector, the cosine of the inclination can be constrained at 68.3% (1σ) confidence to the range $[-1.00, -0.81]$ corresponding to inclination angles between $[144, 180]$ deg. This implies that the plane of the binary orbit is almost, but not quite, perpendicular to our line of sight to the source ($\iota \approx 180$ deg), which is consistent with the observation of a coincident GRB (LVC, GBM, & INTEGRAL 2017 in prep.; Goldstein et al. 2017, ApJL, submitted; Savchenko et al. 2017, ApJL, submitted). We report inferences on $\cos \iota$ because our prior for it is flat, so the posterior is proportional to the marginal likelihood for it from the GW observations.

EM follow-up of the GW sky localization region [Abbott et al., 2017e] discovered an optical transient [Arcavi et al., 2017; Coulter et al., 2017; Lipunov et al., 2017; Soares-Santos et al., 2016; Tanvir et al., 2017; Valenti et al., 2017] in close proximity to the galaxy NGC 4993. The location of the transient was previously observed by the *Distance Less Than 40 Mpc* (DLT40) survey on 2017 July 27.99 UT and no sources were found [Valenti et al., 2017]. We estimate the probability of a random chance association between the optical counterpart and NGC 4993 to be 0.004% (see the Methods section for details). In what follows we assume that the optical counterpart is associated with GW170817, and that this source resides in NGC 4993.

To compute H_0 we need to estimate the background Hubble flow velocity at the position of NGC 4993. In the traditional electromagnetic calibration of the cosmic "distance ladder" [Freedman et al., 2001], this step is commonly carried out using secondary distance indicator information, such as the Tully-Fisher relation [Sakai et al., 2000], which allows one to infer the background Hubble flow velocity in the local Universe scaled back from more distant secondary indicators calibrated in quiet Hubble flow. We do not adopt this approach here, however, in order to preserve more fully the independence of our results from the electromagnetic distance ladder. Instead we

estimate the Hubble flow velocity at the position of NGC 4993 by correcting for local peculiar motions.

NGC 4993 is part of a collection of galaxies, ESO-508, whose center-of-mass recession velocity relative to the frame of the CMB [Hinshaw et al., 2009] is [Crook et al., 2007] $3327 \pm 72 \, \mathrm{km \, s^{-1}}$. We correct the group velocity by $310 \, \mathrm{km \, s^{-1}}$ due to the coherent bulk flow [Carrick et al., 2015; Springob et al., 2014] towards The Great Attractor (see Methods section for details). The standard error on our estimate of the peculiar velocity is $69 \, \mathrm{km \, s^{-1}}$, but recognizing that this value may be sensitive to details of the bulk flow motion that have been imperfectly modelled, in our subsequent analysis we adopt a more conservative estimate [Carrick et al., 2015] of $150 \mathrm{km \, s^{-1}}$ for the uncertainty on the peculiar velocity at the location of NGC 4993, and fold this into our estimate of the uncertainty on v_H. From this, we obtain a Hubble velocity $v_H = 3017 \pm 166 \, \mathrm{km \, s^{-1}}$.

Once the distance and Hubble velocity distributions have been determined from the GW and EM data, respectively, we can constrain the value of the Hubble constant. The measurement of the distance is strongly correlated with the measurement of the inclination of the orbital plane of the binary. The analysis of the GW data also depends on other parameters describing the source, such as the masses of the components [Abbott et al., 2016d]. Here we treat the uncertainty in these other variables by marginalizing over the posterior distribution on system parameters [Abbott et al., 2017b], with the exception of the position of the system on the sky which is taken to be fixed at the location of the optical counterpart.

We carry out a Bayesian analysis to infer a posterior distribution on H_0 and inclination, marginalized over uncertainties in the recessional and peculiar velocities; see the Methods section for details. Figure 6.17 shows the marginal posterior for H_0. The maximum a posteriori value with the minimal 68.3% credible interval is $H_0 = 70.0^{+12.0}_{-8.0} \, \mathrm{km \, s^{-1} \, Mpc^{-1}}$. Our estimate agrees well with state-of-the-art determinations of this quantity, including CMB measurements from Planck [Planck Collaboration et al., 2016] ($67.74 \pm 0.46 \, \mathrm{km \, s^{-1} \, Mpc^{-1}}$, "TT,TE,EE+lowP+lensing+ext") and Type Ia supernova measurements from SHoES [Riess et al., 2016] ($73.24 \pm 1.74 \, \mathrm{km \, s^{-1} \, Mpc^{-1}}$), as well as baryon acoustic oscillations measurements from SDSS [Aubourg et al., 2015], strong lensing measurements from H0LiCOW [Bonvin et al., 2017], high-l CMB measurements from SPT [Henning et al., 2017], and Cepheid measurements from the HST key project [Freedman et al., 2001]. Our measurement is a new and independent determination of this quantity. The close agreement indicates that, although each method may be affected by different systematic uncertainties, we see no evidence at present for a systematic difference between GW and established EM-based estimates. As has been much remarked upon, the Planck and SHoES results are inconsistent at $\gtrsim 3\sigma$ level.

Our measurement does not resolve this tension, and is broadly consistent with both.

One of the main sources of uncertainty in our measurement of H_0 is due to the degeneracy between distance and inclination in the GW measurements. A face-on or face-off binary far away has a similar gravitational-wave amplitude to an edge-on binary closer in. This relationship is captured in Figure 6.18, which shows posterior contours in the H_0–$\cos\iota$ parameter space.

The posterior in Figure 6.17 results from the vertical projection of Figure 6.18, marginalizing out uncertainties in the cosine of inclination to derive constraints on the Hubble constant. Alternatively, it is possible to project horizontally, and thereby marginalize out the Hubble constant to derive constraints on the cosine of inclination. If instead of deriving H_0 independently we take the existing constraints on H_0 [Planck Collaboration et al., 2016; Riess et al., 2016] as priors, we are able to significantly improve our constraints on $\cos\iota$ as shown in Figure 6.19. Assuming the Planck value for H_0, the minimal 68.3% credible interval for the cosine of inclination is $[-1.00, -0.92]$ (corresponding to an inclination angle range $[157, 177]$ deg). For the SHoES value of H_0, it is $[-0.97, -0.85]$ (corresponding to an inclination angle range $[148, 166]$ deg). For this latter SHoES result we note that the face-off $\iota = 180$ deg orientation is just outside the 90% confidence range. It will be particularly interesting to compare these constraints to those from modeling of the short GRB, afterglow, and optical counterpart associated with GW170817 [Abbott et al., 2017e].

We have presented a standard siren determination of the Hubble constant, using a combination of a GW distance and an EM Hubble velocity estimate. Our measurement does not use a "distance ladder", and makes no prior assumptions about H_0. We find $H_0 = 70.0^{+12.0}_{-8.0}\,\mathrm{km\,s^{-1}\,Mpc^{-1}}$, which is consistent with existing measurements [Planck Collaboration et al., 2016; Riess et al., 2016]. This first GW–EM multi-messenger event demonstrates the potential for cosmological inference from GW standard sirens. We expect that additional multi-messenger binary neutron-star events will be detected in the coming years, and combining subsequent independent measurements of H0 from these future standard sirens will lead to an era of precision gravitational-wave cosmology.

Methods

Probability of optical counterpart association with NGC 4993

We calculate the probability that an NGC 4993-like galaxy (or brighter) is misidentified as the host by asking how often the centre of one or more such galaxies falls by random chance within a given angular radius θ of the counterpart. Assuming Poisson counting statistics this probability is given by $P = 1 - \exp\left[-\pi\theta^2 S(< m)\right]$ where $S(< m)$ is the surface density of galaxies with apparent magnitude equal to or brighter than m. From the local galaxy sample distribution in the infrared (K-band) apparent magnitude [Huang et al., 1998] we obtain $S(< K) = 0.68 \times 10^{(0.64(K-10.0)-0.7)} \deg^{-2}$. As suggested by [Bloom et al., 2002], we set θ equal to twice the half-light radius of the galaxy, for which we use NGC 4993's diameter of ~ 1.1 arcmin, as measured in the near infrared band (the predominant emission band for early-type galaxies). Using $K = 9.2$ mag taken from the 2MASS survey [Skrutskie et al., 2006] for NGC 4993, we find the probability of random chance association is $P = 0.004\%$.

Finding the Hubble velocity of NGC 4993

In previous EM determinations of the cosmic "distance ladder", the Hubble flow velocity of the local calibrating galaxies has generally been estimated using redshift-independent secondary galaxy distance indicators, such as the Tully-Fisher relation or type Ia supernovae, calibrated with more distant samples that can be assumed to sit in quiet Hubble flow [Freedman et al., 2001]. We do not adopt this approach for NGC 4993, however, in order that our inference of the Hubble constant is fully independent of the electromagnetic distance scale. Instead we estimate the Hubble flow velocity at the position of NGC 4993 by correcting its measured recessional velocity for local peculiar motions.

NGC 4993 resides in a group of galaxies whose center-of-mass recession velocity relative to the Cosmic Microwave Background (CMB) frame [Hinshaw et al., 2009] is [Crook et al., 2007, 2008] $3327 \pm 72 \, \mathrm{km\,s^{-1}}$. We assume that all of the galaxies in the group are at the same distance and therefore have the same Hubble flow velocity, which we assign to be the Hubble velocity of GW170817. This assumption is accurate to within 1% given that the radius of the group is ~ 0.4 Mpc. To calculate the Hubble flow velocity of the group, we correct its measured recessional velocity by the peculiar velocity caused by the local gravitational field. This is a significant correction [Carrick et al., 2015; Springob et al., 2014]; typical peculiar velocities are $300 \, \mathrm{km\,s^{-1}}$, equivalent

to $\sim 10\%$ of the total recessional velocity at a distance of 40 Mpc.

We employ the 6dF galaxy redshift survey peculiar velocity map [Jones et al., 2009; Springob et al., 2014], which used more than 8,000 Fundamental Plane galaxies to map the peculiar velocity field in the Southern hemisphere out to redshift $z \simeq 0.055$. We weight the peculiar velocity corrections from this catalog with a Gaussian kernel centered on NGC 4993's sky position and with a width of $8h^{-1}$ Mpc; the kernel width is independent of H_0 and is equivalent to a width of $800\,\mathrm{km\,s^{-1}}$ in velocity space, typical of the widths used in the catalog itself. There are 10 galaxies in the 6dF peculiar velocity catalog within one kernel width of NGC 4993. In the CMB frame [Hinshaw et al., 2009], the weighted radial component of the peculiar velocity and associated uncertainty is $\langle v_p \rangle = 310 \pm 69\,\mathrm{km\,s^{-1}}$.

We verified the robustness of this peculiar velocity correction by comparing it with the velocity field reconstructed from the 2MASS redshift survey [Carrick et al., 2015; Huchra et al., 2012]. This exploits the linear relationship between the peculiar velocity and mass density fields smoothed on scales larger than about $8h^{-1}$ Mpc, and the constant of proportionality can be determined by comparison with radial peculiar velocities of individual galaxies estimated from e.g. Tully-Fisher and Type Ia supernovae distances. Using these reconstructed peculiar velocities, which have a larger associated uncertainty [Carrick et al., 2015] of $150\,\mathrm{km\,s^{-1}}$, at the position of NGC 4993 we find a Hubble velocity in the CMB frame of $v_H = 3047\,\mathrm{km\,s^{-1}}$ – in excellent agreement with the result derived using 6dF. We adopt this larger uncertainty on the peculiar velocity correction in recognition that the peculiar velocity estimated from the 6dF data may represent an imperfect model of the true bulk flow at the location of NGC 4993. For our inference of the Hubble constant we therefore use a Hubble velocity $v_H = 3017 \pm 166\,\mathrm{km\,s^{-1}}$ with 68.3% uncertainty.

Finally, while we emphasise again the independence of our Hubble constant inference from the electromagnetic distance scale, we note the consistency of our GW distance estimate to NGC 4993 with the Tully-Fisher distance estimate derived by scaling back the Tully-Fisher relation calibrated with more distant galaxies in quiet Hubble flow [Sakai et al., 2000]. This also strongly supports the robustness of our estimate for the Hubble velocity of NGC 4993.

Summary of the model

Given observed data from a set of GW detectors, x_{GW}, parameter estimation is used to generate a posterior on the parameters that determine the waveform of the GW signal. Parameters are inferred within a Bayesian framework [Veitch et al., 2015] by comparing

strain measurements [Abbott et al., 2017b] in the two LIGO detectors and the Virgo detector with the gravitational waveforms expected from the inspiral of two point masses [Hannam et al., 2014] under general relativity. We use algorithms for removing short-lived detector noise artifacts [Abbott et al., 2017b; Cornish & Littenberg, 2015] and we employ approximate point-particle waveform models [Blanchet, 2014; Buonanno & Damour, 1999; Hannam et al., 2014]. We have verified that the systematic changes in the results presented here from incorporating non-point-mass (tidal) effects [Hinderer & Flanagan, 2008; Vines et al., 2011] and from different data processing methods are much smaller than the statistical uncertainties in the measurement of H_0 and the binary orbital inclination angle.

From this analysis we can obtain the parameter estimation likelihood of the observed GW data, marginalized over all parameters characterizing the GW signal except d and $\cos \iota$,

$$p(x_{\mathrm{GW}} \mid d, \cos \iota) = \int p(x_{\mathrm{GW}} \mid d, \cos \iota, \vec{\lambda}) \, p(\vec{\lambda}) \mathrm{d}\vec{\lambda}. \qquad (6.3)$$

The other waveform parameters are denoted by $\vec{\lambda}$, with $p(\vec{\lambda})$ denoting the corresponding prior.

Given perfect knowledge of the Hubble flow velocity of the GW source, v_H, this posterior distribution can be readily converted into a posterior on $\cos \iota$ and $H_0 = v_H/d$,

$$
\begin{aligned}
p(H_0, \cos \iota | x_{\mathrm{GW}}) \\
\propto (v_H/H_0^2) \, p(x_{\mathrm{GW}} \mid d = v_H/H_0, \cos \iota) \\
\times \, p_d(v_H/H_0) \, p_\iota(\cos \iota), \quad (6.4)
\end{aligned}
$$

where $p_d(d)$ and $p_\iota(\cos \iota)$ are the prior distributions on distance and inclination. For the Hubble velocity $v_H = 3017 \, \mathrm{km \, s^{-1}}$, the maximum a posteriori distance from the GW measurement of $43.8 \, \mathrm{Mpc}$ corresponds to $H_0 = 68.9 \, \mathrm{km \, s^{-1} \, Mpc^{-1}}$, so this procedure would be expected to generate a posterior on H_0 that peaks close to that value.

While the above analysis is conceptually straightforward, it makes a number of assumptions. In practice, the Hubble-flow velocity cannot be determined exactly and it must be corrected for uncertain peculiar velocities. The above does not explicitly set a prior on H_0, but instead inherits a $1/H_0^4$ prior from the usual $p_d(d) \propto d^2$ prior used in GW parameter estimation. In addition, the logic in this model is that a redshift has been obtained first and the distance is then measured using GWs. As GW detectors cannot be pointed, we cannot target particular galaxies or redshifts for GW sources. In practice, we wait for a GW event to trigger the analysis and this introduces potential

selection effects which we must consider. We will see below that the simple analysis described above does give results that are consistent with a more careful analysis for this first detection. However, the simple analysis cannot be readily extended to include second and subsequent detections, so we now describe a more general framework that does not suffer from these limitations.

We suppose that we have observed a GW event, which generated data x_{GW} in our detectors, and that we have also measured a recessional velocity for the host, v_r, and the peculiar velocity field, $\langle v_p \rangle$, in the vicinity of the host. These observations are statistically independent and so the combined likelihood is

$$p(x_{\mathrm{GW}}, v_r, \langle v_p \rangle \mid d, \cos \iota, v_p, H_0) =$$
$$p(x_{\mathrm{GW}} \mid d, \cos \iota)\, p(v_r \mid d, v_p, H_0)\, p(\langle v_p \rangle \mid v_p). \quad (6.5)$$

The quantity $p(v_r \mid d, v_p, H_0)$ is the likelihood of the recessional velocity measurement, which we model as

$$p\left(v_r \mid d, v_p, H_0\right) = N\left[v_p + H_0 d, \sigma_{v_r}^2\right](v_r) \quad (6.6)$$

where $N\left[\mu, \sigma^2\right](x)$ is the normal (Gaussian) probability density with mean μ and standard deviation σ evaluated at x. The measured recessional velocity, $v_r = 3327\,\mathrm{km\,s^{-1}}$, with uncertainty $\sigma_{v_r} = 72\,\mathrm{km\,s^{-1}}$, is the mean velocity and standard error for the members of the group hosting NGC 4993 taken from the two micron all sky survey (2MASS) [Crook et al., 2007, 2008], corrected to the CMB frame [Hinshaw et al., 2009]. We take a similar Gaussian likelihood for the measured peculiar velocity, $\langle v_p \rangle = 310\,\mathrm{km\,s^{-1}}$, with uncertainty $\sigma_{v_p} = 150\,\mathrm{km\,s^{-1}}$:

$$p\left(\langle v_p \rangle \mid v_p\right) = N\left[v_p, \sigma_{v_p}^2\right](\langle v_p \rangle). \quad (6.7)$$

From the likelihood (6.5) we derive the posterior

$$p(H_0, d, \cos \iota, v_p \mid x_{\mathrm{GW}}, v_r, \langle v_p \rangle)$$
$$\propto \frac{p(H_0)}{\mathcal{N}_{\mathrm{s}}(H_0)}\, p(x_{\mathrm{GW}} \mid d, \cos \iota)\, p(v_r \mid d, v_p, H_0)$$
$$\times\, p(\langle v_p \rangle \mid v_p)\, p(d)\, p(v_p)\, p(\cos \iota), \quad (6.8)$$

where $p(H_0)$, $p(d)$, $p(v_p)$ and $p(\cos \iota)$ are the parameter prior probabilities. Our standard analysis assumes a volumetric prior, $p(d) \propto d^2$, on the Hubble distance, but we explore sensitivity to this choice below. We take a flat-in-log prior on H_0,

$p(H_0) \propto 1/H_0$, impose a flat (i.e. isotropic) prior on $\cos \iota$, and a flat prior on v_p for $v_p \in [-1000, 1000]\, \mathrm{km\,s^{-1}}$. These priors characterise our beliefs about the cosmological population of GW events and their hosts before we make any additional measurements or account for selection biases. The full statistical model is summarized graphically in Extended Data Figure 6.1. This model with these priors is our canonical analysis.

In Eq. (6.8), the term $\mathcal{N}_{\mathrm{s}}(H_0)$ encodes selection effects [Abbott et al., 2016d; Loredo, 2004; Mandel et al., 2016]. These arise because of the finite sensitivity of our detectors. While all events in the Universe generate a response in the detector, we will only be able to identify, and hence use, signals that generate a response of sufficiently high amplitude. The decision about whether to include an event in the analysis is a property of the data only, in this case $\{x_{\mathrm{GW}}, v_r, \langle v_p \rangle\}$, but the fact that we condition our analysis on a signal being detected, i.e., the data exceeding these thresholds, means that the likelihood must be renormalized to become the likelihood for detected events. This is the role of

$$\mathcal{N}_{\mathrm{s}}(H_0) = \int\limits_{\mathrm{detectable}} \mathrm{d}\vec{\lambda}\, \mathrm{d}d\, \mathrm{d}v_p\, \mathrm{d}\cos\iota\, \mathrm{d}x_{\mathrm{GW}}\, \mathrm{d}v_r\, \mathrm{d}\langle v_p \rangle$$

$$\times \Big[p(x_{\mathrm{GW}} \mid d, \cos\iota, \vec{\lambda})\, p(v_r \mid d, v_p, H_0)$$

$$\times p(\langle v_p \rangle \mid v_p)\, p(\vec{\lambda})\, p(d)\, p(v_p)\, p(\cos\iota) \Big] , \quad (6.9)$$

where the integral is over the full prior ranges of the parameters, $\{d, v_p, \cos\iota, \vec{\lambda}\}$, and over data sets that would be selected for inclusion in the analysis, i.e., exceed the specified thresholds. If the integral was over all data sets it would evaluate to 1, but because the range is restricted there can be a non-trivial dependence on parameters characterizing the population of sources, in this case H_0.

In the current analysis, there are in principle selection effects in both the GW data and the EM data. However, around the time of detection of GW170817, the LIGO-Virgo detector network had a detection horizon of $\sim 190\,\mathrm{Mpc}$ for BNS events [Abbott et al., 2017b], within which EM measurements are largely complete. For example, the counterpart associated with GW170817 had brightness $\sim 17\,\mathrm{mag}$ in the I band at $40\,\mathrm{Mpc}$ [Arcavi et al., 2017; Coulter et al., 2017; Lipunov et al., 2017; Tanvir et al., 2017; Valenti et al., 2017]; this source would be $\sim 22\,\mathrm{mag}$ at $400\,\mathrm{Mpc}$, and thus still detectable by survey telescopes such as DECam well beyond the GW horizon. Even the dimmest theoretical lightcurves for kilonovae are expected to peak at $\sim 22.5\,\mathrm{mag}$ at the LIGO–Virgo horizon [Metzger & Berger, 2012]. We therefore expect that we are dominated by GW selection effects at the current time and can ignore EM selection

effects. The fact that the fraction of BNS events that will have observed kilonova counterparts is presently unknown does not modify these conclusions, since we can restrict our analysis to GW events with kilonova counterparts only.

In the GW data, the decision about whether or not to analyse an event is largely determined by the signal-to-noise ratio (SNR), ρ, of the event. A reasonable model for the selection process is a cut in SNR, i.e., events with $\rho > \rho_*$ are analysed [Abbott et al., 2016f]. In that model, the integral over x_{GW} in Eq. (6.9) can be replaced by an integral over SNR from ρ_* to ∞, and $p(x_{GW}|d, \cos\iota, \vec{\lambda})$ replaced by $p(\rho|d, \cos\iota, \vec{\lambda})$ in the integrand. This distribution depends on the noise properties of the operating detectors, and on the intrinsic strain amplitude of the source. The former are clearly independent of the population parameters, while the latter scales like a function of the source parameters divided by the luminosity distance. The dependence on source parameters is on redshifted parameters, which introduces an explicit redshift dependence. However, within the $\sim 190\,\mathrm{Mpc}$ horizon, redshift corrections are at most $\lesssim 5\%$, and the Hubble constant measurement is a weak function of these, meaning the overall impact is even smaller. At present, whether or not a particular event in the population ends up being analysed can therefore be regarded as a function of d only. When GW selection effects dominate, only the terms in Eq. (6.9) arising from the GW measurement matter. As these are a function of d only and we set a prior on d, there is no explicit H_0 dependence in these terms. Hence, $\mathcal{N}_s(H_0)$ is a constant and can be ignored. This would not be the case if we set a prior on the redshifts of potential sources instead of their distances, since then changes in H_0 would modify the range of detectable redshifts. As the LIGO–Virgo detectors improve in sensitivity the redshift dependence in the GW selection effects will become more important, as will EM selection effects. However, at that point we will also have to consider deviations in the cosmological model from the simple Hubble flow described in Eq. (6.2) of the main article.

Marginalising Eq. (6.8) over d, v_p and $\cos\iota$ then yields

$$
\begin{aligned}
p(H_0 \mid x_{GW}, v_r, \langle v_p \rangle) \propto p(H_0) \int \mathrm{d}d\,\mathrm{d}v_p\,\mathrm{d}\cos\iota \\
\times\, p(x_{GW} \mid d, \cos\iota)\, p(v_r \mid d, v_p, H_0) \\
\times\, p(\langle v_p \rangle \mid v_p)\, p(d)\, p(v_p)\, p(\cos\iota)\,. \quad (6.10)
\end{aligned}
$$

The posterior computed in this way was shown in Figure 6.17 in the main article and has a maximum a posteriori value and minimal 68.3% credible interval of $70.0^{+12.0}_{-8.0}\,\mathrm{km\,s^{-1}\,Mpc^{-1}}$, as quoted in the main article. The posterior mean is $78\,\mathrm{km\,s^{-1}\,Mpc^{-1}}$ and the standard deviation is $15\,\mathrm{km\,s^{-1}\,Mpc^{-1}}$. Various other summary statistics are given in Extended Data Table 6.4.

Robustness to prior specification

Our canonical analysis uses a uniform volumetric prior on distance, $p(d) \propto d^2$. The distribution of galaxies is not completely uniform due to clustering, so we explore sensitivity to this prior choice. We are free to place priors on any two of the three variables $\{d, H_0, z\}$, where $z = H_0 d/c$ is the Hubble flow redshift of NGC 4993. A choice of prior for two of these variables induces a prior on the third which may or may not correspond to a natural choice for that parameter. A prior on z could be obtained from galaxy catalog observations [Dalya et al., 2016], but must be corrected for incompleteness. When setting a prior on H_0 and z, the posterior becomes

$$
p(H_0, z, \cos \iota, v_p \mid x_{\rm GW}, v_r, \langle v_p \rangle)
$$
$$
\propto \frac{p(H_0)}{\mathcal{N}_{\rm s}(H_0)} \, p(x_{\rm GW} \mid d = cz/H_0, \cos \iota) \, p(v_r \mid z, v_p)
$$
$$
\times \, p(\langle v_p \rangle \mid v_p) \, p(z) \, p(v_p) \, p(\cos \iota), \quad (6.11)
$$

but now

$$
\mathcal{N}_{\rm s}(H_0) = \int\limits_{\rm detectable} {\rm d}z \, {\rm d}v_p \, {\rm d}\cos \iota \, {\rm d}x_{GW} \, {\rm d}v_r \, {\rm d}\langle v_p \rangle
$$
$$
\times \, p(x_{\rm GW} \mid d = cz/H_0, \cos \iota) \, p(v_r \mid z, v_p)
$$
$$
\times \, p(\langle v_p \rangle \mid v_p) \, p(z) \, p(v_p) \, p(\cos \iota) . \quad (6.12)
$$

When GW selection effects dominate, the integral is effectively

$$
\mathcal{N}_{\rm s}(H_0) = \int {\rm d}z \, {\rm d}\cos \iota \, {\rm d}x_{GW}
$$
$$
\times \, p(x_{\rm GW} \mid d = cz/H_0, \cos \iota) p(z) \, p(\cos \iota)
$$
$$
= \int {\rm d}d \, {\rm d}\cos \iota \, {\rm d}x_{GW}
$$
$$
\times \, p(x_{\rm GW} \mid d, \cos \iota) p(dH_0/c) \, p(\cos \iota) \, (H_0/c) , \quad (6.13)
$$

which has an H_0 dependence, unless $p(z)$ takes a special, H_0-dependent form, $p(z) = f(z/H_0)/H_0$. However, if the redshift prior is volumetric, $p(z) \propto z^2$, the selection effect term is $\propto H_0^3$, which cancels a similar correction to the likelihood and gives a posterior on H_0 that is identical to the canonical analysis.

For a single event, any choice of prior can be mapped to our canonical analysis with a different prior on H_0. For any reasonable prior choices on d or z, we would

expect to gradually lose sensitivity to the particular prior choice as further observed events are added to the analysis. However, to illustrate the uncertainty that comes from the prior choice for this first event, we compare in Extended Data Figure 6.2 and Extended Data Table 6.4 the results from the canonical prior choice $p(d) \propto d^2$ to those from two other choices: using a flat prior on z, and assuming a velocity correction due to the peculiar velocity of NGC 4993 that is a Gaussian with width $250\,\mathrm{km\,s^{-1}}$. (To do the first of these, the posterior samples from GW parameter estimation have to be re-weighted, since they are generated with the d^2 prior used in the canonical analysis. We first "undo" the default prior before applying the desired new prior.)

The choice of a flat prior on z is motivated by the simple model described above, in which we imagine first making a redshift measurement for the host and then use that as a prior for analysing the GW data. Setting priors on distance and redshift, the simple analysis gives the same result as the canonical analysis, but now we set a prior on redshift and H_0 and obtain a different result. This is to be expected because we are making different assumptions about the underlying population, and it arises for similar reasons as the different biases in peculiar velocity measurements based on redshift-selected or distance-selected samples [Strauss & Willick, 1995]. As can be seen in Extended Data Table 6.4, the results change by less than 1σ, as measured by the statistical error of the canonical analysis.

By increasing the uncertainty in the peculiar velocity prior, we test the assumptions in our canonical analysis that (1) NGC 4993 is a member of the nearby group of galaxies, and (2) that this group has a center-of-mass velocity close to the Hubble flow. The results in Extended Data Table 6.4 summarizes changes in the values of H_0 and in the error bars.

We conclude that the impact of a reasonable change to the prior is small relative to the statistical uncertainties for this event.

Incorporating additional constraints on H_0

By including previous measurements of H_0 [Planck Collaboration et al., 2016; Riess et al., 2016] we can constrain the orbital inclination more precisely. We do this by setting the H_0 prior in Eq. (6.8) to $p(H_0|\mu_{H_0}, \sigma_{H_0}^2) = N[\mu_{H_0}, \sigma_{H_0}^2]$, where for ShoES [Riess et al., 2016] $\mu_{H_0} = 73.24\,\mathrm{km\,s^{-1}\,Mpc^{-1}}$ and $\sigma_{H_0} = 1.74\,\mathrm{km\,s^{-1}\,Mpc^{-1}}$, while for Planck [Planck Collaboration et al., 2016] $\mu_{H_0} = 67.74\,\mathrm{km\,s^{-1}\,Mpc^{-1}}$ and $\sigma_{H_0} =$

$0.46\,\mathrm{km\,s^{-1}\,Mpc^{-1}}$. The posterior on $\cos\iota$ is then

$$
p(\cos\iota \mid x_{\mathrm{GW}}, v_r, \langle v_p \rangle, \mu_{H_0}, \sigma_{H_0}^2) \propto \int \mathrm{d}d\,\mathrm{d}v_p\,\mathrm{d}H_0
$$
$$
\times\, p(x_{\mathrm{GW}} \mid d, \cos\iota)\, p(v_r \mid d, v_p, H_0)\, p(\langle v_p \rangle \mid v_p)
$$
$$
\times\, p(H_0 | \mu_{H_0}, \sigma_{H_0}^2)\, p(d)\, p(v_p)\,. \quad (6.14)
$$

This posterior was shown in Figure 6.19 of the main article.

UT[a]	MID[b]	Phase[c] (days)	Instrument	Slit/Grism (arcsec)	Exp.Time (s)	Airmass (min/max)	Seeing (arcsec)	F[d]$_{Vis}$	F[d]$_{NIR}$
18.97	57983.97	1.5	VLT/X-shooter	1.0/0.9/0.9	2400	1.45/1.72	0.61	166	40
19.95	57984.95	2.5	Gemini-S/GMOS	–	600	2.5/2.7	–	53	–
20.98	57985.98	3.5	VLT/X-shooter	1.0/0.9/0.9	3600	1.52/2.12	0.9	27.8	36.5
21.98	57986.98	4.5	VLT/FORS2	600RI	1800	1.58/1.86	0.88	18	–
22.03	57987.03	4.5	VLT/FORS2	600B	700	2.60/2.91	0.59	18	–
22.98	57987.98	5.5	VLT/X-shooter	1.0/0.9/0.9	3600	1.58/2.25	0.71	10.8	23.9
23.98	57988.98	6.5	VLT/X-shooter	1.0/0.9/0.9	3600	1.74/2.33	0.87	7.0	15.4
24.98	57989.98	7.5	VLT/X-shooter	1.0/0.9/0.9	3600	1.66/2.44	0.53	6.3	12
25.98	57990.98	8.5	VLT/X-shooter	1.0/0.9/0.9	2400	1.74/1.98	0.65	6.1	8.2
26.97	57991.97	9.5	VLT/X-shooter	1.0/0.9/0.9	3600	1.69/2.50	0.78	5.1	6.0
27.97	57992.97	10.5	VLT/X-shooter	1.0/0.9/0.9	3600	1.70/2.53	0.67	4.7	4.5

Figure 6.9: **Extended Data Table 2: Log of spectroscopic observations.** [a] UT days of Aug 2017. [b] JD - 2,400,000.5. [c] After GW trigger time. [d] Fluxes at 6000 and 15000 Å in 10^{-18} erg s^{-1} cm^{-2} Å^{-1}, not corrected for reddening; uncertainties are $\sim$10%.
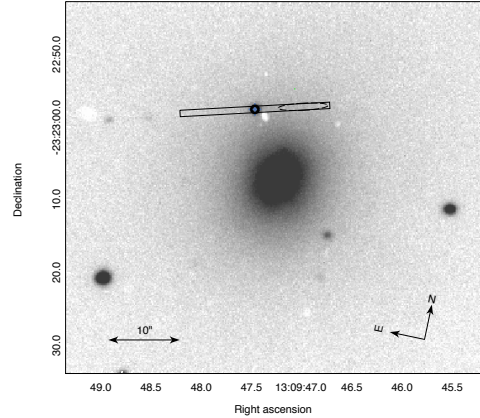
Figure 6.10: **Extended Data Figure 1: Image of the NGC4993 galaxy**. The image was obtained with the X-shooter acquisition camera (z filter). The X-shooter slit overlaid in red. The position of the OT has been marked by a blue circle. The position of the line emission in the slit has been also marked. The dust lanes visible in the host intersects the slit at the position of the line emission.
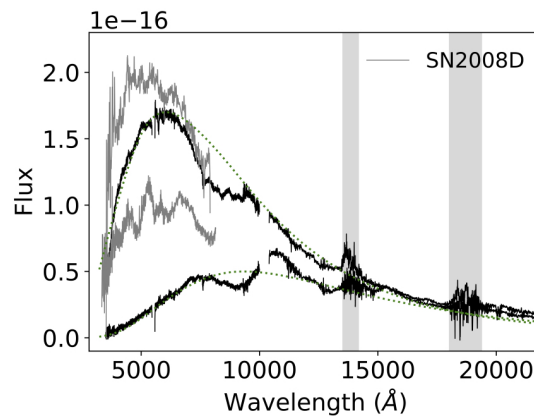
Figure 6.11: **Extended Data Figure 2: Black-body fit to the SSS17a/DLT17ck spectra**. The two early X-shooter spectra of GW170817, obtained 1.5 and 3.5 d after discovery are compared with the spectra of the type Ib SN 2008DMazzali et al. [2008] obtained at 2-5 days after explosion respectively (blue, arbitrarily scaled in flux). The dotted line show the black-body fit of the optical continuum of GW170817 with temperature 5000 and 3200 K respectively.
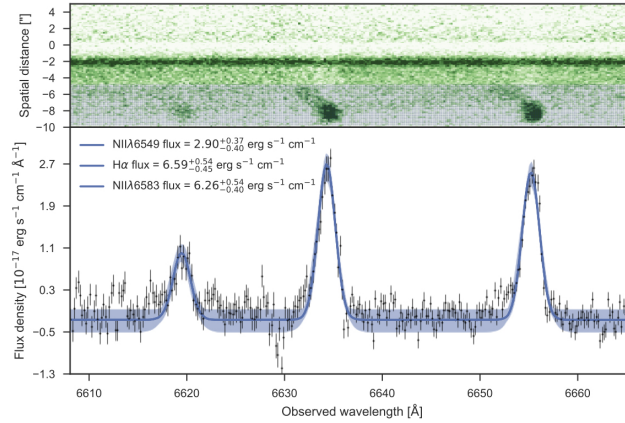
Figure 6.12: **Extended Data Figure 3: 2D image of the SSS17a/DLT17ck spectrum**. The upper panel shows the rectified, X-shooter 2D-image. The dark line visible across the entire spectral window is the bright continuum of the OT and the offset, dark blobs indicate the position of the line emission from NIIλ6549, Hα, and NIIλ6583. The lower panel shows an extraction of the line emission where the line fits are overlain. The integrated line fluxes are given in the labels, normalized by a factor of 10^{-17} for clarity.
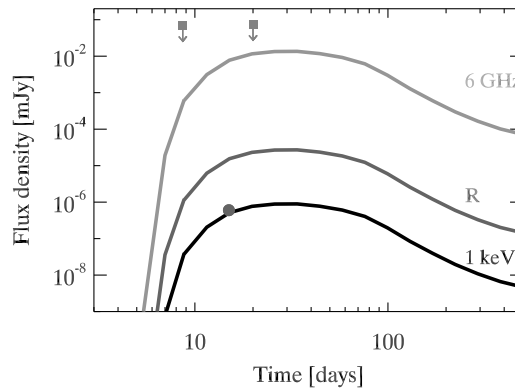
Figure 6.13: **Extended Data Figure 4: Off-axis GRB afterglow modeling**. Synthetic X-ray, optical and radio light curve of the GRB afterglow as predicted in an off-axis jet model. The filled dot symbol shows the X-ray detectionTroja et al. [2017] and the arrows two representative radio upper limits Moldon et al. [2017]; Mooley et al. [2017c].
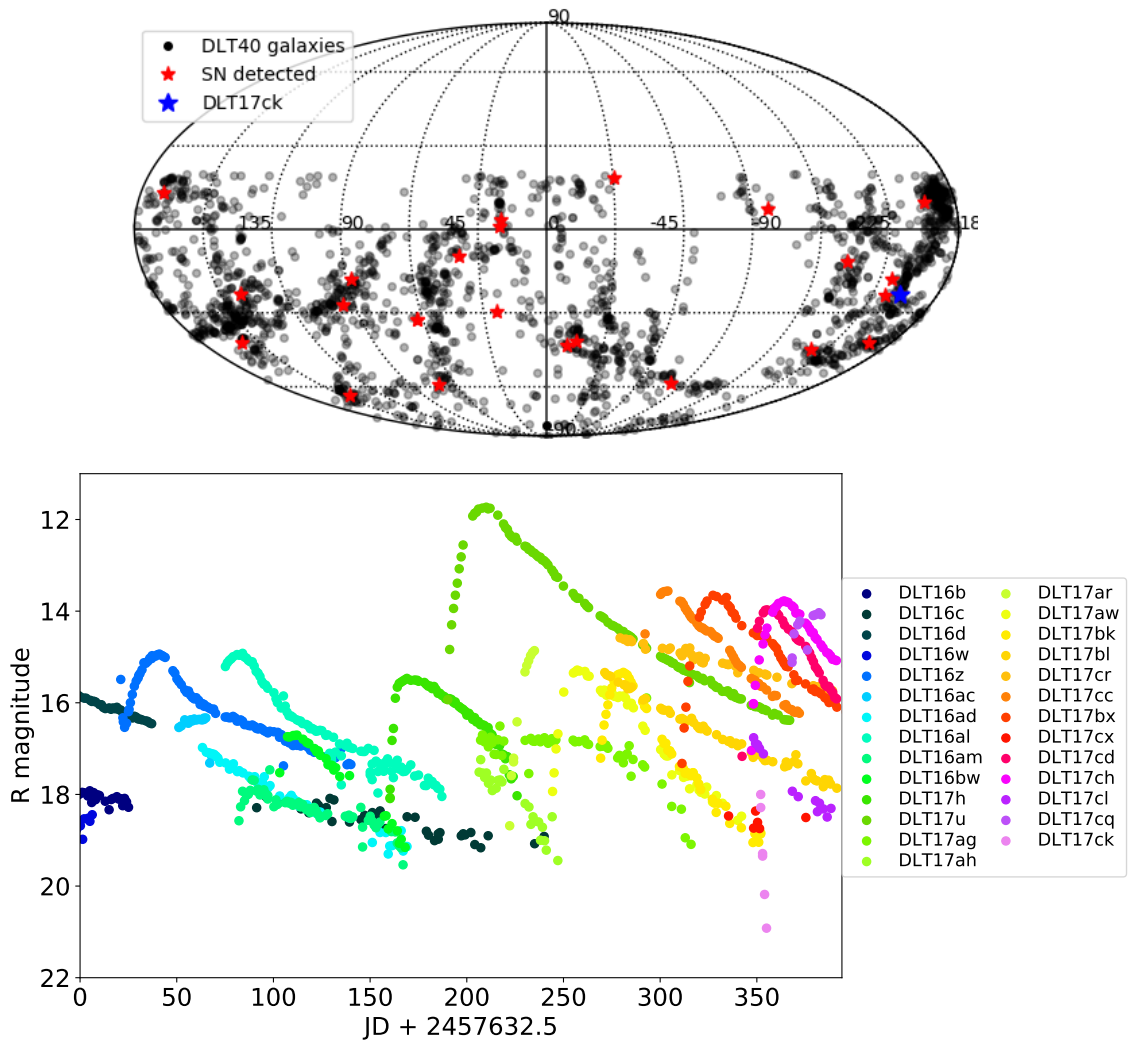
Figure 6.14: Top panel: The DLT40 galaxy catalog (black points). The SNe discovered during the first year of DLT40 are also shown (red points) together with the kilonova DLT17ck (blue point). Lower panel: DLT40 light curves of all the SNe (and the kilonova) discovered during the first year of the search.
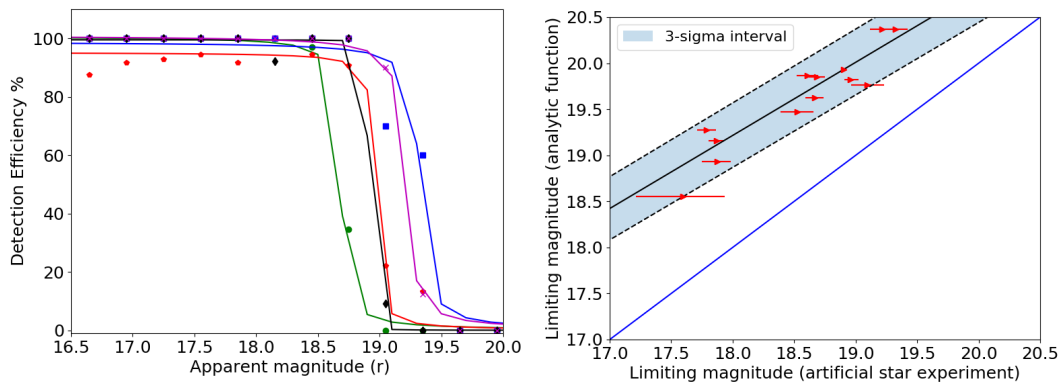
Figure 6.15: Left panel: Transient detection efficiency as a function of apparent magnitude for 5 DLT40 fields. The lines are the best fit to the curve. The limiting magnitude is chosen at 50% efficiency. Right panel: We compare the limiting magnitude computed for each image using its zeropoint and an analytical function with the limiting magnitude computed with artificial star experiments on difference images. This linear relation has been used to scale the limiting magnitude computed for each frame (given its zeropoint) to a more realistic limiting magnitude estimate for SN and/or kilonova detection.
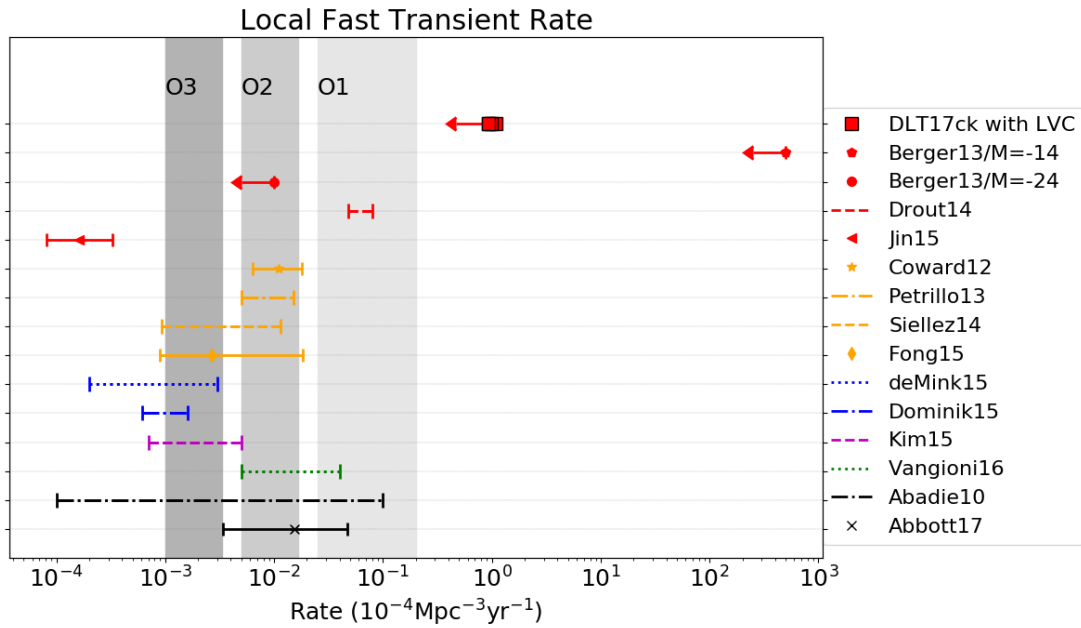
Figure 6.16: DLT40 limit on the kilonova rate (all three reddening scenarios) compared with the rate of sGRB [orange symbols, Coward et al., 2012; Fong et al., 2015; Petrillo et al., 2013; Siellez et al., 2014], the rates of BNS merger from stellar evolution [blue lines, Dominik et al., 2015; de Mink & Belczynski, 2015], cosmic nucleosynthesis [green line, Vangioni et al., 2016], galactic pulsar population [magenta line, Kim et al., 2015], gravitational waves [black lines, Abadie et al., 2010; Abbott et al., 2017c] and fast optical transients [red symbols, Berger et al., 2013b; Drout et al., 2014; Jin et al., 2015].
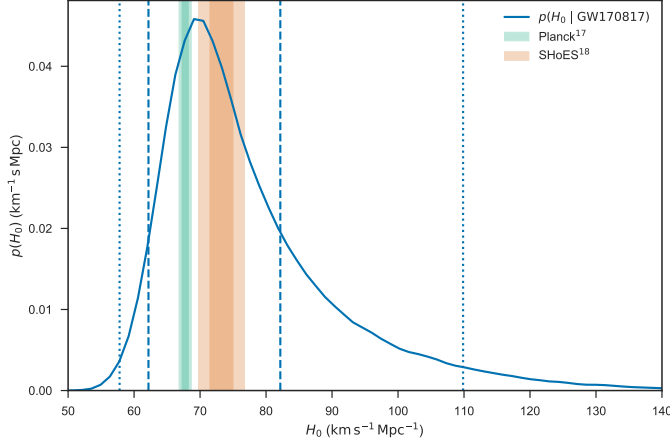
Figure 6.17: **GW170817 measurement of H_0.** Marginalized posterior density for H_0 (blue curve). Constraints at 1- and 2σ from Planck [Planck Collaboration et al., 2016] and SHoES [Riess et al., 2016] are shown in green and orange. The maximum a posteriori value and minimal 68.3% credible interval from this PDF is $H_0 = 70.0^{+12.0}_{-8.0}\,\mathrm{km\,s^{-1}\,Mpc^{-1}}$. The 68.3% ($1\sigma$) and 95.4% ($2\sigma$) minimal credible intervals are indicated by dashed and dotted lines.
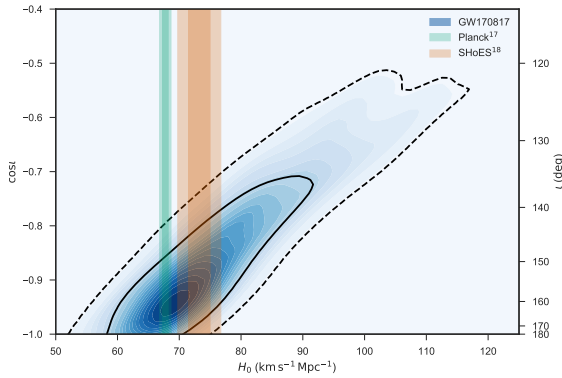
Figure 6.18: **Inference on H_0 and inclination.** Posterior density of H_0 and $\cos\iota$ from the joint GW-EM analysis (blue contours). Shading levels are drawn at every 5% credible level, with the 68.3% (1σ, solid) and 95.4% (2σ, dashed) contours in black. Values of H_0 and 1- and 2σ error bands are also displayed from Planck [Planck Collaboration et al., 2016] and SHoES [Riess et al., 2016]. As noted in the text, inclination angles near $180\,\mathrm{deg}$ ($\cos\iota = -1$) indicate that the orbital angular momentum is anti-parallel with the direction from the source to the detector.
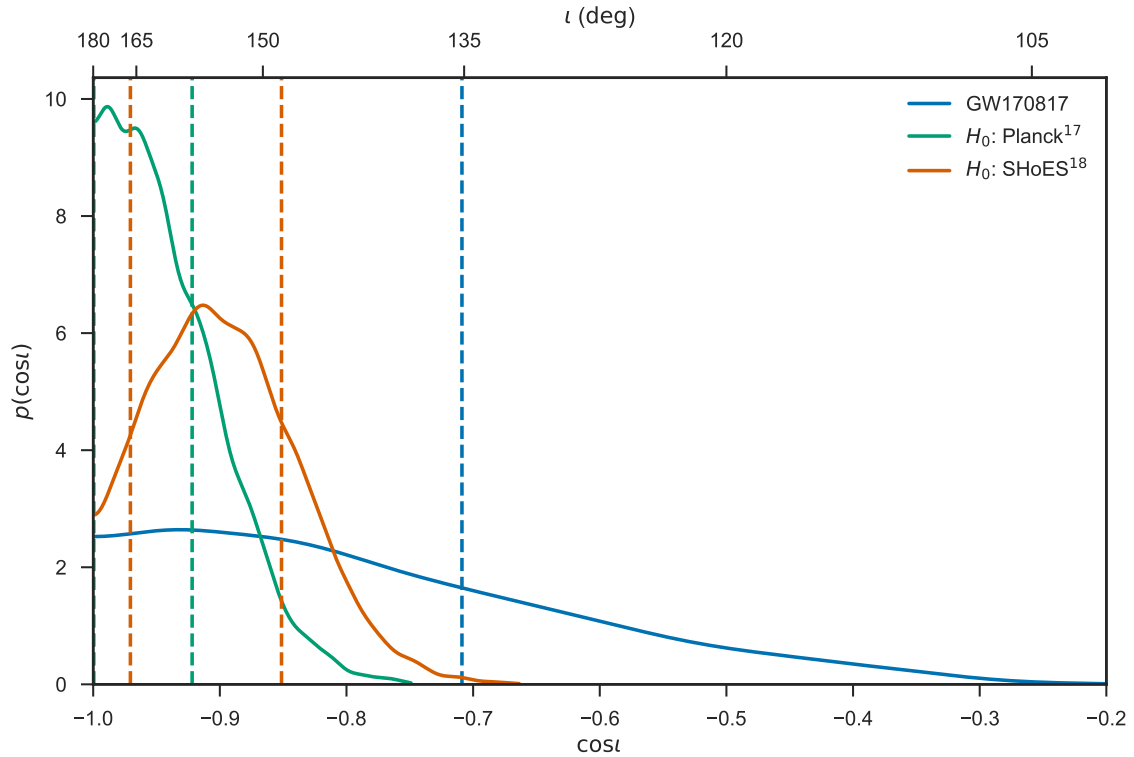
Figure 6.19: **Constraints on the inclination angle of GW170817.** Posterior density on $\cos \iota$, for various assumptions about the prior distribution of H_0. The analysis of the joint GW and EM data with a $1/H_0$ prior density gives the blue curve; using values of H_0 from Planck [Planck Collaboration et al., 2016] and SHoES [Riess et al., 2016] as a prior on H_0 give the green and red curves, respectively. Choosing a narrow prior on H_0 converts the precise Hubble velocity measurements for the group containing NGC 4993 to a precise distance measurement, breaking the distance inclination degeneracy, and leading to strong constraints on the inclination. Minimal 68.3% (1σ) credible intervals are indicated by dashed lines. Because our prior on inclination is flat on $\cos \iota$ the densities in this plot are proportional to the marginalised likelihood for $\cos \iota$.
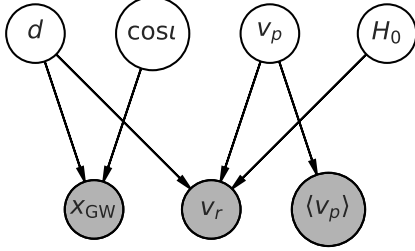
Extended Data Figure 6.1: **Graphical model illustrating the statistical relationships between the data and parameters.** Open circles indicate parameters which require a prior; filled circles described measured data, which are conditioned on in the analysis. Here we assume we have measurements of the GW data, x_{GW}, a recessional velocity (i.e. redshift), v_r, and the mean peculiar velocity in the neighborhood of NGC 4993, $\langle v_p \rangle$. Arrows flowing into a node indicate that the conditional probability density for the node depends on the source parameters; for example, the conditional distribution for the observed GW data, $p\left(x_{\mathrm{GW}} \mid d, \cos\iota\right)$, discussed in the text, depends on the distance and inclination of the source (and additional parameters, here marginalized out).
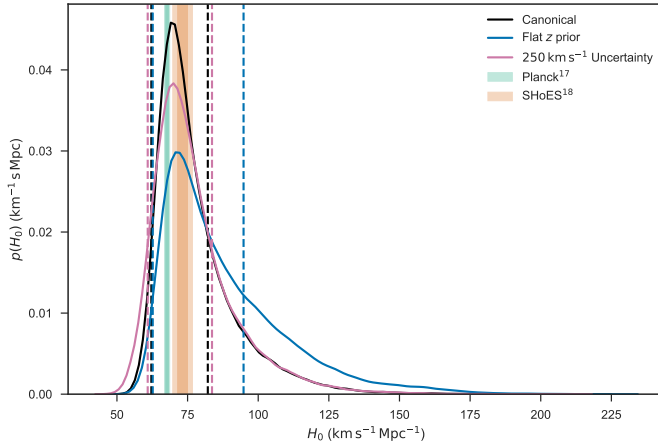
Extended Data Figure 6.2: **Using different assumptions compared to our canonical analysis.** The posterior distribution on H_0 discussed in the main text is shown in black, the alternative flat prior on z (discussed in the Methods section) gives the distribution shown in blue, and the increased uncertainty $(250\,\mathrm{km\,s^{-1}})$ applied to our peculiar velocity measurement (also discussed in the Methods section) is shown in pink. Minimal 68.3% (1σ) credible intervals are shown by dashed lines.

Extended Data Table 6.4: Summary of constraints on the Hubble constant, binary inclination, and distance

Parameter	68.3% Symm.	68.3% MAP	90% Symm.	90% MAP
$H_0/(\mathrm{km\,s^{-1}\,Mpc^{-1}})$	$74.0^{+16.0}_{-8.0}$	$70.0^{+12.0}_{-8.0}$	74.0^{+33}_{-12}	70.0^{+28}_{-11}
$H_0/(\mathrm{km\,s^{-1}\,Mpc^{-1}})$ (flat in z prior)	81^{+27}_{-13}	$71.0^{+23.0}_{-9.0}$	81^{+50}_{-17}	71.0^{+48}_{-11}
$H_0/(\mathrm{km\,s^{-1}\,Mpc^{-1}})$ (250 km s^{-1} σ_{v_r})	$74.0^{+16.0}_{-9.0}$	$70.0^{+14.0}_{-9.0}$	74.0^{+33}_{-14}	70.0^{+29}_{-14}
$\cos\iota$ (GW only)	$-0.88^{+0.18}_{-0.09}$	$-0.974^{+0.164}_{-0.026}$	$-0.88^{+0.32}_{-0.11}$	$-0.974^{+0.332}_{-0.026}$
$\cos\iota$ (SHoES)	$-0.901^{+0.065}_{-0.057}$	$-0.912^{+0.061}_{-0.059}$	$-0.901^{+0.106}_{-0.083}$	$-0.912^{+0.095}_{-0.086}$
$\cos\iota$ (Planck)	$-0.948^{+0.052}_{-0.036}$	$-0.982^{+0.060}_{-0.016}$	$-0.948^{+0.091}_{-0.046}$	$-0.982^{+0.104}_{-0.018}$
ι/deg (GW only)	152^{+14}_{-17}	167^{+13}_{-23}	152^{+20}_{-27}	167^{+13}_{-37}
ι/deg (SHoES)	$154.0^{+9.0}_{-8.0}$	$156.0^{+10.0}_{-7.0}$	154.0^{+15}_{-12}	156.0^{+21}_{-11}
ι/deg (Planck)	$161.0^{+8.0}_{-8.0}$	$169.0^{+8.0}_{-12.0}$	161.0^{+12}_{-12}	169.0^{+11}_{-18}
$d/(\mathrm{Mpc})$	$41.1^{+4.0}_{-7.3}$	$43.8^{+2.9}_{-6.9}$	$41.1^{+5.6}_{-12.6}$	$43.8^{+5.6}_{-13.1}$

Chapter 7

Conclusion

This chapter summarizes the thesis work and discusses perspectives for future research.

7.1 Summary of my contributions

In the last decades, thanks to the significant improvements in technology, scientist had the opportunity to enrich their understandings of the universe with more powerful tools. For instance, in EM channel a number of robotic telescopes are currently available to cover large portion of the sky every night in multiple wavelengths. More interestingly, GWs have finally been detected in 2015, which give us a further chance to detect a source in multiple messenger channels, obtaining complementary physics informations. In this thesis, I focused on the search of such kind of multi-messenger astronomical sources in the framework of GRAWITA and DLT40 collaborations. In particular the searching methods, data processing tools and our results are described in detail in this thesis. I contributed to the discovery and analysis of the the event on 17, August, 2017, with the first time detection of a binary neutron star merging, in both GW and EM channels. Here, I summarize my main contributions to the multi-messenger search, during my PhD stage from 2015-2018:

1. I developed and implemented a dedicated pipeline for VST images aimed to automatically select faint transients in large sky areas, that was used for the follow up of three GW triggers.

2. I contributed to produce accurate photometry for two special transients, iPTF15dld and ATLAS17aeu, in the framework of photometric and spectroscopic follow-up activated to determine their nature and possible association to the GW event.

3. I contributed the GW follow-up search campaign of the DLT40 collaboration, including the independently discovery of AT2017gfo (DLT17ck), which is subsequently identified as a kilonova. I led the work to evaluate the observed rate of kilonova event using DLT40 data.

4. I developed a machine learning approach to automatically exclude false transients, that was successfully implemented in the DLT40 supernova search.

5. I contributed to use the GW distance and the host galaxy recession velocity to study the expansion of the Universe.

6. I contributed through the GRAWITA collaboration to demonstrate that the transient AT2017gfo associated to GW170817 was a kilonova, the counterpart of the first gravitational-wave signal from a binary neutron-star coalescence. The GRAWITA data provided the first spectral identification of the kilonova emission, revealing signatures of the radioactive decay of r-process nucleosynthesis elements.

7.2   Directions for future work

GW detection network, namely LIGO, VIRGO, and somewhat later KAGRA, will start a new observing run by early 2019, which gives us more opportunities to detect multi-messenger sources. During the third GW-EM joint search, our aim is to exploit more telescopes for EM follow-up in particular the 0.9 m robotic Schmidt telescope in Asiago, for GRAWITA and additional 0.4m-class telescopes in Australia, Chile, and China, for DLT40. In this context it is crucial to continue to improve the ML algorithms implementation. We have to consider the expected improvement of GW interferometers sensitivities which will require to explore larger volume and more fainter sources. For this reason we are working to update our search strategy and data management tools.

The future promise huge amount of data. For instance LSST alone is expect to produce 10 million transient candidates per night enlarging by 2/3 order of magnitudes the resources required for data analysis. The works developed during my thesis and the on-going implementations are crucial to set up the ground for this new era were big data and multi-messenger are the keywords.

Appendices

Appendix A

Image difference pipeline

A.1 Overview

A widely used and most effective approach for transient detection is based on the difference of images taken at different epochs. In particular, I contributed to develop an image difference pipeline (`diff-pipe` [1]) for VST imaging systems based on the experiences from the SUDARE project [Cappellaro et al., 2015]. The pipeline is a collection of `python` scripts that include specialized tools for data analysis, e.g. `SExtractor` [2] [Bertin & Arnouts, 1996] for source extraction and `topcat`[3] / `stilts`[4] for catalog handling. For optical images taken from the ground, a main problem is that the PSF is different at different epochs, due to the variable seeing. The PSF match is secured by the `hotpants`[5] code [Becker, 2015], an implementation of the Alard [1999] algorithm for image analysis.

A.2 Installing the software

A.2.1 Software and hardware requirements

The development of `diff-pipe` was made on Unix systems. As mentioned, `diff-pipe` is a collection of `python` scripts. `diff-pipe` call a number of public or astronomical `python` libraries, e.g. `numpy`, `scipy`, `matplotlib`, and `astropy`, `astroquery`,

---

[1] `https://github.com/saberyoung/gw`
[2] `http://www.astromatic.net/software/sextractor`
[3] `http://www.star.bris.ac.uk/~mbt/topcat/`
[4] `http://www.star.bris.ac.uk/~mbt/stilts/`
[5] `http://www.astro.washington.edu/users/becker/v2.0/hotpants.html`

Figure A.1: Initializing interface of `diff-pipe`, which describes all assigned scripts.

`pyraf`, that can all be found in the `astroconda` distribution, see `https://astroconda.readthedocs.io/en/latest/`.

A.2.2 `diff-pipe` repository

`diff-pipe` is currently available only by our GW group. I uploaded a test version to my private github repository, `https://github.com/saberyoung/gw`.

A.2.3 Installation

To install from source, the first step is to uncompress and unarchive the archive:

    git clone git@github.com:saberyoung/gw.git

A new directory called gw should appear at the current position on disk. The user should move into the new directory and follow the instructions in the file called "README".

A.3 Using `diff-pipe` - design, usage and syntax

The `diff-pipe` is initialized in the shell with the following command:

    $ > gw

which make the collection of `python` scripts available to use, see Fig. A.1.

A.3.1   Configuration file

Several often used parameters are either defined as an environmental variable in shell, or stored as in the configuration file, for instance, the `sextractor` threshold. As an example, I show part of configuration file here:

```
1  [global]      ;    ――――――――     used by all scripts
2  PIXEL_SCALE:       0.214
3          ; size of pixel in arcsec
4  SATUR_LEVEL:    21000.0
5                  ; level (in ADUs) at which arises saturation
6  MAG_ZEROPOINT:      30.0
7           ; magnitude zero-point
8  [sextractor] ;    ――――――――――    used by sextractor (all scripts)
9  DETECT_MINAREA:      2.0
10         ; factor scale for fwhm
11 PHOT_APERTURE:  10,15,20
12               ; fixed apertures for photometry
13 PHOT_FLUXFRAC:       0.5
14          ; flux fraction[s] used for FLUX_RADIUS
15 ANALYSIS_THRESH:     1.5
16          ; in unit of detection threshold
17 BACK_SIZE:          64
18             ; Background mesh
19 [hotpants]   ;    ――――――――――  hotpants parameters
20 NRX:               6
21             ; number of image regions in x dimension
22 NRY:               6
23             ; number of image regions in y dimension
24 NSX:              15
25           ; number of each region's stamps in x dimension
26 NSY:              15
27           ; number of each region's stamps in y dimension
28 KO:               2
29             ; spatial order of kernel variation within region
30 BGO:              1
31             ; spatial order of background variation within region
32 [search]     ;    ―――――――――――――――――――――――――――――
33 THRESHOLD:          1.5
34             ; difference search threshold
```

diff_pipe configuration file
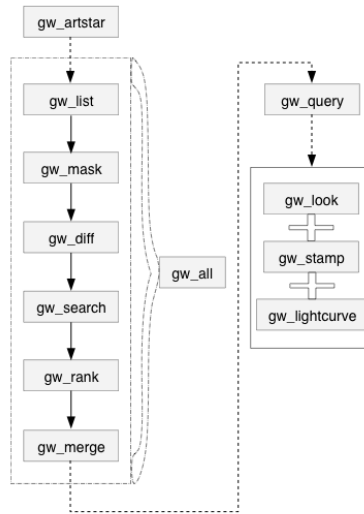
Figure A.2: Layout of the main `diff-pipe` procedures. Dashed arrows represent optional steps.

A.3.2   Scripts

Fig. A.2 outlines the main `diff-pipe` procedures. The standard steps include `gw_list`, `gw_mask`, `gw_diff`, `gw_search`, `gw_rank`, and `gw_merge`. Because of their dependency relationships, these scripts should be ran in order, either step by step separately, or together with `gw_all`. Parallel mode of operation was implemented in the new version which accelerated the process significantly. `gw_artstar` is designed to simulate artificial stars which can be then injected into frames with specific parameters, e.g. coordinates, magnitudes, etc. After the artificial star injected, the standard runs can be performed to search the input sources. This can be used to test the performances of the survey. `gw_query` can be used to query known databases, e.g. `Simbad`, `Ned`, `Skybot`, `Gaia`, etc, checking whether the candidate are known sources or they are located within known galaxies. `gw_look` is designed to show image stamps of candidate sources, together with complementary informations. `gw_stamp` is designed to create stamps for a given coordinate within a specific radius. `gw_lightcurve` generates accurate light curves, via PSF photometry, for selected sources.

In the following, I review scripts scope, usages and syntaxes:

A.3.2.1   gw_list

`gw_list` search images of a specific GW trigger at all epochs and pointings from the defined input directory, list them and their informations in order. Afterwards, it checks the astrometry of images, see if there are overlapping region, generating a diff-list, that records all images to be subtracted. All informations are stored in our `Mysql` database, which can be queried in `https://www.grawita.inaf.it/~gwpadova/phpMyAdmin/`.

The `gw_list` is run from the shell with the following syntax:

```
% gw_list [−h] [−p POINTING] [−v] [−c] trigger

List VStube reduced files or search status

positional arguments:
  trigger                 trigger name

optional arguments:
  −h, −−help              show this help message and exit
  −p POINTING, −−ponting POINTING
                          pointing number (default: all)
  −v, −−verbose           show detail (default: False)
  −c, −−clobber           CLobber existing files (default: False)
```

gw_list help file

The part enclosed within brackets is optional. Any "-Parameter Value" statement in the command-line overrides the corresponding definition in the configuration file or any default value.

A.3.2.2   gw_mask

As mentioned, the GRAWITA images are firstly calibrated by `VSTtube` and then archived to cluster for image handling of `diff-pipe`. `VSTtube` generate dedicated weight files, to remove the bad pixels, saturated stars, and so on. However, such weight files cannot be directly recognised by `Hotpants`. In `diff-pipe`, we use `gw_mask` to produce proper bad pixel mask file.

```
% gw_mask [−h] [−b BADPIX_LIM BADPIX_LIM] [−c] [−t THRESHOLD] [−v]
    trigger {g,r,i} date pointing

Build bad pixel masks

positional arguments:
  trigger                 trigger name
```

```
 7    {g , r , i }                     filter
 8    date                            epoch
 9    pointing                        pointing number
10
11  optional arguments:
12    −h ,  −−help              show this  help  message and exit
13    −b BADPIX_LIM BADPIX_LIM,  −−badpix_lim BADPIX_LIM
14                              Bad pixel mask limit (default: None)
15    −c ,  −−clobber           CLobber existing files (default: False)
16    −t THRESHOLD,  −−threshold THRESHOLD
17                              sextractor threshold (default: 2.0)
18    −v ,  −−verbose           Disable task progress report (default: False)
```

gw_mask help file

A.3.2.3 gw_diff

gw_diff is the most essential and time consuming step. The key part of gw_diff is the operation of `hotpants`, that is used to compare the source profiles in the two images, convolve the image with the best seeing to match the other, and perform image difference.

In the following is listed an example of to call of `hotpants`. All the parameters are read from the configuration file.

```
 1      hotpants = "hotpants −inim "+fnew+" −tmplim "+fref+\
 2          " −imi "+inweight1+\
 3          " −tmi "+inweight2+\
 4          " −tl −150 −il −150 "+\
 5          " −outim "+fdiff+\
 6          ' −nrx '+optlist['hotpants']['nrx']+\
 7          ' −nry '+optlist['hotpants']['nry']+\
 8          ' −nsx '+optlist['hotpants']['nsx']+\
 9          ' −nsy '+optlist['hotpants']['nsy']+\
10          ' −ko '+optlist['hotpants']['ko']+\
11          ' −bgo '+optlist['hotpants']['bgo']+\
12          ' −r '+str(rkernel)+' −rss '+str(radius)+\
13          ' −tu '+str(tuthresh)+' −tuk '+str(tucthresh)+\
14          ' −iu '+str(iuthresh)+' −iuk '+str(iucthresh)+\
15          ' −sconv −n '+normalize
16
17      pid = subprocess.Popen(shlex.split(hotpants),
18                  stdout=subprocess.PIPE, stderr=subprocess.PIPE)
19      output, error = pid.communicate()
```

```
20
21    pid = subprocess.Popen(["modhead",fdiff,"FWHM',
22              str(max_seeing)],stdout=subprocess.PIPE)
23    output,error = pid.communicate()
```

hotpants example

```
1 % gw_diff [−h] [−c] [−v] trigger {g,r,i} date_new date_ref coo
2
3 image difference with psf match (hotpants)
4
5 positional arguments:
6   trigger          trigger name
7   {g,r,i}          filter
8   date_new         date new
9   date_ref         reference epoch
10  coo              coordinate
11
12 optional arguments:
13  −h, −−help       show this help message and exit
14  −c, −−clobber    CLobber existing files (default: False)
15  −v, −−verbose    Enable task progress report (default: False)
```

gw_diff help file

A.3.2.4 gw_search

After image difference step, `gw_search` can be called to extract source list from the differencing images, via `sextractor`. The `sextractor` configuration file defines the options for extraction.

```
1     sexrun = "sex "+img+".fits"+\
2         " −catalog_name tmp_"+ss+'.'+outcatext+\
3         " −c "+gw_scripts+"default/default.sex"+\
4         " −PARAMETERS_NAME "+gw_scripts+"/default/default.param"+\
5         " −STARNNW_NAME "+gw_scripts+"/default/default.nnw"+\
6         " −FILTER_NAME "+gw_scripts+'/default/'+gauss+\
7         " −PIXEL_SCALE "+optlist['global']['pixel_scale']+\
8         " −PHOT_APERTURES "+optlist['sextractor']['phot_aperture']+\
9         " −ANALYSIS_THRESH  "+\
10             str(float(optlist['sextractor']['analysis_thresh'])*
                   threshold)+\
11        " −DETECT_MINAREA "+\
12             str(float(optlist['sextractor']['detect_minarea'])*fwhm)+\
```

```
13        " --DETECT_THRESH  "+str(threshold)+\
14        " --BACK_SIZE "+optlist['sextractor']['back_size']+\
15        " --MAG_ZEROPOINT "+optlist['global']['mag_zeropoint']+\
16        " --SATUR_LEVEL "+optlist['global']['satur_level']+\
17        " --SEEING_FWHM "+str(seeing)+\
18        " --VERBOSE_TYPE "+sex_verbose+\
19      " --CATALOG_TYPE "+outformat
20
21    pid = subprocess.call(shlex.split(sexrun))
```

sextractor example

```
1 % gw_search [-h] [-s {p,n,b}] [-c] [-v]  trigger {g,r,i} date_new
      date_ref coo
2
3 Search candidates
4
5 positional arguments:
6   trigger                trigger name
7   {g,r,i}                filter
8   date_new               date new
9   date_ref               reference epoch
10  coo                    pointing number
11
12 optional arguments:
13  -h, --help             show this help message and exit
14  -s {p,n,b}, --search {p,n,b}
15                         Search direction (p-ositive, n-egative, b-oth)
16                         (default: b)
17  -c, --clobber          Clobber existing files (default: False)
18  -v, --verbose          Enable task progress report (default: False)
```

gw_search help file

A.3.2.5 gw_rank

At this stage, we have a candidate transient source list, together with the image stamps. The next step is to select interesting transients that, in case, deserve detailed follow-up. However, as shown in chapter 1, there are many bogus candidates, that need to be scrutinized. To reduce the need for human interaction we developed a ranking algorithm.

gw_rank, which is referred as TR in the thesis, is a tool to rank the candidates by thresholding several measured parameters for the sources, most of which obtained
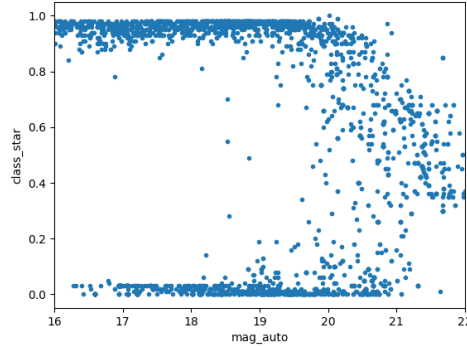
Figure A.3: The parameter class_star estimated by Sextractor is applying a machine learning algorithm to judge if the source is a star-like or not. The plot shows that the parameter, class_star is significant for sources up to 20 mag. Here, the candidates are selected from the VST residual image when triggering GW170814 towards 1 deg^2 FoV region with the center ra=39.7 and dec=45.3 between the subtraction of epoch 2017-08-14 and reference 2017-09-28 in r band.

from `sextractor`. The selected parameters and the thresholding conditions are based on artificial star experiments. For instance, the parameter class_star is estimated by `sextractor` that can preliminary judge one source like a "star" or "galaxy". In Fig. A.3 shows the estimation of class_star, as a function of magnitude, for a field of sources. As shown, the class_star evaluation is significant when the sources are bright, and as a consequence, the combination of class_star and mag_auto can be used to judge if the candidate is pointed or extended.

`gw_rank` assigns to each source an initial score (60), a further parameter judgement would increase or decrease the score. The source list can be then listed in order of ranking, showing first the most interesting objects.

Our current ranking conditions are shown below, in Tab A.1.

Table A.1: Condition of `gw_rank`

condition	threshold	score
mask threshold	$mask >= 3$	-30
mask threshold	$mask >= 2$	-30
not detected on target	$X\_IMAGE\_2 > 0$	-30
low isoarea	$ISOAREA\_IMAGE\_1 < 2.*fwhm$	-30

low isoarea	$ISOAREA\_IMAGE\_1 < 3.*fwhm$	-30
FWHM too high	$FWHM\_IMAGE\_1/fwhm > 1.75$	-30
FWHM too high	$FWHM\_IMAGE\_1/fwhm > 2.25$	-30
low FLUXRADIUS on target	$FLUX\_RADIUS\_2/(fwhmn/1.6) < 0.65$ $\&search = 'P'$	-30
low FLUXRADIUS on target	$FLUX\_RADIUS\_2/(fwhmn/1.6) < 0.65$ $\&search = 'N'$	-30
low FLUXRADIUS	$FLUX\_RADIUS\_1/(fwhm/1.6) < 0.6$	-30
high FLUXRADIUS	$FLUX\_RADIUS\_1/(fwhm/1.6) > 1.6$	-30
low class star	$CLASS\_STAR\_1 < 0.4 \quad \& \quad MAG\_AUTO\_1 < 20$	-30
low class star	$CLASS\_STAR\_1 < 0.03 \quad \& \quad MAG\_AUTO\_1 < 2$	-30
near bright star	$CLASS\_STAR > 0.7 \quad \& \quad MAG\_AUTO < 17$	-45
good pixel	$rgood <= 0.70$	-30
good pixel	$rgood <= 0.60$	-30
near galaxy	$X\_IMAGE > 0$ $\&CLASS\_STAR < 0.3$ $\& MAG\_AUTO < 19$	30
cross talk	$CrossTalk < 20$	-90

```
% gw_rank [-h] [-c] [-v] trigger {g,r,i} date_new date_ref pointing

Rank candidates

positional arguments:
  trigger          trigger name
  {g,r,i}          filter
  date_new         date new
  date_ref         reference epoch
  pointing         pointing number

optional arguments:
  -h, --help       show this help message and exit
  -c, --clobber    CLobber existing files (default: False)
  -v, --verbose    Enable task progress report (default: False)
```

gw_rank help file

As described in chapter 4, an alternative ranking algorithm, `asml`, using a machine learning approach, has been tested, and is being implemented in `gw_rank`. `asml` details are presented in section B.

A.3.2.6   gw_merge

The candidate list include duplicates since a transient source can appear in different images. `gw_merge` is used to merge them to the final global source list.

```
% gw_merge [-h] [-p POINTING] [-x XTASKS] [-c] [-a] [-s SCORE] [-v]   {
    G184098,G211117,GW170814} {g,r,i}

merge all epochs for one pointing and then join all pointings

positional arguments:
  {G184098,G211117,GW170814}
                          trigger name
  {g,r,i}                 filter

optional arguments:
  -h, --help              show this help message and exit
  -p POINTING, --ponting POINTING
                          pointing number or range (eg. 0,10) (default:
                            None)
  -x XTASKS, --xtasks XTASKS
                          run g-lobal, a-ll (default: ga)
  -c, --clobber           CLobber existing files (default: False)
  -a, --artstar           if arstar experiment or not (default: False)
  -s SCORE, --score SCORE
                          score threshold (default: 30)
  -v, --verbose           Enable task progress report (default: False)
```

gw_merge help file

A.3.2.7   gw_all

Till the point, we have accomplished all the standard `diff-pipe` procedures. If the processing of the different pointings/epochs is sequential, the accomplishment creates a final source list, indicating all the candidate transients, Considering the process consuming time is fairly long, i.e. up to two days for 90 pointings in 6 epochs. Therefore we combined all tasks in one script, `gw_all` that provides an option for users to run

the single steps together. And also, we offer an option to run the pipeline in parallel
mode.

```
1 % gw_all [-h] [-d DATE_NEW] [-p POINTING] [-x XTASKS] [-c] [-v] [-n] [-
    s SCORE] [-a] [--core CORE] [--phot {sex,aper,psf}] {G184098,G211117,
    G297595,GW170814} {g,r,i}
2
3 Run mask,diff,search,rank,merge
4
5 positional arguments:
6   {G184098,G211117,G297595,GW170814}
7                         trigger name
8   {g,r,i}               filter
9
10 optional arguments:
11   -h, --help            show this help message and exit
12   -d DATE_NEW, --date_new DATE_NEW
13                         date (default: None)
14   -p POINTING, --pointing POINTING
15                         pointing (default: None)
16   -x XTASKS, --xtasks XTASKS
17                         run m-ask, d-iff, s-earch, r-ank, g-lobal, a-ll (
                            default: mdsrga)
18   -c, --clobber         CLobber existing files (default: False)
19   -v, --verbose         Enable task progress report
20       (default: False)
21   -n, --noproc          Show operation to be performed (default: False)
22   -s SCORE, --score SCORE
23                         score threeshold (default: 30)
24   -a, --artstar         if arstar experiment or not (default: False)
25   --core CORE           number of cores for parallel computing; 1 means
        no
26                         parallel (default: 1)
27   --phot {sex,aper,psf}
28                         photometry methods (default: aper)
```

gw_all help file

The parallel mode is run by using a **parallel python** (pp) module, used as follows:

```
1 import pp
2 ppservers = ("10.0.0.1",)
3 ncpus = int(ncore)  # choose cores as you want
4 job_server = pp.Server(ncpus, ppservers=ppservers)
5
6 # add task
```

```
7  jobs.append(job_server.submit(gw_mask.gw_bpm, (datain,dataou,filein,
       optlist,'',clobber,2.5,verbose), (), ("gw","numpy",)))
8  jobs.append(job_server.submit(gw_diff.gw_diff, (datain,dataou,img,refimg,
       trigger,filtro,ra,dec,optlist,clobber,verbose), (), ("gw","numpy","
       subprocess","shlex",)))
9  jobs.append(job_server.submit(gw_search.gw_search, (datain,dataou,dir1,
       dir2,trigger,filtro,ra,dec,epoch1,epoch2,optlist,'b',clobber,verbose),
        (), ("gw","subprocess","numpy",)))
10 jobs.append(job_server.submit(gw_rank.gw_rank, (dataou,trigger,filtro,d,
       imglist[p][d],p,args.clobber,args.verbose,False,'','','',''), (gw_rank
       .gw_score,), ("pyfits","gw","subprocess","numpy",)))
11 jobs.append(job_server.submit(gw_merge.gw_global_rank, (dataou,trigger,
       filtro,imglist,args.verbose,False,'','','','',args.clobber), (), ("
       pyfits","gw","subprocess","numpy",)))
12 jobs.append(job_server.submit(gw_merge.gw_all_rank, (dataou,trigger,
       filtro,imglist,args.score,args.clobber,args.verbose,False,'',''), (),
       ("pyfits","gw","subprocess","numpy",)))
13
14 # do task
15 job_server.print_stats()
```

parallel python example

A.3.2.8   gw_query

The standard `diff-pipe` procedures generate a source list, that provide targets for
further follow-up. In order to know if they are know source or newly burst, or to check
if they're located close to a galaxy, the `gw_query` script is designed to query the sources
with some public databases.

```
1  % gw_query [-h] [-r RADIUS] {G184098,G211117,G297595,GW170814} {g,r,i}  {
       skybot,simbad,ned,gaia,ogle}
2
3  Query database
4
5  positional arguments:
6    {G184098,G211117,G297595,GW170814}
7                          trigger name
8    {g,r,i}               filter
9    {skybot,simbad,ned,gaia,ogle}
10                         database
11
12 optional arguments:
13   -h, --help            show this help message and exit
```

Figure A.4: Example to show the `gw_look` interface.

```
14   −r RADIUS, −−radius RADIUS
15                          radius (default: 3)
```

gw_query help file

A.3.2.9   gw_look

`gw_look` can be used to visualize the candidates, sorted with score, from either the final global source list, or list of specific pointing and epoch. In the process of visual inspection, user attach a label to the source that is then stored into our database. In Figure A.4 is showing the `gw_look` interface.

```
1  %gw_look.py [−h] [−d DATE_NEW] [−p POINTING] [−n NSTART] [−u] [−g] [−i]
          [−w] [−c] [−r] [−v]   {G184098,G211117,G297595,GW170814} {g,r,i}
2
3  Show stamps for candidates sorted
4
5  positional arguments:
6    {G184098,G211117,G297595,GW170814}
7                          trigger name
8    {g,r,i}                 filter
9
10 optional arguments:
11   −h, −−help             show this help message and exit
```
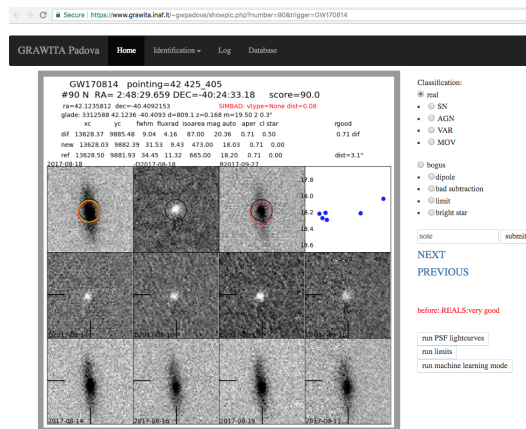
Figure A.5: Example to show the `gw_look` webpage.

```
12    -d DATE_NEW, --date_new DATE_NEW
13                        date (default: None)
14    -p POINTING, --pointing POINTING
15                        pointing number or coordinates (default: None)
16    -n NSTART, --nstart NSTART
17                        Number of candidate to start (default: 1)
18    -u, --unknown       Show unknown sources (SIMBAT/SKYBOT) (default:
          False)
19    -g, --galaxy        Show sources near catalogued galaxies (default:
          False)
20    -i, --igaia         Show sources from gaia catalog (default: False)
21    -w, --web           Web output (default: False)
22    -c, --clobber       Clobber existing stamps (default: False)
23    -r, --rankshow      show ranking scores (default: False)
24    -v, --verbose       Enable task progress report (default: False)
```

gw_look help file

Besides the terminal version of gw_look, I designed `https://www.grawita.inaf.it/~gwpadova`, with `PHP`, in order to make the eyeballing process more friendly for a group of users. Figure A.5 is showing the `gw_look` webpage available to registered users, providing options for users, which can be used for labelling candidates.

A.3.2.10 gw_stamp

`gw_stamp` provide `gw_look` interface via input coordinates, instead of showing candidates from high ranking.

```
1 % gw_stamp [−h] [−n NUM] [−p POINTING] [−c CUTS] [−s SIZE] [−r]   trigger
      {g,r,i} coo
2
3 Show stamps for arbitrary position
4
5 positional arguments:
6   trigger                 trigger name
7   {g,r,i}                 filter
8   coo                     Stamp center (ra,dec)
9
10 optional arguments:
11  −h, −−help              show this help message and exit
12  −n NUM, −−num NUM       num (default: 0)
13  −p POINTING, −−ponting POINTING
14                          pointing (default: None)
15  −c CUTS, −−cuts CUTS    Cuts (low,high) (default: None)
16  −s SIZE, −−size SIZE    Stamp window size (default: 50)
17  −r, −−rankshow          show ranking scores (default: False)
```

gw_stamp help file

A.3.2.11   gw_lightcurve

`gw_look` can provide a preliminary light curve, based on aperture photometry. In order to get a more accurate photometry, `gw_lightcurve` adopts PSF photometry, as is implement in the SNOoPY package. See `http://sngroup.oapd.inaf.it/snoopy.html` for more details about SNOoPY.

```
1 %gw_lightcurve.py [−h] [−p POINTING] [−n] [−−size SIZE] [−s SNRLIM]   [−−
      recenter] [−r {l,e}] [−x XTASKS] [−v] trigger {g,r,i} coo
2
3 Measure accurate light curve for one object
4
5 positional arguments:
6   trigger                 trigger name
7   {g,r,i}                 filter
8   coo                     candidate number or coordinates (hh:mm:ss or deg
      or _x,_y pixels)
9
10 optional arguments:
11  −h, −−help              show this help message and exit
12  −p POINTING, −−pointing POINTING
13                          pointing number (default: None)
```

```
14   −n , −−nomask              Do  not  use  bad  pixel  mask  in  hotpants  (default :
         False )
15   −−size  SIZE               image  section  size  (default :  1500)
16   −s  SNRLIM,  −−snrlim  SNRLIM
17                              S/N  threshold  for  limit  (default :  2.5)
18   −−recenter                 recentering  (default :  False )
19   −r  {l , e}                 reference  association :  l−ate , e−arly  [l]  (default :
20                              None )
21   −x  XTASKS,  −−xtasks  XTASKS
22                              run  t−rim ,  d−iff ,  s−how  img ,  p−sf ,  f−it ,  l−ight
                                   curve
23                              (default :  tdspfl )
24   −v ,  −−verbose             Enable  task  progress  report  (default :  False )
```

gw_lightcurve help file

A.3.2.12   gw_artstar

In order to test the performance of the VST transient search, we design the script, `gw_artstar`. It can be used to manually inject in the target image a number of fake stellar sources simulated using `Daophot/ADDSTAR`. The standard `diff-pipe` procedures are then run, the resulting source list is cross matched with the injected source list, to verify the number of recovered sources . The fraction of recovered over injected sources is defined as the detection efficiency, while the limiting magnitude can be defined as the magnitude where the detection efficiency is 50%. `gw_artstar` is currently being upgraded, in order to be further used to simulate real sources, for machine learning training samples.

```
1 % gw_artstar  [−h]  [−f  {g , r , i }]  [−d  DATE_NEW]  [−p  POINTING]  [−c ]  [−v ]   [−n
     ]  [−e  EXPERIMENT]  [−x  XTASKS]  [−s  SEGMENT]  [−m  MAGART]  [−t  THRESHOLD]
     [−−b  BADPIX_LIM  BADPIX_LIM]  [−−trial ]   [−−show]  [−−fit  {l ,L, e , d}]   {
     G184098 , G211117}
2
3 Perform  artificial  star  experiment
4
5 positional  arguments :
6   {G184098 , G211117}       trigger  name
7
8 optional  arguments :
9   −h ,  −−help               show  this  help  message  and  exit
10   −f  {g , r , i } ,  −−filter  {g , r , i }
11                              filter  (default :  None )
12   −d  DATE_NEW,  −−date_new  DATE_NEW
```

```
13                              date ( default : None)
14   −p POINTING , −−pointing POINTING
15                              pointing number or range ( eg . 0 ,10) ( default :
                                   None)
16   −c , −−clobber           CLobber existing files ( default : False )
17   −v , −−verbose           Enable task progress report ( default : False )
18   −n , −−noproc            Show operation to be performed ( default : False )
19   −e EXPERIMENT , −−experiment EXPERIMENT
20                              Number of artstar experiments ( default : 1)
21   −x XTASKS , −−xtasks XTASKS
22                              run c−opy , p−sf , a−dd star run m−ask , d−iff , s−
                                   earch ,
23                              r−ank , g−lobal , j−udge , f−ind , ( a−ll ) ( default :
24                              cpamdsrgj )
25   −s SEGMENT , −−segment SEGMENT
26                              Segment (0 for whole image ) ( default : 3)
27   −m MAGART , −−magart MAGART
28                              Artifical star mag range −step && model injection
                                   (−m
29                              model , kiloniva ,2) kilonova7 sGRB2 lGRB2 ( default :
30                              20. ,20. ,.5)
31   −t THRESHOLD , −−threshold THRESHOLD
32                              sextractor threshold ( default : 3)
33   −b BADPIX_LIM BADPIX_LIM , −−badpix_lim BADPIX_LIM BADPIX_LIM
34                              Bad pixel mask limit ? ( default : None)
35   −−trial                  try and get the reclist ( default : False )
36   −−show                   Show plot ( default : False )
37   −−fit {l ,L, e , d}        fitting method : l−inear , L−og , e−xp , d−rop (
         default :
38                              None)
```

gw_artstar help file

Appendix B

Machine learning algorithms

B.1 Overview

I implemented a machine learning tool (`asML`) for candidates ranking, and hereafter tested its performance with both VST and DLT40 images. Here, I present the `asML`, by taking its implement for DLT40, as an example.

B.2 Current status

`asml` is currently still under testing, and partly available in my github repository, `https://github.com/saberyoung/asML`.

B.3 Design and usage of `asml`

B.3.1 Machine Learning with `sklearn`

The `dlt40ml` is run from the shell with the following syntax:

```
%dlt40ml.py filename or prog --type b or prog --type j

> dlt40 machine learning function

Options:
  --version        show program's version number and exit
  -h, --help       show this help message and exit
  --database       Build table ML_candidates
  --npz            Build table ML_candidatesStore matix in npz file
```
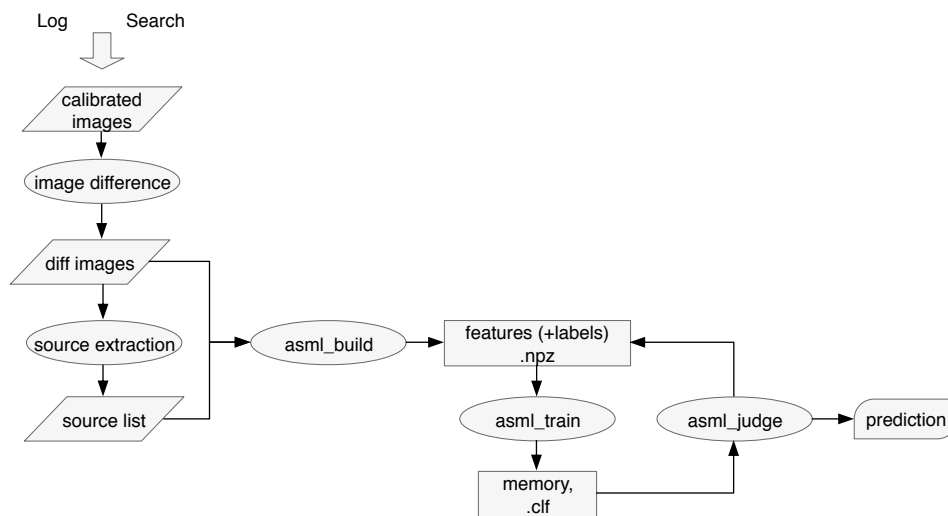
Figure B.1: Flowchart presenting the `asml` procedures.

```
10   −−test              split npz into training and test set
11   −−clf               do ML to create memory − clf file
12   −−runml=RUNML       −−runml filename          [none]
13   −−memory=MEMORY     clf
14   −−type=TYPE         −−type: [pre] check, [c]reate memory, [b]uild dataset,
15                       [e]yeball library or [j]udge ML or [p]redict ML [m]
                            ulti−ml
16   −−size=SIZE         −−stamp size      [20]
17   −−model=MODEL       −−model ML model selection
18                       Supervised/Classification:see database           [2]
19   −−tsize=TSIZE       −−tsize test_size       ML parameters    [0.2]
20   −−nshow=NSHOW       −−nshow Number of candidates for eyeballing      [100]
21   −c, −−clobber       clobber files
22   −−show              show candidates one by one                       [
        False]
23   −v, −−verbose       Show statistics plot
```

dlt40_ml help

Fig. B.1 outlines the main `asML` procedures: Firstly, `asML` offer an option to visualize the candidate's stamps, enabling the user to prepare and store a training/test set. The classified candidate list is stored in the `Mysql` database.

Then, `asML` can be used to extract feature, and labels only if user want to test

with unsupervised learning, for each object. As mentioned in chapter 4, `ml_build_npz`
script offers three options for the feature extraction, namely, M1, M2, and M3. As
an example, I show the code selection for M1, that makes use of image stamps as ML
feature, as following:

```
1   # Step 1 - read stamp matrices, bu querying classified source list,
        together with stored images
2   # The matrix should be normalized
3   matrixlist = []
4   label = []
5   command = ['select * from ML_candidates']
6   lista = dlt40.dlt40sql.query(command, dlt40.dlt40sql.conn)
7   for nn, line0 in enumerate(lista):
8       img = line0['filepath']+line0['filename']
9       cx = line0['xpos']
10      cy = line0['ypos']
11      _cl = line0['class']
12      matrix = read_fits(img, cx, cy, _size)
13      if len(matrix)>0:
14          nmatrix = norm_matrix(matrix)
15      matrixlist.append(nmatrix[0])
16      label.append(_cl)
17      print nn, 'of', len(lista)
18  X, y = np.array(matrixlist), np.array(label)
19
20  # Step2 - store data to npz file
21  np.savez(memodir + npzfile, X=X, y=y)
```

ml_build_npz example

`ml_build_npz` reads and normalizes stamps and store the result, together with label
informations in a .npz file, a zipped file archive, using a tool from the `Numpy` library.
After the data have been prepared we use `scikit-learn` (`sklearn`) to run a ML
process. The usage of `scikit-learn` is fully described in `http://scikit-learn.org/`.
The outcomes of the ML training, namely the ML memory, can be stored into a .clf
file using `joblib`. The `ml_build_clf` shown in the following, describes this process:

```
1   # Step 1 - read raw data from npzfile, as 2 dictionaries, that, X for
        features, and y for labels.
2   # in particular, X should be reshaped as a 1-d array, because sklearn
        works for 1-d data.
3
4   npzpath, npzfile, _id = check_memory_npz(_size, 'full')
5   _rr = np.load(npzpath+npzfile)
```

```
 6     X, y = _rr ['X'], _rr ['y']
 7     X =  X.reshape (X.shape [0], -1)
 8
 9     # Step 2 - peferom ML on pre-processed data
10     # model is chosen in advance, namely, which build-in models, e.g.
           random forest, or decision trees, or ...
11
12     from sklearn import clone
13     clf = clone (model)
14
15     # A judging process, which is simple and I will now show here, have
           been done in advance to judge the ML type.
16     # if the chosen model is supervised or unsupervised, will decide what
           data is need for ML training
17
18     if _mtype == 'supervised':
19         clf = model.fit (X, y)
20     elif _mtype == 'unsupervised':
21         clf = model.fit (X)
22     else:
23         sys.exit ('model to be developed !!!')
24
25     # Step 3 - store clf memory
26     joblib.dump( clf, memodir + clffile )
```

ml_build_clf example

A further *ML-judge* function is designed to evaluate the ML performances. The idea is to split the known samples into two parts, T1 and T2, that ML is trained with T1, and tested with T2. After ML tested, a number of merits can be adopted to visualize the performance:

1. built-in methods: `sklearn` provides several merits to show the ML performances, throughout built-in methods. Different methods are dedicated for specific algorithms, and their details are presented online. Here, I show some simple examples:

```
1     # Step 1 - perform ML with training dataset
2     clf = _model.fit (X_train, y_train)
3
4     # Step 2 - call several built-in methods
5     # Notice that not all of them are available for all algorithms,
           for instance, only random forest can provide the feature
           importance.
6     # Usages are described in detail in sklearn webpages
```

```
7
8      scores = clf.score(X_test, y_test)
9      y_pred = clf.predict(X_test)
10     y_prob = clf.predict_proba(X_test)
11     y_prob = clf.decision_function(X_test)
12     y_importance = clf.feature_importances_
13     ......
```

<div align="center">built-in methods</div>

2. A confusion matrix: `sklearn` provides also an option for generating the confusion matrix.

```
1  # Step 1 - define the functions for visualization of confusion
        matrix
2  def plot_confusion_matrix(cm, classes, normalize=False, title='
        Confusion matrix', cmap=plt.cm.Blues):
3      """
4      This function prints and plots the confusion matrix.
5      Normalization can be applied by setting 'normalize=True'.
6      """
7      plt.imshow(cm, interpolation='nearest', cmap=cmap)
8      plt.title(title)
9      plt.colorbar()
10     tick_marks = np.arange(len(classes))
11     plt.xticks(tick_marks, classes, rotation=45)
12     plt.yticks(tick_marks, classes)
13
14     if normalize:
15         cm = (cm.astype('float') / cm.sum(axis=1)[:, np.newaxis]).
                round(2)
16         print("Normalized confusion matrix")
17     else:
18         print('Confusion matrix, without normalization')
19
20     print(cm)
21
22     thresh = cm.max() / 2.
23     for i, j in itertools.product(range(cm.shape[0]), range(cm.shape
            [1])):
24         plt.text(j, i, cm[i, j],
25                  horizontalalignment="center",
26                  color="white" if cm[i, j] > thresh else "black")
27
28     plt.tight_layout()
```

```
29       plt.ylabel('True label')
30       plt.xlabel('Predicted label')
31       plt.show()
32
33 # Step 2 - build in the confusion matrix
34 from sklearn.metrics import confusion_matrix
35 cnf_matrix = confusion_matrix(y_test, y_pred)
36 plt.figure(figsize=cnf_matrix.shape)
37 cllist = []
38 for ii,jj in zip(y_test,y_pred):
39    cllist.append(ii)
40    cllist.append(jj)
41 classes=np.unique(cllist)
42
43 # Step 3 -call for visualization
44 plot_confusion_matrix(cnf_matrix, classes=classes, normalize=False)
```

confusion matrix example

3. The figure of merit, described in the thesis, namely, the histograms of each class, and the ROC curve for showing the FPR against MDR.

```
1 # Step 1 - define functions for generating the histograms, and
      depending on the input threshold, y_diff, output the
      corresponding MDR and FPR.
2 def hist_plot(prob, flag, ydiff, verbose):
3     pp = []
4     for ii in range(len(prob)): pp.append(prob[ii])
5     pp=np.array(pp)
6
7     r_real = pp[np.where(flag=='real')]
8     r_bogus = pp[np.where(flag=='bogus')]
9
10     if verbose:
11         plt.figure(1)
12         plt.hist(r_real, 50, histtype='step', color='r', label='real
             ')
13         plt.hist(r_bogus, 50, histtype='step', color='k', label='
             bogus')
14         plt.plot([ydiff,ydiff],[0,1200],'--')
15         plt.legend(prop={'size': 10})
16         plt.xlabel('Hypothesis')
17         plt.ylabel('Frequency')
18
19     #   MDR,FPR
```

```
20        _bogus = float(len(np.where(r_real>ydiff)[0]))
21        _real = float(len(np.where(r_bogus<ydiff)[0]))
22
23        return _bogus/len(np.where(flag=='real')[0]),\
24            _real/len(np.where(flag=='bogus')[0])
25
26  # Step 2 - set a range as for threshold running,
27  mdrlist,fprlist,answ = [],[],''
28  for ydiff in np.arange(0,1,0.01):
29
30    # for each specific threshold, the defined function is call for
           the histograms
31    mdr,fpr = hist_plot(y_prob,y_test,ydiff,verbose)
32    mdrlist.append(mdr)
33    fprlist.append(fpr)
34    if answ == 'Y':continue
35    answ = raw_input('continue(Y/N)')
36
37  # Step 3 - after threshold running obtain the ROC curve
38  plt.plot(mdrlist,fprlist,'-')
39  plt.legend(prop={'size': 10})
40  plt.xlabel('MDR')
41  plt.ylabel('FPR')
42  raw_input('...')
```

confusion matrix plot

B.3.2   Deep Learning with `tensorflow`

In `asml` I also implemented the use of deep learning with `tensorflow`. `tensorflow` is
an open source software library for deep learning, which a particular branch of machine
learning with special application for image recognition. `tensorflow` is developed by
researchers and engineers from the Google Brain team. Following is a simple example
showing the working process of `tensorflow` on DLT40 image recognition, using the
Inception-v3 model:

```
1  def classify_init(_label,_pb):
2      os.environ['TF_CPP_MIN_LOG_LEVEL']='2'
3      label_lines = [line.rstrip() for line
4                    in tf.gfile.GFile(_label)]
5      with tf.gfile.FastGFile(_pb, 'rb') as f:
6          graph_def = tf.GraphDef()
7          graph_def.ParseFromString(f.read())
```

```
8          _ = tf.import_graph_def(graph_def, name='')
9      with tf.Session() as sess:
10          softmax_tensor = sess.graph.get_tensor_by_name('final_result:0')
11      return sess, softmax_tensor, label_lines
12
13 def classify(img, sess, softmax_tensor, label_lines, verbose):
14      scorelist = {}
15      image_data = tf.gfile.FastGFile(img, 'rb').read()
16      ##
17      predictions = sess.run(softmax_tensor, \
18                                {'DecodeJpeg/contents:0': image_data})
19      top_k = predictions[0].argsort()[-len(predictions[0]):][::-1]
20      for node_id in top_k:
21          human_string = label_lines[node_id]
22          score = predictions[0][node_id]
23          if verbose:
24              print('%s (score = %.5f)' % (human_string, score))
25          scorelist[human_string] = score
26    return scorelist
27
28 sess, softmax_tensor, label_lines = classify_init('retrained_labels.txt', '
        retrained_graph.pb')
29 output = classify(_ff, sess, softmax_tensor, label_lines, verbose)
```

a tensorflow example

Appendix C

Galaxy priorization script

C.1 Overview

For DLT40 I developed a galaxy priorization script that is used for an efficient search of GW counterpart signal. Here, I show its design and usage.

C.2 Current status

The galaxy priorization script is currently embedded into the DLT40 pipeline, and a test version is also available in my github repository, `https://github.com/saberyoung/galaxy_priorization`.

C.3 Design and usage

The idea is to assign score to galaxies selected from a given catalog, by weighting with not only their position in the GW probability map, but also other factors, such as, galaxy masses, the GW distance uncertainty distribution.

Once a GW signal detected, the LIGO and ViRGO provide GW map to the astronomical community in `HEALPix` format, which produces a subdivision of a spherical surface in which each pixel covers the same surface area as every other pixel. For our galaxy priorization process, firstly, the script maps all DLT40 galaxies into the GW map with specific radius, using `Healpy`, the `python` version of `HEALPix`. Then, we add attribute of galaxy mass, smoothed to each pixel. At the same time, galaxy distance with respect to GW error, could be also evaluated.

```python
def makefitsmap_cat(ra,dec,dist,bmag,kmag,dmin,dmax,filtro,nside,radius,
    coord,ordering,norm,verbose,label,rot_phi,rot_theta):
    h_nside=nside
    smoothing=radius
    hubbleconstant=72
    speedoflight=3E5

    # Step 1 - as mentioned, we use luminosity as for the weight of mass.
    # and at this point, ask for a choose of filter, either K band or B
        band, since GWGC provides their informations for each galaxies.
    if not filtro in ['K','B']:
        print 'fliter not in dlt40 catalogue'
        return False
    elif filtro == 'K':MAG=kmag
    else:MAG=bmag

    # Step 2 - generation of the mass map, which is a 1-d array, i.e.
        galpixels_Range_lum, with each index of array corresponding to the
        coordinate, through healpy transformation.
    MAG,DIST,RA,DEC =np.array(MAG),np.array(dist),np.array(ra),np.array(
        dec)
    Lum=10**((-1)*(MAG/2.5))
    galpixels_Range_lum= np.zeros(hp.nside2npix(h_nside))
    include_me = np.logical_and((DIST > float(dmin)),\
                        np.logical_and((DIST < float(dmax)),\
                                        (MAG != 0.0)))
    ra_Range          = RA[include_me]
    dec_Range         = DEC[include_me]
    lum_Range         = Lum[include_me]
    galpixels_Range_lum[pix_num_Range]+=lum_Range
    print("Number of objects with %g < d < %g : %d" % (float(dmin),float(
        dmax),len(ra_Range)))

    # Step 3 - map smoothing with specific radius
    map2 = hp.sphtfunc.smoothing(galpixels_Range_lum,sigma = smoothing) #
        mass density

    # Step 4 - healpix figure show, and output the mass map.
    if verbose:
        maxv2=50*float(max(np.median(map2),np.mean(map2)))
        hp.mollview(rotate_map(map2,rot_theta,rot_phi),title='Relative
            Surface mass Density of Galaxies(%s): %g < d < %g '%(label,dmin
            ,dmax), unit='prob',nest=ordering,max=maxv2,coord=coord,norm=
            norm)
```

```
35   return map2
```

DLT40 pixelation script

The GW distance information was not included for galaxy priorization in O2, but will be implemented in O3, since LVC is expected to release this information along with GW triggers. The GW distance uncertainty was considered to have a Gaussian distribution, whose mean and variance communicated by LVC.

```
1   def galaxy_ranking(_dist, ligodist):
2       # as input, _dist is a 1-d array, containing distance informations of
               all galaxy samples.
3       # while in ligodist is a string, like 'mean,var', indicating the
             parameters constructed for a Gaussian distribution
4       score = []
5       dmean, dsigma = ligodist.split(',')
6       dmean, dsigma = float(dmean), float(dsigma)
7       for dist in _dist:
8           _score = np.e**(-(dist-dmean)**2/2./dsigma**2)
9           score.append(_score)
10      return np.array(score)
```

distance informations

The GW and galaxy weight normalized map are convolved and a galaxy priorization map, C is finally produced. Each galaxies is assigned a score by considering their contributions to C.

```
1   def calprob(skymap, ra, dec, nside, _radius, _verbose, _coord, _ordering, _norm):
2       problist = []
3
4       # Determine the HEALPix resolution.
5       deg2perpix = hp.nside2pixarea(nside, degrees=True)
6
7       # Convert from RA, Dec in degrees to spherical polar coordinates.
8       for ii, xx in enumerate(ra):
9           theta = 0.5 * np.pi - np.deg2rad(dec[ii])
10          phi = np.deg2rad(ra[ii])
11          vec = hp.ang2vec(theta, phi)
12          pix = hp.query_disc(nside, vec, _radius)
13          _theta, _phi = hp.pix2ang(nside, pix)
14
15          # query number from healpy map with specific coordinates
16          _prob = hp.get_interp_val(skymap, _theta, _phi)
17          prob = sum(_prob)
```

```
18          problist.append(prob)
19       problist = np.array(problist)
20    return problist
```

calculate probabilities

From this we can retrieve a list of galaxies sorted by priorization score which is then used for the observing schedule for the observing schedules afterwards.

Appendix D

"Kilonova" chat
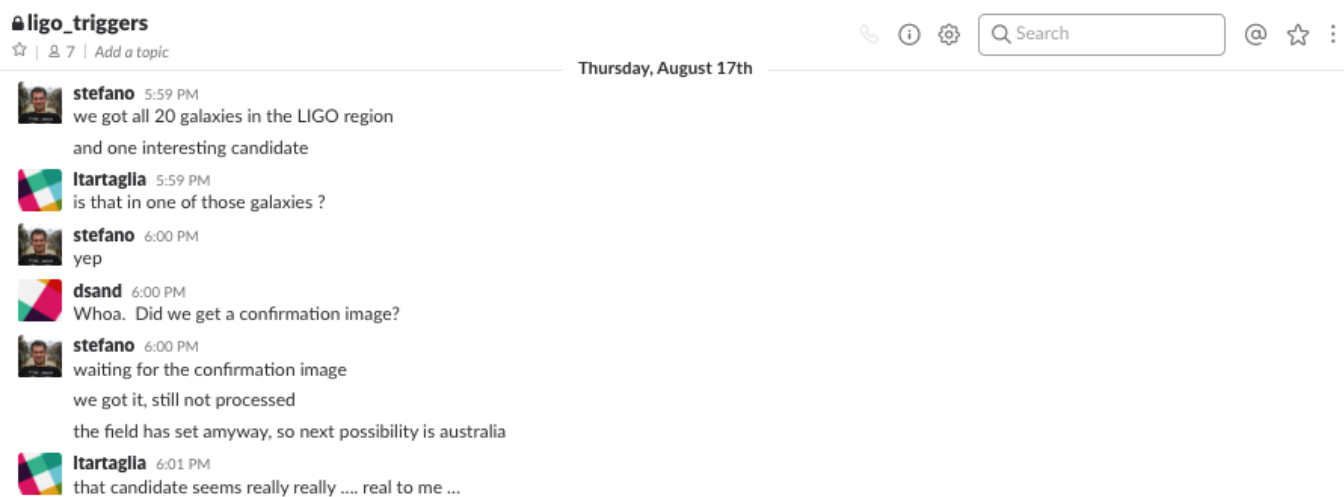
Figure D.1: An internal chat when detecting DLT17ck. At the moment, I was driving back home...

Bibliography

Aasi, J., Abbott, B. P., et al. 2015, Classical and Quantum Gravity, 32, 074001.

Aasi, J., Abadie, J., Abbott, B. P.,et al. 2015, Classical and Quantum Gravity, 32, 115012

Abadie, J., Abbott, B. P., Abbott, R., et al. 2010, Classical and Quantum Gravity, 27, 173001

Abbott, B. P., Abbott, R., Abbott, T. D., et al. 2016a, Physical Review D, 94, 102001

Abbott, B. P., Abbott, R., Abbott, T. D., et al. 2016b, Physical Review Letters, 116, 061102

Abbott, B. P., Abbott, R., Abbott, T. D., et al. 2016c, Physical Review Letters, 116, 241103

Abbott, B. P., Abbott, R., Abbott, T. D., et al. 2016d, Physical Review X, 6, 041015

Abbott, B. P., Abbott, R., Abbott, T. D., et al. 2016e, Astrophysical Journal, Supplement, 225, 8

Abbott, B. P., Abbott, R., Abbott, T. D., et al. 2016f, Astrophysical Journal, Supplement, 227, 14

Abbott, B. P., Abbott, R., Abbott, T. D., et al. 2016g, Astrophysics Journal, Letters, 818, L22

Abbott, B. P., Abbott, R., Abbott, T. D., et al. 2016h, Astrophysics Journal, Letters, 826, L13

Abbott, B. P., Abbott, R., Abbott, T. D., et al. 2016i, Astrophysics Journal, Letters, 832, L21

Abbott, B. P., Abbott, R., Abbott, T. D., et al. 2016j, Living Reviews in Relativity, 19, 1

Abbott, B. P., Abbott, R., Abbott, T. D., et al. 2017a, Physical Review Letters, 118, 221101

Abbott, B. P., Abbott, R., Abbott, T. D., et al. 2017b, Physical Review Letters, 119, 161101

Abbott, B. P., Abbott, R., Abbott, T. D., et al. 2017c, Physical Review Letters, 1, L21

Abbott, B. P., Abbott, R., Abbott, T. D., et al. 2017d, Astrophysics Journal, Letters, 851, L35

Abbott, B. P., Abbott, R., Abbott, T. D., et al. 2017e, Astrophysics Journal, Letters, 848, L12

Abbott, B. P., Abbott, R., Abbott, T. D., et al. 2017f, Nature, 551, 85

Abbott, B. P., Abbott, R., Abbott, T. D., et al. 2018, Living Reviews in Relativity21, 3

Acernese, F., Agathos, M., Agatsuma, K., et al. 2015, Classical and Quantum Gravity, 32, 024001

Adams, S. M., Kasliwal, M. M., & Blagorodnova, N. 2017, GRB Coordinates Network, 21816

Adrián-Martínez, S., Albert, A., André, M., et al. 2016, Physical Review D, 93, 122010

Agostini, M., Altenmüller, K., Appel, S., et al. 2017, Astrophysics Journal, 850, 21

Aguiar, O. D., 2010, arXiv: 1009.1138

Alard C., 1999, ArXiv Astrophysics e-prints,

Albert, A., André, M., Anghinolfi, M., et al. 2017d, Astrophysics Journal, Letters, 850, L35

Alexander, K. D., et al., 2017, Astrophysics Journal, Letters, 848, 2

Allam, S., Annis, J., Berger, E., et al. 2017, GRB Coordinates Network, 21530

Amati, L., et al. 2002, Astronomy and Astrophysics, 390, 81

Amati L., 2006, Monthly Notices of the RAS, 372, 233

A. Mller, S. Chang, C. W. 2017, GRB Coordinates Network, 21542

Anderson, J. P., Habergham, S. M., James, P. A., & Hamuy, M. 2012, Monthly Notices of the RAS, 424, 1372

Arcavi, I., Hosseinzadeh, G., Howell, D. A., et al. 2017, Nature, 551, 64

Arcavi, I., McCully, C., Hosseinzadeh, G., et al. 2017, Astrophysics Journal, Letters, 848, L33

Arnett, W. D. 1982, Astrophysics Journal, 253, 785

Arnouts, S., Cristiani, S., Moscardini, L., et al. 1999, Monthly Notices of the RAS, 310, 540.

Aso, Y., Michimura, Y., Somiya, K., et al. 2013, Physical Review D, 88, 043007

Astone P., Ballantini R.,, Babusci D., et al. 2008, Classical and Quantum Gravity, 25, 114048

Aubourg, É., Bailey, S., Bautista, J. E., et al. 2015, Physical Review D, 92, 123516

Bailey, S., Aragon, C., Romano, R., et al. 2007, Astrophysics Journal, 665, 1246

Baltay, C., Rabinowitz, D., Hadjiyska, E., et al. 2013, Publications of the Astronomical Society of the Pacific, 125, 683

Bannister, K., Lynch, C., Kaplan, D., et al.,, 2017, GRB Coordinates Network, 21559

Barbon R., Buondí V., Cappellaro E., Turatto M., 1999, Astronomy and Astrophysics, Supplement, 139, 531

Barnes J., Kasen D., 2013, Astrophysics Journal, 775, 18

Barnes, J., & Kasen, D. 2013, Astrophysics Journal, 775, 18

Bartos, I., Kowalski, M., 2017, Multimessenger Astronomy, 2399, 1

Bartos I., Kocsis B., Haiman Z., Márka S., 2017, Astrophysics Journal, 835, 165

Bartos, I., Countryman, S., Finley, C., et al. 2017a, GRB Coordinates Network, 21511

Bartos, I., Countryman, S., Finley, C., et al. 2017b, GRB Coordinates Network, 21568

Becker, A. 2015, Astrophysics Source Code Library, ascl:1504.004

beischer, B., Doetinchem, P. V., Gast, H., et al. 2009, New Journal of Physics, 11, 105021

Belczynski, K., Perna, R., Bulik, T., et al., 2006, Astrophysics Journal, 648, 1110

Bellm, E. 2014, The Third Hot-wiring the Transient Universe Workshop, 27

Benetti, S., Tomasella, L., Cappellaro, E., et al. 2015, GCN18563

Berger, E., Fong, W., & Chornock, R., 2013a, Astrophysics Journal, 774, L23

Berger, E., Leibler, C. N., Chornock, R., et al. 2013b, Astrophysics Journal, 779, 18

Berger, E. 2014, Annual Review of Astron and Astrophys, 52, 43

Berry C. P. L., et al., 2015, Astrophysics Journal, 804, 114

Bertin, E., & Arnouts, S. 1996, Astronomy and Astrophysics, Supplement, 117, 393

Bertin E., 2006, in Gabriel C., Arviset C., Ponz D., Enrique S., eds, Astronomical Society of the Pacific Conference Series, 351, 112

Bhalerao, V., Battacharya, D., Rao, A.R., & Vadawale, S., 2017a, GRB Coordinates Network, 20412

Bhalerao, V., Kasliwal, M. M., Battacharya, D., et al. 2017b, Astrophysics Journal, 845, 152

Bianco, F. B., Modjaz, M., Hicken, M., et al. 2014, Astrophysical Journal, Supplement, 213, 19

Blanchet, L. 2014, Living Reviews in Relativity, 17, 2

Blanton, M. R., Hogg, D. W., Bahcall, N. A., et al. 2003, Astrophysics Journal, 592, 819

Bloom, J. S., Kulkarni, S. R., Djorgovski, S. G., et al. 1999, Nature, 401, 453

Bloom, J. S., Kulkarni, S. R., & Djorgovski, S. G. 2002, Astronomical Journal, 123, 1111

Bonifazi P., Visco M.,1992, Il Nuovo Cimento C, 15, 943

Bonvin, V., Courbin, F., Suyu, S. H., et al. 2017, Monthly Notices of the RAS, 465, 4914

Botticella M. T., et al., 2016, The Universe of Digital Sky Surveys, 42, 197

Botticella, M. T., Smartt, S. J., Kennicutt, R. C., et al. 2012, Astronomy and Astrophysics, 537, A132

Breeveld, A. A., Curran, P. A., Hoversten, E. A., et al. 2010, Monthly Notices of the RAS, 406, 1687

Breiman L., 2001, Machine learning, 45, 5

Brink, H., Richards, J. W., Poznanski, D., et al. 2013, Monthly Notices of the RAS, 435, 1047

Brocato, E., et al. 1999, Astrophysics Journal, 527, 230

Brocato, E., Castellani, V., Poli, F. M., & Raimondo, G. 2000, Astronomy and Astrophysics, Supplement, 146, 91

Brocato E., et al., 2015a, GRB Coordinates Network, 18336

Brocato E., et al., 2015b, GRB Coordinates Network, 18397

Brocato, E., Branchesi, M., Cappellaro, E., et al. 2018, Monthly Notices of the RAS, 474, 411

Brown, P. J., Holland, S. T., Immler, S., et al. 2009, Astronomical Journal, 137, 4517

Brown, P. J., Roming, P. W. A., Milne, P., et al. 2010, Astrophysics Journal, 721, 1608

Brown, T. M., Baliber, N., Bianco, F. B., et al. 2013, Publications of the Astronomical Society of the Pacific, 125, 1031

Brown P. J., Breeveld A. A., Holland S., Kuin P., Pritchard T., 2014, Astrophysics and Space Science, 354, 89

Brown, P. J., Smitka, M. T., Wang, L., et al. 2015, Astrophysics Journal, 805, 74

Bufano, F., Pian, E., Sollerman, J., et al. 2012, Astrophysics Journal, 753, 67

Buonanno, A., & Damour, T. 1999, Physical Review D, D59, 084006

Calzetti, D., Armus, L., Bohlin, R. C., et al. 2000, Astrophysics Journal, 533, 682

Campana, S., Mangano, V., Blustin, A. J., et al. 2006, Nature, 442, 1008

Cano, Z., Bersier, D., Guidorzi, C., et al. 2011a, Astrophysics Journal, 740, 41

Cano, Z., Bersier, D., Guidorzi, C., et al. 2011b, Monthly Notices of the RAS, 413, 669

Capaccioli, M., Mancini D., Sedmak, G. 2003, MmSAI, 74, 450.

Capaccioli M., Schipani P., 2011, The Messenger, 146, 2

Capaccioli M., et al., 2015, Astronomy and Astrophysics, 581, A10

Cappellaro, E., Turatto, M., Benetti, S., et al. 1993, Astronomy and Astrophysics, 268, 472

Cappellaro, E., Turatto, M., Tsvetkov, D. Y., et al. 1997, Astronomy and Astrophysics, 322, 431

Cappellaro, E., Evans, R., & Turatto, M. 1999, Astronomy and Astrophysics, 351, 459

Cappellaro E., et al., 2001, Astrophysics Journal, Letters, 549, L215

Cappellaro E., et al., 2015, Astronomy and Astrophysics, 584, A62

Cardelli, J. A., Clayton, G. C., & Mathis, J. S. 1989, Astrophysics Journal, 345, 245

Carrick, J., Turnbull, S. J., Lavaux, G., & Hudson, M. J. 2015, Monthly Notices of the RAS, 450, 317

Castro-Tirado, A. J., & Gorosabel, J. 1999, Astronomy and Astrophysics, Supplement, 138, 449

Castro-Tirado, A. J., Sokolov, V. V., Gorosabel, J., et al. 2001, Astronomy and Astrophysics, 370, 398

Cerdonio M., Bonaldi M., Carlesso D., et al. 1997, Classical and Quantum Gravity, 14, 1491

Chambers, K. C., Huber, M. E., Smartt, S. J., et al. 2017, GRB Coordinates Network, 21553

Chincarini, G., Zerbi, F., Antonelli, L. A., et al., 2003, The Messenger, 113, 40

Clocchiatti A., Suntzeff N. B., Covarrubias R., Candia P., 2011, Astronomical Journal,141, 163

Collaboration, L. 2017a, GRB Coordinates Network, 21509

Collaboration, L. 2017b, GRB Coordinates Network, 21527

Connaughton, V., Burns, E., Goldstein, A., et al. 2016, Astrophysics Journal, Letters, 826, L6

Cooke, J., et al.,*manuscript in preparation*

Cornish, N. J., & Littenberg, T. B. 2015, Classical and Quantum Gravity, 32, 135012

Corsi, A., Ofek, E. O., Frail, D. A., et al. 2011, Astrophysics Journal, 741, 76

Corsi, A., Ofek, E. O., Gal-Yam, A., et al. 2012, Astrophysics Journal, 747, L5

Corsi, A., Gal-Yam, A., Kulkarni, S. R., et al. 2016, Astrophysics Journal, 830, 42

Corsi, A., et al. 2017, GRB Coordinates Network, 20396

Corsi, A., Hallinan, G., Mooley, K., et al. 2017, GRB Coordinates Network, 21815

Cortes C., Vapnik V., 1995, Machine learning, 20, 273

Coulter, D. A., Foley, R. J., Kilpatrick, C. D., et al. 2017, Science, 358, 1556

Cover T., Hart P., 1967, IEEE Transactions on Information Theory archive, 13, 21

Coward, D. M., Howell, E. J., Piran, T., et al. 2012, Monthly Notices of the RAS, 425, 2668

Crook, A. C., Huchra, J. P., Martimbeau, N., et al. 2007, Astrophysics Journal, 655, 790

Crook, A. C., Huchra, J. P., Martimbeau, N., et al. . 2008, Astrophysics Journal, 685, 1320

Crowther, P. A. 2013, Monthly Notices of the RAS, 428, 1927

D'Avanzo, P., Salvaterra, R., Sbarufatti, B., et al. 2012, Monthly Notices of the RAS, 425, 506

D'Avanzo, P., Salvaterra, R., Bernardini, M. G., et al., 2014, Monthly Notices of the RAS, 442, 234

D'Avanzo, P., Melandri, S., Covino, S., et al., 2017, GRB Coordinates Network, 21653

D'Elia, V., Pian, E., Melandri, A., et al. 2015, Astronomy and Astrophysics, 577, A116

Dálya, G., Galgóczi, G., Dobos, L., et al. 2018, Monthly Notices of the RAS, 479, 2374

Dalal, N., Holz, D. E., Hughes, S. A., & Jain, B. 2006, Physical Review D, 74, 063006

Dalya, G., Frei, Z., Galgoczi, G., Raffai, P., & de Souza, R. S. 2016, VizieR Online Data Catalog, 7275

de Mink, S. E.; King, A. 2017, Astrophysics Journal, Letters, 839,1, L7.

Del Pozzo, W. 2012, Physical Review D, D86, 043011

Delgado, A. and Harrison, D. and Hodgkin, S. and Leeuwen, M. V. and Rixon, G. and Yoldas, A., 2017, Transient Name Server Discovery Report, 632

Della Valle, M., Malesani, D., Benetti, S., et al. 2003, Astronomy and Astrophysics, 406, L33

Della Valle, M., Malesani, D., Bloom, J. S., et al. 2006, Astrophysics Journal, 642, 103

Dennefeld M., et al., 2015, The Astronomer's Telegram, 8268

Doctor, Z., Kessler, R., Chen, H. Y., et al. 2017, Astrophysics Journal, 837, 57

Dominik, M., Berti, E., O'Shaughnessy, R., et al. 2015, Astrophysics Journal, 806, 263

Drout, M. R., Soderberg, A. M., Gal-Yam, A., et al. 2011, Astrophysics Journal, 741, 97

Drout, M. R., Chornock, R., Soderberg, A. M., et al. 2014, Astrophysics Journal, 794, 23

Eichler, D., Livio, M., Piran, T., & Schramm, D., 1989, Nature, 340, 126

Einstein, A., 1905a, On the Electrodynamics of Moving Bodies. Annalen der Physik (ser. 4), 17, 891

Einstein, A., 1905b, Does the Inertia of a Body Depend upon its Energy Content? Annalen der Physik (ser. 4), 18, 639

Einstein, A., 1914, The Formal Foundation of the General Theory of Relativity. Sitzungsber. Preuss. Akad. Wiss. Berlin (Math. Phys.), 1914:1030

Einstein, A., 1915a, On the General Theory of Relativity. Sitzungsber. Preuss. Akad. Wiss. Berlin (Math. Phys.), 1915:778

Einstein, A., 1915b, The Field Equations of Gravitation. Sitzungsber. Preuss. Akad. Wiss. Berlin (Math. Phys.), 1915:844

Einstein, A., 1915c, Approximative Integration of the Field Equations of Gravitation. Sitzungsber. Preuss. Akad. Wiss. Berlin (Math. Phys.), 1916:688

Einstein A., 1916, Sitzungsberichte der Königlich Preußischen Akademie der Wissenschaften (Berlin), Seite 688

Einstein A., 1918, Sitzungsberichte der Königlich Preußischen Akademie der Wissenschaften (Berlin), Seite 154

Essick R., Vitale S., Katsavounidis E., Vedovato G., Klimenko S., 2015, Astrophysics Journal, 800, 81

Evans, P.A., Kennea, J.A., Barthelmy, S. et al. 2015, GRB Coordinates Network18569

Evans, P. A., Kennea, J. A., Palmer, D. M., et al. 2016, Monthly Notices of the RAS, 462, 1591

Evans, P. A., et al. 2017a, GRB Coordinates Network, 20390

Evans, P. A., et al. 2017b, GRB Coordinates Network, 20415

Evans, P.A., et al., 2017c, Science, 358, 1565

Ferrero, P., Kann, D. A., Zeh, A., et al. 2006, Astronomy and Astrophysics, 457, 857

Feulner, G., et al. 2005, Monthly Notices of the RAS, 358, 1

Filippenko, A. V., Barth, A. J., Matheson, T., et al. 1995, Astrophysics Journal, 450, L11

Filippenko, A. V. 1997, Annual Review of Astron and Astrophys, 35, 309

Firth, R. E., Sullivan, M., Gal-Yam, A., et al. 2015, Monthly Notices of the RAS, 446, 3895

Foley, R. J., Papenkova, M. S., Swift, B. J., et al. 2003, Publications of the Astronomical Society of the Pacific, 115, 1220

Fong, W. & Berger, E., 2010, Astronomical Journal, 708, 9

Fong, W., Berger, E., Chornock, R., et al. 2013, Astrophysics Journal, 769, 56

Fong, W., Margutti, R., Chornock, R., et al., 2016, Astronomical Journal, 833, 151

Fong, W., Berger, E., Margutti, R., & Zauderer, B. A. 2015, Astrophysics Journal, 815, 102

Fong, W., Margutti, R., & Haggard, D. 2017, GRB Coordinates Network, 21786

Freedman, W. L., Madore, B. F., Gibson, B. K., et al. 2001, Astrophysics Journal, 553, 47

Freudling, W., Romaniello, M., Bramich, D. M., et al., 2013, Astronomy and Astrophysics, 559, A96

Freund, Y., Schapire, R. E., 1997, Journal of Computer and System Sciences, 55: 119

Fried, D. L. 1966, J. Opt. Soc. Am., 56, 10

Friedman N., Geiger D., Goldszmidt M., 1997, Machine Learning - Special issue on learning with probabilistic representations archive, 29, 131

Frohmaier C., Dimitriadis G., Firth R. e. a., 2016, GRB Coordinates Network, 18806

Fryer C., New, K., 2011, Living Reviews in Relativity, 14,1

Górski, K. M., Hivon, E., Banday, A. J., et al. 2005, Astrophysics Journal, 622, 759

Gal-Yam, A., Ofek, E. O., & Shemmer, O. 2002, Monthly Notices of the RAS, 332, L73

Galama T. J., et al., 1998,Nature, 395, 670

Galama, T. J., Tanvir, N., Vreeswijk, P. M., et al. 2000, Astrophysics Journal, 536, 185

Gallo Rosso, A., Mascaretti, C., Palladino, A., & Vissani, F. 2018, European Physical Journal Plus, 133, 267

Gehrels, N. 1986, Astrophysics Journal, 303, 336

Gehrels, N., Cannizzo, J. K., Kanner, J., et al. 2016, Astrophysics Journal, 820, 136

Geurts P., Ernst D., Wehenkel L., 2006, Machine Learning, 63, 3

Ghirlanda, G., Nava, L., Ghisellini, G., et al., 2012, Monthly Notices of the RAS, 420, 483

Ghirlanda, G., Salafia, O. S., Pescalli, A., et al., 2016, Astronomy and Astrophysics, 594, A84

Ghirlanda G., et al., 2016,Astronomy and Astrophysics, 594, A84

Ghisellini, G., Ghirlanda G., Mereghetti, S., et al., 2006, Monthly Notices of the RAS, 372, 1699

Gieseke, F., Bloemen, S., van den Bogaard, C., et al. 2017, Monthly Notices of the RAS, 472, 3101

Glampedakis, K., & Gualtieri, L. 2017, arXiv:1709.07049

Goldstein, A., Veres, P., von Kienlin, A., et al., 2017a, GRB Coordinates Network, 21528

Goldstein, A., Veres, P., Burns, E., et al. 2017, Astrophysics Journal, Letters, 848, L14

Goobar, A. 2008, Astrophysics Journal, Letters, 686, L103

Gossan, S. E., Sutton, P., Stuver, A., et al. 2016, Physical Review D, 93, 042002

Grado A., Capaccioli M., Limatola L., Getman F., 2012, Memorie della Societa Astronomica Italiana Supplementi, 19, 362

Grado A., 2015, GRB Coordinates Network, 18734

Grado, A., Cappellaro, E., Greco, G., et al., 2017a, GRB Coordinates Network, 21598

Grado, A., Getman, F., Limatola, L., et al., 2017b, GRB Coordinates Network, 21703

Greco, G., et al. 2017, GRB Coordinates Network, 21498

Greiner, J., Klose, S., Salvato, M., et al. 2003, Astrophysics Journal599, 1223

Guillochon J., Parrent J., Kelley L. Z., Margutti R., 2017, Astrophysics Journal, 835, 64

Gupta, R. R., Kuhlmann, S., Kovacs, E., et al. 2016, Astronomical Journal, 152, 154

Haggard, D., et al., 2017, Astrophysics Journal, Letters, 848, 2

Hallinan, G., et al., 2017, Science, 358,1579

Hannam, M., Schmidt, P., Bohé, A., et al. 2014, Physical Review Letters, 113, 151101

Harmanen J., et al., 2015, The Astronomer's Telegram, 8264

Harutyunyan, A., Pfahler, P., Pastorello, A., et al., 2008, Astronomy and Astrophysics, 488, 383

Heger, A., Fryer, C. L., Woosley, S. E., Langer, N., & Hartmann, D. H. 2003, Astrophysics Journal, 591, 288

Henning, J. W., Sayre, J. T., Reichardt, C. L., et al. 2018, Astrophysics Journal, 852, 31

Hinderer, T., & Flanagan, É. É. 2008, Physical Review D, 78, 064028

Hinshaw, G., Weiland, J. L., Hill, R. S., et al. 2009, Astrophysical Journal, Supplement, 180, 225

Hirata K., Kajita T., Koshiba M., et al. 2016, Physical Review Letters, 58, 1490

Hjorth, J., Sollerman, J., Moller, P., et al. 2003, Nature, 423, 847

Holz, D. E., & Hughes, S. A. 2005, Astrophysics Journal, 629, 15

Horne, K. 1986, Publications of the Astronomical Society of the Pacific, 98, 609

Hosseinzadeh, G., Sand, D. J., Valenti, S., et al. 2017, Astrophysics Journal, Letters, 845, L11

Huang, J.-S., Cowie, L. L., & Luppino, G. A. 1998, Astrophysics Journal, 496, 31

Huber, M., Chambers, K. C., Flewelling, H., et al. 2015, The Astronomer's Telegram, 7153

Huchra, J. P., Macri, L. M., Masters, K. L., et al. 2012, Astrophysical Journal, Supplement, 199, 26

Hulse, R. A., & Taylor, J. H. 1975, Astrophysics Journal, Letters, 195, L51

Hunt, L. K., Palazzi, E., Michałowski, M. J., et al. 2014, Astronomy and Astrophysics, 565, A112

Hunter, D. J., Valenti, S., Kotak, R., et al. 2009, Astronomy and Astrophysics, 508, 371

Daniel Clery [IceCube Collaboration], 2018, Science, 361, 115

Ilbert, O., Arnouts, S., McCracken, H. J., et al. 2006, Astronomy and Astrophysics, 457, 841

Iwamoto K., et al., 1998, Nature, 395, 672

Iwamoto, K., Nakamura, T., Nomoto, K., et al. 2000, Astrophysics Journal, 534, 660

Japelj, J., Vergani, S. D., Salvaterra, R., et al. 2016, å, 590, 129

Jin, Z.-P., Covino, S., Della Valle, M., et al. 2013, Astrophysics Journal, 774, 114

Jin, Z.-P., Li, X., Cano, Z., et al. 2015, Astrophysics Journal, Letters, 811, L22

Jin, Z.-P., Hotokezaka, K., Li, X., et al. 2016, NatureCommunications, 7, 12898

Jones, D. H., Read, M. A., Saunders, W., et al., 2009, Monthly Notices of the RAS, 399, 683

Jones, A., & Noll, S., Kausch, W., et al., 2013, Astronomy and Astrophysics, 560, A91

Kalogera, V., Kim, C., Lorimer, D. R., et al. 2004, Astrophysics Journal, Letters, 601, L179

Kasen, D., Badnell, N. R., & Barnes, J. 2013, Astrophysics Journal, 774, 25

Kasen, D., & Fernández, R., Metzger, B. D. 2015, Monthly Notices of the RAS, 450, 1777

Kasliwal, M. M., Cenko, S. B., Kulkarni, S. R., et al. 2011, Astrophysics Journal, 735, 94

Kasliwal, M., Adams, S., Vedantham, H., et al. 2017,GRB Coordinates Network, 20393

Kasliwal, M.M., et al., 2017, Science, 358, 1559

Kausch, W., & Noll, S., Smette, A., et al., 2015, Astronomy and Astrophysics, 576, A78

Kawaguchi K., Kyutoku K., Shibata M., Tanaka M., 2016, Astrophysics Journal, 825, 52

Kessler, R., Becker, A. C., Cinabro, D., et al. 2009, Astrophysical Journal, Supplement, 185, 32

Khazov, D., Yaron, O., Gal-Yam, A., et al. 2016, Astrophysics Journal, 818, 3

Kim, C., Perera, B. B. P., & McLaughlin, M. A. 2015, Monthly Notices of the RAS, 448, 928

Kinney, A. L., Calzetti, D., Bohlin, R. C., et al. 1996, Astrophysics Journal, 467, 38

Klimenko S., et al., 2016, Physical Review D, 93, 042004

Komatsu, E., Smith, K. M., Dunkley, J., et al. 2011, Astrophysical Journal, Supplement, 192, 18

Kopparapu, R. K., Hanna, C., Kalogera, V., et al. 2008, Astrophysics Journal, Letters, 675, 1459

Kuijken, K. 2011, The Messenger,146, 8

Kulkarni, S. R., Modelling Supernova-like Explosions Associated with Gamma-ray Bursts with Short Durations, 2005, astro-ph/0510256

Kulkarni, S. R. 2013, The Astronomer's Telegram, 4807

LIGO Scientific Collaboration et al., 2015, Classical and Quantum Gravity, 32, 074001

LIGO Scientific Collaboration 2016, GRB Coordinates Network, 19145

LIGO/VIRGO Scientific Collaboration 2015a, GRB Coordinates Network, 18330

LIGO/VIRGO Scientific Collaboration 2015b, GRB Coordinates Network, 18728

LIGO/VIRGO Scientific Collaboration 2015c, GRB Coordinates Network, 18889

LIGO Scientific Collaboration and Virgo, 2015d, GRB Coordinates Network, 18442

LIGO/VIRGO Scientific Collaboration 2016a, GRB Coordinates Network, 18858

LIGO Scientific Collaboration and Virgo, 2016b, GRB Coordinates Network, 18626

LIGO Scientific Collaboration, Aasi, J., Abbott, B. P., et al. 2015, Classical and Quantum Gravity, 32, 074001

LIGO/Virgo Collaboration. 2017a, GRB Coordinates Network, 21505

LIGO/Virgo Collaboration. 2017b, GRB Coordinates Network, 21513

The LIGO Scientific Collaboration & the Virgo Collaboration 2017c, Physical Review Letters, 119, 161101

LIGO/Virgo Scientific Collaboration. 2017a, GRB Coordinates Network, 21505

LIGO/Virgo Scientific Collaboration. 2017b, GRB Coordinates Network, 21513

LIGO/Virgo Scientific Collaboration. 2017c, GRB Coordinates Network, 20364

The LIGO Scientific Collaboration, the Virgo Collaboration, Abbott, B. P., et al. 2018, arXiv:1805.11581

Larson, D., Dunkley, J., Hinshaw, G., et al. 2011, Astrophysical Journal, Supplement, 192, 16

Lattimer, J. M., Mackie, F., Ravenhall, D. G., & Schramm, D. N., 1977, Astrophysics Journal, 213, 225

Lattimer, J. M. 2012, Annual Review of Nuclear and Particle Science, 62, 485

Law, N.M., Kulkarni, S.R., Dekany, R.G., et al., 2009, Publications of the Astronomical Society of the Pacific, 121, 1395

Lazzati, D., Lopez-Camara, D., Cantiello, M., et al., 2017, Astrophysics Journal, Letters, 848, 7

Leaman, J., Li, W., Chornock, R., & Filippenko, A. V. 2011, Monthly Notices of the RAS, 412, 1419

Levan, A.J., et al., 2017a, Astrophysics Journal, 848, L28

Levan, A. J., Lyman, J. D., Steeghs, D.T.H., et al., 2017b), GRB Coordinates Network, 21681

Li, W., Leaman, J., Chornock, R., et al. 2011, Monthly Notices of the RAS, 412, 1441

Li, L.-X., & Paczyński, B. 1998, Astrophysics Journal, Letters, 507, L59

Liang, E.-W, Li, L., Gao, H., et al., 2013, Astrophysics Journal, 774, 13

Lipunov, V. M., Gorbovskoy, E., Kornilov, V. G., et al. 2017, Astrophysics Journal, Letters, 850, L1

Lipunov, V., Gorbovskoy, E., V.G.Kornilov, et al. 2017, GRB Coordinates Network, 21546

Lira P., et al., 1998, Astronomical Journal, 116, 1006

Loeb, A. 2016, Astrophysics Journal, Letters, 819, L21

Loh W. Y., 2014, International Statistical Review, 82, 3, 329

Loredo, T. J. 2004, AIP Conference Series, 735, 195

Lyman, J. D., Bersier, D., James, P. A., Mazzali, P. A., Eldridge, J. J., Fraser, M., & Pian, E. 2016, MNRAS, 457, 328

Lyman, J., Homan, D., Maguire, K., et al. 2017, GRB Coordinates Network, 21582

Maeda, K., Kawabata, K., Mazzali, P. A., et al. 2008, Science, 319, 1220

Makarov D., Prugniel P., Terekhova N., Courtois H., Vauglin I., 2014, Astronomy and Astrophysics, 570, A13

Malesani, D., Tagliaferri, G., Chincarini, G., et al. 2004, Astrophysics Journal, 609, 5

Malesani, D., Watson, D., Hjorth, J., et al. 2017, GRB Coordinates Network, 21577

Mandel, I., Farr, W. M., & Gair, J. 2016, Extracting distribution parameters from multiple uncertain observations with selection biases, Tech. rep., LIGO, `https://dcc.ligo.org/LIGO-P1600187/public`

Marcinkovski, R., Xiao, H., & Hajdas, W., 2017, GRB Coordinates Network, 20387

Masci, F. J., Laher, R. R., Rebbapragada, U. D., et al. 2017, Publications of the Astronomical Society of the Pacific, 129, 014002

Matheson, T., Filippenko, A. V., Li, W., Leonard, D. C., & Shields, J. C. 2001, Astronomical Journal, 121, 1648

Mauceli, E., Geng, Z. K., Hamilton, W. O., et al. 1996, Physical Review D, 54, 1264

Mazzali, P. A., Iwamoto, K., & Nomoto, K. 2000, Astrophysics Journal, 545, 407

Mazzali, P. A., Deng, J., Maeda, K., et al. 2002, Astrophysics Journal, 572, L61

Mazzali, P. A., Kawabata, K. S., Maeda, K., et al. 2005, Science, 308, 1284

Mazzali, P. A., Deng, J., Nomoto, K., et al. 2006, Nature, 442, 1018

Mazzali, P., Valenti, S., Della Valle, M. 2008, Science, 321, 1185

Mazzali P. A., Walker E. S., Pian E., Tanaka M., Corsi A., Hattori T., Gal-Yam A., 2013, Monthly Notices of the RAS, 432, 2463

Melandri, A., Pian, E., Ferrero, P., et al. 2012, Astronomy and Astrophysics, 547, A82

Melandri, A., Pian, E., D'Elia, V., et al. 2014, Astronomy and Astrophysics, 567, 29

Melandri, A., Campana, S., Covino, S., et al. 2017a, GRB Coordinates Network, 21532

Melandri, A., D'Avanzo, P., Campana, S., et al., 2017b, GRB Coordinates Network, 21556

Messenger, C., & Veitch, J. 2013, NJP, 15, 053027

Metzger, B. D., Martínez-Pinedo, G., Darbha, S., et al. 2010, Monthly Notices of the RAS, 406, 2650

Metzger, B. D., & Berger, E. 2012, Astrophysics Journal, 746, 48

Metzger, B. D. 2017, arXiv:1710.05931

Metzger17, B. D. 2017, Living Reviews in Relativity, 20, 3

Millard, J., Branch, D., Baron, E., et al. 1999, Astrophysics Journal, 527, 746

Miller, A. A., Kulkarni, M. K., Cao, Y., et al. 2017, Astronomical Journal, 153, 73

Mirabal, N., Halpern, J. P., An, D., Thorstensen, J. R., & Terndrup, D. M., Astrophysics Journal, 643, 99

Modigliani, A., Goldoni, P., Royer, F., et al., 2010, Proceedings of the SPIE, 7737

Modjaz, M., Blondin, S., Kirshner, R. P., et al. 2014, Astronomical Journal, 147, 99

Moehler, S., Modigliani, A., Freudling, W., et al., 2014, Astronomy and Astrophysics, 568, A9

Moharana, R., Razzaque, S., Gupta, N., & Mészáros, P. 2016, Physical Review D, 93, 123011

Moldon, J., & Beswick, R. 2017, GRB Coordinates Network, 21804

Monard L. A. G., et al., 2015, Central Bureau Electronic Telegrams, 4081

Mooley, K. P., et al. 2017a, GRB Coordinates Network, 20425

Mooley, K., Hallinan, G., & Corsi, A. 2017b, GRB Coordinates Network, 21814

Mooley, K., et al., 2017c, GRB Coordinates Network, 21891

Mukhopadhyay, S., Lahiri, J., Atta, D., Imam, K., & Basu, D. N. 2018, Physical Review C, 97, 065804

Munari, U. & Zwitter, T., 1997, Astronomy and Astrophysics, 318, 269

Munari, U. & Tomasella, L., Fiorucci, M., et al., 2008, Astronomy and Astrophysics, 488, 969

Nakar, U. & Piran, T. 2017, Astrophysics Journal, 834, 28

Nava, L., Salvaterra, R., Ghirlanda, G., et al. 2012, Monthly Notices of the RAS, 421, 1256

Newton, I., 1687, Philosophi naturalis principia mathematica, Londini, Jussu Societatis Regi ac Typis Josephi Streater. Prostat apud plures Bibliopolas. Anno 1687

Nissanke, S., Holz, D. E., Hughes, S. A., Dalal, N., & Sievers, J. L. 2010, Astrophysics Journal, 725, 496

Nissanke, S., Holz, D. E., Dalal, N., et al. 2013, arXiv:1307.2638

Noll, S., Kausch, W., Barden, M., et al., 2012, Astronomy and Astrophysics, 543, A92

Nomoto, K., & Hashimoto, M. 1988, Phys. Rep., 163, 13

Ofek, E.O., Laher, R., Surace, J., et al. 2012, Publications of the Astronomical Society of the Pacific, 124, 62

Ott, C. D., O'Connor, E. P., Gossan, S., et al. 2013, Nuclear Physics B Proceedings Supplements, 235, 381

Palliyaguru, N. T., Corsi, A., Kasliwal, M. M., et al. 2016, Astrophysics Journal, Letters, 829, L28

Pan Y.-C., Downing S., Foley R. J., Jha S. W., Rest A., Scolnic D., 2016, The Astronomer's Telegram, 8506

Pan, Y.-C., et al., 2017, Astrophysics Journal, 848

Patat F., et al., 2001, Astrophysics Journal, 555, 900

Patricelli, B., Razzano, M., Cella, G., et al., 2016, Journal of Cosmology and Astroparticle Physics, 11, 056

Perley, D. A., Quimby, R. M., Yan, L., et al. 2016, Astrophysics Journal, 830, 13

Perna R., Lazzati D., Giacomazzo B., 2016, Astrophysics Journal, Letters, 821, L18

Pescalli A., Ghirlanda G., Salafia O. S., Ghisellini G., Nappo F., Salvaterra R., 2015, Monthly Notices of the RAS, 447, 1911

Petrillo, C. E., Dietz, A., & Cavaglià, M. 2013, Astrophysics Journal, 767, 140

Pian E., et al., 2000, Astrophysics Journal, 536, 778

Pian, E., Mazzali, P. A., Masetti, N., et al. 2006, Nature, 442, 1011

Pian, E., D'Elia, V., Piranomonte, S., et al., 2017, GRB Coordinates Network, 21592

Pian, E., & D'Avanzo, P., & Benetti, S., et al., 2017 , Nature, 551, 67

Pignata, G., Stritzinger, M., Soderberg, A., et al. 2011, Astrophysics Journal, 728, 14

Piran, T., Nakar, E., & Rosswog, S. 2013, Monthly Notices of the RAS, 430, 2121

Planck Collaboration, Ade, P. A. R., Aghanim, N., et al.2015, Astronomy and Astrophysics, 594, 63

Planck Collaboration, Ade, P. A. R., Aghanim, N., et al. 2016, Astronomy and Astrophysics, 594, A13

Pogge, R. W., Atwood, B., Brewer, D. F., et al. 2010, Proc. SPIE, 7735, 77350A

Poole, T. S., Breeveld, A. A., Page, M. J., et al. 2008, Monthly Notices of the RAS, 383, 627

Poznanski, D., Prochaska, J. X., & Bloom, J. S., 2012, Monthly Notices of the RAS, 426, 1465

Prentice, S. J,, Mazzali, P. A., Pian, E., et al. 2016, Monthly Notices of the RAS, 458, 2973

Pritchard, T. A., Roming, P. W. A., Brown, P. J., Bayless, A. J., & Frey, L. H. 2014, Astrophysics Journal, 787, 157

Rabinowitz, D., Baltay, C., Ellman, N., et al. 2015, GRB Coordinates Network18572

Rabinowitz, D., & Baltay, C. 2017, GRB Coordinates Network, 21599

Racusin, J. L., Liang, E. W., Burrows, D. N., et al. 2009, Astrophysics Journal, 698, 43

Radovich M., et al., 2004, Astronomy and Astrophysics, 417, 51

Raimondo, G. 2009, Astrophysics Journal, 700, 1247

Rau, A., et al., 2009, Publications of the Astronomical Society of the Pacific, 121, 1334

Reichart, D., Nysewander, M., Moran, J., et al. 2005, Nuovo Cimento C Geophysics Space Physics C, 28, 767

Richmond, M. W., Van Dyk, S. D., Ho, W., et al. 1996, Astronomical Journal, 111, 327

Riess, A. G., Macri, L. M., Hoffmann, S. L., et al. 2016, Astrophysics Journal, 826, 56

Riles, K., Gravitational Waves: Sources, Detectors and Searches, 2013, Progress in Particle and Nuclear Physics, 68, 1

Romano R. A., Aragon C. R., Ding C. 2006, Proceedings - 5th International Conference on Machine Learning and Applications, ICMLA 2006, IEEE, 77

Rossi, A., Piranomonte, S., Savaglio, S., et al. 2014, Astronomy and Astrophysics, 572, A47

Rosswog, S., Feindt, U., Korobkin, O., et al., 2017, Classical and Quantum Gravity, 34, 104001

Sadler, E. M., Allison, J. R., Kaplan, D. L., Murphy, T., & on behalf of the VAST collaboration. 2017, GRB Coordinates Network, 21645

Sakai, S., Mould, J. R., Hughes, S. M. G., et al. 2000, Astrophysics Journal, 529, 698

Salafia, O. S., Ghisellini, G., Pescalli, A., Ghirlanda, G., Nappo, F. 2015, Monthly Notices of the RAS, 450, 3549

Salafia, O. S., Ghisellini, G., Pescalli, A., Ghirlanda, G., & Nappo, F., 2016, Monthly Notices of the RAS, 461, 3607

Sari, R., Piran, T., & Narayan, R. 1998, Astrophysics Journal, Letters, 497, L17

Sari, R., Piran, T., & Halpern, J. P. 1999, Astrophysics Journal, Letters, 519, L17

Sathyaprakash, B.S., 2009, Living Reviews in Relativity, 12, 141

Savaglio, S., Glazebrook, K., & Le Borgne, D. 2009, Astrophysics Journal, 691, 182

Savchenko, V., et al. 2017, Astrophysics Journal, Letters, 848

Scalzo R., Yuan F., Childress M., Tucker B., Zhang B., Ruiter A., Seitenzahl I., Schmidt B., 2015, Central Bureau Electronic Telegrams, 4115

Schipani P., et al., 2016, in Ground-based and Airborne Instrumentation for Astronomy VI. p. 990841

Schlafly, E. F., & Finkbeiner, D. P. 2011, Astrophysics Journal, 737, 103

Schutz, B. F. 1986, Nature, 323, 310

Schulze, S., Klose, S., Björnsson, G., et al. 2011, Astronomy and Astrophysics, 526, A23

Schulze, S., Malesani, D., Cucchiara, A., et al. 2014, Astronomy and Astrophysics, 566, A102

Scolnic, D., Kessler, R., & Brout, D. 2018, Astrophysics Journal, Letters, 852, 7

Seitenzahl, I. R., Herzog, M., Ruiter, A. J., et al. 2015, Physical Review D, 92, 124013

Shapee B. J., et al. 2017, Science, 358, 6370, 1574

Sharma, V., Bhalerao, V., Battacharya, D., Rao, A.R., & Vadawale, S., 2017, GRB Coordinates Network, 20389

Shivvers I., Yuk H., Graham M. L., Filippenko A. V., 2015, The Astronomer's Telegram, 7955

Siegel, M. H., Porterfield, B. L., Linevsky, J. S., et al. 2014, Astronomical Journal, 148, 131

Siellez, K., Boër, M., & Gendre, B. 2014, Monthly Notices of the RAS, 437, 649

Singer L. P., et al., 2013, Astrophysics Journal, Letters, 776, L34

Singer L. P., et al., 2014, Astrophysics Journal, 795, 105

Singer, L.P., Kasliwal, M.M., Ferretti, R., et al. 2015, GRB Coordinates Network18497

Singer, L. P., Chen, H.-Y., Holz, D. E., et al. 2016, Astrophysics Journal, Letters, 829, L15

Singer, L. P., & Price, L. R. 2016, Physical Review D, 93, 024013

Skrutskie, M. F., Cutri, R. M., Stiening, R., et al. 2006, Astronomical Journal, 131, 1163

Smart R. L., Nicastro L., 2014, Astronomy and Astrophysics, 570, A87

Smartt, S. J., Valenti, S., Fraser, M., et al. 2015, Astronomy and Astrophysics, 579, A40

Smartt S. J., et al., 2016a, Monthly Notices of the RAS, 462, 4094

Smartt, S. J., Chambers, K. C., Smith, K. W., et al. 2016b, Astrophysics Journal, Letters, 827, L40

Soares-Santos M., et al., 2016, Astrophysics Journal, Letters, 823, L33

Soares-Santos, M., Holz, D. E., Annis, J., et al. 2017, Astrophysics Journal, Letters, 848, L16

Soderberg, A. M., Chakraborti, S., Pignata, G., et al. 2010, Nature, 463, 513

Sollerman, J., Jaunsen, A. O., Fynbo, J. P. U., et al. 2006, Astronomy and Astrophysics, 454, 503

Sparre, M., Sollerman, J., Fynbo, J. P. U., et al. 2011, Astrophysics Journal, 735, 24

Spiro, S., Pastorello, A., Pumo, M. L., et al. 2014, Monthly Notices of the RAS, 439, 2873

Springob, C. M., Magoulas, C., Colless, M., et al. 2014, Monthly Notices of the RAS, 445, 2677

Spurio, Maurizio, 2015, Particles and Astrophysics: A Multi-Messenger Approach, Springer, 46.

Stalder, B., Tonry, J., Smartt, S. J., et al. 2017, Astrophysics Journal, 850, 149

Starling R. L. C., et al., 2011, Monthly Notices of the RAS, 411, 2792

Steele, I. A., Smith, R. J., Rees, P. C., et al. 2004, Proc. SPIE, 5489, 679

Steele, I.A., Copperwheat, C.M., & Piascik, A.S. 2015, GRB Coordinates Network18573

Stetson, P. B. 1987, Publications of the Astronomical Society of the Pacific, 99, 191

Strauss, M. A., & Willick, J. A. 1995, Phys. Rep., 261, 271

Stritzinger M., et al., 2012, Astrophysics Journal, 756, 173

Svinkin, D., et al., 2017, GRB Coordinates Network, 20406

Szegedy, C., Vanhoucke, V., Ioffe, S., Shlens, J., & Wojna, Z. 2015, arXiv:1512.00567

Taddia, F., Sollerman, J., Leloudas, G., et al. 2015, Astronomy and Astrophysics, 574, A60

Tanaka, M., & Hotokezaka, K., 2013, Astrophysics Journal, 775, 113

Tanaka, M., & Kato, D., Gaigalas, G., et al., 2018, Astrophysics Journal, 852, 12

Tanvir, N. R., Levan, A., Fruchter, A. S., et al., 2013, Nature, 500, 547

Tanvir, N. R., Levan, A. J., González-Fernández, C., et al. 2017, Astrophysics Journal, Letters, 848, L27

Tartaglia, L., Sand, D. J., Valenti, S., et al. 2018, Astrophysics Journal, 853,16

Tattersall, O. J., Ferreira, P. G., & Lagos, M. 2018, Physical Review D, 97, 084005

Taubenberger, S., Pastorello, A., Mazzali, P. A., et al. 2006, Monthly Notices of the RAS, 371, 1459

Tody, D. 1993, A.S.P. Conference Ser,52, 173

Tolstoy, E., Hill, V., & Tosi, M. 2009, Annual Review of Astron and Astrophys, 47, 371

Tomasella, L., Cappellaro, E., Brocato, E., et al. 2015a, GRB Coordinates Network18561

Tomasella, L., Cappellaro, E., D'Avanzo, P. , et al. 2015b, GRB Coordinates Network18566

Tonry, J., et al., 2017, GRB Coordinates Network, 20382

Troja, E., Piro, L., van Eerten, H. J., et al., 2017, Nature, 551, 71

Turatto, M. 2003, Supernovae and Gamma-Ray Bursters, 598, 21

Usman, S. A., Nitz, A. H., Harry, I. W., et al. 2016, Classical and Quantum Gravity, 33, 215004

Valenti, S., Benetti, S., Cappellaro, E., et al. 2008a, Monthly Notices of the RAS, 383, 1485

Valenti, S., Elias-Rosa, N., Taubenberger, S., et al. 2008b, Astrophysics Journal, 673, L155

Valenti, S., & David, Sand, & Yang, S, et al. 2017, Astrophysics Journal, Letters, 848, L24

Van Eerten, H. J, Leventis, K., Meliani, Z., et al., 2010, Monthly Notices of the RAS, 403, 300

Vangioni, E., Goriely, S., Daigne, F., François, P., & Belczynski, K. 2016, Monthly Notices of the RAS, 455, 17

Veitch, J., Raymond, V., Farr, B., et al. 2015, Physical Review D, 91, 042003

Vergani, S. D., Salvaterra, R., Japelj, J., et al. 2015, Astronomy and Astrophysics, 581, 102

Vernet, J., Dekker, H., DOdorico, S., et al., 2011, Astronomy and Astrophysics, 536, A105

Vines, J., Flanagan, É. É., & Hinderer, T. 2011, Physical Review D, 83, 084051

Walker, E. S., Mazzali, P. A., Pian, E., et al. 2014, Monthly Notices of the RAS, 442, 2768

Walker, E. S., Baltay, C., Campillay, A., et al. 2015, Astrophysical Journal, Supplement, 219, 13

Wanderman, D. & Piran T. 2015, Monthly Notices of the RAS, 448, 3026

Waters, C. Z., Zepf, S. E., Lauer, T. R., et al. 2006, Astrophysics Journal, 650, 885

Wenger M., et al., 2000, Astronomy and Astrophysics, Supplement, 143, 9

Wheeler, J. C., Yi, I., Höflich, P., & Wang, L. 2000, Astrophysics Journal, 537, 810

White, D. J., Daw, E. J., & Dhillon, V. S. 2011, Classical and Quantum Gravity, 28, 085016

Willingale, R., Starling, R. L. C., Beardmore, A. P., Tanvir, N. R., & O'Brien, P. T. 2013, Monthly Notices of the RAS, 431, 394

Wolf, C., Chang, S., & Muller, A. 2017, 2017, GRB Coordinates Network, 21560

Wollaeger, R. T., Korobkin, O., Fontes, C. J., et al., 2018, Monthly Notices of the RAS, 478, 3298

Wright, D. E., Smartt, S. J., Smith, K. W., et al. 2015, Monthly Notices of the RAS, 449, 451

Wyrzykowski L., Kostrzewa-Rutkowska Z., Udalski A., Kozlowski S., Kubiak M., Sitek M., 2014, The Astronomer's Telegram, 6753

Yamazaki R., Asano K., Ohira Y., 2016, Progress of Theoretical and Experimental Physics, 2016, 051E01

Yamazaki R., Yonetoku D., Nakamura T., 2003, Astrophysics Journal, Letters, 594, L79

Yang, S., Valenti, S., Sand, D., et al. 2017a, GRB Coordinates Network, 21531

Yang, S., Valenti, S., Sand, D., et al. 2017b, GRB Coordinates Network, 21579

Yang, S, & Valenti. S, & Cappellaro, E. et al. 2017, Astrophysics Journal, Letters, 851, L2

Zeh, A., Klose, S., & Hartmann, D. H. 2004, Astrophysics Journal, 609, 952

Zhang, B., Fan, Y. Z., Dyks, J., et al. 2006, Astrophysics Journal, 642, 354

Zhang S.-N., Liu Y., Yi S., Dai Z., Huang C., 2016, preprint, (arXiv:1604.02537)

Zwicky, F. 1942, Astrophysics Journal, 96, 28

de Mink, S. E., & Belczynski, K. 2015, Astrophysics Journal, 814, 58

de Mink S. E., King A., 2017, Astrophysics Journal, Letters, 839, L7

du Buisson, L., Sivanandam, N., Bassett, B. A., & Smith, M. 2015, Monthly Notices of the RAS, 454, 2026

van Eerten, H. J., & MacFadyen, A. I. 2011, Astrophysics Journal, Letters, 733, L37

van der Kruit, P. C. 1987, Astronomy and Astrophysics, 173, 59

Weber, J., 1960, Physical Review, 117: 306

Weber, J., 1967, Physical Review Letters, 18: 498

Weber, J., 1968, Physical Review Letters, 20: 1307

Weber, J., 1969, Physical Review Letters, 22: 1320

Weber, J., 1972, Popular Science, 200: 106 & 190